

Mathematical Analysis and Numerical Simulation of Electromigration

by

Jon Arthur Wilkening

B.S. (University of Arizona) 1996

A dissertation submitted in partial satisfaction of the
requirements for the degree of
Doctor of Philosophy

in

Mathematics

in the

GRADUATE DIVISION

of the

UNIVERSITY of CALIFORNIA at BERKELEY

Committee in charge:

Professor James A. Sethian, Chair
Professor Alexandre J. Chorin
Professor Andrew K. Packard

Spring 2002

Mathematical Analysis and Numerical Simulation of Electromigration

Copyright 2002

by

Jon Arthur Wilkening

Abstract

Mathematical Analysis and Numerical Simulation of Electromigration

by

Jon Arthur Wilkening

Doctor of Philosophy in Mathematics

University of California at BERKELEY

Professor James A. Sethian, Chair

We develop a model for mass transport phenomena in microelectronic interconnect lines, study its mathematical properties, and present a number of new numerical methods which are useful for simulating the process.

The central focus of the work is an investigation of the well-posedness of the grain boundary diffusion problem. The equation is stiff and non-local and depends on gradients of the stress components σ_{ij} , which contain singularities near corners and grain boundary junctions. We show how to recast the problem as an ODE on a Hilbert space, and prove that the non-selfadjoint compact operator involved has a real, non-negative spectrum and a set of eigenfunctions which is dense in $L^2(\Gamma)$, where Γ is the grain boundary network. We show that in the limit of an infinite interconnect line, the eigenfunctions are sines and cosines, and through numerical studies show that for a finite line, in spite of non-orthogonality, the eigenfunctions form a well conditioned basis for $L^2(\Gamma)$. We develop a numerical method for simulating the evolution process, and obtain results which are self-consistent under mesh-refinement and make physical sense.

The main tool we develop for solving the elasticity equations with high resolution near corners and grain boundary junctions is a singularity capturing extension of the First Order System Least Squares finite element method. We call the method XFOSLS. The method is designed for polygonal domains with corners, cracks, and interface junctions, and can handle complicated jump discontinuities along interfaces while maintaining smooth displacement and stress fields (which may be unbounded near corners) within each region of the domain. Several self-similar (not necessarily singular) solutions may be adjoined to each

corner or junction, and the supports of the extra basis functions may overlap one another.

We also present a number of new techniques for computing bases of self-similar solutions for corners and interface junctions. These include an algorithm for removing rank deficiency from the basis matrix at isolated parameter values, a stabilization algorithm for removing near linear dependency from the power solutions corresponding to characteristic exponents which are clustered together, and a new theorem about Keldysh chains which leads to an algorithm for computing associated functions. Several examples are given which illustrate the techniques.

Professor James A. Sethian
Dissertation Committee Chair

To Anna and my parents

Contents

List of Figures	v
1 Introduction	1
1.1 Literature Survey: Modeling	2
1.2 Literature Survey: Numerics	3
1.3 The Grain Growth Problem	4
1.4 Stable Asymptotics Near Corners	6
1.5 Some Pitfalls: How Did We Get Here?	8
1.6 Capturing Singularities: XFOSLS	10
2 A Model of Mass Transport in Interconnect Lines	15
2.1 The Setup	16
2.1.1 The Potential Problem	16
2.1.2 The Elasticity Problem	17
2.1.3 The Separation Function	18
2.1.4 Further Boundary Conditions	20
2.2 Mass Conservation	21
2.2.1 Vacancy Evolution in the Grains	22
2.2.2 Void Evolution	23
2.2.3 Grain Boundary Evolution	23
2.3 Driving Forces for Diffusion	23
2.3.1 The Einstein-Nernst Relation	24
2.3.2 The Chemical Potential at a Surface	26
2.3.3 The Chemical Potential at a Grain Boundary	26
2.3.4 The Chemical Potential in the Bulk	27
2.3.5 Elastic Energy	28
2.3.6 Electromigration and Summary	28
2.4 Interface Junctions	29
2.4.1 Grain Boundary Network	30
3 The Grain Growth Problem	33
3.1 Plane Elasticity as a First Order ADN System	36
3.1.1 New Variables	37

3.1.2	The Operators L and B	38
3.1.3	ADN Indices	40
3.1.4	A Few Remarks	41
3.2	Complex Variable Methods in Plane Elasticity	42
3.3	An Infinite Interconnect Line	44
3.3.1	Elastic Equations for Sinusoidal Separation	44
3.3.2	Evolution for an Arbitrary Initial Separation	48
3.3.3	Steady Current	49
3.4	A Finite Geometry	49
3.4.1	Two Model Problems	50
3.4.2	Operator Adjoints	53
3.4.3	A Reformulation	55
3.4.4	Desired Properties of K	59
3.4.5	Numerical Strategy	64
3.4.6	Results	71
3.4.7	More Complicated Geometries	82
3.4.8	More Results	90
3.4.9	Properties of B and K	100
4	Corner Singularities	107
4.1	Interface Problems	108
4.2	Examples	109
4.3	Mellin Transform	112
4.4	Homogeneous Solutions	114
4.5	A Basis for $\mathcal{W}(\lambda)$	116
4.6	The Boundary Condition Matrix $A(\lambda)$	120
4.7	Computing the Roots of $\Delta(\lambda)$	122
4.7.1	Implementation	125
4.8	Computing Pure and Associated Power Solutions	127
4.9	Stabilizing the Self-Similar Basis Functions	135
5	XFOSLS	139
5.1	Data Structures for Extending the Finite Element Space	141
5.2	The Fringe Region	143
5.3	An Affine Subspace	145
5.4	Boundary Conditions	147
5.5	A Minimization Problem	151
5.6	Constructing the Stiffness and Jump Matrices	152
5.7	Results	155
6	Conclusion	161
	Bibliography	163

List of Figures

1.1	Left: Scanning Electron Micrograph picture of a multilevel CMOS integrated circuit with the intermetallic dielectric etched away. (From <i>Solid State Electronic Devices</i> , Streetman/Banerjee [73]). Right: Schematic view of the components of a microchip. (From <i>Microchip Fabrication</i> , Van Zant [81]). . . .	2
2.1	Geometry of an interconnect line.	16
2.2	Arbitrary local orientation of grain boundary segment determines tangential and normal directions, left and right grain labels, etc.	18
2.3	Meaning of the separation function g . The regions between dashed and solid lines in the top two pictures represent material which has been added or removed from each grain during the transport process. The actual displacements would be much smaller than those shown here.	19
2.4	Compatibility condition on the separation function g at a triple point. . . .	20
2.5	Volume and surface fluxes \mathbf{J} and \mathbf{J}_s give the number of atoms crossing area and line elements $d\mathbf{A}$ and $d\mathbf{l}$ when dotted with them. In 2D simulations we are still modeling 3D objects, so the units are $(\text{cm}^2\text{s})^{-1}$ and $(\text{cm s})^{-1}$, respectively.	21
2.6	The continuity equation and void growth equation are a consequence of mass conservation.	22
2.7	Left: high resolution TEM microscope image of a large tilt angle grain boundary in a gold thin film. (From <i>Electronic Thin Film Science for Electrical Engineers and Materials Scientists</i> , Tu/Mayer/Feldman [77]). Right: grain growth occurs when more atoms flow into a region of the grain boundary than out.	24
2.8	Two systems in thermal and diffusive contact must have equal chemical potentials.	25
2.9	The energy of formation of a vacancy and the activation energy for exchanging a vacancy with an adjacent atom both decrease in the vicinity ($\delta =$ a few lattice constants) of a grain boundary [44, 77].	29
2.10	The electric field can lead to a flux imbalance at a triple point which must be compensated by stress gradients to satisfy mass conservation.	31

3.1	Top: Summary of equations and boundary conditions for the grain growth problem. Bottom: Flowchart illustrating the relationship between the major topics of Chapter 3.	34
3.2	The force per unit area exerted <i>by</i> the positive side <i>on</i> the negative side of a surface with normal \mathbf{n} is given by $\sigma \mathbf{n}$	39
3.3	The geometry and boundary conditions for the grain growth problem on an infinite strip.	45
3.4	A plot of $C(\omega)$ for $h = 1$ and $\kappa = 1.15, 1.4, 2.0, 3.0$. Note that $C(\omega)$ diverges in the incompressible ($\kappa \rightarrow 1$), long wavelength ($\omega \rightarrow 0$) limit.	47
3.5	A plot of the dissipation rate $C(\omega)\omega^2$ for $h = 1$ and $\kappa = 1.001, 1.01, 1.1, 2.0$. Note that even though $C(\omega)$ is not monotonic for $\kappa < 2$, $C(\omega)\omega^2$ is monotonic for $\omega \geq 0$. The envelope of the graphs approaches $\frac{3}{2} + \frac{27}{10}\omega^2$ near the origin as $\kappa \rightarrow 1$	48
3.6	The geometry and boundary conditions of a finite interconnect line with a single horizontal grain boundary running through its center.	55
3.7	A contour plot of $\sigma_{22}(x, y)$ corresponding to the steady state solution. Note that σ_{22} decreases linearly along the grain boundary to balance the constant electromigration force that arises due to the linearly increasing potential ψ . (s22 is σ_{22}).	56
3.8	It suffices to be able to solve $g_t = -LSg$ for $g \in L^2_{MZ}$	57
3.9	A plot of the absolute value of $f(z) = \frac{1}{z}(e^{-z} - 1) + 1$ along the rays $z = s$, $z = \frac{1+2i}{\sqrt{5}}s$, $z = \frac{1+7i}{\sqrt{50}}s$, $z = is$. The maximum principle together with the graph along $z = \pm is$ gives that $ f(z) < 1.5$ for all z in the right half plane.	63
3.10	Each grain is triangulated separately, leading to an unstructured mesh with duplicate nodes along grain boundaries. This particular mesh corresponds to a mesh parameter $h = 0.05$ for an interconnect line of unit height and length two.	65
3.11	Sparsity pattern for several matrices. (a) The stiffness matrix A which results from the least squares finite element method for the mesh in Fig. 3.10. (b) The lower triangle of the matrix \tilde{A} obtained from A using <i>symamd</i> to re-order the rows and columns. (c) The Cholesky factorization L , where $LL^T = \tilde{A}$	67
3.12	The first 14 basis functions e_i for the space of separations. Each of the three special basis functions shown consists of a power solution piece (of the form $\text{Re}\{cr^\lambda\}$) and a quadratic piece. The exponents involved here are $\lambda = 0.680$ and $1.709 \pm 0.604i$	68
3.13	Evolution of the normal stress η along the grain boundary for the two meshes at $t = 0.005, 0.01, 0.02, 0.04, 0.08, 0.16, 0.32$	75
3.14	Evolution of the separation function g along the grain boundary for the two meshes at $t = 0.005, 0.01, 0.02, 0.04, 0.08, 0.16, 0.32$	76
3.15	Log-Log plot of eigenvalues λ_j of K vs. index j . The red and blue curves (a) and (b) show the eigenvalues obtained from the coarse and fine meshes, respectively. The green line (c) is a plot of $0.32j^{-3}$, which appears to be the asymptotic limit of the spectrum of K for large j . In the bottom plot, we zoom in on a portion of the top plot.	77

3.16	The first 4 eigenfunctions φ_k of K . Note that the eigenfunctions are smooth, oscillatory, and satisfy zero flux boundary conditions at the endpoints. The scales are arbitrary (normalized as vectors in R^n rather than in L^2).	78
3.17	The first 4 eigenfunctions ϕ_k of \tilde{K} . Note that they are smooth, oscillatory, and satisfy the zero displacement boundary conditions at the endpoints. The scales are arbitrary (normalized as vectors in R^n rather than in L^2).	79
3.18	The first 3 eigenfunctions φ_k^* of K^* along with the corresponding (rescaled) eigenfunctions ϕ_k of \tilde{K} . A surprising discovery: $\tilde{K} = K^*$. The coefficients in the expansion $\eta = \sum a_k \varphi_k$ are determined by $a_k = \int \eta \varphi_k^*$, so these functions can be thought of as linear functionals.	80
3.19	Steady state solution.	81
3.20	Arbitrary local orientation of grain boundary segment determines tangential and normal directions, left and right grain labels, etc.	82
3.21	Each grain is triangulated separately, leading to an unstructured mesh with duplicate nodes along grain boundaries and triple nodes at triple junctions. Offsets have been added to the nodes of each grain here to show the finite element connectivity of the spacially coincident grain boundary nodes to the interior nodes. This particular mesh corresponds to a mesh parameter $h = 0.06$ for an interconnect line which fits in a rectangle of length 4.25 and height 2.	86
3.22	The normal stress variables are ordered by taking the grain boundary endpoints and triple points first, and then sweeping through the interior of each grain boundary segment. The separation variables include the special basis functions used to capture asymptotic behavior near corners and triple junctions. These basis functions all have zero normal stress on grain boundaries. The apparently large amplitude of the coefficients on these special basis functions is an artifact of how they are normalized in the code. This evolution will be further discussed in Section 3.4.8.	87
3.23	To visualize an evolution such as the one shown in Fig. 3.22, we define a matrix which maps the jumbled variables to a picture of the result on that segment, taking into account the singular basis functions. Shown here is the support of the operator for the segment from corner 16 to corner 24, and its use in visualizing the evolution on this segment.	88
3.24	Compatibility condition on the separation function g at a triple point.	89
3.25	Top: Corners and grain boundary junctions are numbered arbitrarily. Middle: The electrostatic potential ψ satisfies Laplace's equation with Dirichlet boundary conditions at the ends and Neumann boundary conditions on the side walls. We use standard variational finite elements with quadratic elements on the mesh used in the elasticity problem to determine ψ along Γ . Bottom: A plot of the number of degrees of freedom that affect the variables at a given vertex or edge node. In this simulation, 101 extra basis functions near corners and junctions are used to capture asymptotic behavior.	93

- 3.26 The evolution of g and η on the segment from junction 16 to junction 24 in Fig. 3.25. Times shown are $t = .03, .06, .12, .24, .48, .96, \infty$. The plot was obtained by applying the visualization operator for this segment (c.f. Fig. 3.23) to the evolution of the variables shown in Fig. 3.22 on Page 87. 94
- 3.27 The evolution of g and η on the segment from junction 24 to junction 27 at $t = .03, .06, .12, .24, .48, .96, \infty$. Note that initially material leaves this segment, but the flux of mass at the triple point changes sign around $t = .045$ and ultimately the grains separate along this segment. 95
- 3.28 The evolution of g and η on the segment from junction 25 to junction 7 at $t = .03, .06, .12, .24, .48, .96, \infty$. Note that unlike the simple horizontal geometry, the steady state normal stress $\eta = P^*(-\psi|_{\Gamma})$ does not vary linearly along grain boundary segments. Also note that g develops an infinite slope at the endpoints due to singularities. Asymptotically, $g \sim \sum c_i r^{\lambda_i}$ with $\lambda_i^{(7)} \in \{0, .799, .886\}$ and $\lambda_i^{(25)} \in \{0, .725, .951\}$. The other stress components diverge at the ends (like $r^{\lambda-1}$ with $\lambda^{(7)} \in \{.799, .886\}$ and $\lambda^{(25)} \in \{.725, .951\}$), but η remains well behaved. 96
- 3.29 Top: Magnified view of the steady state separation $g(\mathbf{x})$, obtained by plotting $\mathbf{x} + C\mathbf{u}^+(\mathbf{x})$ and $\mathbf{x} + C\mathbf{u}^-(\mathbf{x})$ with \mathbf{x} along the grain boundary. Bottom: Contour plot of the magnitude of the displacements in each grain, together with streamlines tangent to the displacement vector field. Note that material is transported from the left end of the interconnect line to the right, causing the grains to move toward each other ($g < 0$) on the left side and to separate ($g > 0$) on the right. 97
- 3.30 Contour plots of the steady state values of $p = \frac{1}{2}(\sigma_{11} + \sigma_{22})$, $\mu^{-1}\sigma_{ij}\epsilon_{ij} = \frac{\kappa-1}{2}p^2 + \gamma^2 + \tau^2$, and $(\gamma^2 + \tau^2)^{\frac{1}{2}}$. Note that the left and right ends of the line are generally in a state of tension and compression, respectively, due to the transport of mass from left to right. Also note that the stresses are largest where the grains have separated the most, and at re-entrant corners and grain boundary junctions where they have singularities. 98
- 3.31 Contour plots of the steady state values of $(u^2 + v^2)^{\frac{1}{2}}$, p , τ , and $\frac{\kappa-1}{2}p^2 + \gamma^2 + \tau^2$ for a grain boundary network with two connected components. On each component, material has been transported from left to right until the gradient of σ_{nn} balances the electromigration force. The break in the network in the middle of the line acts as a barrier to limit the effective length of the line. Large stresses develop at the gb-wall junctions where the centermost grain is being pushed to the right by grain growth on its left and grain annihilation on its right, but is clamped in place at the top and bottom. The net result of the barrier, however, is to reduce the distance over which the stress gradient must balance the electromigration force, and hence the maximum stress is smaller than it would be for a single component grain boundary network on an interconnect line of this length. 99

3.32	Each grain is traversed counterclockwise with unit inward normal \mathbf{n} . The contribution of a particular grain boundary segment to the total elastic energy $E = \sum E_k$ contains precisely one term from the left grain and one term from the right grain.	100
4.1	The angles ω_k divide \mathbb{R}^2 into several regions Ω_k	108
4.2	Geometry of Example 9: a corner with Dirichlet boundary conditions imposed along one ray and traction boundary conditions imposed along the other. Recall (page 39) that $u_{\parallel} = \mathbf{u} \cdot \mathbf{t}$, $u_{\perp} = \mathbf{u} \cdot \mathbf{n}$, $\sigma_s = \mathbf{t} \cdot \boldsymbol{\sigma} \mathbf{n}$, $\sigma_{\perp} = \mathbf{n} \cdot \boldsymbol{\sigma} \mathbf{n}$, and $\mathbf{T} = \boldsymbol{\sigma} \mathbf{n}$	111
4.3	<i>Top:</i> Radial and angular dependence of the six components u , v , p , q , γ , τ of a nontrivial solution of the form $w_j(r, \theta) = r^{\lambda+t_j} \phi_j(\theta)$ ($\lambda = 0.6157$) to the incompressible Lamé equations with Dirichlet boundary conditions on each ray of the region ($-\pi/6 < \theta < 7\pi/6$). <i>Bottom:</i> A 3D plot of the variable τ	117
4.4	Contour plots of the zero level sets of the real and imaginary parts of $\Delta(\lambda)$ along with the contours generated by the clustering algorithm for finding roots. Top: wall-gb-wall geometry with $\omega_0 = 90^\circ$, $\omega_1 = 173^\circ$, $\omega_2 = 270^\circ$. Bottom: triple grain boundary junction with $\omega_0 = -174^\circ$, $\omega_1 = -51^\circ$, $\omega_2 = 45^\circ$, $\omega_3 = 186^\circ$. Note that some clusters contain multiple (or nearly multiple) roots which must be resolved accurately.	126
4.5	Algorithm for finding all Keldysh chains at λ_0	132
4.6	<i>Top:</i> Contour plot of the zero level sets of the real and imaginary parts of $\Delta(\lambda)$ for a T-shaped triple grain boundary junction with angles $\omega_0 = -90^\circ$, $\omega_1 = 90^\circ$, $\omega_2 = 180^\circ$, $\omega_3 = 270^\circ$ and elastic constant $\kappa = 1.6$. There is a zero of order 6 at $\lambda = 0$, a simple zero at $\lambda = 0.6298473$, a zero of order 4 at $\lambda = 1$, and a zero of order 3 at $\lambda = 2$. At $\lambda = 0$, the kernel of $A(\lambda)$ has dimension 3 and there are 3 linearly independent Keldysh chains of length two. At $\lambda = 1$ and $\lambda = 2$, the dimension of the kernel is respectively 4 and 3, so there are no associated functions at these values of λ . <i>Bottom:</i> When the geometry is perturbed, ($\omega_1 \rightarrow 80^\circ$ here), the root at $\lambda = 0$ remains unchanged (including Keldysh chain structure), the root at $\lambda = 1$ splits into a simple root at $\lambda \approx 1$ and a threefold root at $\lambda = 1$, and the root at $\lambda = 2$ splits into three simple roots, one equal to 2 and the others complex. This example illustrates many of the complicated possibilities that can occur.	133
4.7	Contour plot of the zero level sets of the real and imaginary parts of $\Delta(\lambda)$ for a checkerboard pattern of two materials with Lamé coefficients $\mu_1 = 1$, $\mu_2 = 10$, $\kappa_1 = 1$, $\kappa_2 = 2.4$. Note the four nearly identical roots near $\lambda = 2.8 \pm .96i$	136
5.1	Each grain is triangulated separately, leading to an unstructured mesh with duplicate nodes along grain boundaries. This particular mesh corresponds to a mesh parameter $h = 0.033$ for an interconnect line of unit height and length two.	142

5.2	The fringe region of a regular hexagonal mesh corresponding to <i>fringe_radius</i> =3. Nodes within a radius of $3h$ inclusive are “near” nodes. Triangles with some near nodes and some far nodes are “fringe” triangles. If several singularities exist at the corner, each may have a different <i>fringe_radius</i>	144
5.3	Typical entry in the boundary condition file.	148
5.4	Geometry of a junction where a grain boundary meets a wall.	149
5.5	Comparison of γ for the steady state solution to the grain growth problem near a corner using XFOSLS (top) and standard Galerkin finite elements (bottom). The roughness of the contours in the top plot is an artifact of visualization, where linear interpolation is being used to compute contour lines on the four sub-triangles joining the six nodes of each triangular element; see also Figure 5.6.	156
5.6	A contour plot showing the behavior of the solution γ from Figure 5.5 near a grain boundary junction with a wall. Points were uniformly sampled within the triangles of the mesh shown.	157
5.7	The solution obtained via the Galerkin method with a much finer grid still exhibits undesirable behavior near the corner, where the stress obtained via Lagrange multipliers differs significantly from the stress obtained by differentiating the displacements.	158
5.8	The solution of the Lamé equations with $\kappa = 1$ on a hexagonal geometry. Here the inner hexagon remains fixed while the outer hexagon has boundary conditions corresponding to rotation clockwise by a radian.	159

Acknowledgements

I am very grateful to my dissertation committee, James Sethian, Alexandre Chorin, and Andrew Packard. Thank you for tolerating my tendency to wait until the last possible minute to finish things.

I owe special thanks to Len Borucki for all the time and energy he put into working on the electromigration problem with Jamie and myself during his extended visits to LBL over the past several years. Len, it has been a pleasure working with you.

My thanks to G. I. Barenblatt for many useful conversations, and for offering a unique and insightful perspective (both mathematical and historical) on many occasions. I would also like to thank the many wonderful professors I have taken classes with and gotten to know over the years, especially James Sethian, Alexandre Chorin, G. I. Barenblatt, Ole Hald, Jim Demmel, John Strain, Craig Evans, Michael Christ, William Arveson, Alan Weinstein, Hendrik Lenstra, James Colliander, Charles Pugh, Alistair Sinclair, Doug Pickrell, William Conway, Johann Rafelski, Charles Falco, Donald Huffman, Eugene Commins, Steven Louie, and Eyvind Wichmann. They have been excellent role models as scientists and mathematicians.

I have been very fortunate to have the opportunity to work in the mathematics group at the Lawrence Berkeley National Laboratory. I would especially like to thank Valerie Heatlie for all her kindness and support. She is without doubt the anchor which binds the group together socially. Thanks for everything, Val. I would also like to thank David Adalsteinsson, Ravi Malladi, Anton Kast, Raz Kupferman, Andreas Wiegmann, Sergey Fomel, Alex Vladimirsky, Alina Chertock, Maria Garzon, Mayya Tokman and Thomas Deschamps, my recent office mates Alek Shestakov, Dror Givon, and Mike Campbell, and my fellow students Kevin Lin, Eugene Ingerman, Chris Cameron, Masha Kourkina, Panos Stinis, Pavel Okunev, Theresa Chow, and Helen Shvets.

I'd like to thank my good friends Kenley Jung, Charles Holton, Joe Fendel and Kurt Schneider for all the cut-throat poker and monopoly nights, Kevin Lin for braving several physics courses with me, Darren Kessner for making my first year of graduate school bearable, and Steve, Rachel, Dell, Anna R., Super Dave, Eric, Abby, Polly and Helen for being partners in crime at the swimming pool.

I was supported from 1997 through 2001 by a Department of Energy Computational Science Graduate Student Fellowship. This fantastic program helped connect me to

the world of scientific computing, and I am very grateful to have had the opportunity to be a part of the program. I very much enjoyed my practicum experience in the T7 and CNLS divisions at Los Alamos in the summer of 1999. I would particularly like to thank Pieter Swart, Dave Moulton, Joel Dendy, Mac Hyman, and Antti Pihlaja for making this visit so enjoyable.

Finally, I get to thank my advisor, James Sethian, for being my friend and mentor, for being optimistic in the face of difficulties, for being tough on me when I get off track, for keeping things in perspective and helping me do the same, and for being an exceptional applied mathematician whom I will always respect and admire. Thank you Jamie.

And to Anna, Mom, Dad, Tom, Katie, Mike, Linda, Louis, Ali and Jason, what can I say? You guys are the greatest, and I love you dearly.

Chapter 1

Introduction

A microelectronic circuit consists of a silicon substrate with doped regions which function as circuit elements (transistors, diodes, resistors, and capacitors), metal lines and vias (interconnects) which connect the circuit elements together, intermetallic dielectric material which keeps the interconnects in place and insulated from each other, various oxide layers and diffusion barriers which are primarily needed in the manufacturing stage to control the doping process and keep the aluminum from diffusing into the silicon, and passivation to keep all the components in place and protected [73, 81]. See Figure 1.1.

A typical interconnect line might be an alloy of Al-0.5%Cu, have dimensions of $0.5 \times 0.5 \times 300$ microns, and carry a current density of $20 \text{ mA}/\mu\text{m}^2$. As electrons flow through the line, they are scattered by imperfections in the crystal lattice of the metal and impart momentum to the ion cores. This "electron wind" force is stronger than the opposing direct force of the electric field, so ions are transported in the same direction as the flow of electrons. This process is known as electromigration, and is a dominant failure mechanism in microelectronic devices.

Grain boundaries, void surfaces, and passivation interfaces are fast diffusion paths along which the diffusion constant is typically 7-8 orders of magnitude higher than in the grains; therefore, most of the mass transport occurs at these locations. The inhomogeneous redistribution of atoms leads to the development of stresses in the line. Stress gradients along grain boundaries and surface tension at void surfaces both contribute to the flux of atoms, usually opposing the electromigration term and increasing the lifetime of the line. Significant residual stresses left over from thermal contraction during the manufacturing process also affect the formation of voids and the transport of atoms.

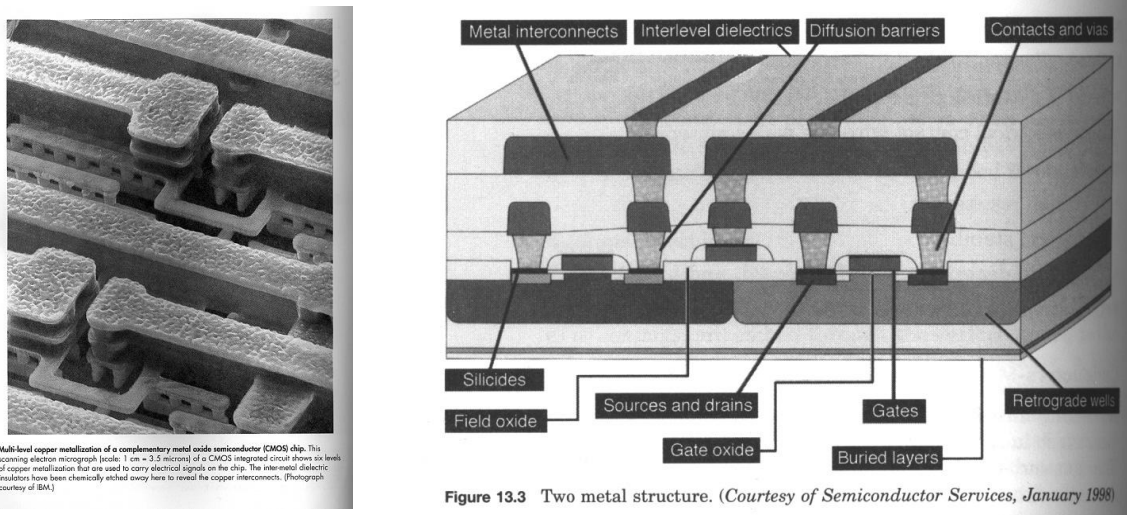


Figure 1.1: Left: Scanning Electron Micrograph picture of a multilevel CMOS integrated circuit with the intermetallic dielectric etched away. (From *Solid State Electronic Devices*, Streetman/Banerjee [73]). Right: Schematic view of the components of a microchip. (From *Microchip Fabrication*, Van Zant [81]).

1.1 Literature Survey: Modeling

A good reference on electromigration is the review article by Ho and Kwok [38]. The concept of the “electron wind” force was formulated by Fiks (1959) and by Huntington and Grone (1961) [40]. In his experimental work in the 70’s, Blech [7] studied the behavior of thin films of aluminum and Titanium-Nickel when large currents were passed through them, and demonstrated the phenomenon of the existence of a threshold current density below which no damage occurs, which varies inversely with the stripe length. Shortly thereafter, Blech and Herring [8] offered the explanation that stress gradients were developing along grain boundaries in the sample to counter the electron wind force, but could only be sustained up to a critical threshold. Once this threshold was reached, there was no physical mechanism to stop the transport of material, and the stripe was eroded at one end and formed hillocks at the other. Herring is best known for his work in the theory of of chemical potentials of atoms at free surfaces due to surface tension, and along grain boundaries due to stresses [37]. The growth of grain boundary voids in copper wires under stress was studied experimentally by Hull and Rimmer in 1959 [39].

Recent theoretical models attempt to explain the role of various combinations of electromigration, stress gradients, diffusion, temperature, anisotropy, surface tension, and hillock formation on the mass transport of atoms in the bulk grains, along void surfaces, along grain boundaries, and at passivation interfaces. Noteworthy theoretical papers that we are familiar with are the paper of Mullins [56], Korhonen et. al. [47], Sarychev et. al. [68], Kirchheim [42], and Bower/Craft [9]. The Mullins paper presents a nice overview of mass transport along surfaces and grain boundaries, and discusses Cobble creep and grain boundary grooving. The papers [68] and [42] are primarily interested in electromigration, stress driven diffusion, and vacancy generation in the grains, and [47] focuses on electromigration and grain boundary diffusion. The latter three papers use a statistical argument about the orientation of the grain boundaries in order to model the stress as a scalar variable instead of a tensor; one should keep in mind, however, that for any particular sample, the grain boundaries have a specific geometry, and singularities can occur in the stress field which get ignored with this simplifying assumption. In [64], the authors attempt to give a quantum mechanical explanation of the electron wind force experienced by an adatom at the surface of a current-carrying metal. There is no universal agreement in the electromigration community on exactly how all the phenomena fit together, especially at junctions where grain boundaries meet voids or other grain boundaries, and the process of void nucleation is far from being understood. It is fairly well established, however, that high current densities together with gradients in chemical potential drive mass transport, which is enough to build computational models of varying degrees of complexity.

1.2 Literature Survey: Numerics

There have been several numerical simulations of void evolution which take surface diffusion and electromigration (but not stress) into account. In [69], a boundary element method is used to follow the evolution of a void in an infinite domain with a constant current boundary condition at infinity. They investigate the stability of the void shape and speed of propagation as a function of void size. In [52] and [2], level set methods [70] are employed to track void evolution for a finite geometry. The former uses the immersed interface method [51] to compute the electrostatic potentials, and the latter uses black box multigrid [28]. Both suffer from serious timestep limitations due to a CFL condition from surface diffusion, and neither uses an accurate enough electrostatic solver to compute two derivatives of

the electrostatic potential along the void boundary. Both exhibit grid effects. In [6], the self-similar pinchoff problem for axisymmetric surface diffusion is studied, in which they introduce a very nice implicit finite difference method which deals effectively with the CFL problems encountered in the previously mentioned papers. None of these papers includes the effect of stress or the transport of atoms along grain boundaries or in the bulk.

The most comprehensive computational models with which we are familiar are described in several papers by Bower, Craft, Fridline and collaborators; see, for example, [9] and [33]. They use an advancing front algorithm to generate a sequence of adaptive, evolving finite element meshes, and have studied grain growth, void evolution, hillock formation, and grain boundary sliding for possibly anisotropic materials responding to stress, surface tension, thermal expansion, and electromigration. They use some clever semi-implicit techniques to overcome timestep limitations due to the stiffness of the equations.

1.3 The Grain Growth Problem

In the present work, we focus attention on the grain growth problem with a network of grain boundaries but no voids. We are particularly interested in the effect of singularities in the stress field near corners and triple points on the solution, and on questions of well-posedness of the equations and boundary conditions.

In the limiting case of an interconnect line of infinite length with a single grain boundary running through its center, we show that it is possible to write down an explicit formula for the solution by using methods of analytic function theory in planar elasticity. This formula is useful in understanding the similarities and differences between the grain growth problem and two well understood parabolic equations, namely $u_t = u_{xx}$ (the heat equation) and $u_t = -u_{xxxx}$ (the linearized surface diffusion equation). It provides useful insight into the nature of the diffusion process involved, and offers reassurance that the high frequency eigenfunctions for a finite geometry will be almost orthogonal, which is the one thing we are unable to prove rigorously in our study of the well-posedness of the grain boundary diffusion problem.

There are several difficulties that make the grain growth problem on a finite domain with corners and triple points interesting. First, there is the basic numerical challenge that the equations are stiff, and depend on taking two derivatives of the stress tensor σ_{ij} , which itself is a sensitive function of the grain boundary separation g (the jump in

normal component of displacement across a grain boundary). Second, for most functions g , the corresponding σ will contain singularities near corners and grain boundary junctions, which are amplified when derivatives are taken. Since some of the boundary conditions are expressed in terms of derivatives of the stress components at these points, it is essential that we understand the precise nature of the singularities there. We will see that the components of the stress field that enter into the equations and boundary conditions remain finite and well-behaved near these corners even though the stress tensor as a whole becomes singular. Third, both the equations and boundary conditions are non-local due to the fact that the flux depends on g through σ . Flux type boundary conditions constrain the stress field σ at grain boundary endpoints and junctions, which impose global constraints on the evolution of g , and are not easy to enforce directly. Stated differently, the rate of growth at a point on the grain boundary and the boundary conditions which arise as a consequence of mass conservation and chemical potential continuity at an endpoint or triple point depend on the current state of the entire system rather than on derivatives of g at that point. One has to be careful that such constraints on g are compatible with the evolution equation. Using well understood model problems as a guide, we know that for some problems (such as the heat equation), it is not possible to specify both Dirichlet and flux boundary conditions at a boundary. For other problems (such as $u_t = -u_{xxxx}$), obtaining a unique solution requires that two boundary conditions such as these be specified. Therefore it is important to investigate the possibility that we have included too many boundary conditions on our “wish list” of physical properties we would like to hold true. In our analysis, it will turn out that the grain boundary diffusion problem requires both Dirichlet and flux boundary conditions, so the physical considerations of Chapter 2 lead to a mathematically well-posed evolution problem.

The key idea that allows us to handle these difficulties is the reformulation of the problem as an ordinary differential equation on a Hilbert space. The question of well-posedness becomes a question of the nature of the spectrum and eigenspaces of a compact (but non-self-adjoint) operator, and the problem of computing the grain growth evolution with all the correct boundary conditions enforced becomes a matter of developing a machinery for computing this operator numerically. Through numerical computations, we discovered a property of the operator that led us to a proof that the spectrum is real and non-negative and that the eigenfunctions are dense in $L^2(\Gamma)$, where Γ is the grain boundary network. Our numerical work also shows that although these eigenfunctions are not orthog-

onal, they form a well conditioned basis for $L^2(\Gamma)$ because the high frequency eigenfunctions are nearly orthogonal to one another. Together with the exact solution we derived for the infinite interconnect line, this provides strong evidence that the grain boundary diffusion problem is well-posed.

From a programming perspective, just being able to solve and visualize the solution to the heat equation on a network of line segments poses a challenging book-keeping problem due to the lack of a natural ordering of the nodes. But the grain boundary diffusion problem is considerably more complicated than the heat equation. We must keep track of two levels of finite element structures which can readily communicate with each other, namely a large finite element space on which the two dimensional Poisson and Lamé equations are solved, and a small finite element space of grain boundary separations and normal stresses defined on an essentially one dimensional network of line segments. A considerable amount of effort was required to design appropriate data structures and algorithms capable of coping with the complications of jump discontinuities across grain boundaries, singular behavior of the stress field near corners and junctions, and non-trivial compatibility constraints in the boundary conditions.

1.4 Stable Asymptotics Near Corners

In Chapter 4, we develop a method of computing stable asymptotics for the solution of the elastic equations (or any other Agmon-Douglis-Nirenberg elliptic system) near corners. The problem of understanding the asymptotic behavior of solutions of elliptic systems near corners in the domain is a well developed subject, and a good deal has been written about it. Asymptotic solutions to the Laplace equation near a corner of the form $r^{\pi/\omega} \sin \omega$ (ω is the opening angle), and the characteristic $r^{-1/2}$ behavior of the stress field near a crack tip in the Lamé equations, have been understood since the 1930's and 1950's, respectively. The work of Kondratiev, Mazya, Plamenevskij and others in the 1960's made extensive use of transform methods to prove isomorphism theorems which characterize the asymptotic nature of solutions of general elliptic systems in R^n near angular points in the domain; see the papers [45, 54], the review articles [46, 63], and the books [36, 24] for further details. These results are appealing mathematically, but are difficult to work with in practice due to the technical nature of the spaces and the non-constructive description of the results. Many papers have been written analyzing special cases and equations; for the biharmonic

equation, see [45, 36]; for the Lamé system, see [35, 67].

For problems in the plane, the asymptotics near a corner can typically be determined by solving a generalized eigenvalue problem for an ordinary differential equation. This has led to a number of computational methods in which this eigenproblem is solved numerically (with finite elements, for example) in order to determine the characteristic exponents and angular functions; see [50, 60]. The paper [21] by Costabel and Dauge offers a nice improvement, in that it gives a constructive description of the singularities for a general Agmon-Douglis-Nirenberg elliptic system in the plane without recourse to an extraneous ODE. It becomes possible to solve for the characteristic exponents and angular functions semi-analytically (only the exponents are inexact), and thus to much higher accuracy for less computation. They use their method in [23] for non-isotropic linear elasticity. We have taken their method as a point of departure, and have simplified and solved some of the technicalities that prevent it from working in special cases. Specifically, we present a new algorithm for removing rank deficiency from the analytic basis matrix and show how to handle multiple or tightly clustered roots of the characteristic determinant $\Delta(\lambda)$ when finding the critical exponents.

Costabel and Dauge also wrote a paper [22] on *stable* representations of the asymptotics of the solutions, but these representations seem to be of little practical use due to the fact that they are given in the form of Cauchy integrals with integrands obtained by existence theorems from the theory of several complex variables; this hides many of the difficulties of dealing with crossings and branchings of the roots and offers little help in computations, but is still of theoretical interest. The problem of stability will be further explained in Chapter 4, but for the present purposes, it means that the most natural choice of basis functions becomes linearly dependent at certain critical angles of the corner, and as a result, the coefficients with respect to this basis blow up near these angles.

We present a new algorithm for choosing a different basis for clusters of self-similar solutions which does not become linearly dependent at the critical angle. We also present a new theorem about Keldysh chains which leads to an algorithm for computing associated functions and understanding the structure of the power solutions simply by knowing the boundary condition matrix $A(\lambda)$ and its first few derivatives at a critical value of λ . We have found that our stabilization procedure has the nice feature that at a nearly critical angle of the geometry, it will give nearly the same power solution basis as the Keldysh chain procedure at exactly the critical angle. This stabilization process is essential for employing

self-similar basis functions in the finite element computations of Chapter 3 due to the fact that clustered characteristic exponents frequently arise in triple point geometries, and the corresponding non-stabilized basis functions tend to be highly linearly dependent, leading to ill-conditioned stiffness matrices if nothing is done for stability.

1.5 Some Pitfalls: How Did We Get Here?

In our initial attempts at solving the grain growth problem, we used variational finite elements to solve for the normal stresses along grain boundaries given the separation function g , which is the jump in normal component of displacement. The components of stress σ_{ij} are obtained from the displacements u_i via the relations

$$\sigma_{ij} = \lambda \epsilon_{kk} \delta_{ij} + 2\mu \epsilon_{ij}, \quad \epsilon_{ij} = \frac{1}{2}(\partial_i u_j + \partial_j u_i), \quad (\text{summation implied}) \quad (1.1)$$

where λ and μ are constants. Because the evolution equation (Eqn. (1.6) below) relates the rate of change of g to components of σ along the grain boundary, we want the stress field to be continuous throughout the domain (with a well defined value at each node). By (1.1), this requires that the displacements be continuously differentiable within each grain and satisfy special compatibility conditions along the grain boundary. For a horizontal grain boundary, for example, the conditions

$$u_1^+ = u_1^-, \quad u_2^+ = u_2^- + g \quad (1.2)$$

along the grain boundary imply that

$$\partial_x u_1^+ = \partial_x u_1^-, \quad \partial_x u_2^+ = \partial_x u_2^- + g'. \quad (1.3)$$

Using (1.1) and (1.3) to express stress continuity in terms of displacements, we find that

$$\sigma_{22}^+ = \sigma_{22}^- \quad \Rightarrow \quad \partial_y u_2^+ = \partial_y u_2^- \quad (\Rightarrow \quad \sigma_{11}^+ = \sigma_{11}^-) \quad (1.4)$$

$$\sigma_{12}^+ = \sigma_{12}^- \quad \Rightarrow \quad \partial_y u_1^+ = \partial_y u_1^- - g'. \quad (1.5)$$

Our initial approach was to model the displacements with C^1 Clough-Tocher finite elements [10] subject to the above constraints on the u_i and their derivatives across grain boundaries.

In the simplest case of a horizontal grain boundary with electromigration turned off, the grain boundary diffusion problem takes the form

$$g_t = -\sigma_{22}[g]_{xx} \quad (\text{in interior}); \quad g = 0, \quad \partial_x \sigma_{22} = 0 \quad (\text{at endpoints}). \quad (1.6)$$

Here $g \mapsto \sigma_{22}[g]_{,xx}$ is a linear functional which maps a given separation function g defined on the grain boundary to the second derivative of the corresponding normal stress along the grain boundary obtained by solving the elasticity equations. We immediately ran into problems due to the fact that the stress components did not belong to the same spaces as the displacements, being expressed in terms of derivatives of the displacements. Note that the natural thing to do for Equation (1.6) in the finite element setting is to multiply by a test function, integrate the right hand side by parts, and split the left hand side into a finite difference, possibly using a backward Euler, Crank-Nicholson, or Runge-Kutta scheme. This doesn't work when g and σ belong to different spaces. We also ran into difficulties deciding just what boundary conditions to enforce at the walls and triple junctions — after all, how does one enforce a global constraint like $\partial_x \sigma_{22} = 0$ on g ? (We answer this question in Chapter 3). It was not clear at the time that the desired boundary conditions from a physical point of view were leading to a mathematically well-posed problem. We also were feeling uncomfortable about what we should do near corners and triple points where the stress field could develop singularities, and yet also where we wanted flux conditions enforced, which are expressed in terms of gradients of the stress field. At this point we abandoned this approach, having learned a good deal about the obstacles involved in solving the problem.

The need for compatible spaces for the stresses and displacements leads to the literature on mixed finite element methods, where instead of computing the stresses from derivatives of the displacements, additional variables are added to the system, and the stresses are expressed in terms of some combination of the new variables and the displacements. (Sometimes the stress components are the new variables). This reformulation changes the problem from a minimization problem to a saddle point problem; see the book [10] by Braess for details. It turns out that the spaces used for stress and displacement cannot be chosen arbitrarily in this framework, but must satisfy the so called inf-sup or Babuška-Brezzi condition. These methods were primarily designed for the case of nearly incompressible elastic materials, and there have been quite a variety of strategies used to construct optimal methods [10, 72, 41, 31, 32], the last containing a class of methods known as CBB (Circumventing Babuška-Brezzi condition) methods. Unfortunately, all of them have some property which makes them unsuitable for solving equation 1.6, such as discontinuous stresses or displacements.

One interesting way to get around the problem of the stress variables belonging to the wrong spaces is by choosing standard displacement based C^0 finite elements, but using

Lagrange multipliers to obtain the stresses along grain boundaries instead of differentiating the displacements. This is analogous to the standard way of imposing a traction boundary condition, with a few modifications to make it work for a jump condition along a grain boundary. This is the approach used by Bower, Craft, Fridline, and their collaborators (see, e.g. [9, 33]). Their approach seems to work quite well, and they have incorporated an impressive number of interesting phenomena in their model. The method of Lagrange multipliers does not give stresses at junctions where grain boundaries meet passivation or other grain boundaries, and there can be large discrepancies near corners between the stress obtained via Lagrange multipliers and the stress obtained by differentiating the displacements. It is not clear that singularities near corners and triple points can safely be ignored in this problem, so we take a different approach in order to focus on these issues.

1.6 Capturing Singularities: XFOSLS

In Chapter 5, we develop a singularity capturing, least squares finite element method for plane elasticity. One can think of standard displacement based variational finite elements as a problem of finding the state which minimizes the energy functional. In least squares finite elements (LSFE), we look for the state which minimizes the residual obtained by plugging the numerical solution into the PDE. The least squares finite element idea goes back to 1970 with the papers of Bramble and Schatz [11], [12]. There is a nice paper of Aziz, Kellogg and Stephens [3] written in 1985 which describes how to apply the least squares finite element method to an arbitrary Agmon-Douglis-Nirenberg elliptic system; specifically they show how to weight the residuals for the equations and boundary conditions based on the ADN indices in order to achieve optimal error bounds on the solution. The primary drawback of their approach is that it leads to unnecessarily bad condition numbers for the resulting linear systems — a second order system will result in condition numbers of order h^{-4} instead of h^{-2} for the standard Galerkin method. This drawback was removed (e.g. [18, 62, 15]) with the realization that if the system is first reduced via the Agmon-Douglis-Nirenberg reduction process [1] to a first order system, then the condition number is $O(h^{-2})$ even for problems like the biharmonic equation where the Galerkin method is $O(h^{-4})$. The most active work in this direction has led to the FOSLS (First Order System Least Squares) methodology of Cai, Manteuffel, McCormick and others, where they have applied it to general second order systems [15], the Stokes problem [16], the pure traction

problem of planar elasticity [17], and many other problems.

One benefit of using least squares finite elements instead of the Galerkin method is that there is no Babuška-Brezzi condition to be satisfied [62]. We are free to choose the spaces for stress and displacement independently. This means that instead of getting stresses in a space of derivatives of another space, we can use standard quadratic elements for both displacement and stresses. This is a huge advantage for the grain growth problem. The other benefit is that we have an a-posteriori gauge of how accurate the solution is, because we have minimized a residual instead of an energy. On each element of the mesh, we have a number which tells how accurately the PDE is satisfied on that element. This idea is made rigorous by Berndt, Manteuffel and McCormick in [4] and [5].

The primary drawback of the FOSLS method is that it requires H^2 regularity in the solution; if the solution is not in H^2 , the method may fail to converge. One of the key features which has made variational finite elements so successful is that only H^1 regularity is necessary. When the domain has re-entrant corners, or a change in boundary condition type from Dirichlet to traction boundary conditions, there is typically a singularity present that destroys H^2 regularity even when the data is smooth. In the grain growth problem, there are many such singularities, so something must be done in order to get FOSLS to work. The approach currently being pursued by Manteuffel and McCormick to deal with this problem is known as FOSLS* [14], but this requires giving up the two benefits that led us to FOSLS in the first place: that the stresses belong to nice spaces and that there is an a-posteriori error gauge.

Even in the Galerkin setting, singularities invalidate (or weaken the conclusions of) convergence and regularity proofs, and can make iterative numerical schemes slow. The idea of augmenting finite element spaces with appropriate singular functions in order to “capture” the correct asymptotic behavior near corners is an area of active research in the fracture mechanics community; see [75] and [25] for a sample of some of the recent work in this field. In the FOSLS framework, Berndt has developed a method of augmenting the finite element space near interface junctions for the steady state diffusion problem $-\nabla \cdot (\alpha \nabla u) = f$, where the scalar function α may have large jumps across material interfaces. Once these singularities have been included in the basis set, only the regular part of the solution (the part that remains when the singularity is subtracted off) needs to be in H^2 , and the method converges.

In fracture mechanics, one is primarily interested in crack growth problems, so

the difficulty of finding the singularity exponents for each geometry is not confronted – the geometry is usually a crack, and the characteristic $r^{1/2}$ behavior for the displacements at a crack tip has long been known. They do not attempt to include any further terms in the asymptotic expansion to improve convergence. Berndt’s implementation is also limited to a single singular function per interface junction, and because he is solving $-\nabla \cdot (\alpha \nabla u) = f$, he does not face the difficulties of branching and crossing roots or degenerate or nearly degenerate singular basis functions that can occur in more general elliptic systems like elasticity.

In Chapter 5, we develop an approach to augmenting each corner and interface junction with an arbitrary number of singular functions. We have adopted the name XFOSLS for our method, following the terminology used by the developers of the extended finite element method (XFEM) for crack problems [25]. A single singular function is a chain (usually of length one) of power solutions. They may include logarithm terms, or simply be an appropriate linear combination of nearly linearly dependent power solutions to deal with the stability problem discussed in Chapter 4. Each singular function has a near region, where it is a solution to the PDE, a fringe region, where it transitions to zero, and a far region where it is zero. Singular functions with smaller real parts are given larger supports to give the singularity room to die out and become well approximated by the standard quadratic basis functions. The beauty of the least squares finite element framework over the Galerkin framework for adjoining singular functions is that because the singular functions satisfy the PDE in the near and far regions, only the fringe region is relevant for computing the inner products in the LSFE setting. Therefore inner products only need to be computed in regions where the functions are well-behaved, and numerical integration schemes like Gaussian quadrature are fine. By contrast, to adjoin singular functions in variational finite elements, special methods must be used to get the integration right, and it is quite difficult to compute the inner products between two different singular functions.

We compare the solution obtained using XFOSLS to solve the Lamé equations near a corner with Dirichlet boundary conditions on one wall and traction boundary conditions on the other to the solution obtained using the Galerkin finite element method with a locally refined mesh. When viewed on a large scale, the solutions appear to agree perfectly, but when we zoom in on one of the corners, we find that the stress components obtained using the Galerkin method have very large discontinuities near the corner, and exhibit a large discrepancy between the stress obtained from the displacements using Eqn. (1.1) and the

specified traction (Lagrange multiplier). In contrast, using a much coarser mesh, XFOSLS easily resolves the singularity smoothly. We also use XFOSLS to solve the elastic equations in the incompressible limit (the method works fine over the entire range of poisson ratio) on a complicated geometry with re-entrant corners to show the effectiveness of the method outside of the electromigration problem.

Chapter 2

A Model of Mass Transport in Interconnect Lines

In this chapter, we develop a continuum model of mass transport in the bulk grains, at void surfaces, and along grain boundaries for an interconnect line in a microelectronic circuit. A typical interconnect line might be made of an alloy of Al-0.5%Cu and have a diameter of $0.5\mu\text{m}$, which is only 1700 times larger than the nearest neighbor distance for aluminum, which has an FCC lattice structure with a lattice constant of 4.05\AA and a nearest neighbor spacing of 2.86\AA . These interconnects are beginning to approach the limit in size where it becomes questionable whether there is an intermediate scaling regime which is large enough that details of the discrete interactions of the atoms in the lattice can be neglected, but small enough to be considered small in comparison to the geometry of the macroscopic sample; nevertheless, we believe a continuum approach is useful for understanding the process of electromigration.

In Section 2.1, we describe the quasi-static aspects of the problem, namely solving for the electrostatic potential, stress tensor, and displacement field with the void geometry frozen in time. We define the separation function (jump in normal component of displacement across a grain boundary), derive appropriate boundary conditions at junctions and endpoints, and discuss the consequences of having jump discontinuities in the displacement field along grain boundaries. Although these ideas are implicit in [33, 9], no one has previously singled out the separation function as a key tool for studying the grain growth problem.

In Sections 2.2–2.4, we describe the role of mass conservation, chemical potential continuity and the various driving forces for diffusion on the evolution of vacancies, void surfaces, and grain growth. Although we will ultimately focus on the grain growth problem in Chapter 3, it is useful to develop our model of grain boundary diffusion in the context of the more general problem with voids and vacancies taken into account — parallel treatment helps develop physical insight (and the phenomena are closely related anyway). We treat the problem as three dimensional in these sections when there is no essential difference between the two and three dimensional theory.

2.1 The Setup

2.1.1 The Potential Problem

Consider the interconnect line shown in Figure 2.1. We assume the conductivity of the metal to be homogeneous, and that grain boundaries do not significantly affect the flow of electric current in the line. The cathode and anode ends of the line are respectively held at potentials of $\psi = 0$ and $\psi = \psi_0$, where ψ_0 is chosen (depending on the resistivity of the metal) to produce an average current density across the line of approximately 10^6 Amp/cm². We take ψ_0 to be positive, so that electrons are flowing from left to right in the figure. The other outer walls of the line are assumed to be insulated, so the electric field $\mathbf{E} = -\nabla\psi$ has no component in the normal direction of these walls. Likewise, we take the voids to be non-conducting, so the electric field is tangent to void surfaces and Neumann boundary

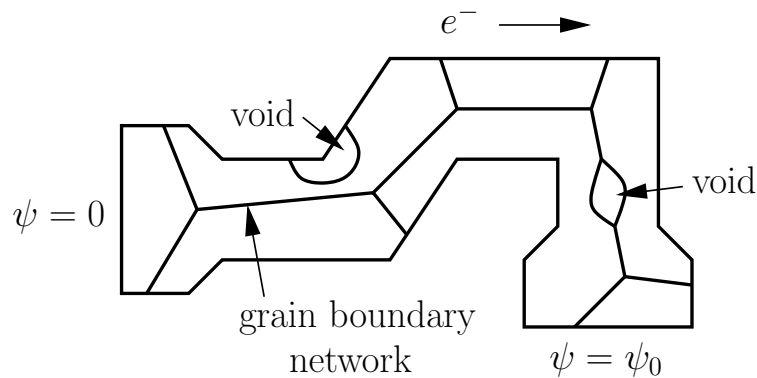


Figure 2.1: Geometry of an interconnect line.

conditions hold there as well. In summary, at any given instant in time, we assume a steady current flows through the line, which is modeled by an electrostatic potential ψ satisfying:

$$\nabla^2 \psi = 0 \quad \text{in interior (even at grain boundaries),} \quad (2.1)$$

$$\psi = 0, \quad \psi = \psi_0 \quad \text{at the ends,} \quad (2.2)$$

$$\partial_n \psi = 0 \quad \text{at other walls and at void boundaries.} \quad (2.3)$$

We remark that although the geometry of the line changes in time, the timescale on which a void changes shape is practically infinite in comparison to the time it takes for the current to find its steady state distribution, which justifies this quasi-steady assumption.

2.1.2 The Elasticity Problem

Each grain is assumed to deform elastically, and to satisfy the Lamé equations of linear elasticity. More general non-isotropic linear relationships between stress and strain can easily be used instead, but we are satisfied with the Lamé and Hooke relations:

$$\text{Lamé: } \sigma = 2\mu\epsilon + \lambda \text{tr}(\epsilon)I, \quad (2.4)$$

$$\text{Hooke: } \epsilon = \frac{1+\nu}{E}\sigma - \frac{\nu}{E}\text{tr}(\sigma)I. \quad (2.5)$$

Here σ is the stress tensor, $\epsilon_{ij} = \frac{1}{2}(\partial_i u_j + \partial_j u_i)$ are the components of the strain tensor, \mathbf{u} is the displacement vector field, $\text{tr}(\cdot)$ is the trace operator, μ and λ are the Lamé coefficients, and E and ν are Young's modulus and the Poisson's ratio; see [48, 19].

When dealing with problems in the plane, we adopt the convention that \mathbf{u} has two components, that σ and ϵ are 2×2 tensors, and that $\text{tr}(\sigma)$ means $\sigma_{11} + \sigma_{22}$. For plane strain, we modify (2.5) to account for the neglected $\sigma_{33} = \nu(\sigma_{11} + \sigma_{22})$ term:

$$\text{Hooke: } \epsilon = \frac{1+\nu}{E}\sigma - \frac{\nu(1+\nu)}{E}\text{tr}(\sigma)I. \quad (\text{plane strain}) \quad (2.6)$$

For plane stress, we modify (2.4) to account for the neglected $\epsilon_{33} = -\frac{\lambda}{\lambda+2\mu}(\epsilon_{11} + \epsilon_{22})$ term by using a different expression for λ in terms of E and ν . It is readily verified from (2.4), (2.5) and (2.6) that the relationship between λ , μ , E and ν is given by

$$\mu = \frac{E}{2(1+\nu)}, \quad \nu = \frac{\lambda}{(n-1)\lambda + 2\mu}, \quad (2.7)$$

$$\lambda = \frac{E\nu}{(1+\nu)[1 - (n-1)\nu]}, \quad E = \frac{\mu(n\lambda + 2\mu)}{\frac{1}{2}(n-1)\lambda + \mu}, \quad (2.8)$$

where $n = 2$ in the plane stress case and $n = 3$ in the plane strain and 3D cases. It will also prove useful later to make use of the dimensionless parameter κ , defined by

$$\kappa = \frac{\lambda + 3\mu}{\lambda + \mu} = \begin{cases} 3 - 4\nu & \text{plane strain (or 3D),} \\ \frac{3-\nu}{1+\nu} & \text{plane stress.} \end{cases} \quad (2.9)$$

The two dimensional Lamé equations (c.f. Sec. 3.1) are to be satisfied in the interior of each grain:

$$\mu\Delta\mathbf{u} + (\lambda + \mu)\nabla(\nabla \cdot \mathbf{u}) = 0. \quad (2.10)$$

2.1.3 The Separation Function

At any given instant in time, we are given a separation function g which is defined on the grain boundary network to be the jump in normal component of displacement across the grain boundary. For any segment on the grain boundary, we choose an orientation for the segment arbitrarily, which defines a local arclength parameter s , a tangent vector \mathbf{t} pointing in the direction of increasing s , a right adjacent grain (facing in the \mathbf{t} direction), a left adjacent grain, and a normal vector \mathbf{n} pointing from right to left (see Figure 2.2). At a point x in the interior of such a grain boundary segment, we impose four interface boundary conditions, two which relate the displacement on the right grain to the displacement on the left grain, and two which express a local balance of forces:

$$\mathbf{t} \cdot (\mathbf{u}_{\text{left}} - \mathbf{u}_{\text{right}}) = 0, \quad (2.11)$$

$$\mathbf{n} \cdot (\mathbf{u}_{\text{left}} - \mathbf{u}_{\text{right}}) = g, \quad (2.12)$$

$$\mathbf{t} \cdot (\sigma_{\text{left}}\mathbf{n} - \sigma_{\text{right}}\mathbf{n}) = 0, \quad (2.13)$$

$$\mathbf{n} \cdot (\sigma_{\text{left}}\mathbf{n} - \sigma_{\text{right}}\mathbf{n}) = 0. \quad (2.14)$$

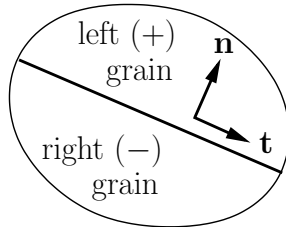


Figure 2.2: Arbitrary local orientation of grain boundary segment determines tangential and normal directions, left and right grain labels, etc.

Equations (2.11) and (2.14) imply that

$$\mathbf{t} \cdot (\sigma_{\text{left}} \mathbf{t} - \sigma_{\text{right}} \mathbf{t}) = 0, \quad (2.15)$$

which may be seen by differentiating (2.11) along the grain boundary and writing (2.14) and (2.15) in terms of derivatives of \mathbf{u}_{left} and $\mathbf{u}_{\text{right}}$. Thus we conclude that all components of the stress tensor are continuous across grain boundaries.

Choosing the opposite orientation for the grain boundary segment will change the sign of \mathbf{n} and swap the right and left labels, so the sign of g is well defined. Physically, a positive value of g means that two points that were once adjacent to each other on either side of the grain boundary in the unstressed reference configuration have separated relative to each other; the gap (in the deformed configuration) between them is to be interpreted as being filled in by new material that has been added to the grains at the grain boundary. The orientation of the lattice structure of the new material aligns partly with one grain and partly with the other; the details of this are not part of our model. Similarly, a negative value of g means that adjacent points on the grain boundary in the reference

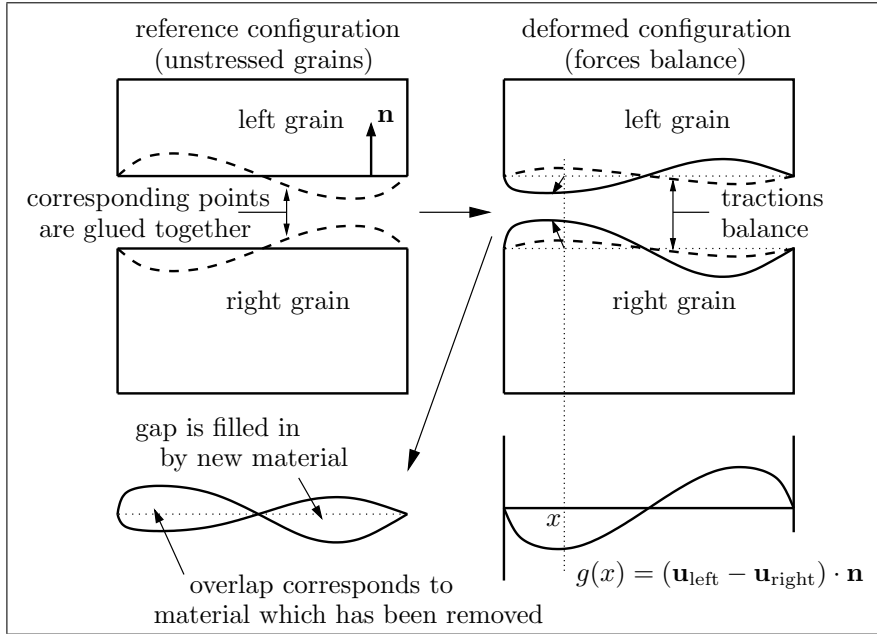


Figure 2.3: Meaning of the separation function g . The regions between dashed and solid lines in the top two pictures represent material which has been added or removed from each grain during the transport process. The actual displacements would be much smaller than those shown here.

configuration have passed through each other so that an overlap region has developed near the grain boundary in the deformed state. This seems a little odd at first thought, but within the linear elasticity model, it is the natural way to represent the physical phenomenon of removing material from each grain near the grain boundary in the unstressed state and then gluing the two resulting surfaces together. The overlapping region is the image of the empty space left behind in the reference configuration rather than a superposition of material. In Figure 2.3, the displacements are defined on the rectangles bounded by the solid lines in the reference configuration; the curved dashed lines represent our mental picture of the grain growth process we are modeling within the linear elasticity framework, but are not part of the mathematical description; and the curved solid lines in the stressed state are the images of the displacements along the dotted lines for each grain.

2.1.4 Further Boundary Conditions

At exterior walls, we assume the passivation to be infinitely rigid, and impose the Dirichlet boundary conditions $\mathbf{u} = 0$. Void surfaces are assumed to be traction free, so if \mathbf{t} and \mathbf{n} are tangent and normal vectors to the void surface at x , then $\mathbf{t} \cdot \sigma(x)\mathbf{n} = 0$ and $\mathbf{n} \cdot \sigma(x)\mathbf{n} = 0$. The separation g is assumed to go to zero at the walls, as it must since both \mathbf{u}_{left} and $\mathbf{u}_{\text{right}}$ approach zero there. There is a basic compatibility condition on g where three (or more) grain boundary segments meet at a point, namely that if we follow the jump in displacement from grain to grain (counterclockwise, for example), the net jump must be zero when we get back to the grain we started with. For example, in Figure 2.4, we would require

$$g(x_1)\mathbf{n}_1 + g(x_2)\mathbf{n}_2 + g(x_3)\mathbf{n}_3 = 0. \quad (2.16)$$

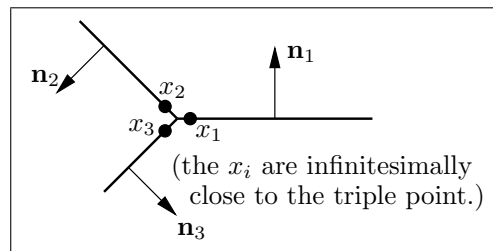


Figure 2.4: Compatibility condition on the separation function g at a triple point.

We assume g is continuous on each grain boundary segment and has a limiting value at the endpoints, but the limit is generally different when approaching a triple point from different segments, subject to the above condition.

Just as we did when computing the electric field, we treat the elasticity problem as a quasi-steady phenomenon. Although the void geometry will change with time, the timescale on which voids change shape is very large in comparison to the time it takes the grains to find their elastic equilibrium, i.e. the speed of void evolution is slow in comparison to the speed of sound. Thus we may consider the void geometry frozen when determining the stresses from the separation function g .

In summary, at any instant in time the state of stress of the system is obtained from the data g by solving the Lamé system (2.10) subject to the interface boundary conditions (2.11)–(2.14) along grain boundaries, the Dirichlet boundary conditions $\mathbf{u} = 0$ along walls, and traction free boundary conditions at void surfaces.

2.2 Mass Conservation

So far we have only looked at the static aspects of the problem. The dynamics of mass transport in interconnect lines is governed by mass conservation and various constitutive laws governing the flux of atoms. In Sections 2.2 and 2.3 we will develop a 3D model of mass transport in interconnect lines. At each point in the interior of each grain, there is a flux vector \mathbf{J} with units $(\text{cm}^2\text{s})^{-1}$ such that for any area element $d\mathbf{A}$ the number of atoms

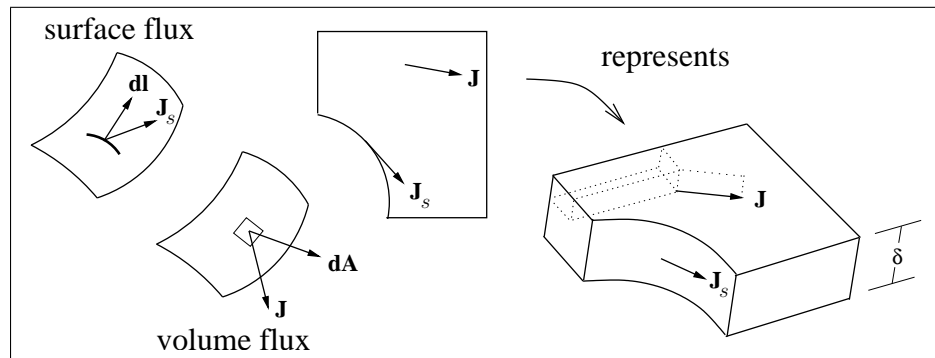


Figure 2.5: Volume and surface fluxes \mathbf{J} and \mathbf{J}_s give the number of atoms crossing area and line elements $d\mathbf{A}$ and $d\mathbf{l}$ when dotted with them. In 2D simulations we are still modeling 3D objects, so the units are $(\text{cm}^2\text{s})^{-1}$ and $(\text{cm s})^{-1}$, respectively.

crossing $d\mathbf{A}$ per unit time is given by $\mathbf{J} \cdot d\mathbf{A}$. At each point on a void or grain boundary surface (speaking three dimensionally here), we have a surface flux \mathbf{J}_s (denoted \mathbf{J}_b for grain boundaries) with units $(\text{cm s})^{-1}$ such that for any line element $d\mathbf{l}$ the number of atoms crossing $d\mathbf{l}$ per unit time is given by $\mathbf{J}_s \cdot d\mathbf{l}$. In order to conform as much as possible to common practice in the electromigration literature, we represent our fluxes, concentrations, etc. in the units appropriate for three dimensional objects even though our simulations are done in two dimensions. We simply give the sample a thickness δ and assume all fields are independent of the coordinate in the transverse direction.

2.2.1 Vacancy Evolution in the Grains

Mass conservation in the bulk grains is expressed via a continuity equation. At each point in a grain, there is an atomic concentration c which is related to the vacancy concentration c_v and the lattice concentration c_{lat} by

$$c + c_v = c_{\text{lat}}. \quad (2.17)$$

If we integrate the flux over a control volume V (see Figure 2.6) and use the divergence theorem, we obtain the integral form of mass conservation

$$\frac{\partial}{\partial t} \iiint_V c dV = - \iint_{\partial V} \mathbf{J} \cdot \mathbf{n} dA = - \iiint_V \nabla \cdot \mathbf{J} dA, \quad (2.18)$$

from which the continuity and vacancy evolution equations follows immediately:

$$\frac{\partial c}{\partial t} + \nabla \cdot \mathbf{J} = 0, \quad -\frac{\partial c_v}{\partial t} + \nabla \cdot \mathbf{J} = 0. \quad (2.19)$$

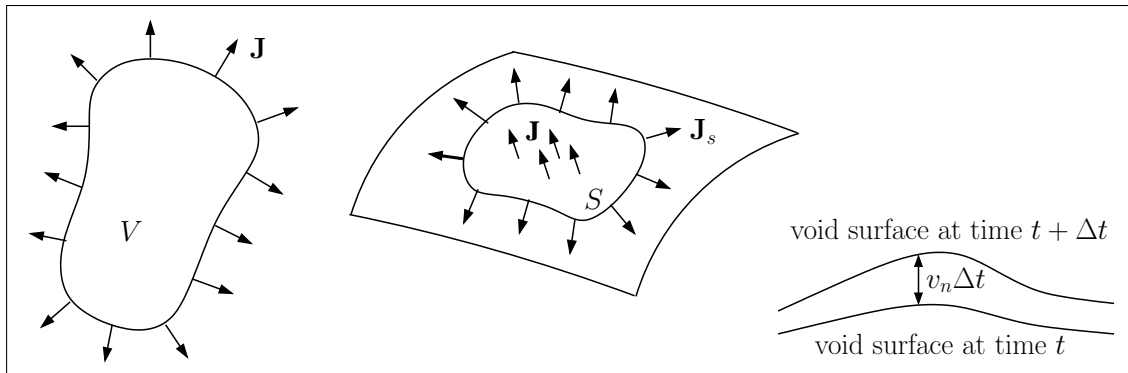


Figure 2.6: The continuity equation and void growth equation are a consequence of mass conservation.

In the vacancy equation, one must keep in mind that \mathbf{J} is the atomic flux rather than the (equal and opposite) vacancy flux.

2.2.2 Void Evolution

At void surfaces (speaking three dimensionally), an accumulation of atoms in a region leads to growth in the normal direction (see Figure 2.6):

$$\frac{1}{\Omega} \iint_S v_n dA = \iint_S \mathbf{J} \cdot \mathbf{n} dA - \int_{\partial S} \mathbf{J}_s \cdot \mathbf{n}_s dl = \iint_S \mathbf{J} \cdot \mathbf{n} - \nabla_s \cdot \mathbf{J}_s dA. \quad (2.20)$$

Here v_n is the normal velocity of the void surface, Ω is the volume of an atom in the lattice, \mathbf{n}_s is the outward unit surface normal to ∂S (which is tangent to the surface but normal to the curve ∂S), $\nabla_s \cdot \mathbf{J}_s$ is the surface divergence of \mathbf{J}_s , \mathbf{n} is the unit normal pointing away from the bulk (into the void), and $\mathbf{J} \cdot \mathbf{n}$ represents the flow of atoms from the bulk (or grain boundaries) up to the surface. The differential version of this equation gives the void growth equation

$$v_n + \Omega \nabla_s \cdot \mathbf{J}_s = \Omega \mathbf{J} \cdot \mathbf{n} \quad (2.21)$$

2.2.3 Grain Boundary Evolution

Similarly, if along a grain boundary interface there are more atoms flowing into a region than out (see Fig. 2.7), then the accumulation of atoms will lead to grain growth (i.e. an increase in grain separation g), which is expressed by the equation

$$\frac{\partial g}{\partial t} + \Omega \nabla_s \cdot \mathbf{J}_b = 0. \quad (2.22)$$

The primary difference here is that we do not include the possibility of atoms flowing from the bulk onto the grain boundary surface; all the physics we have in this model results in the flow from the right grain to the grain boundary being equal to the flow from the grain boundary to the left grain, so the net contribution from the bulk is zero.

2.3 Driving Forces for Diffusion

In the previous section we saw how the vacancy concentration (Eqn. 2.19), void surface velocity (Eqn. 2.21), and grain separation rate (Eqn. 2.22) depend on the fluxes \mathbf{J} , \mathbf{J}_s , and \mathbf{J}_b . In this section we discuss constitutive laws which express the fluxes in terms of the geometry and state of the system.

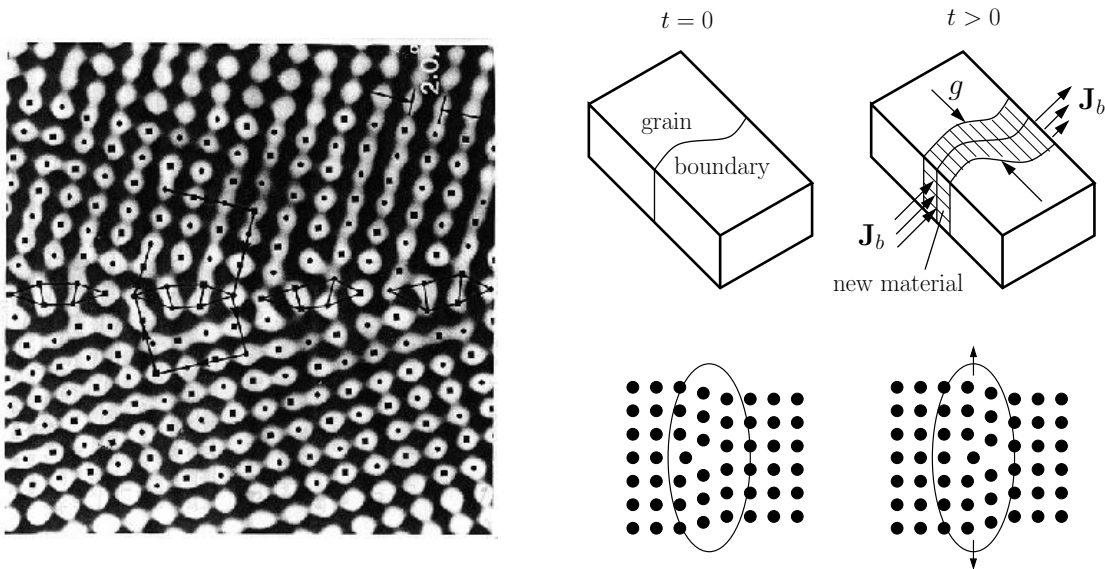


Figure 2.7: Left: high resolution TEM microscope image of a large tilt angle grain boundary in a gold thin film. (From *Electronic Thin Film Science for Electrical Engineers and Materials Scientists*, Tu/Mayer/Feldman [77]). Right: grain growth occurs when more atoms flow into a region of the grain boundary than out.

2.3.1 The Einstein-Nernst Relation

The central concept in deriving these constitutive laws is the concept of the chemical potential μ of an atom, which in turn relies on the concept of free energy. Free energy is a measure of the balance between lowering internal energy and raising entropy. In a gas at constant volume, for example, a system in contact with a heat reservoir will be at thermal equilibrium when its Helmholtz free energy $F = U - TS$ is minimized; see [43, 82]. If two systems of a single chemical species are placed in diffusive contact with each other and in thermal contact with a heat reservoir, the free energy of the combined system will be minimized at equilibrium with respect to particle exchange between them. Assuming the free energy is additive, this means we must have equality of the rates of change of each system with respect to the number of particles (holding temperature and volume fixed), or else the free energy could be lowered by moving a particle from one system to the other. This gives the physical importance of the chemical potential μ , defined as

$$\mu(T, V, N) = \left(\frac{\partial F}{\partial N} \right)_{T, V} = \left(\frac{\partial G}{\partial N} \right)_{T, p}. \quad (2.23)$$

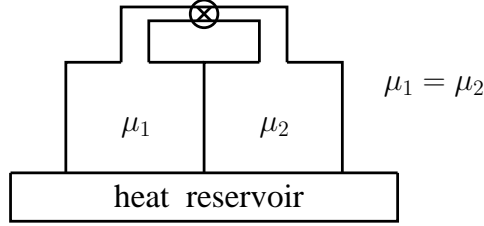


Figure 2.8: Two systems in thermal and diffusive contact must have equal chemical potentials.

Here $G = U - TS + pV$ is the Gibbs free energy, which is frequently useful, and plays the same role as the Helmholtz free energy in the constant pressure case; see Figure 2.8.

In solid mechanics, if an elastic medium occupies a volume V and we perturb the boundary ∂V infinitesimally to create virtual displacements $\delta \mathbf{u}$ while keeping the system in mechanical equilibrium, we obtain the following expression for the work done on the system by the external forces acting on the boundary (\mathbf{n} points outward):

$$\begin{aligned} \int_{\partial V} \delta \mathbf{u} \cdot (\boldsymbol{\sigma} \mathbf{n}) dA &= \int_V \partial_j (\delta u_i \sigma_{ij}) dV = \int_V \overbrace{(\partial_j \sigma_{ij})}^0 \delta u_i + \sigma_{ij} (\partial_j \delta u_i) dV \\ &= \int_V \sigma_{ij} \left(\frac{\partial_j \delta u_i + \partial_i \delta u_j}{2} \right) dV = \int_V \sigma_{ij} \delta \epsilon_{ij} dV. \end{aligned} \quad (2.24)$$

The first law of thermodynamics $dU = TdS - pdV$ for a gas is therefore replaced by

$$dU = TdS + \int_V \sigma_{ij} d\epsilon_{ij} dV, \quad (2.25)$$

and the definition of G becomes $G = U - TS - \int_V \sigma_{ij} \epsilon_{ij} dV$. At each point in the interconnect line, we consider a volume V centered at this point which is small compared to the macroscopic dimensions of the sample but large with respect to the atomic spacing, and compute a value for the chemical potential for the system contained in this volume using the above formula for G at constant stress. We assume the value μ so obtained becomes independent of the volume as the volume shrinks to zero (i.e. there is a limit), and in this way we obtain a spatially varying intensive variable μ , the chemical potential. If the system were in its final equilibrium stage, μ would be a constant throughout the system. It is assumed that when the system is not in equilibrium, the chemical potential is continuous, and the flux of atoms is proportional to the gradient in chemical potential. This is known

as the Einstein-Nernst relation:

$$\mathbf{J} = -\frac{c_v D}{kT} \nabla \mu, \quad (\text{in bulk}), \quad \mathbf{J}_s = -\frac{\nu_s D_s}{kT} \nabla_s \mu, \quad (\text{on void and gb surfaces}). \quad (2.26)$$

Here c_v is the vacancy concentration ($1/\text{cm}^3$), ν_s is the number of participating atoms per unit area ($1/\text{cm}^2$), D and D_s are the diffusion constants (cm^2/s), and k is Boltzmann's constant (erg/K). See [56] for further discussion.

2.3.2 The Chemical Potential at a Surface

In [37], Herring argued that the chemical potential of an atom just beneath a curved surface has the form

$$\mu_s = \mu_0 - \gamma \Omega (\kappa_1 + \kappa_2), \quad (2.27)$$

where μ_0 is a constant independent of the curvature, γ is the surface tension (typically $\sim 0.1 \text{ erg}/\text{cm}^2$), and κ_1 and κ_2 are the principal curvatures of the surface (positive for a spherical void); see also [13]. Considering the flat case, we see that μ_0 is negative and equal to the cohesive energy per atom in the lattice, or stated differently, the energy required to form separated neutral atoms divided by the number of atoms. His argument is based on determining the change in G by looking at the increase in surface energy of a tiny smooth hump of volume Ω added to the curved surface; the curvature terms come in due to the fact that the mean curvature $\kappa_1 + \kappa_2$ is equal to the rate at which the surface area decreases as the surface moves normally to itself at unit speed. His analysis was done in the more general case when γ depends on the orientation of the surface, but it reduces to the above in the isotropic case we are considering.

2.3.3 The Chemical Potential at a Grain Boundary

A similar argument leads to an expression for the chemical potential of an atom near a grain boundary (see [8]):

$$\mu_b = \mu_0 - \Omega \sigma_{nn}. \quad (2.28)$$

Here Ω is the volume of an atom in the lattice and $\sigma_{nn} = \mathbf{n} \cdot \boldsymbol{\sigma} \mathbf{n}$ is the normal-normal component of the stress tensor. This can easily be understood by considering the work done by the stress field when a layer of atoms is added to the grain boundary: only the top and bottom walls of a small cylindrical control volume placed perpendicular to the grain boundary move when the layer is added, and only the normal force acting on these walls

does work. If the cross section of the control volume is A and the change in height of the control volume when the layer is added is δ , then the work done by the normal forces is $\sigma_{nn}A\delta$. Dividing by the number of participating atoms ($A\delta/\Omega$) gives the desired result. The constant μ_0 is again the cohesive energy per atom in the lattice.

2.3.4 The Chemical Potential in the Bulk

To determine the chemical potential of an atom in the bulk, we assume [42, 68] the existence of a vacancy relaxation factor f between 0 and 1 (typically between 0.2 and 0.4 for a metal [42]) which has the physical interpretation that $f\Omega$ is the change in volume of any macroscopic volume V of the lattice when a vacancy inside V is filled with an atom. Assuming the inelastic strain field which is responsible for this volume change is localized at the filled vacancy location and is spherically symmetric, and assuming the stress field does not change much when a mere vacancy is filled, we find from Eqn. (2.24) that the work done by the traction forces acting on the boundary of any such V in the process of filling the vacancy at x is $f\Omega \text{tr}(\sigma(x))$:

$$\int_V \sigma_{ij} \delta \epsilon_{ij} dV \approx \sigma_{ij}(x) \int_V \delta \epsilon_{ij} dV = \sigma_{ij}(x) \left(f\Omega \frac{\delta_{ij}}{3} \right) = f \text{tr}(\sigma)\Omega. \quad (2.29)$$

Also including the standard entropy term to account for the increased number of configurations with a given energy which arise when the number of vacancies increases [77], we obtain the expression

$$\mu = \mu_1 - f\Omega \text{tr}(\sigma) - kT \log \frac{c_v}{c_e} \quad (2.30)$$

for the chemical potential of an atom in the bulk. Here c_v is the vacancy concentration, c_e is the equilibrium vacancy concentration, and μ_1 is negative in sign and equal to the energy of formation of a vacancy in the unstressed state, i.e. the energy required to pluck an atom out of the middle of the lattice and move it to infinity. If the surrounding atoms did not adjust their relative positions when a vacancy is formed (which would be the $f = 0$ case), we would have $\mu_1 = 2\mu_0$ by a standard “when we sum over the atoms we count each bond twice” argument. But since there is a considerable amount of relaxation energy involved in forming a vacancy, μ_1 is somewhat smaller in magnitude than $2\mu_0$.

The papers [42] and [68] also include a model for vacancy generation or annihilation at dislocations (uniformly distributed) in the bulk grains in which the generation rate of

vacancies is proportional to the difference in chemical potential from the equilibrium value:

$$\text{vacancy generation rate} = L_v(\mu - \mu_1), \quad (2.31)$$

with $L_v > 0$ and μ, μ_1 as in Eqn. (2.30).

2.3.5 Elastic Energy

One could also include an elastic energy term in each of the above chemical potentials to account for the increase in volume of stressed material; see [9]. This is a second order effect (in comparison to the inelastic effects above) under the small strain assumption, as $\int_{\Omega} \sigma : \epsilon dV$ is much smaller than $\|\sigma\|\Omega$. One should be careful near singularities where the small strain assumption no longer holds, but we have not pursued this line of thought; (it is not pursued in [9] either).

2.3.6 Electromigration and Summary

Recalling the Einstein-Nernst relations (2.26) on page 26 and including the electron wind force (so $\nabla\mu \rightarrow \nabla\mu + Z^*e\nabla\psi$), we get constitutive expressions for the fluxes in terms of the field variables:

$$\text{bulk : } \mathbf{J} = \frac{c_v D}{kT} \left(f\Omega \nabla \text{tr}(\sigma) + kT \frac{\nabla c_v}{c_v} - Z^* e \nabla \psi \right), \quad (2.32)$$

$$\text{grain boundary : } \mathbf{J}_b = \frac{\nu_b D_b}{kT} (\Omega \nabla_s \sigma_{nn} - Z^* e \nabla_s \psi), \quad (2.33)$$

$$\text{void surface : } \mathbf{J}_s = \frac{\nu_s D_s}{kT} (\gamma \Omega \nabla_s (\kappa_1 + \kappa_2) - Z^* e \nabla_s \psi). \quad (2.34)$$

Here e is the elementary electronic charge ($e = 1.6 \times 10^{-19} C$) and Z^* is a phenomenological effective charge for an atom. Since the electron wind force is stronger than the opposing direct force of the electric field, (i.e. atoms move in the direction of the electrons) we find that $Z^* < 0$. For a good conductor [56, 77], Z^* is typically on the order of -5 ; for aluminum at $533K$ [68], Z^* is approximately -1.3 . Combined with appropriate boundary conditions, the potential and elastic problems, and the continuity equations

$$-\frac{\partial c_v}{\partial t} + \nabla \cdot \mathbf{J} = 0, \quad (\text{note } \nabla c_v \neq 0 \text{ in } \nabla \cdot \mathbf{J}) \quad (2.35)$$

$$\frac{\partial g}{\partial t} + \Omega \nabla_s \cdot \mathbf{J}_b = 0, \quad (2.36)$$

$$v_n + \Omega \nabla_s \cdot \mathbf{J}_s = \Omega \mathbf{J} \cdot \mathbf{n}, \quad (2.37)$$

we get a closed set of equations for the evolution of the vacancy concentration c_v , the grain separation g , the electrostatic potential ψ , the stress field σ , and the void geometry Γ .

2.4 Interface Junctions

The first assumption we make is that mass transport in the bulk is negligible in comparison to mass transport along grain boundaries, void surfaces, and passivation interfaces. This assumption is justified by the experimental fact that in the operating temperature range of a microchip, the diffusion constants D , D_b and D_s are [56] respectively on the order of 10^{-15} , 10^{-8} and 10^{-7} cm^2/s . This is essentially due to the fact that the atoms are bound less tightly at grain boundaries and void surfaces, and the activation energy required to move them is significantly lower; see Fig. 2.9. Taking $c_v = 1.4 \times 10^{19} \text{cm}^{-3}$ [68], and $\nu_b = \nu_s = 1.5 \times 10^{15} \text{cm}^{-2}$ [56], we find the ratio of $\frac{c_v D}{kT}$ to $\frac{\nu_b D_b}{kT}$ and $\frac{\nu_s D_s}{kT}$ in Equations (2.32)–(2.34) to be $0.9 \times 10^{-7} \mu\text{m}^{-1}$ and $0.9 \times 10^{-8} \mu\text{m}^{-1}$. This means we can expect a typical flux from the bulk through a square micron to be 7 or 8 orders of magnitude smaller than a typical flux across a linear micron of grain boundary or void surface.

We also neglect mass transport along passivation interfaces (the outer walls), even though in practice they can transport as much material as grain boundaries. This is not an essential assumption for the implementation of our numerical method, but seemed like a convenient idealization to work with when we started working on the problem. Including this phenomenon would change the zero flux boundary condition (2.38) below at passivation to the flux balance type boundary condition (2.40) used at triple points. This would not

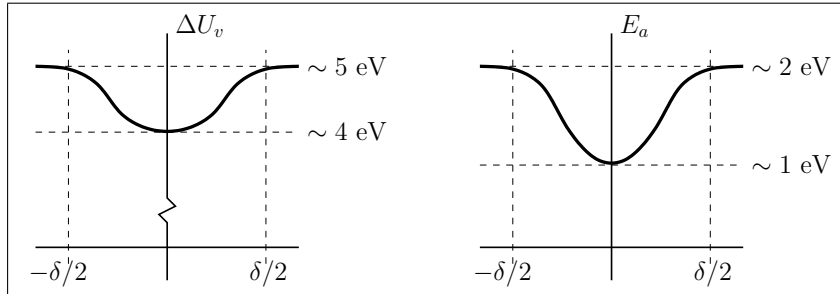


Figure 2.9: The energy of formation of a vacancy and the activation energy for exchanging a vacancy with an adjacent atom both decrease in the vicinity ($\delta =$ a few lattice constants) of a grain boundary [44, 77].

add any new complexity to the problem, and in fact would simplify things somewhat in Chapter 3 due to the fact that there would be only one connected component to the grain boundary structure on which mass must be conserved. Transport along passivation interfaces is included in the simulations described in [9, 33]. The same effect can be achieved in our model by adding a grain boundary immediately adjacent to the passivation.

2.4.1 Grain Boundary Network

Suppose we are dealing with a grain boundary network with no voids. We have already discussed in Section 2.1.4 that the Dirichlet boundary conditions for displacement at passivation require that the separation g should be 0 there. We also wish to impose the condition that the passivation act as a flux barrier so that no atoms may flow in or out of the grain boundary network at passivation junctions (points where grain boundary segments meet the outer walls). From Equation (2.33), we see that this is a condition on the derivative of σ_{nm} , namely

$$\partial_s \sigma_{nm} = \frac{Z^* e}{\Omega} \partial_s \psi, \quad (2.38)$$

where ∂_s is the derivative with respect to arclength along the grain boundary segment at the passivation junction. At triple points, we have seen (Eqn. 2.16) that there is a compatibility condition on the limiting values of g along the incident segments. We also wish to impose continuity of chemical potential and mass conservation through a balance of flux entering and leaving the triple point. From Equation (2.28), we see that chemical potential continuity requires that

$$\sigma_{n_1 n_1} = \sigma_{n_2 n_2} = \sigma_{n_3 n_3}, \quad (2.39)$$

where $\sigma_{n_i n_i} = \mathbf{n}_i \cdot \boldsymbol{\sigma} \mathbf{n}_i$, the \mathbf{n}_i are as in Figure 2.4, and the stress tensor is evaluated at the triple point. Here we have used the fact that unlike the displacement field, the stress tensor is continuous across grain boundaries. Even when we include singularities in the stress field in Chapter 4, the values of $\sigma_{n_i n_i}$ will remain finite along each grain boundary and will be equal to each other at the triple point. From Equation (2.33), we obtain the condition for flux balance at the triple point

$$\partial_{s_1} \sigma_{n_1 n_1} + \partial_{s_2} \sigma_{n_2 n_2} + \partial_{s_3} \sigma_{n_3 n_3} = \frac{Z^* e}{\Omega} (\partial_{s_1} \psi + \partial_{s_2} \psi + \partial_{s_3} \psi), \quad (2.40)$$

where ∂_{s_i} is differentiation with respect to arclength along the i th incident grain boundary segment away from the triple point. Note that the right hand side need not be zero, as

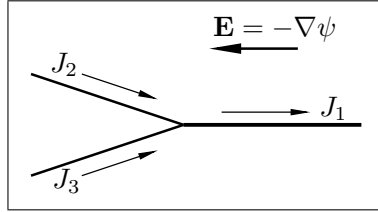


Figure 2.10: The electric field can lead to a flux imbalance at a triple point which must be compensated by stress gradients to satisfy mass conservation.

shown in Fig. 2.10. See also [56].

The boundary conditions (2.38), (2.39) and (2.40) introduce a number of mathematical difficulties. First of all, the state of stress is already completely determined by g and the geometry of the grain boundary network. We are not free to go in and impose additional boundary conditions on the stress tensor. This means we have to interpret the additional conditions as constraints on the evolution of g so that the resulting σ will always have these properties. Secondly, it is not obvious that such constraints on g are compatible with the evolution equation obtained from (2.33) and (2.36), namely

$$\frac{\partial g}{\partial t} = \frac{\nu_b D_b \Omega}{kT} \left(-\Omega \frac{\partial^2 \sigma_{nn}}{\partial s^2} + Z^* e \frac{\partial^2 \psi}{\partial s^2} \right). \quad (2.41)$$

For some problems (such as $u_t = u_{xx}$), it is not possible to specify both Dirichlet and flux boundary conditions at a boundary because the evolution is already completely determined by the Dirichlet conditions. For other problems (such as $u_t = -u_{xxxx}$), obtaining a unique solution requires that two boundary conditions such as these be specified. The added complication of obtaining the flux by applying an unbounded, non-local, non-self-adjoint operator ($g \mapsto C \partial_s \sigma_{nn}[g]$) further complicates the story. Providing answers to these questions is the topic of Chapter 3.

Chapter 3

The Grain Growth Problem

In this chapter, we focus attention on the grain boundary diffusion problem with a network of grain boundaries but no voids. We are particularly interested in the effect of singularities in the stress field near corners and triple points, and on questions of well-posedness of the equations and boundary conditions, which are summarized in Figure 3.1. As a brief reminder, the grain growth problem involves solving the Laplace equation for the electric potential, the Lamé equations for the stress and displacement fields, and the evolution equation for the separation function g , given by

$$\frac{\partial g}{\partial t} = \frac{\nu_b D_b \Omega}{kT} \left(-\Omega \frac{\partial^2 \sigma_{nn}}{\partial s^2} + Z^* e \frac{\partial^2 \psi}{\partial s^2} \right), \quad (3.1)$$

subject to the boundary conditions described in Chapter 2 and summarized in Fig. 3.1. If we choose an arbitrary length scale L ($\sim 1\mu\text{m}$) and define the timescale $t_0 = \frac{kTL^3}{\nu_b D_b \Omega^2 \mu}$, then in dimensionless variables ($\tilde{t} = \frac{t}{t_0}$, $\tilde{g} = \frac{g}{L}$, $\tilde{\sigma} = \frac{\sigma}{\mu}$, $\tilde{\psi} = -\frac{Z^* e}{\Omega \mu} \psi = \frac{|Z^*|e}{\Omega \mu} \psi$, etc.) we obtain

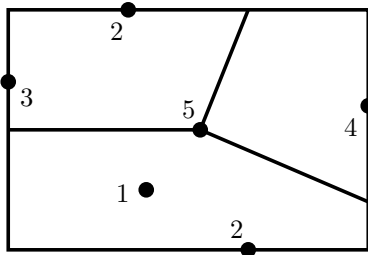
$$\frac{\partial \tilde{g}}{\partial \tilde{t}} = \left(-\frac{\partial^2 \tilde{\sigma}_{nn}}{\partial \tilde{s}^2} - \frac{\partial^2 \tilde{\psi}}{\partial \tilde{s}^2} \right). \quad (3.2)$$

We will drop the tildes and use the dimensionless equations when convenient.

We begin by presenting the basic framework of Agmon-Douglis-Nirenberg elliptic systems and recast the Lamé equations as a first order ADN system. By incorporating the rotation variable into the equations (on equal footing with the stress variables), the equations exhibit a transparent Cauchy-Riemann structure with coefficients which are uniformly bounded in the incompressible limit (where they become the Stokes equations). To our knowledge, no one has previously used the rotation variable in this way for elasticity.

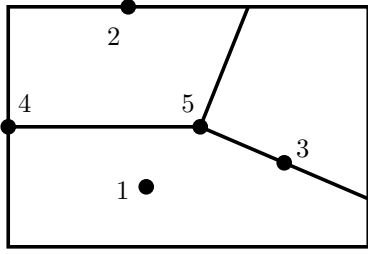
Electric Potential

1. $\nabla^2 \psi = 0$
2. $\partial_n \psi = 0$
3. $\psi = 0$
4. $\psi = \psi_0$
5. Grain boundaries are invisible to ψ .



Elasticity and Grain Growth

1. $\mu \Delta \mathbf{u} + (\lambda + \mu) \nabla (\nabla \cdot \mathbf{u}) = 0$
2. $\mathbf{u} = 0$
3. $\mathbf{u}_{\text{left}} - \mathbf{u}_{\text{right}} = g \mathbf{n}$,
 $\sigma_{\text{left}} = \sigma_{\text{right}}$
 $\partial_t g = \frac{\nu_b D_b \Omega}{kT} (-\Omega \partial_s^2 \sigma_{nn} + Z^* e \partial_s^2 \psi)$
4. $g = 0$
 $\partial_s \sigma_{nn} = \frac{Z^* e}{\Omega} \partial_s \psi$
5. $g(x_1) \mathbf{n}_1 + g(x_2) \mathbf{n}_2 + g(x_3) \mathbf{n}_3 = 0$
 $\sigma_{n_1 n_1} = \sigma_{n_2 n_2} = \sigma_{n_3 n_3}$
 $\partial_{s_1} \sigma_{n_1 n_1} + \partial_{s_2} \sigma_{n_2 n_2} + \partial_{s_3} \sigma_{n_3 n_3} = \frac{Z^* e}{\Omega} (\partial_{s_1} \psi + \partial_{s_2} \psi + \partial_{s_3} \psi)$



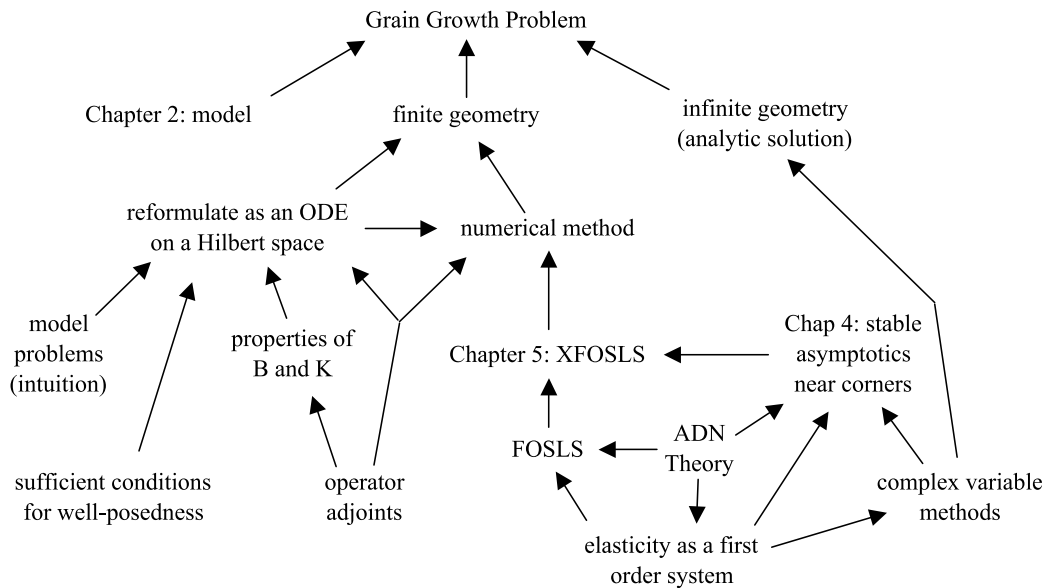


Figure 3.1: Top: Summary of equations and boundary conditions for the grain growth problem. Bottom: Flowchart illustrating the relationship between the major topics of Chapter 3.

This material will also be needed in Chapters 4 and 5. Writing the equations as a first order ADN system, it is straightforward to relate the stress functions of Airy, Kolosov and Muskhelishvili to the new variables. These complex variable methods prove useful in Chapter 4 for constructing a power solution basis for self-similar behavior near corners and grain boundary junctions, and are the essential tool we use to solve the grain growth problem for an infinite geometry.

Next we study the limiting case of an interconnect line of infinite length with a single grain boundary running through its center. We show that it is possible to write down an explicit formula for the solution by using methods of analytic function theory in planar elasticity. This formula is useful in understanding the similarities and differences between the grain growth problem and two well understood parabolic equations, namely $u_t = u_{xx}$ (the heat equation) and $u_t = -u_{xxxx}$ (the linearized surface diffusion equation). It also provides useful insight into the nature of the diffusion process involved, and offers reassurance that the high frequency eigenfunctions for a finite geometry will be almost orthogonal, which is the one thing we are unable to prove rigorously in our study of the well-posedness of the grain boundary diffusion problem.

In order to develop a strategy for the finite geometry, we review the solution to the heat equation and the linearized surface diffusion equation on a finite geometry, and discuss the expected similarities and differences for the grain boundary diffusion problem in light of its lack of self-adjointness. We then include a short section on operator adjoints, which play an important role in understanding eigenfunction expansions for diagonalizable but non-selfadjoint operators. This section also helps us interpret finite element results when a non-orthogonal finite element basis is being used.

Next we show how to reformulate the grain boundary diffusion problem as an ordinary differential equation on a Hilbert space

$$\frac{\partial}{\partial t} K\eta(t) = -\eta(t), \quad \eta(0) = \eta_0. \quad (3.3)$$

Here K is a compact operator and $\eta \in L^2(\Gamma)$ is the value of normal component $\mathbf{n} \cdot \boldsymbol{\sigma} \mathbf{n}$ of the stress tensor along the grain boundary network Γ . This reformulation absorbs all the boundary conditions into the operator K , and the well-posedness of the original problem is transformed into a question of the properties of the spectrum and eigenfunctions of the operator K . We present sufficient conditions for this equation to have a solution, and propose a numerical strategy to investigate whether these conditions hold.

Our numerical approach uses the XFOSLS method we develop in Chapter 5 for the two dimensional elastic equations to construct an approximation of the operators K and K^* , find their eigenvalues and eigenfunctions, and use them to solve the ODE (3.3). This is done first in the context of a simple finite geometry with a single horizontal grain boundary, from which we learn (by studying the numerical results) that the operator K is a product of two self-adjoint, negative operators. In Section 3.4.9 we prove this rigorously, and also prove that the spectrum of K is real and non-negative, and that its eigenfunctions are dense in $L^2(\Gamma)$. This is almost enough to satisfy the sufficient conditions derived in Section 3.4.4, the remaining requirement being that the eigenfunctions should form a well-conditioned basis for $L^2(\Gamma)$. Although we cannot prove this rigorously, the exact solution we derived for the infinite interconnect line and the condition numbers obtained in our numerical simulations provide strong evidence that the grain boundary diffusion problem is well-posed.

Next we refine the theory and numerical method to be able to handle more complicated grain boundary network geometries. The technical challenges include resolving singularities in the stress field in a stable way, dealing with the lack of a natural ordering of the nodes on the grain boundary network, handling very complicated jump discontinuity constraints along grain boundaries and at junctions, maintaining data structures that allow communication between the finite element space used for elasticity and the space used for g and η on Γ , incorporating extra basis functions near corners and junctions which may overlap each other, dealing with the possibility that Γ consists of several disjoint components, handling mass matrices which link separations g to normal stresses η on the grain boundary network even though g and η belong to slightly different finite element spaces, setting up the problem cleanly, and visualizing the results. We have obtained results which are self-consistent under mesh refinement, make physical sense, and exhibit interesting behavior such as the reversal of flux sign into a segment during the course of the evolution.

3.1 Plane Elasticity as a First Order ADN System

It will be very useful in what follows to reformulate the Lamé equations as a first order elliptic system of Agmon-Douglis-Nirenberg [1] type. Doing this leads to an easy derivation of complex variable techniques for plane elasticity [53, 57, 58], which are used in Section 3.3 to solve the grain growth problem on an infinite interconnect line. It will also prove useful in computing asymptotics near corners in Chapter 4, and in defining the error functional

for the least squares finite element method in Chapter 5. By including the rotation variable (q below) in the equations, we obtain an operator with a transparent Cauchy-Riemann structure with coefficients which are uniformly bounded over the entire range of Poisson ratio, and which is equivalent to the Stokes equations in the incompressible limit. To our knowledge, no one has made extensive use of the rotation variable in elasticity before.

3.1.1 New Variables

The Lamé equations $\mu\Delta\mathbf{u} + (\lambda + \mu)\nabla(\nabla \cdot \mathbf{u}) + \mathbf{F} = 0$ are obtained from the equations of mechanical equilibrium for an elastic solid acted upon by a body force \mathbf{F} , namely

$$\mathbf{div} \sigma + \mathbf{F} = 0, \quad (3.4)$$

by applying the Lamé relation

$$\sigma = \lambda \operatorname{tr}(\epsilon)I + 2\mu\epsilon \quad (3.5)$$

for linear isotropic materials, along with the small strain relation

$$\epsilon_{ij} = \frac{1}{2}(\partial_i u_j + \partial_j u_i). \quad (3.6)$$

The relationship between the Lamé coefficients μ and λ , Young's modulus E and the Poisson ratio ν was stated in Section 2.1.2. We restrict attention to the planar case, and define the dimensionless parameter κ ($1 \leq \kappa \leq 3$) by

$$\kappa = \frac{\lambda + 3\mu}{\lambda + \mu} = \begin{cases} 3 - 4\nu & \text{plane strain,} \\ \frac{3-\nu}{1+\nu} & \text{plane stress.} \end{cases} \quad (3.7)$$

The variables u, v, p, q, γ, τ are defined by

$$\mathbf{u} = \begin{pmatrix} u_1 \\ u_2 \end{pmatrix} = \begin{pmatrix} u \\ v \end{pmatrix}, \quad \sigma = \mu \begin{pmatrix} p - \gamma & \tau \\ \tau & p + \gamma \end{pmatrix}, \quad q = \frac{2}{\kappa + 1}(v_x - u_y). \quad (3.8)$$

Note that p, q, γ, τ are dimensionless (like components of strain), and correspond physically to the hydrostatic pressure ($-\mu p$), the rotation ($\frac{\kappa+1}{4}q$), and the deviatoric stress components

$$S = \mu \begin{pmatrix} -\gamma & \tau \\ \tau & \gamma \end{pmatrix}. \quad (3.9)$$

Using (3.5) and (3.6) to express σ in terms of \mathbf{u} [$\sigma_{11} = (\lambda + 2\mu)u_x + \lambda v_y, \dots$], we get

$$u_x - v_y = -\gamma, \quad (3.10)$$

$$u_y + v_x = \tau,$$

$$v_x - u_y = \frac{\kappa + 1}{2}q, \quad (3.11)$$

$$v_y + u_x = \frac{\kappa - 1}{2}p.$$

Expressing (3.4) in terms of the new variables, we find that

$$\gamma_x - \tau_y = p_x + \mu^{-1}F_1, \quad (3.12)$$

$$\gamma_y + \tau_x = -p_y - \mu^{-1}F_2.$$

From (3.10) and (3.11) we have

$$-\gamma_x + \tau_y = \Delta u = \frac{\kappa - 1}{2}p_x - \frac{\kappa + 1}{2}q_y, \quad (3.13)$$

$$\gamma_y + \tau_x = \Delta v = \frac{\kappa - 1}{2}p_y + \frac{\kappa + 1}{2}q_x,$$

from which it follows that (3.12) is equivalent to

$$p_x - q_y = -\frac{2\mu^{-1}}{\kappa + 1}F_1, \quad (3.14)$$

$$p_y + q_x = -\frac{2\mu^{-1}}{\kappa + 1}F_2.$$

Note the Cauchy-Riemann structure of the left hand side of each pair of equations, and that in this form, the coefficients do not diverge in the incompressible limit $\kappa \rightarrow 1$.

3.1.2 The Operators L and B

Defining the vector $w = (u, v, p, q, \gamma, \tau)^T$, the system of equations (3.10), (3.11), (3.14) may be written in the form $L(\partial_x, \partial_y)w = f$, where

$$L(a, b) = \begin{pmatrix} a & -b & 0 & 0 & 1 & 0 \\ b & a & 0 & 0 & 0 & -1 \\ -b & a & 0 & -\frac{\kappa+1}{2} & 0 & 0 \\ a & b & -\frac{\kappa-1}{2} & 0 & 0 & 0 \\ 0 & 0 & a & -b & 0 & 0 \\ 0 & 0 & b & a & 0 & 0 \end{pmatrix}, \quad f = -\frac{2\mu^{-1}}{\kappa + 1} \begin{pmatrix} 0 \\ 0 \\ 0 \\ 0 \\ F_1 \\ F_2 \end{pmatrix}. \quad (3.15)$$

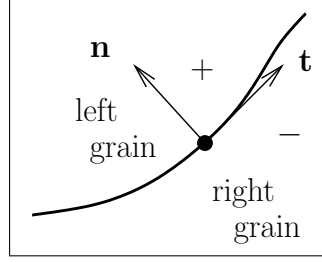


Figure 3.2: The force per unit area exerted *by* the positive side *on* the negative side of a surface with normal \mathbf{n} is given by $\sigma \mathbf{n}$

The common boundary conditions for elasticity are particularly easy to express in terms of the new variables due to the fact that it is not necessary to express conditions on stress in terms of derivatives of displacement. Along an arc with tangent vector $\mathbf{t} = (\cos \theta, \sin \theta)$ and normal vector $\mathbf{n} = (-\sin \theta, \cos \theta)$, we have

$$\begin{aligned}
 u_{\parallel} &= \mathbf{u} \cdot \mathbf{t} = (\cos \theta, \sin \theta, 0, 0, 0, 0) \cdot w, \\
 u_{\perp} &= \mathbf{u} \cdot \mathbf{n} = (-\sin \theta, \cos \theta, 0, 0, 0, 0) \cdot w, \\
 \sigma_s &= \mathbf{t} \cdot \sigma \mathbf{n} = \mu(0, 0, 0, 0, \sin 2\theta, \cos 2\theta) \cdot w, \\
 \sigma_{\perp} &= \mathbf{n} \cdot \sigma \mathbf{n} = \mu(0, 0, 1, 0, \cos 2\theta, -\sin 2\theta) \cdot w, \\
 \sigma_{\parallel} &= \mathbf{t} \cdot \sigma \mathbf{t} = \mu(0, 0, 1, 0, -\cos 2\theta, \sin 2\theta) \cdot w.
 \end{aligned} \tag{3.16}$$

With this sign convention, \mathbf{n} is the unit inward normal at a wall when the boundary is traversed counterclockwise, which is convenient for setting up local coordinates but inconvenient in that the external traction vector is $\sigma(-\mathbf{n})$. Along grain boundaries this convention is quite natural as \mathbf{n} points from the negative side (the right grain) to the positive side (the left grain). We are using the standard meaning of σ , which is that $\sigma \mathbf{n}$ is the force per unit area exerted *by* the positive side *on* the negative side of a surface with normal \mathbf{n} ; see Figure 3.2.

From (3.16), we see, for example, that Dirichlet boundary conditions can be expressed as $Bw = 0$, where

$$B = \begin{pmatrix} \cos \theta & \sin \theta & 0 & 0 & 0 & 0 \\ -\sin \theta & \cos \theta & 0 & 0 & 0 & 0 \end{pmatrix}. \tag{3.17}$$

At a grain boundary interface, we may express Eqns. (2.11)–(2.14) on page 18 as $Bw^{\pm} = \phi$,

where $B = (B_1, -B_1)$ and

$$w^\pm = \begin{pmatrix} w^+ \\ w^- \end{pmatrix}, \quad B_1 = \begin{pmatrix} \cos \theta & \sin \theta & 0 & 0 & 0 & 0 \\ -\sin \theta & \cos \theta & 0 & 0 & 0 & 0 \\ 0 & 0 & 0 & 0 & \sin 2\theta & \cos 2\theta \\ 0 & 0 & 1 & 0 & \cos 2\theta & -\sin 2\theta \end{pmatrix}, \quad \phi = \begin{pmatrix} 0 \\ g \\ 0 \\ 0 \end{pmatrix}. \quad (3.18)$$

3.1.3 ADN Indices

The system $Lw = f$ together with two of the boundary conditions (3.16) fits into the framework of Agmon-Douglis-Nirenberg elliptic systems [1, 55, 80, 79], which generalizes the method of reducing an ordinary differential equation to a first order system of equations. The essential idea is to assign each variable, equation, and boundary condition an index (or weight) which describes its “order”; in our system, the stress variables are obtained from the displacements through differentiation, so we may take the variable indices to be

$$(t_j) = (0, 0, -1, -1, -1, -1). \quad (3.19)$$

The equation weights s_i are chosen so that $s_i + t_j$ is an upper bound on the degree of $L_{ij}(a, b)$ as a polynomial in a and b . If $s_i + t_j < 0$, L_{ij} must be identically zero. The principal part L' of L is obtained by taking those terms with degree exactly equal to $s_i + t_j$ (or zero if $\deg L_{ij}(a, b) < s_i + t_j$), and L is said to be *homogeneous of multi-degree* if $L = L'$. In our case, L is homogeneous of multi-degree with

$$(s_i) = (1, 1, 1, 1, 2, 2). \quad (3.20)$$

Normally the normalization is taken so that $\max s_i = 0$, but it will be more useful for us when constructing corner singularities to normalize with $\max t_j = 0$. Even with such normalization, it can happen that the indices are not uniquely determined, as can be seen from the example of two copies of the Cauchy-Riemann equations, where $(t_j) = (0, 0, -k, -k)$, $(s_i) = (1, 1, 1 + k, 1 + k)$ will work for any $k \geq 0$. The theory of ADN-elliptic systems applies for any choice of these indices, but it is usually clear in practical cases which choice of indices is the “most natural” to use. We note that the definition of L' together with the fact that the determinant is a sum of products, each with precisely one factor from each row and column, ensures that $[\det L'(a, b)]$ is a homogeneous polynomial in a and b of degree $\sum_1^N (s_i + t_i)$. The system is said to be elliptic provided that

$$\det L'(a, b) \neq 0 \quad (a, b) \in \mathbb{R}^2 \setminus (0, 0), \quad (3.21)$$

and is said to be properly elliptic under the further condition that $2m := \sum_1^N (s_i + t_i)$ is even and the equation $[\det L'(\xi + z\xi') = 0]$ has exactly m roots with positive imaginary part and m with negative imaginary part for any linearly independent $\xi, \xi' \in R^2$. Ellipticity implies proper ellipticity in dimension greater than two [55]. In our case, $\det L'(a, b) = (a^2 + b^2)^2$, so proper ellipticity holds with $m = 2$.

The parameter m determines the number of appropriate boundary conditions to impose. They are given in the form

$$B(\partial_x, \partial_y)w = \phi, \quad (3.22)$$

where $B(a, b)$ is an $m \times N$ matrix and we have boundary condition indices q_i such that $\deg B_{ij} \leq q_i + t_j$. The principal part B' of B consists of the entries of B of degree exactly equal to $q_i + t_j$, and B' and L' must *complement* each other by satisfying the Lopatinskij condition; see [1, 55] and Section 3.1.4 below. Any two of our boundary conditions (3.16) satisfy this condition, taking $q_i = 0$ for displacement boundary conditions and $q_i = 1$ for stress boundary conditions. A convenient feature of the resulting B is that even for stress boundary conditions, $B(a, b)$ is a constant matrix (of degree zero in a and b); we don't have derivatives in the boundary conditions.

3.1.4 A Few Remarks

Through the ADN reduction process, we transformed a second order 2×2 system to a first order 6×6 system, leaving the parameter m invariant. This reduction will be particularly useful in the least squares finite element method, and in constructing corner singularities in Chapter 4. In [1, 55], the theory of ADN systems is presented in the more general case of n dimensions with the coefficients of the polynomials $L(x_1, \dots, x_n; \partial_{x_1}, \dots, \partial_{x_n})$ and $B(x_1, \dots, x_n; \partial_{x_1}, \dots, \partial_{x_n})$ depending on position.

There are many theorems on the regularity and normal solvability of ADN elliptic systems. For smooth domains, the original paper [1] uses Schauder estimates and boundary integral methods for a half space to get useful coercive inequalities for Hölder and L^p spaces. The paper [54] generalizes the results in [45] on the solvability of elliptic equations on domains with corners and angular points to the case of ADN elliptic systems. Existence, uniqueness and regularity results may also be obtained for the Lamé equations using Sobolev spaces; see [29, 19].

I am not familiar with any papers describing interface boundary conditions such as Eqn. (3.18) in the ADN framework. One way of characterizing the Lopatinskij covering condition is as follows. Change variables locally to flatten the boundary and freeze the coefficients of L at (x_0, y_0) . On the half-space $y > 0$, use separation of variables $w = v(y)e^{ix\xi}$ to convert the system of PDE's to a system of ODE's:

$$L(x_0, y_0; \partial_x, \partial_y)v(y)e^{ix\xi} = 0 \quad \Rightarrow \quad L(x_0, y_0; i\xi, \partial_y)v(y) = 0. \quad (3.23)$$

Note that this system is degenerate in the sense that A does not necessarily have full rank if it is expressed in the form $Av' + Bv = 0$. The Complementing Condition requires that for every $\xi \neq 0$, $v \equiv 0$ is the only bounded solution for $y > 0$ which satisfies the homogeneous boundary conditions at $y = 0$. Presumably the correct generalization of this to the interface case will lead to two ordinary differential equations on $-\infty < y < 0$ and $0 < y < \infty$ with boundary conditions at $y = 0$ which may link $v^-(0)$ to $v^+(0)$. The requirement should be the same, namely that $v^- \equiv v^+ \equiv 0$ is the only solution to the homogeneous problem with v^- and v^+ bounded at $-\infty$ and ∞ , respectively. Considering the case when v^- and v^+ are decoupled, we expect that $2m$ boundary conditions are needed at interfaces, which is compatible with what we are enforcing in Eqn. (3.18).

3.2 Complex Variable Methods in Plane Elasticity

In this section we show how complex variable methods for plane elasticity fit in with our ADN variables. We use these methods in the next section to solve the grain growth problem on an infinite interconnect line, and to generate a basis for the singular functions near corners and interface junctions in Chapter 4.

In the case that $\mathbf{F} = 0$, we see from Eqn. (3.14) that p and q satisfy the Cauchy-Riemann equations:

$$\begin{aligned} p_x - q_y &= 0, \\ p_y + q_x &= 0. \end{aligned} \quad (3.24)$$

Therefore there is a harmonic function Φ such that

$$p + iq = 2\Phi. \quad (3.25)$$

Using the standard notation

$$\frac{\partial}{\partial \bar{z}} = \frac{1}{2}\left(\frac{\partial}{\partial x} + i\frac{\partial}{\partial y}\right), \quad \frac{\partial}{\partial z} = \frac{1}{2}\left(\frac{\partial}{\partial x} - i\frac{\partial}{\partial y}\right), \quad (3.26)$$

we have that

$$\frac{\partial}{\partial \bar{z}}(\bar{z}\Phi') = \Phi' = \frac{1}{2}(p_x + iq_x) = \frac{1}{2}(p_x - ip_y). \quad (3.27)$$

From Eqn. (3.12) with $\mathbf{F} = 0$, we have

$$\begin{aligned} \gamma_x - \tau_y &= p_x, \\ \gamma_y + \tau_x &= -p_y. \end{aligned} \quad (3.28)$$

Therefore

$$\frac{\partial}{\partial \bar{z}}(\gamma + i\tau - \bar{z}\Phi') = 0 \quad (3.29)$$

and there exists a harmonic function Ψ such that

$$\gamma + i\tau = \bar{z}\Phi' + \Psi. \quad (3.30)$$

Φ and Ψ are known as Kolosov functions.

If the domain is simply connected, there exist harmonic ϕ , ψ and χ such that $\phi' = \Phi$, $\psi' = \Psi$, and $\chi' = \psi$. One readily checks that

$$\frac{\partial}{\partial \bar{z}} \left(\frac{1}{2}[\kappa\phi - z\bar{\Phi} - \bar{\psi}] \right) = -z\bar{\Phi}' - \bar{\Psi} = -\gamma + i\tau, \quad (3.31)$$

$$\frac{\partial}{\partial z} \left(\frac{1}{2}[\kappa\phi - z\bar{\Phi} - \bar{\psi}] \right) = \frac{1}{2}(\kappa\Phi - \bar{\Phi}) = \frac{\kappa-1}{2}p + i\frac{\kappa+1}{2}q, \quad (3.32)$$

so the expression in parentheses on the left hand side satisfies Equations (3.10) and (3.11):

$$u_x - v_y = -\gamma, \quad (3.33)$$

$$u_y + v_x = \tau,$$

$$v_x - u_y = \frac{\kappa+1}{2}q, \quad (3.34)$$

$$v_y + u_x = \frac{\kappa-1}{2}p.$$

Since solutions to (3.33) and (3.34) for fixed p, q, γ, τ differ by at most a constant vector (due to the fact that the difference satisfies $\nabla u = \nabla v = 0$), we may add appropriate constants to ϕ and ψ so that the displacements satisfy

$$u + iv = \frac{1}{2}[\kappa\phi - z\bar{\Phi} - \bar{\psi}]. \quad (3.35)$$

The functions ϕ and ψ are known as Muskhelishvili functions.

The function $U = \text{Re}\{\bar{z}\phi + \chi\}$ is known as the Airy stress function. Since ϕ and χ are holomorphic, U satisfies the biharmonic equation

$$\Delta^2 U = 16 \frac{\partial^4 U}{\partial \bar{z}^2 \partial z^2} = 0, \quad (3.36)$$

and using $\partial_x = (\partial_z + \partial_{\bar{z}})$, $\partial_y = i(\partial_z - \partial_{\bar{z}})$ we compute $U_x = \text{Re}\{\bar{z}\Phi + \psi + \phi\}$, $U_y = \text{Re}\{i(\bar{z}\Phi + \psi - \phi)\}$, $U_{xx} = \text{Re}\{\bar{z}\Phi' + \Psi + 2\Phi\}$, $U_{xy} = \text{Re}\{i(\bar{z}\Phi' + \Psi)\}$, and $U_{yy} = \text{Re}\{-\bar{z}\Phi' - \Psi + 2\Phi\}$, which means

$$\sigma_{11} = \mu U_{yy}, \quad \sigma_{22} = \mu U_{xx}, \quad \sigma_{12} = -\mu U_{xy}. \quad (3.37)$$

Often μ is omitted here and included in Φ , Ψ , ϕ , ψ , χ and U . In the multiply connected case, it can be necessary to include logarithm terms in ϕ , ψ , χ for each connected component of the complement of the domain. For more information on the use of complex function theory in plane elasticity, see [53, 57, 58]. The functions ϕ and ψ will prove useful in the next section, and again in Chapter 4 when we compute corner singularities. In summary, on a simply connected domain, for any solution to the Lamé equations there exist analytic functions ϕ and ψ such that

$$p + iq = 2\phi', \quad (3.38)$$

$$\gamma + i\tau = \bar{z}\phi'' + \psi', \quad (3.39)$$

$$u + iv = \frac{1}{2} [\kappa\phi - z\bar{\phi}' - \bar{\psi}]. \quad (3.40)$$

3.3 An Infinite Interconnect Line

In this section, we work out an exact solution to the grain boundary diffusion problem $g_t = -\sigma_{22}[g]_{xx}$ for an infinite interconnect line with a single grain boundary running through the center. This provides useful insight about the problem without the complication of boundary conditions at grain boundary endpoints or singularities in the stress field. The approach is to solve the elastic equations for a sinusoidal separation function g , and then use separation of variables and the Fourier transform to determine the evolution for an arbitrary initial condition.

3.3.1 Elastic Equations for Sinusoidal Separation

As shown in Fig. 3.3, let the center of the interconnect line (the grain boundary) coincide with the x -axis, and let h denote the width of each grain. By symmetry, for any separation

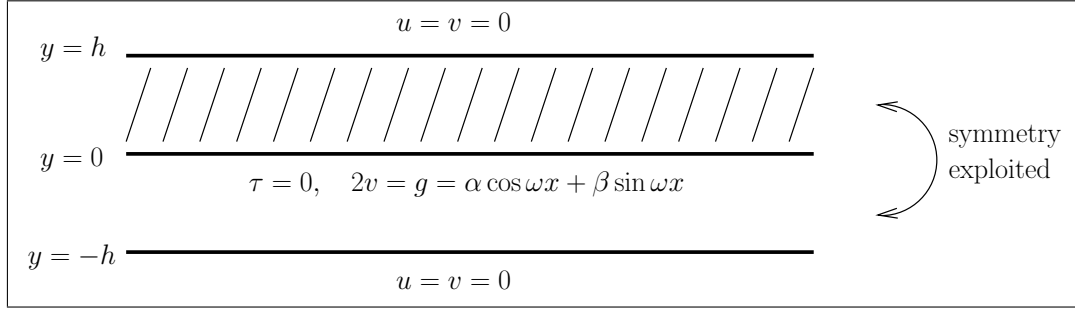


Figure 3.3: The geometry and boundary conditions for the grain growth problem on an infinite strip.

$g(x)$ the displacements in the top grain will be related to the displacements in the bottom grain via

$$u^+(x, y) = u^-(x, -y), \quad v^+(x, y) = -v^-(x, -y). \quad (3.41)$$

From (3.10) and (3.11), we see that the other variables will be related through

$$p^+(x, y) = p^-(x, -y), \quad q^+(x, y) = -q^-(x, -y), \quad (3.42)$$

$$\gamma^+(x, y) = \gamma^-(x, -y), \quad \tau^+(x, y) = -\tau^-(x, -y). \quad (3.43)$$

It is therefore sufficient to restrict attention to the top grain. At $y = h$, we impose the Dirichlet boundary conditions $u = v = 0$, and along the grain boundary, the four conditions $u^+ = u^-$, $v^+ - v^- = g$, $p^+ + \gamma^+ = p^- + \gamma^-$, $\tau^+ = \tau^-$ reduce via symmetry to $\tau = 0$, $v = g/2$. We observe that in the limit as $h \rightarrow \infty$, these boundary conditions coincide with the problem of a rigid stamp without friction on a half-space, and can be solved using singular integrals [58]. We omit details since the result for finite h covers this case in the limit.

For finite h , the singular integral approach doesn't work (at least not easily), so instead we make an ansatz for the form of the Muskhelishvili functions:

$$\phi = (a_1 + ia_2) \cos \omega z + (a_3 + ia_4) \sin \omega z, \quad (3.44)$$

$$\psi = (a_5 + ia_6) \cos \omega z + (a_7 + ia_8) \sin \omega z + (a_9 + ia_{10})z \cos \omega z + (a_{11} + ia_{12})z \sin \omega z, \quad (3.45)$$

and wish to determine if there are real coefficients a_i for which the boundary conditions are satisfied. We begin by constructing the 4×12 real matrix $A_0(\omega, \kappa, h, x)$ whose i^{th}

column contains the boundary conditions $u(y = h)$, $v(y = h)$, $v(y = 0)$, $\tau(y = 0)$ for the corresponding ϕ and ψ . For example, the second column corresponds to $\phi = i \cos \omega z$, $\psi = 0$:

$$\text{col}_2(A_0) = \frac{1}{2} \begin{pmatrix} \omega h \sin \omega x \cosh \omega h - \omega x \cos \omega x \sinh \omega h + \kappa \sin \omega x \sinh \omega h \\ -\omega h \cos \omega x \sinh \omega h - \omega x \sin \omega x \cosh \omega h + \kappa \cos \omega x \cosh \omega h \\ -\omega x \sin \omega x + \kappa \cos \omega x \\ -2\omega^2 x \cos \omega x \end{pmatrix}. \quad (3.46)$$

Next we define the 16×12 real matrix $A(\omega, \kappa, h)$ by expanding each row of A_0 into four rows containing the coefficients of $\cos(\omega x)$, $\sin(\omega x)$, $x \cos(\omega x)$, $x \sin(\omega x)$. In order to satisfy the boundary conditions in Fig. 3.3, we need to find $a \in R^{12}$ such that $Aa = b$, where b contains the desired coefficients of the terms $\cos(\omega x)$, $\sin(\omega x)$, $x \cos(\omega x)$, $x \sin(\omega x)$ in the boundary conditions. Explicitly, b and the second column of A are given by

$$b = \frac{1}{2} \begin{pmatrix} 0 \\ 0 \\ 0 \\ 0 \\ 0 \\ 0 \\ 0 \\ 0 \\ 0 \\ \alpha \\ \beta \\ 0 \\ 0 \\ 0 \\ 0 \\ 0 \end{pmatrix}, \quad \text{col}_2(A) = \frac{1}{2} \begin{pmatrix} 0 \\ \omega h \cosh \omega h + \kappa \sinh \omega h \\ -\omega \sinh \omega h \\ 0 \\ -\omega h \sinh \omega h + \kappa \cosh \omega h \\ 0 \\ 0 \\ -\omega \cosh \omega h \\ \kappa \\ 0 \\ 0 \\ -\omega \\ 0 \\ 0 \\ -2\omega^2 \\ 0 \end{pmatrix}. \quad (3.47)$$

We verify that a solution exists by computing the nullspace of A^T symbolically and checking that $b \in (\ker A^T)^\perp = \text{image } A$. We then select 12 linearly independent rows of A (and the corresponding rows of b) and solve $Aa = b$ symbolically. The resulting a determines ϕ and ψ , which we use to compute $\sigma_{22} = p + \gamma$ along the grain boundary. This only has to be done

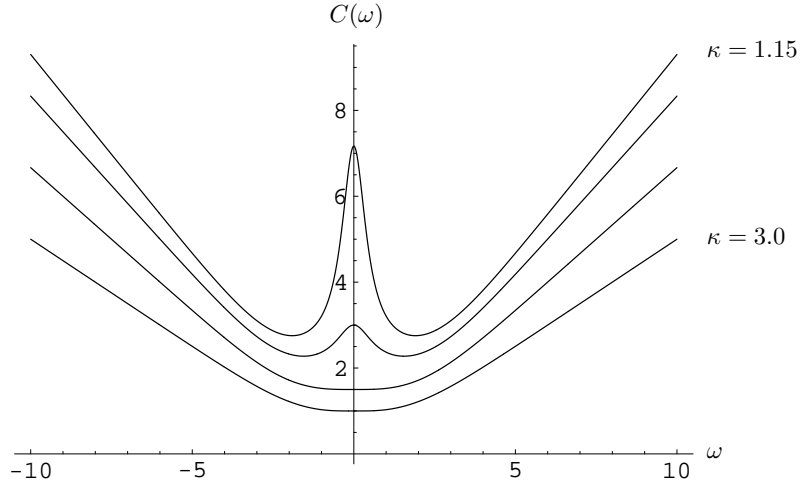


Figure 3.4: A plot of $C(\omega)$ for $h = 1$ and $\kappa = 1.15, 1.4, 2.0, 3.0$. Note that $C(\omega)$ diverges in the incompressible ($\kappa \rightarrow 1$), long wavelength ($\omega \rightarrow 0$) limit.

once since the parameters such as κ and h appear symbolically. All of this, including the construction of A_0 and A via (3.38), (3.39), (3.40), (3.44), and (3.45), can be done without difficulty using Mathematica or Maple.

The result of this computation is that along the grain boundary, σ_{22} is a constant multiple of g for any α, β, ω :

$$\sigma_{22}(x, y = 0) = -C(\omega)g(x), \quad C(\omega) = \frac{\omega[1 + \kappa^2 + 4h^2\omega^2 + 2\kappa \cosh 2h\omega]}{(1 + \kappa)[\kappa \sinh 2h\omega - 2h\omega]}. \quad (3.48)$$

A plot of $C(\omega)$ for a few values of κ is given in Fig. 3.4. For large and small ω , we see that $C(\omega)$ has the asymptotic form

$$C(\omega) = \frac{2\omega}{1 + \kappa}, \quad (|h\omega| \gg 1), \quad (3.49)$$

$$C(\omega) = \frac{1}{h} \left\{ \frac{\kappa + 1}{2(\kappa - 1)} - \frac{(\kappa - 2)(\kappa - 3)}{3(\kappa - 1)^2} (h\omega)^2 + \dots \right\}, \quad (|h\omega| \ll 1). \quad (3.50)$$

The fact that σ_{22} is proportional to g when g varies harmonically will allow us to use the Fourier transform to solve the grain boundary diffusion problem for an arbitrary initial separation $g(x, t = 0)$.

3.3.2 Evolution for an Arbitrary Initial Separation

Because $\sigma_{22}(x) = -C(\omega)g(x)$ when $g(x)$ varies harmonically, we see that the solution to $g_t = -\sigma_{22}[g]_{xx}$ with initial condition $g(x, t = 0) = \cos \omega x$ is given by

$$g(x, t) = e^{-C(\omega)\omega^2 t} \cos \omega x. \quad (3.51)$$

This gives the time evolution of each Fourier mode for an arbitrary initial separation: if we write g at $t = 0$ as

$$g(x, 0) = \int_{-\infty}^{\infty} e^{i\omega x} \hat{g}(\omega, 0) d\omega, \quad (3.52)$$

then at any later time g will be

$$g(x, t) = \int_{-\infty}^{\infty} e^{i\omega x} \hat{g}(\omega, t) d\omega = \int_{-\infty}^{\infty} e^{i\omega x} e^{-C(\omega)\omega^2 t} \hat{g}(\omega, 0) d\omega. \quad (3.53)$$

It is instructive to compare the dissipation rate $C(\omega)\omega^2$ to that for the heat equation and the linearized surface diffusion equation:

Dissipation Rate	Equation
$b\omega^2$	$u_t = bu_{xx} \quad (b > 0)$
$C(\omega)\omega^2$	$g_t = -\sigma_{22}[g]_{xx}$
$b\omega^4$	$u_t = -bu_{xxxx} \quad (b > 0)$

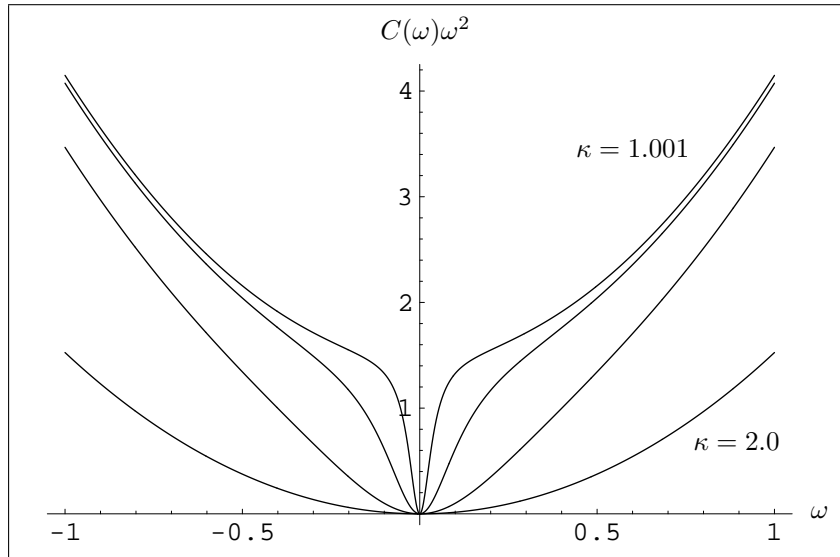


Figure 3.5: A plot of the dissipation rate $C(\omega)\omega^2$ for $h = 1$ and $\kappa = 1.001, 1.01, 1.1, 2.0$. Note that even though $C(\omega)$ is not monotonic for $\kappa < 2$, $C(\omega)\omega^2$ is monotonic for $\omega \geq 0$. The envelope of the graphs approaches $\frac{3}{2} + \frac{27}{10}\omega^2$ near the origin as $\kappa \rightarrow 1$.

Looking back at Figure 3.4 and Equations (3.48)–(3.50), we see that low frequency modes decay like the heat equation with $b = (\kappa + 1)[2h(\kappa - 1)]^{-1}$, whereas high frequency modes decay as $\exp(-b|\omega|^3)$ with $b = 2(1 + \kappa)^{-1}$, which is halfway between the heat equation and the linearized surface diffusion equation. This is an interesting observation, as it gives us an understanding of the type of diffusion process involved. Even though $C(\omega)$ is not monotonic in ω when $\kappa < 2$, the dissipation rate $C(\omega)\omega^2$ is monotonic for $\omega \geq 0$, as can be seen from Figure 3.5.

3.3.3 Steady Current

In the above analysis, we considered the equation $g_t = -\sigma_{22}[g]_{xx}$ with no electromigration term. For the infinite interconnect line, a steady current would be characterized by the potential $\psi(x, y) = \alpha x$, which does not contribute to Equation (3.2) on page 33, so in fact we have solved the problem for the steady current case as well. At first sight, it is surprising that a steady current has no effect on the solution, but this is due to the fact that the atoms are simply migrating down the line due to electromigration; they don't accumulate anywhere and there are always more atoms upstream to replace the atoms that leave a given section of the line. This situation will change dramatically for a finite geometry, where zero flux boundary conditions at grain boundary endpoints act as barriers which lead to depletion and accumulation of atoms in their vicinity as soon as an electric current is present.

3.4 A Finite Geometry

In this section we reformulate the grain boundary diffusion problem as an ordinary differential equation on a Hilbert space. This transforms the question of well-posedness into a question about the nature of the spectrum and eigenspaces of a compact operator. This reformulation provides a nice solution to the issue of how to enforce non-local boundary conditions, and leads directly to a numerical method for solving the problem. We begin by looking at two well understood model problems to provide intuition and help us formulate a strategy.

3.4.1 Two Model Problems

It was shown earlier that for an infinite geometry, the grain boundary diffusion problem was in a sense halfway between the equations $u_t = u_{xx}$ and $u_t = -u_{xxxx}$. Understand how these problems change when the domain becomes finite will help us formulate a strategy for the grain growth problem.

The heat equation and linearized surface diffusion equation are “easy” because the operators ($u \mapsto -u_{xx}$) and ($u \mapsto u_{xxxx}$) (with appropriate boundary conditions) are self-adjoint. Self-adjointness implies [20, 59] the existence of a complete, L^2 -orthonormal basis of eigenfunctions for the operator, with real eigenvalues that accumulate only at $\pm\infty$. Explicitly, the boundary value problem

$$Lu = -u_{xx}, \quad Uu = (u(0), u(1))^T = 0 \quad (3.54)$$

has eigenfunctions and eigenvalues

$$\varphi_k(x) = \sqrt{2} \sin k\pi x, \quad \lambda_k = k^2\pi^2, \quad k = 1, 2, \dots \quad (3.55)$$

and the boundary value problem

$$Lu = u_{xxxx}, \quad Uu = (u(0), u(1), u'(0), u'(1))^T = 0 \quad (3.56)$$

has eigenfunctions and eigenvalues

$$\varphi_k(x) = \begin{cases} c_k [\cos \omega_k \pi (x - \frac{1}{2}) - \frac{\cos(\omega_k \pi/2)}{\cosh(\omega_k \pi/2)} \cosh \omega_k \pi (x - \frac{1}{2})] & k = 1, 3, 5, \dots \\ c_k [\sin \omega_k \pi (x - \frac{1}{2}) - \frac{\sin(\omega_k \pi/2)}{\sinh(\omega_k \pi/2)} \sinh \omega_k \pi (x - \frac{1}{2})] & k = 2, 4, 6, \dots \end{cases} \quad (3.57)$$

$$\lambda_k = \omega_k^4 \pi^4, \quad \omega_k = 1.5056, 2.4998, 3.50001, 4.4999995, 5.50000002, \dots \quad (3.58)$$

Here the c_k are chosen so that $(\varphi_k, \varphi_k)_{L^2} = 1$. Writing the equations ($u_t = u_{xx}$) and ($u_t = -u_{xxxx}$) in the form

$$u_t = -Lu, \quad Uu = 0, \quad u(x, t = 0) = u_0(x), \quad (3.59)$$

we obtain the solution by decomposing the initial condition u_0 into the eigenfunctions of the operator L

$$u_0(x) = \sum_{k=1}^{\infty} a_k \varphi_k(x), \quad (3.60)$$

and then evolving each component separately

$$u(x, t) = \sum_{k=1}^{\infty} a_k e^{-\lambda_k t} \varphi_k(x). \quad (3.61)$$

Because the spectrum of L is positive and goes to infinity, high frequency modes decay very rapidly, and it is easy to show that Eqn. (3.61) satisfies (3.59).

In practice, Equation (3.59) would normally be solved using an implicit method such as Backward Euler or Crank-Nicholson [74]. An alternative to this approach is to make use of (3.61) to compute the “time t evolution operator” by solving eigenvalue problems to compute the φ_k . For the grain growth problem, we have found the latter approach to be more fruitful, so we focus on this approach in the remainder of this section.

The proof [20] of the expansion and completeness theorem for self-adjoint boundary value problems is based on the construction of a compact operator K which is the inverse of the unbounded operator L in the sense that

$$LKf = f, \quad KLu = u \quad (3.62)$$

for all $f \in C[a, b]$ and $u \in C^r[a, b]$ ($r = \text{order of } L$) satisfying $Uu = 0$. L and K have the same eigenfunctions with reciprocal eigenvalues. Standard theorems on the spectrum and eigenspaces of a self-adjoint compact operator on a Hilbert space are then readily applicable [30, 66]. The operator K may be expressed as an integral operator in terms of a Green’s function $G(x, \xi)$:

$$Kf(x) = \int_0^1 G(x, \xi) f(\xi) d\xi. \quad (3.63)$$

For $Lu = -u_{xx}$ and $Lu = u_{xxxx}$ respectively, G has the explicit form

$$G(x, \xi) = \begin{cases} (1 - \xi)x, & x < \xi \\ (1 - x)\xi, & x > \xi \end{cases}, \quad G(x, \xi) = \begin{cases} \frac{1}{6}(1 - \xi)^2 x^2 (3\xi - x - 2x\xi), & x < \xi \\ \frac{1}{6}(1 - x)^2 \xi^2 (3x - \xi - 2x\xi), & x > \xi \end{cases}. \quad (3.64)$$

In addition to being of theoretical interest in the expansion and completeness theorem, the compact operator K is useful to work with numerically for solving eigenvalue problems. If we didn’t know the expansions (3.55), (3.57) explicitly, we could compute them using finite elements or finite differences. Either method provides an approximation to K by providing a solution u for any right hand side f such that

$$Lu = f, \quad Uu = 0. \quad (3.65)$$

The fact that K is compact means that it is well approximated by finite rank operators, which is why it is possible to compute the spectra in this way.

Focusing on the finite element approach [10], we can approximately solve

$$Lu = \lambda u \quad (3.66)$$

by choosing a finite element space S_h with basis $\varepsilon_1, \dots, \varepsilon_m$ and seeking all λ and $z \in R^m$ such that $u_h = \sum z_k \varepsilon_k$ satisfies

$$(\varepsilon_k, Lu_h)_{L^2} = \lambda (\varepsilon_k, u_h)_{L^2} \quad (k = 1, \dots, m), \quad (3.67)$$

the left hand side taken in the weak sense using integration by parts. For the model problems considered here, this leads to a generalized eigenvalue problem from linear algebra on R^m , namely

$$Az = \lambda Mz, \quad (3.68)$$

where A and M are symmetric, sparse, and positive definite. Note that M is generally not the identity because the basis ε_k is generally not orthogonal. Special techniques [27] exist to exploit the sparsity of A and M to solve (3.68), but in one dimension the matrices are generally small enough that dense linear algebra can be used without difficulty. The operator $A^{-1}M$ is our approximation for K on the subspace spanned by the ε_k , expressed as a matrix in this basis. The approximate eigenvalues μ of K are the reciprocals of the λ 's obtained by solving (3.68), and the corresponding eigenfunctions are obtained from the eigenvectors z via $\sum z_k \varepsilon_k$.

The largest eigenvalues of K correspond to smooth eigenfunctions which can be accurately represented by standard finite element spaces, and therefore accurately computed. The small eigenvalues of K correspond to large eigenvalues of L , which by (3.61) decay extremely rapidly. This means that it is not important to resolve small eigenvalues and their eigenfunctions insofar as failing to do so does not prevent an accurate computation of the large eigenvalues and corresponding eigenfunctions. Due to the guaranteed orthogonality of the eigenfunctions for a self-adjoint problem, the coefficients a_k in (3.60) are simply given by $(u_0, \varphi_k)_{L^2}$, and therefore do not depend on the other φ_l . This situation could be quite different if K were not self-adjoint. Everything that can happen in the finite dimensional case (such as Jordan chains of generalized eigenvectors) can happen here, and in fact there need not be any eigenvectors at all (e.g. the Volterra operator $Vf(x) = \int_0^x f(t) dt$ has no

eigenfunctions). Even if K has eigenfunctions which span a dense subspace of L^2 , the eigenfunctions corresponding to smaller eigenvalues could become highly linearly dependent on the earlier eigenfunctions. In that case, if an expansion like (3.60) is possible at all, the coefficients a_k are obtained by taking the inner product of u_0 with a vector φ_k^* in the orthogonal complement of the span of the other φ_l , and determining them could become difficult or impossible depending on the severity of the linear dependence in the limit as $k \rightarrow \infty$. The vector φ_k^* is an eigenfunction of K^* with eigenvalue $\bar{\mu}_k$; see Section 3.4.2.

In the grain boundary diffusion problem $g_t = -\sigma_{22}[g]_{xx}$ on a finite geometry, the operator ($g \mapsto \sigma_{22}[g]_{xx}$) is not self-adjoint, so we will have to watch out for these difficulties. In the case of the infinite interconnect line, the eigenfunctions turned out to be orthogonal, and the dissipation rate $C(\omega)\omega^2$ was seen to behave asymptotically as $|\omega|^3$ for large $|\omega|$. For a finite interconnect line, we can expect to lose orthogonality, and don't have any guarantee that the spectrum will even be real, much less positive. (In fact we do have this guarantee — see Section 3.4.9; the spectrum of K is both real and non-negative). In the case of $u_t = -u_{xxxx}$, the effect of the endpoints remains localized due to the fact that the cosh and sinh terms in Eqn. (3.57) are only significant near the ends. We may hope that the grain boundary diffusion problem exhibits the same behavior, in which case the infinite interconnect line should provide a good description of the behavior of high frequency modes away from the ends. This suggests that the spectrum of K will behave asymptotically like $\lambda_k = ck^{-3}$, and the high frequency eigenfunctions will be nearly orthogonal. This prediction is verified numerically in Section 3.4.6; see Figure 3.15 on page 77.

3.4.2 Operator Adjoints

As mentioned in the previous section, adjoints play an important role in non-self-adjoint problems, so we briefly present a convenient framework for dealing with them. Let H_1 and H_2 be Hilbert spaces. We adopt the convention that an inner product is linear in the second argument and conjugate linear in the first. The adjoint of an operator $X : H_1 \rightarrow H_2$ is uniquely defined as the mapping $X^* : H_2 \rightarrow H_1$ such that

$$(X^*u, v)_{H_1} = (u, Xv)_{H_2}, \quad (u \in H_2, v \in H_1). \quad (3.69)$$

Let us assume that H_1 is either R^n or l^2 with inner product

$$(x, y)_{H_1} = \sum_i \bar{x}_i y_i = \bar{x}^T y. \quad (3.70)$$

If $U : H_1 \rightarrow H_2$ is invertible, then $(U^{-1})^* : H_1 \rightarrow H_2$ satisfies

$$((U^{-1})^* e_i, U e_j)_{H_2} = (e_i, U^{-1} U e_j)_{H_1} = \delta_{ij}, \quad (3.71)$$

thus the “columns” of U and $(U^{-1})^*$ are dual to one another as bases in H_2 . We will denote the j th column of U by φ_j and the i th column of $(U^{-1})^*$ by φ_i^* so that

$$(\varphi_i^*, \varphi_j)_{H_2} = \delta_{ij}. \quad (3.72)$$

Suppose $K : H_2 \rightarrow H_2$ can be diagonalized by an invertible operator $U : H_1 \rightarrow H_2$. Then $(U^{-1})^*$ diagonalizes K^* :

$$K = U \Lambda U^{-1} \quad \Rightarrow \quad K^* = (U^{-1})^* \bar{\Lambda} U^*, \quad (3.73)$$

where we have used the fact that the adjoint of a composition is the composition of the adjoints in reverse order, that $((U^{-1})^*)^{-1} = U^*$, and that the adjoint of a diagonal matrix $\Lambda : H_1 \rightarrow H_1$ is its complex conjugate. This last fact only holds when H_1 is given the inner product (3.70). By (3.72), the eigenvectors φ_i of K are dual to the eigenvectors φ_i^* of K^* . Note that when K is self-adjoint, orthogonality of the eigenvectors implies $U^* = U^{-1}$.

If we wish to decompose a vector $w \in H_2$ in terms of the φ_i , we may write

$$w = \sum_i a_i \varphi_i = U a, \quad (3.74)$$

which means that $a = U^{-1} w$, and hence the a_i are given by

$$a_i = (e_i, U^{-1} w)_{H_1} = ((U^{-1})^* e_i, w)_{H_2} = (\varphi_i^*, w)_{H_2}. \quad (3.75)$$

Thus the vectors φ_i^* act as linear functionals on H_2 to give the coefficients of an expansion in terms of the basis $\{\varphi_i\}$.

We primarily have two cases in mind in which to apply this framework. First, denoting the grain boundary network by Γ , the case when $H_1 = l^2$ and $H_2 = L^2(\Gamma)$ is helpful in understanding eigenfunction expansions for diagonalizable but non-self-adjoint operators. Second, the case when H_1 and H_2 are finite dimensional helps us understand how to deal with a non-orthonormal finite element basis. Let $H_1 = R^n$ with the standard inner product (3.70), and let $H_2 = R^n$ with the inner product inherited from $L^2(\Gamma)$ with respect to the finite element basis $\{\varepsilon_i\}_{i=1}^n$, given by

$$(u, v)_{H_2} = (u, v)_M = \bar{u}^T M v, \quad M_{ij} = (\varepsilon_i, \varepsilon_j)_{L^2(\Gamma)}. \quad (3.76)$$

To compute the adjoint of $K : H_2 \rightarrow H_2$ in this case, we note that M is real, symmetric, and positive definite, and therefore the equation $(u, Kv)_{H_2} = (K^*u, v)_{H_2}$ means that

$$\bar{u}^T M K v = \overline{(K^*u)}^T M v = \bar{u}^T (\bar{K}^*)^T M v \quad \Rightarrow \quad K^* = M^{-1} \bar{K}^T M. \quad (3.77)$$

When we diagonalize K , we obtain a diagonal matrix $\Lambda : H_1 \rightarrow H_1$ and an invertible matrix $U : H_1 \rightarrow H_2$ such that $K = U \Lambda U^{-1}$, and we verify that $(u, (U^{-1})^* x)_{H_2} = (U^{-1}u, x)_{H_1}$ implies

$$\bar{u}^T M (U^{-1})^* x = \bar{u}^T \bar{U}^{-T} x \quad \Rightarrow \quad (U^{-1})^* = M^{-1} \bar{U}^{-T}. \quad (3.78)$$

The columns of $M^{-1} \bar{U}^{-T}$ are the φ_i^* which determine the coefficients a_i in expansion (3.74) via (3.75).

3.4.3 A Reformulation

We begin by considering the simplest possible finite geometry, shown in Fig. 3.6. The grain boundary is aligned with the x -axis between $x = 0$ and $x = l$, and each grain has width y_1 . In this section, we will assume that no current is flowing through the line. The solution when a current is present can be found as follows. First, we find the values of g and σ_{22} that correspond to the steady solution. Using dimensionless variables (c.f. Eqn. (3.2)), they will satisfy

$$\sigma_{22} = -\psi + c, \quad (3.79)$$

where c is determined by mass conservation ($\int g_{\text{steady}} = \int g_0$). Note that for this simple geometry, ψ simply increases linearly with x . Then we set up a side problem with no current but initial conditions equal to $g_0 - g_{\text{steady}}$. The analysis below is applied to the

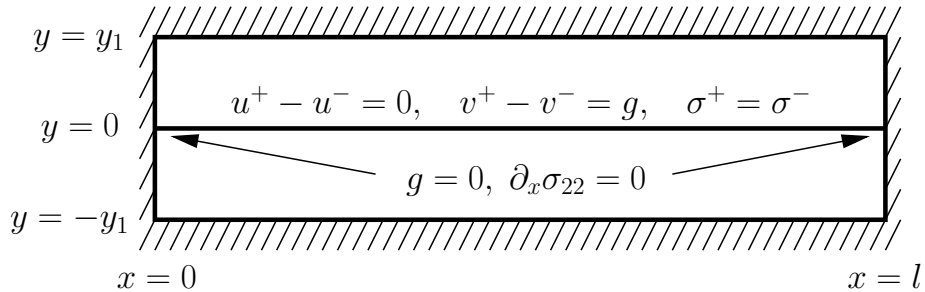


Figure 3.6: The geometry and boundary conditions of a finite interconnect line with a single horizontal grain boundary running through its center.

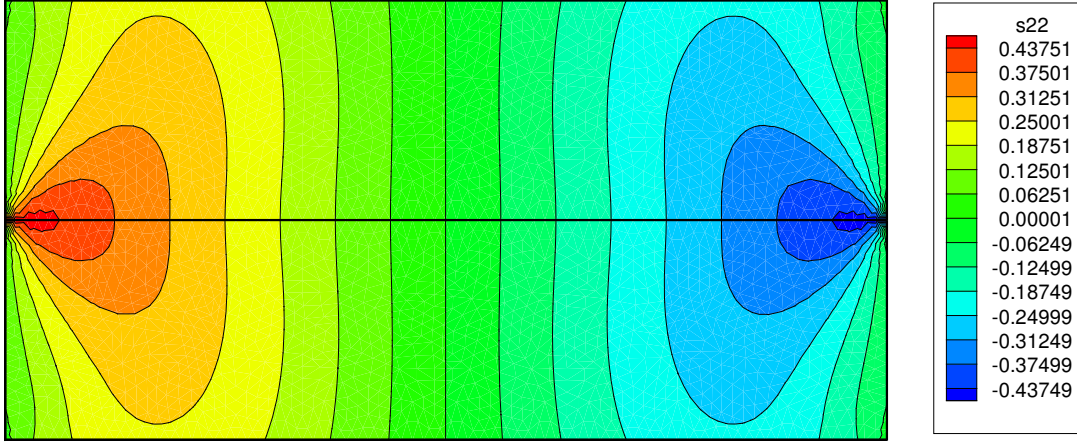


Figure 3.7: A contour plot of $\sigma_{22}(x, y)$ corresponding to the steady state solution. Note that σ_{22} decreases linearly along the grain boundary to balance the constant electromigration force that arises due to the linearly increasing potential ψ . (s22 is σ_{22}).

side problem, and at any time t we just add g_{steady} to obtain the solution for the original problem. Therefore it is sufficient to be able to find the steady solution and to know how to solve for the evolution with no current present.

The symbol σ_{22} is being used in this section to represent the normal stress at points along the grain boundary. Both g and σ_{22} are scalar functions of the position x along the grain boundary, and of time. This does not mean that the “ambient” $\sigma_{22}(x, y, t)$ (which agrees with $\sigma_{22}(x, t)$ on the grain boundary) is independent of y ; see Fig. 3.7.

We denote the separation to stress map by S (i.e. the mapping which gives the normal stress along the grain boundary for a given separation), and the second derivative operator by L :

$$g \xrightarrow{S} \sigma_{22} \xrightarrow{L} \partial_x^2 \sigma_{22}. \quad (3.80)$$

The separation g and the normal stress σ_{22} are constrained at all times to satisfy the boundary conditions

$$g(0) = g(l) = 0, \quad (\partial_x \sigma_{22})(0) = (\partial_x \sigma_{22})(l) = 0. \quad (3.81)$$

The evolution of g is governed by

$$g_t = -LSg, \quad g(x, t = 0) = g_0(x). \quad (3.82)$$

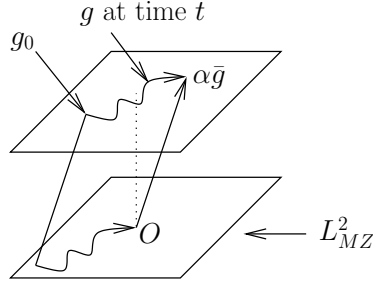


Figure 3.8: It suffices to be able to solve $g_t = -LSg$ for $g \in L^2_{MZ}$.

Integrating by parts, we see that any twice differentiable function $\eta(x)$ which satisfies $\eta'(0) = \eta'(l)$ has the property that $L\eta$ has mean zero, i.e. $\int L\eta dx = 0$. Since g_t is in the range of L and $Sg = \sigma_{22}$ satisfies (3.81), mass is conserved:

$$\frac{\partial}{\partial t} \int_0^l g(x) dx = \int_0^l \frac{\partial g}{\partial t} dx = 0. \quad (3.83)$$

Let $e(x) \equiv 1$, and let $\bar{g}(x)$ denote the separation corresponding to a constant normal stress $\sigma_{22}(x) \equiv 1$ along the grain boundary:

$$S\bar{g} = e, \quad LS\bar{g} = 0. \quad (3.84)$$

Let L^2_{MZ} denote the space of “mean zero” functions $f \in L^2(0, l)$ which satisfy $\int f = 0$. If $g_0 \notin L^2_{MZ}$, let $\alpha = (\int \bar{g})^{-1}(\int g_0)$ and note that $[g(x, t) - \alpha\bar{g}(x)]$ satisfies $g_t = -LSg$ and has mean zero for all time due to (3.83). Thus, if we can solve (3.82) when $g_0 \in L^2_{MZ}$, we can solve it for any g_0 by a simple parallel translation; see Fig. 3.8. We therefore assume without loss that $g_0 \in L^2_{MZ}$.

The key idea to reformulating the problem is to turn all the maps around so that we are dealing with compact operators instead of unbounded operators. Let $B = S^{-1}$ denote the stress to separation map (which takes normal stress values on the grain boundary and returns the separations there), and let $G = (L|_{L^2_{MZ}})^{-1}$ solve the Poisson problem $\Delta\eta = f$, $\eta'(0) = \eta'(l) = 0$ with f and η restricted to L^2_{MZ} to avoid difficulties with the nullspace of L . Let P be the (non-orthogonal) projector onto L^2_{MZ} along \bar{g} given by

$$P = id - \bar{g} \frac{(e, \cdot)}{(e, \bar{g})}, \quad (3.85)$$

and consider the composite map $\tilde{K} = PBG : L^2_{MZ} \rightarrow L^2_{MZ}$

$$g \xleftarrow{P} \tilde{g} \xleftarrow{B} \tilde{\sigma}_{22} \xleftarrow{G} \partial_x^2 \sigma_{22}. \quad (3.86)$$

Here the tildes reflect the possibility that $\widetilde{\sigma}_{22}$ may differ from σ_{22} by a constant, and \tilde{g} may differ from g by a multiple of \bar{g} , both due to the fact that L kills constants and G likely selects the wrong one. The operator \tilde{K} is the inverse of the operator LS in the sense that

$$LS\tilde{K} = id_{L^2_{MZ}}, \quad \tilde{K}LS = id_{\mathcal{D}(LS)}, \quad (3.87)$$

where the linear subspace $\mathcal{D}(LS) \subset L^2_{MZ}$ is the (dense but non-closed) domain of the unbounded operator LS [61]. As discussed in the previous section, G is a compact operator, and I believe that B is bounded (and probably even compact since it is a type of Neumann to Dirichlet map), therefore \tilde{K} is compact. The idea now is to solve $g_t = -LSg$ by finding the eigenfunctions and eigenvalues of the operator LS as the eigenfunctions and reciprocal eigenvalues of the operator \tilde{K} . If we apply \tilde{K} to both sides of $g_t = -LSg$, we can also think of this as solving the equation

$$\frac{\partial}{\partial t} \tilde{K}g = -g, \quad (3.88)$$

which is in many ways nicer to work with than the original equation since \tilde{K} is defined on all of L^2_{MZ} , whereas LS is only defined on a dense subspace. In particular, the boundary conditions (3.81) have been built into \tilde{K} through the definition of G and B . These conditions posed a problem for us in (3.82) due to the fact that functions in L^2 aren't smooth enough for (3.81) to be defined in the trace sense. They are defined for functions in $\mathcal{D}(LS)$, but the L^2 norm does not majorize them in any way when limits are taken. On the other hand, \tilde{K} is defined for all $g \in L^2_{MZ}$, and $\tilde{K}g$ and $S\tilde{K}g$ satisfy (3.81) for any choice of g . By writing \tilde{K} as a composite map with separate boundary conditions built into B and G , we have found a way to address the difficulty that the flux conditions on σ_{22} in (3.81) impose a global constraint on g (rather than a local constraint like $g(0) = 0$).

It is inconvenient to deal with L^2_{MZ} and to have the intermediate variables $\widetilde{\sigma}_{22}$ and \tilde{g} differ from σ_{22} and g by functions in a one dimensional subspace. We can overcome these technicalities by transferring the evolution problem from the space of separation functions g over to the space of normal stresses σ_{22} . Let us denote the area functional in L^2 by w^T . In other words, for any separation $g(x)$, we write $w^T g = (e, g) = \int g$. With this notation, we may transfer the projection P over to the space of stresses via

$$PB = B\tilde{P}, \quad \tilde{P} = I - e(w^T B e)^{-1} w^T B. \quad (3.89)$$

The projection \tilde{P} projects along constants onto the subspace $L^2_{MZ\sigma}$ of normal stresses with mean zero separations. Note that $w^T B$ is a linear functional which maps σ_{22} to the integral

of the corresponding $g = B\sigma_{22}$. Now we apply S to each side of the expression

$$\tilde{K}g = \lambda g \quad (3.90)$$

and write

$$\tilde{K} = PBG = B\tilde{P}G \overbrace{BS}^I \quad (3.91)$$

to conclude that

$$\tilde{P}GB\sigma_{22} = \lambda\sigma_{22}, \quad (3.92)$$

where $\sigma_{22} = Sg$. Thus we see that the operators \tilde{K} and $\tilde{P}GB$ have the same spectrum and the eigenfunctions of one can be obtained from the other by applying S or B . The operator $\tilde{P}GB$ only makes sense on $L^2_{MZ\sigma}$ since G is only defined on L^2_{MZ} , but we may extend it to the whole stress space L^2 without altering its eigenfunctions and eigenvalues (aside from the obvious addition of a one dimensional kernel) by inserting the projection P between G and B . We denote the resulting compact operator by K :

$$K = \tilde{P}GPB. \quad (3.93)$$

By construction, K annihilates constants and has range $L^2_{MZ\sigma}$.

Assuming σ_{22} starts out in $L^2_{MZ\sigma}$ at $t = 0$, it will remain there since g remains in L^2_{MZ} . In that case, the evolution of σ_{22} is governed by the equation

$$\frac{\partial}{\partial t} K\sigma_{22} = -\sigma_{22}. \quad (3.94)$$

We emphasize that $\sigma_{22} \in L^2_{MZ\sigma}$ does not mean that $\int \sigma_{22} = 0$ nor even that $\int \sigma_{22}$ remains constant; it means $\int B\sigma_{22} = 0$. If σ_{22} starts out in some coset of $L^2_{MZ\sigma}$, it will remain in that coset, just as g will remain in its initial coset of L^2_{MZ} in Fig. 3.8. We simply subtract off a constant c so that $\eta := (\sigma_{22} - c)$ is in $L^2_{MZ\sigma}$ and evolve η according to $\partial_t K\eta = -\eta$; at all times σ_{22} is given by $\sigma_{22} = \eta + c$.

See Section 3.4.7 for the generalization of this reformulation to the case of a more general geometry.

3.4.4 Desired Properties of K

In this section we derive sufficient conditions on the operator K for the ODE (3.94) to be well-posed. This section was written before we had a proof that the spectrum of K was

real and non-negative, so the condition in Proposition 3 that the spectrum lie in a cone is overkill. The case is still useful to us numerically, however, as occasionally one of the high frequency, poorly resolved eigenvalues deviates slightly (by perhaps 10^{-5} radians) from the real axis.

Formally, the solution of the equation

$$\partial_t K\eta = -\eta, \quad \eta(0) = \eta_0 \quad (3.95)$$

in a Banach space is given by the formula

$$\eta(t) = \exp(-K^{-1}t)\eta_0. \quad (3.96)$$

There are many situations where a formal solution such as (3.96) turns out to be nonsense, such as the backward heat equation $u_t = -u_{xx}$. Such problems are ill posed in the sense of Hadamard, and we must investigate this possibility for the grain boundary diffusion problem. The fact that the solution is well behaved for an infinite geometry is reassuring. The biggest question is whether the boundary conditions for a finite geometry are compatible with the equation. We wish to impose both flux and displacement boundary conditions. This clearly cannot be done for the heat equation since the conditions $u(0) = u(l) = 0$ already uniquely determine the solution. On the other hand, for the equation $u_t = -u_{xxxx}$, we saw that two boundary conditions [e.g. $u(0) = u'(0) = u(l) = u'(l) = 0$] were *required* at each end. It remains to be seen if the boundary conditions for the grain boundary diffusion problem that seem most appropriate physically also lead to a well posed mathematical problem.

Generally speaking, it is better to invert the identity plus a compact operator rather than a compact operator. This is the reason that boundary integral methods lead to such well conditioned matrices. In the case of Eqn. (3.96), however, it is the combination of the exponential and the inverse that has the potential of being well behaved. If K were self-adjoint and injective, and its spectrum consisted of zero together with a sequence of positive real numbers converging to zero, we could apply the spectral theorem [61] to produce the operator $\exp(-K^{-1}t)$ for any t . This works because $e^{-1/x}$ is continuous from the right at zero, and hence is continuous on the spectrum of Kt (which accumulates only at zero). This procedure is essentially what was done in the expansion (3.61) for the two model problems. On the other hand, this would not work if the spectrum of K contained a subsequence approaching the origin from the negative side since $e^{-1/x}$ is not continuous

on $(-\epsilon, 0]$ for any $\epsilon > 0$. This is the situation for the backward heat equation. Since K for the grain boundary diffusion problem is not self-adjoint (nor even normal), the continuous functional calculus from the theory of C^* -algebras discussed above does not apply, and we must look for an alternative construction of $\exp(-K^{-1}t)$.

Let us suppose that K can be diagonalized by a bounded, invertible operator $U : l^2 \rightarrow L^2$, i.e. that there exist U and Λ such that

$$KU = U\Lambda, \quad (3.97)$$

where the ‘‘columns’’ of U are (possibly complex valued) L^2 functions and Λ is an infinite diagonal matrix with i th diagonal entry $\lambda_i = \alpha_i + i\beta_i$. We assume that $\alpha_i > 0$ for all i , that $C := \sup \beta_i/\alpha_i$ is finite, and that (α_i) is a non-increasing sequence which converges to zero. In other words, we assume that the spectrum of K lies in the cone $|\operatorname{Im} z| \leq C \operatorname{Re} z$ in the right half plane, that we don’t encounter any Jordan blocks during the process of diagonalizing K , and that the eigenvectors of K are linearly independent enough that U is invertible. We then have

$$e^{-K^{-1}t} = Ue^{-\Lambda^{-1}t}U^{-1}, \quad (3.98)$$

where $e^{-\Lambda^{-1}t}$ is diagonal with i th diagonal entry equal to e^{-t/λ_i} . Note that because $\alpha_i > 0$, we have that $|e^{-t/\lambda_i}| < 1$. Moreover, since $|\beta_i| < C\alpha_i$, and $\alpha_i \rightarrow 0$, we have that $\lim_i e^{-t/\lambda_i} = 0$ for any fixed t . Thus $e^{-\Lambda^{-1}t}$ is compact for any $t > 0$. For any fixed i , we have $\lim_{t \rightarrow 0} e^{-t/\lambda_i} = 1$. This does not, of course, imply that $e^{-\Lambda^{-1}t}$ converges to the identity in the norm topology. It cannot since the set of compact operators is norm closed and the identity is not compact. However, we do have the following:

Proposition 1. $e^{-\Lambda^{-1}t}$ (and hence $e^{-K^{-1}t}$) converges to the identity in the strong operator topology, i.e. for any $x \in l^2$,

$$\lim_{t \rightarrow 0} e^{-\Lambda^{-1}t}x = x. \quad (3.99)$$

Proof. Let $\epsilon > 0$ and choose n large enough that $\sum_{n+1}^{\infty} |x_i|^2 < \epsilon$. Pick t_0 small enough that

$$\max_{1 \leq i \leq n} |1 - e^{-t_0/\lambda_i}|^2 < \epsilon. \quad (3.100)$$

Then for any positive $t < t_0$

$$\begin{aligned} \|x - e^{-\Lambda^{-1}t}x\|^2 &\leq \sum_1^n |(1 - e^{-t/\lambda_i})x_i|^2 + \sum_{n+1}^{\infty} (|x_i|^2 + |e^{-t/\lambda_i}x_i|^2) \\ &\leq \sum_1^n |x_i|^2 \epsilon + 2\epsilon \leq (\|x\|^2 + 2)\epsilon. \end{aligned} \quad (3.101)$$

□

The importance of this result is that it shows that the solution $\eta(t) = e^{-K^{-1}t}\eta_0$ of (3.95) has the right limit as $t \rightarrow 0$. Now we verify that $\partial_t K\eta(t) = -\eta(t)$.

Proposition 2. *For any $x \in l^2$ and $t > 0$, $\Lambda e^{-\Lambda^{-1}t}x$ is differentiable at t and*

$$\frac{d}{dt}\Lambda e^{-\Lambda^{-1}t}x = -e^{-\Lambda^{-1}t}x. \quad (3.102)$$

Proof. Fix $t > 0$, $x \in l^2$. For $-t < h < t$, define

$$e(h)^2 := \left\| \frac{\Lambda e^{-\Lambda^{-1}(t+h)}x - \Lambda e^{-\Lambda^{-1}t}x}{h} + e^{-\Lambda^{-1}t}x \right\|^2 = \sum_1^\infty \left| e^{-\frac{t}{\lambda_i}} \left[\frac{\lambda_i}{h} (e^{-\frac{h}{\lambda_i}} - 1) + 1 \right] x_i \right|^2. \quad (3.103)$$

We must show that $\lim_{h \rightarrow 0} e(h) = 0$. Define $f(z)$ on the right half plane by

$$f(z) = \frac{1}{z}(e^{-z} - 1) + 1. \quad (3.104)$$

It is readily verified that $f(0) = 0$ and that $|f(z)|$ is bounded above by some constant c . The latter fact follows from the continuity of f on $\{\operatorname{Re} z \geq 0\}$ and the observation that $f(z) \rightarrow 1$ for large $|z|$ in the right half plane. A plot of $f(z)$ along various rays in the complex plane appears in Fig. 3.9. Note also that $|e^{-\frac{t}{\lambda_k}}| \leq 1$ for all k . Let $\epsilon > 0$, and choose n large enough that $|e^{-\frac{t}{\lambda_k}}| < \frac{\epsilon}{c}$ for $k > n$. Choose h_0 small enough that $\max_{1 \leq k \leq n} |f(\frac{h}{\lambda_k})| < \epsilon$ for $|h| < h_0$. Then for $|h| < h_0$ we have

$$e(h)^2 \leq \left(\sup_{1 \leq k \leq \infty} |e^{-\frac{t}{\lambda_k}} f(\frac{h}{\lambda_k})|^2 \right) \sum_1^\infty |x_i|^2 \leq \epsilon^2 \|x\|^2, \quad (3.105)$$

as desired. □

Because the operator K maps real L^2 functions to real L^2 functions, we may arrange to have the “columns” of U and the entries of Λ real. The only trade-off is that Λ will acquire a 2×2 block for each complex conjugate pair of eigenvalues. If $Kw = (\alpha + i\beta)w$ with $\beta > 0$, then we also have $K\bar{w} = (\alpha - i\beta)\bar{w}$, and therefore writing $u = \operatorname{Re} w$, $v = \operatorname{Im} w$ we find that

$$Ku = \alpha u - \beta v, \quad Kv = \beta u + \alpha v. \quad (3.106)$$

Thus we may replace a complex conjugate pair of eigenvectors in U by their real and imaginary parts, and replace the corresponding diagonal entries λ_i , $\lambda_{i+1} = \bar{\lambda}_i$ of Λ by the

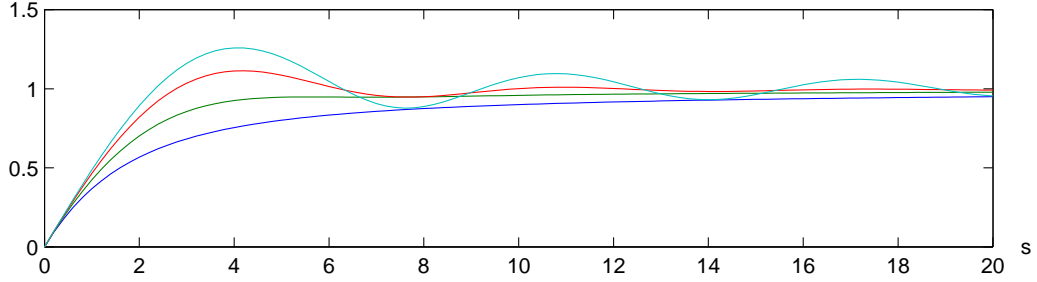


Figure 3.9: A plot of the absolute value of $f(z) = \frac{1}{z}(e^{-z} - 1) + 1$ along the rays $z = s$, $z = \frac{1+2i}{\sqrt{5}}s$, $z = \frac{1+7i}{\sqrt{50}}s$, $z = is$. The maximum principle together with the graph along $z = \pm is$ gives that $|f(z)| < 1.5$ for all z in the right half plane.

2×2 block

$$\begin{pmatrix} \alpha_i & \beta_i \\ -\beta_i & \alpha_i \end{pmatrix} \quad (0 < \beta_i \leq C\alpha_i). \quad (3.107)$$

The corresponding block of $e^{-\Lambda^{-1}t}$ becomes

$$e^{-\frac{t}{\tau_i}} \begin{pmatrix} \cos \frac{\beta_i t}{\alpha_i \tau_i} & \sin \frac{\beta_i t}{\alpha_i \tau_i} \\ -\sin \frac{\beta_i t}{\alpha_i \tau_i} & \cos \frac{\beta_i t}{\alpha_i \tau_i} \end{pmatrix}, \quad \tau_i = \alpha_i \left[1 + \left(\frac{\beta_i}{\alpha_i} \right)^2 \right] \leq \alpha_i(1 + C^2). \quad (3.108)$$

This decomposition is very useful in practice when we are dealing with real functions in L^2 .

The assumption that K is diagonalizable can presumably be weakened considerably, but has proved sufficient for the numerical solution of the grain boundary diffusion problem. The following proposition summarizes what we have shown in this section.

Proposition 3. *If the compact operator K is diagonalizable by an invertible mapping $U : l^2 \rightarrow L^2$ so that*

$$K = U\Lambda U^{-1}, \quad (3.109)$$

and if K is injective and its spectrum consists of zero together with a sequence of points converging to zero which lie in a cone $|\operatorname{Im} z| \leq C \operatorname{Re} z$ in the complex plane, then the operator

$$e^{-K^{-1}t} \quad (3.110)$$

exists, and for any initial condition η_0 , the solution to

$$\partial_t K \eta = -\eta, \quad \eta(0) = \eta_0 \quad (3.111)$$

is given by $\eta(t) = e^{-K^{-1}t}\eta_0$.

3.4.5 Numerical Strategy

The plan is to compute the operator $K = \tilde{P}GPB$ as a matrix in a reasonable basis, solve the eigenproblem for K using standard (dense) linear algebra techniques to compute the real block diagonal decomposition $K = U\Lambda U^{-1}$, and then compute $\sigma_{22}(x, t) = e^{-K^{-1}t}\sigma_{22}(x, 0)$ using (3.98) for the desired values of t . The well-posedness of the problem will be checked by monitoring the eigenvalues and the condition number of U . The following properties will be investigated:

- For the problem to be well-posed, the eigenvalues should lie in a cone in the right half plane. We know from Sec. 3.4.9 that the eigenvalues of K form a decreasing sequence of positive real numbers converging to zero. We expect the effect of the ends to remain localized near the ends, in which case the solution for the infinite interconnect line (by analogy with the model problems) suggests that we should have $\lambda_k \sim ck^{-3}$.
- The high frequency eigenfunctions should be sinusoidal far away from the ends since the eigenfunctions for the infinite geometry are sinusoidal. The condition number of U should not be too large since we expect high frequency eigenfunctions to be almost orthogonal. The eigenfunctions should satisfy the flux boundary conditions $\partial_x\sigma_{22}(0) = \partial_x\sigma_{22}(l) = 0$.
- The solution should be preserved under mesh refinement.
- The resulting evolution should make physical sense in terms of the development of stress in the line and the profile of the grain separation g .

We compute K in two stages. First, we need to be able to compute the stress to separation map B . For this purpose, we use the singularity capturing least squares finite element method developed in Chapter 5. We choose a mesh parameter h and choose equally spaced points no larger than h along each wall, and along the grain boundary. We triangulate each grain separately using a freely available triangulation program [71]. This leads to an unstructured mesh with duplicate nodes along grain boundaries. In the mesh shown in Fig. 3.10, there are 1264 triangles, 734 nodes and 1996 edges. Quadratic C^0 elements are used for each of the six elasticity variables u, v, p, q, γ and τ , except that v is given an extra degree of freedom along the grain boundary to allow for a jump discontinuity in normal component of displacement. This leads to a system of 15013 equations and

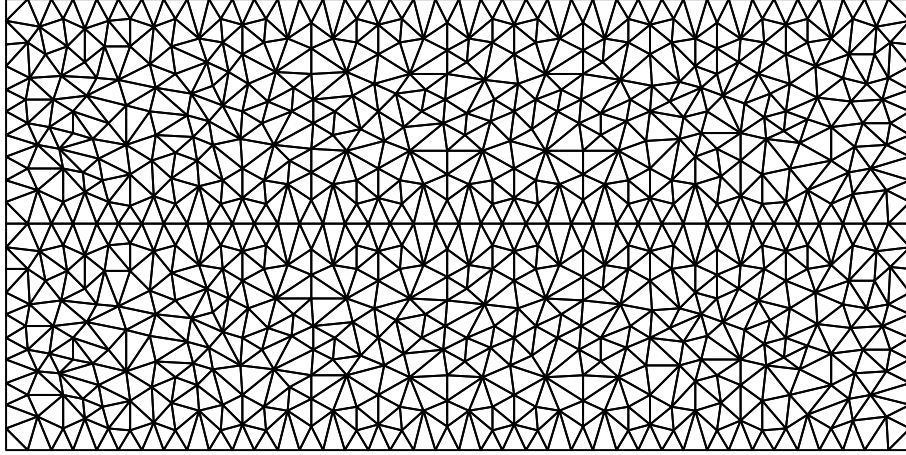


Figure 3.10: Each grain is triangulated separately, leading to an unstructured mesh with duplicate nodes along grain boundaries. This particular mesh corresponds to a mesh parameter $h = 0.05$ for an interconnect line of unit height and length two.

unknowns. 10 of these unknowns correspond to special basis functions used to capture self-similar asymptotic behavior: one in each of the four corners, and three at each end of the grain boundary. There are 81 normal stress (σ_{22}) degrees of freedom to be specified along the grain boundary, and 85 separation degrees of freedom, (79 standard degrees of freedom for g along the grain boundary, and 6 corner degrees of freedom which affect g).

The restriction of σ_{22} to the grain boundary is a one dimensional, continuous, piecewise quadratic function that will be denoted by η to avoid confusion with the two dimensional function σ_{22} . The separation $g = v^+ - v^-$ is also continuous, and is piecewise quadratic except near the ends, where it is a sum of piecewise quadratic and power solution terms of the form $\text{Re}\{cr^\lambda\}$. At the endpoints, $g = 0$ and η is finite. The stress tensor can have singularities near the ends of the grain boundary, but the σ_{22} component *along the grain boundary* will remain well behaved. The reason for this is that the self-similar solutions that determine the asymptotic behavior near junctions and corners are solutions to the *homogeneous* boundary value problem, which in this case implies that the σ_{22} component of each such function vanishes along the grain boundary, but the contribution to g does not. This will be explained in Chapter 4. For any η , the elastic solver provides a solution to the

problem

$$Lw = 0 \quad (\text{c.f. Sec. 3.1}) \quad (3.112)$$

$$u = v = 0 \quad \text{along walls} \quad (3.113)$$

$$u^+ = u^-, \quad \sigma_{12}^+ = \sigma_{12}^-, \quad \sigma_{22}^\pm = \eta \quad \text{along grain boundary.} \quad (3.114)$$

This solution is defined at every node in the structure. In particular, it gives a value of $g = v^+ - v^-$ along the grain boundary. To determine the separation to stress matrix B , we repeatedly solve (3.112)–(3.114) as η ranges over all the quadratic basis elements for the grain boundary, and record the solution g as a column of B . For the mesh in Fig. 3.10, there are 81 degrees of freedom for η and 85 degrees of freedom for g , so we solve the system of 15013 equations 81 times, recording a column with 85 entries for each.

The least squares finite element method is a machinery for converting an elliptic system of partial differential equations into a sparse, symmetric, positive definite linear system. Much work has been done in developing iterative methods such as the preconditioned conjugate gradient method or multigrid to rapidly solve the resulting equations. In our case, however, we have to solve the linear system repeatedly with many different right hand sides, so it is actually better to do a sparse Cholesky factorization once, and then repeatedly backsolve for each right hand side. In our implementation (written in C), we have used a variant of the min-degree heuristic known as *symamd* [49] to re-order the matrix for our fast sparse Cholesky solver, which stores the matrix efficiently, re-orders the rows and columns, computes the factorization with as few memory access bottlenecks as possible, solves the linear system repeatedly, does iterative refinement, and computes LAPACK estimates for various quantities such as condition number, forward and backward error, etc. Fig. 3.11 shows the sparsity pattern for the stiffness matrix A corresponding to the mesh in Fig. 3.10, the re-ordered matrix \tilde{A} , and the Cholesky factor L such that $LL^T = \tilde{A}$. The ratio of nonzero to zero entries in the lower triangle of \tilde{A} is .0038 compared to .0165 for L . Due to re-ordering, the matrix L has only 4.34 times as many nonzero entries as \tilde{A} , so once L is computed, it takes only 4.34 times as long to solve $Ax = b$ for a given b as it takes to compute Ax for a given x .

The second stage of the computation of K is the computation of G . For this, we use standard Galerkin finite elements, except that the solution and the right hand side belong to slightly different finite element spaces. The operator G takes a function g in the space of separations and gives a function η in the space of normal stresses along the grain

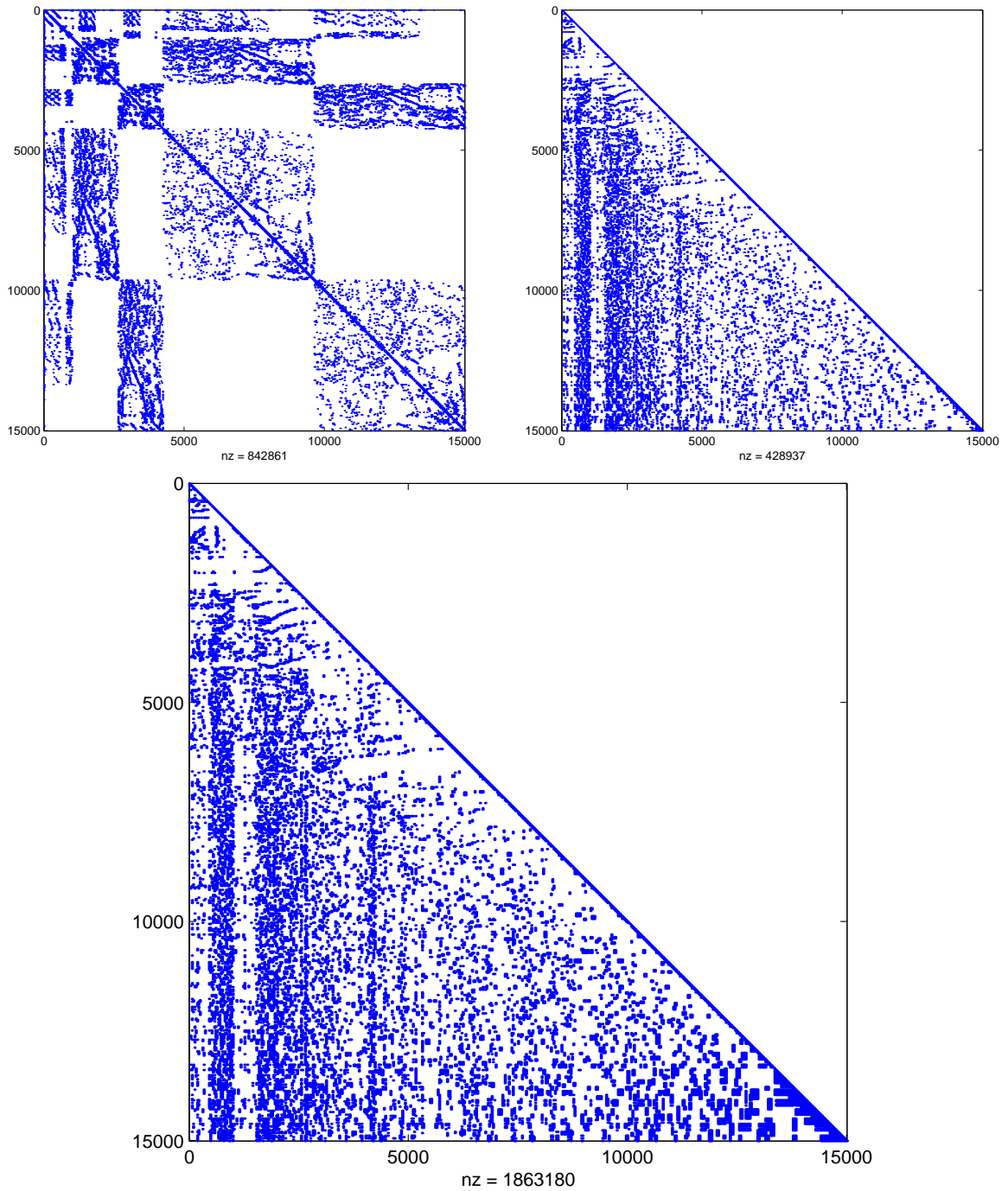


Figure 3.11: Sparsity pattern for several matrices. (a) The stiffness matrix A which results from the least squares finite element method for the mesh in Fig. 3.10. (b) The lower triangle of the matrix \tilde{A} obtained from A using *symamd* to re-order the rows and columns. (c) The Cholesky factorization L , where $LL^T = \tilde{A}$.

boundary such that

$$\eta''(x) = g, \quad \eta'(0) = \eta'(l) = 0. \quad (3.115)$$

A solution exists only if $\int g = 0$, and in that case the solution is only defined up to a constant. We denote the basis elements for the space of separations by $\{e_i\}_{i=1}^n$ and for the space of stresses by $\{\varepsilon_i\}_{i=1}^m$. For the mesh in Fig. 3.10, each of the $m = 81$ functions ε_i is a piecewise quadratic, continuous function; 79 of the $n = 85$ functions e_i are also piecewise quadratic, continuous functions – two fewer than m due to the constraint that the separation is zero at the endpoints. The remaining six e_i are special basis functions made up of a power solution piece and a quadratic piece. See Fig. 3.12.

Adopting the summation convention on repeated indices, we write $g = g_i e_i$, $\eta = \eta_i \varepsilon_i$ and integrate (3.115) against each ε_i to obtain m equations in the m unknown η_i

$$-A\eta = \tilde{M}g, \quad A_{ij} = (\partial_x \varepsilon_i, \partial_x \varepsilon_j)_{L^2}, \quad \tilde{M}_{ij} = (\varepsilon_i, e_j)_{L^2}, \quad M_{ij} = (\varepsilon_i, \varepsilon_j)_{L^2}. \quad (3.116)$$

Note that the stiffness matrix A is $m \times m$ while the mass matrix \tilde{M} is $m \times n$. We point out that there are two stiffness matrices for this problem: the large matrix used to solve the elasticity equations that was Cholesky factored above, and the small matrix A used here, which is the standard one dimensional stiffness matrix for quadratic elements. The mass matrix \tilde{M} in the current context is unusual due to the constraint that $g(0) = g(l) = 0$, and due to the use of extra power solution basis functions. All entries of \tilde{M} are computed

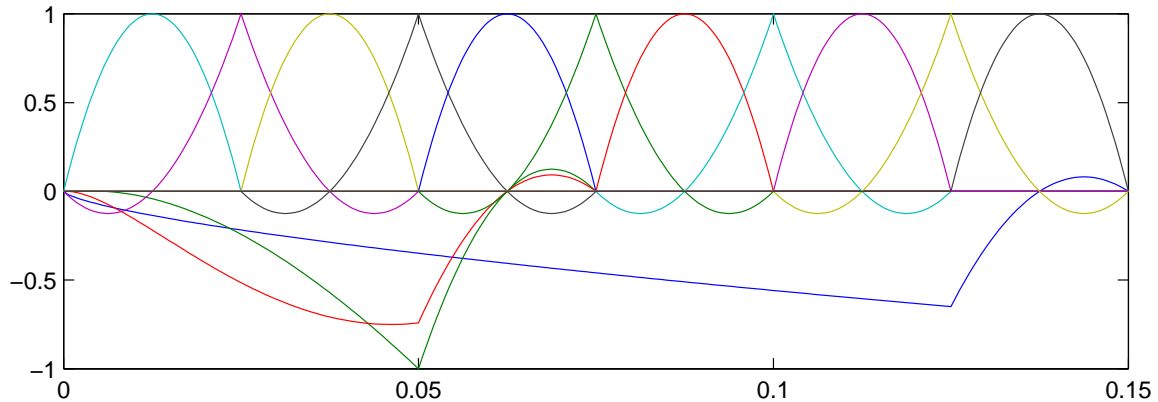


Figure 3.12: The first 14 basis functions e_i for the space of separations. Each of the three special basis functions shown consists of a power solution piece (of the form $\text{Re}\{cr^\lambda\}$) and a quadratic piece. The exponents involved here are $\lambda = 0.680$ and $1.709 \pm 0.604i$.

analytically, including the entries that involve the integration of a power solution e_j against a piecewise quadratic ε_i . Most of the matrix \tilde{M} agrees with the standard mass matrix M for quadratic elements due to the fact that we are able to use the same elements for both stress and displacement in the ambient elasticity problem. This is a major selling point for the least squares finite element method for this problem. If we were to use standard displacement based finite elements for the elasticity solver, the stress variables would not belong to nice continuous spaces because they are determined from the displacements through differentiation. Even for mixed finite element methods, the Babuška-Brezzi inf-sup condition [32, 10] usually prevents the simultaneous use of continuous spaces for both stress and displacement. The use of Lagrange multipliers to determine the η_i is one way of overcoming this problem [9, 33], but it is still not possible to determine η at the endpoints, (and later at triple points), and there can be a large discrepancy (due to the singularity in the stress field) between the η obtained as a Lagrange multiplier and the σ_{22} obtained by differentiating the displacements near the ends; see Fig. 5.7 on page 158.

We are now in a position to compute the matrix $K = \tilde{P}GPB$. G is given by $-A^{-1}\tilde{M}$, except that A has a one dimensional kernel, so we use the pseudo-inverse of A instead. This is perfectly acceptable since the projection P is already being employed to deal with this issue. The area functional w^T is obtained by taking advantage of the definition of \tilde{M} and the fact that the ε_i are a partition of unity:

$$w^T = e^T \tilde{M}. \quad (3.117)$$

Here $e \equiv 1$ is a vector of length m consisting of ones, and has nothing to do with the finite element basis $\{e_i\}_{i=1}^n$ for separations. The projections P and \tilde{P} onto L^2_{MZ} and $L^2_{MZ\sigma}$ along $\bar{g} = Be$ and e , respectively, are given by

$$P = I_n - \bar{g}(w^T \bar{g})^{-1} w^T, \quad \tilde{P} = I_m - e(w^T \bar{g})^{-1} w^T B. \quad (3.118)$$

Thus we obtain $K = \tilde{P}GPB$ in the form of an $m \times m$ matrix with respect to the non-orthogonal quadratic finite element basis $\{\varepsilon_i\}$.

The next step is to obtain the time t evolution operator E_t for the the grain boundary diffusion problem in the absence of an electric field. We begin by solving the eigenproblem

$$KU = U\Lambda \quad (3.119)$$

using standard LAPACK-based dense linear algebra routines (with Matlab or Octave, for example). Next, we re-order the columns of U so that the real parts of the diagonal of Λ appear in decreasing order, and if any eigenvalues are complex, we use the procedure from Section 3.4.4 to convert complex conjugate pairs into 2×2 real blocks, as was done in Eqn. (3.107). At this point we verify that the resulting spectrum lies in a cone in the right half plane with a very small opening angle (ideally $sp(K) \subset [0, \infty)$), and that the kernel of K consists only of the one dimensional space of constant functions. In our computations, the spectrum has turned out to be real and positive most of the time, although for some geometries we have encountered a single complex eigenvalue with $\beta_i \sim .00001\alpha_i$. The index i of this eigenvalue is always very large — well into the region where the corresponding eigenfunction has too high a frequency to be properly resolved by the grid — therefore our numerical results are in agreement with the theory of Section 3.4.9. Decomposing L^2 as a direct sum $L_{MZ\sigma}^2 \oplus \mathbb{C}e$ and writing $K = K_0 \oplus 0$, where K_0 is the restriction of K to the invariant subspace $L_{MZ\sigma}^2$, the time t evolution operator may be written $E_t = \exp(-K_0^{-1}t) \oplus id$. Here the identity on the last component ensures mass conservation for any initial state (i.e. $\int g(x, t) dx = \int g_0(x) dx$ for all time). Having ordered the vectors of U so that the basis vector for the kernel appears last, we write $\Lambda = \Lambda_0 \oplus 0$ and compute

$$E_t = U(\exp(-\Lambda_0^{-1}t) \oplus I_{1 \times 1})U^{-1}. \quad (3.120)$$

The final step is to find the steady state solution η_{steady} when an electric current is present, and to use Eqn. (3.120) to determine the evolution of η via

$$\eta(x, t) = \eta_{\text{steady}}(x) + E_t[\eta_0(x) - \eta_{\text{steady}}(x)]. \quad (3.121)$$

This requires solving Laplace's equation for the electrostatic potential ψ , and then determining the constant c so that the solution to (3.112)–(3.114) with

$$\eta_{\text{steady}} = -\psi|_{\Gamma} + c \quad (3.122)$$

yields a g_{steady} such that $\int g_{\text{steady}} = \int g_0$. For the simple geometry here, ψ simply increases linearly in x from 0 on the left wall to ψ_0 on the right wall. Normally we take g_0 to be identically zero, which physically means no grain growth has occurred prior to turning on the electric current. In that case c is chosen to project the restriction of $-\psi|_{\Gamma}$ onto $L_{MZ\sigma}^2$:

$$\eta_{\text{steady}} = \tilde{P}(-\psi|_{\Gamma}). \quad (3.123)$$

We re-iterate that this does not imply that $\int \eta_{\text{steady}} = 0$.

In our implementation, the setup of the geometry is done with Xfig, Perl, and Triangle [71]. The computation of power solutions is done in C++, Perl and Mathematica. The computation of ψ , B , A and \tilde{M} is done using our least squares/variational finite element C++ code; much of the setup of data for boundary conditions is done in Perl. The sparse Cholesky code is written in C. We use Matlab or Octave to compute K , U , E_t , and η_{steady} . The computation of stress and displacement for visualization is done with C, C++ and Perl. We use LAPACK extensively, and have also used the packages ARPACK, MINPACK, Colamd, and Meschach. We use Tecplot, Gnuplot, Matlab and IBM Data Explorer for visualization. Version control is handled with CVS, and we are very much indebted to the developers of Linux, GCC, GDB, Perl, LAPACK, etc.

As a final remark for this section, the dense linear algebra being done here is quite inexpensive in comparison to the time it takes to set up and solve the stress problem to construct the matrix B . For the mesh we have been using for illustration, to compute B we need to solve a system of 15013 equations 81 times, yielding an 85×81 matrix. After that, we are only working with matrices with around 80 rows and columns, which can be diagonalized in less than a second on a 500 MHz single processor machine. For one of the more complicated geometries in a later section, we must solve a system of 80000 equations 500 times to construct B , and then do dense linear algebra on matrices with around 500 rows and columns. Because the stress problem is sparse, however, it scales significantly better with problem size than the dense linear algebra does, and for that problem the time spent computing Λ and U is comparable to the time it takes to compute B (a few minutes). For a very long, narrow geometry, the ratio of grain boundary nodes to total nodes can be large enough that it takes longer to compute K , Λ and U than it takes to set up B , but we have not encountered a situation where it was worth the effort to find alternatives to using standard dense linear algebra for this stage of the computation.

3.4.6 Results

In this section we compare the results obtained using the mesh (Fig. 3.10) discussed in the previous section, which has a mesh parameter $h = .05$, and a mesh which is twice as fine with $h = .025$ (and approximately four times as many triangles).

In Figures 3.13 and 3.14, we show the evolution of normal stress η and separation

g to steady state. The normal stress is solved using Eqn. (3.121), and the separation is obtained by applying the operator B . We use a Poisson ratio for aluminum of 0.35 (so $\kappa = 1.6$), and take $\psi_0 = 1$ on the right wall, deferring use of the correct dimensionless value until (3.124) below. Using $L = 10\mu\text{m}$, $\mu = 24.4\text{ GPa}$, $\Omega = 1.68 \times 10^{-23}\text{ cm}^3$, $\nu_b = 1.5 \times 10^{15}$, $D_b = 10^{-8}\text{ cm}^2/\text{s}$, $T = 533\text{ K}$, and $k = 1.38 \times 10^{-23}\text{ J/K}$, we calculate the timescale $t_0 = \frac{kTL^3}{\nu_b D_b \Omega^2 \mu}$ to be 71000 s = 20 h. A more realistic geometry would be 10 times as long (increasing t_0 by a factor of 1000) but would also have an aspect ratio 50 times larger (resulting in the attainment of steady state at a dimensionless time approximately 50 times smaller). To get physical values of stress, we multiply the computed stress by

$$\sigma^* = \mu\psi_0 = \frac{|Z^*|e}{\Omega}\psi_0^{\text{physical}}. \quad (3.124)$$

Taking the resistivity of aluminum to be $3.6\mu\text{ohm-cm}$ and a current density of $20\text{ mA}/\mu\text{m}^2$, we compute $\psi_0^{\text{physical}} = (.72\text{ V/cm})(20\mu\text{m}) = 1.44\text{ mV}$. Using $Z^* = -1.3$ [68], we obtain the rough estimate $\sigma^* = 18\text{ MPa}$.

Qualitatively, the evolution behaves the way we expect. The flux boundary conditions are immediately realized, causing the stress to have slope $-1/2$ at $x = 0, 2$. Small depletion and accumulation regions appear near the ends shortly after the current is turned on. In between these regions, there is a steady flux caused by the electromigration force, but as was true in the infinite geometry, this does not lead to grain growth initially because atoms don't accumulate unless the flux is decreasing with position. These regions grow in size and move toward each other at a progressively slower rate until the S-shaped steady state separation is reached (within some tolerance), which corresponds to a linearly decreasing normal stress which perfectly balances the electromigration force.

In Figure 3.15, we plot the eigenvalues λ_j of K versus the index j . The following table gives a comparison of selected eigenvalues computed on the two meshes:

j	λ_j^{fine}	$(\lambda_j^{\text{coarse}} - \lambda_j^{\text{fine}})/\lambda_j^{\text{fine}}$
1	8.0×10^{-2}	-4.8×10^{-5}
2	1.97×10^{-2}	-1.33×10^{-4}
4	3.9×10^{-3}	-1.27×10^{-3}
8	5.7×10^{-4}	-1.39×10^{-2}
16	7.6×10^{-5}	-9.8×10^{-2}
32	9.0×10^{-6}	-3.1×10^{-1}
64	8.1×10^{-7}	-7.7×10^{-1}

We see that the eigenvalues that are most important for correctly modeling the evolution (those with smallest index) are the eigenvalues that are computed most accurately. We

also observe that our prediction that the spectrum would asymptotically behave as cj^{-3} for large j appears to be correct.

In Figures 3.16 and 3.17 we plot the first few eigenfunctions φ_j of K and ϕ_j of \tilde{K} ; (recall $\phi_j = B\varphi_j$). By construction, the normal stress eigenfunctions satisfy $\varphi_j'(0) = \varphi_j'(l) = 0$ and the separation eigenfunctions satisfy $\phi_j(0) = \phi_j(l) = 0$. The condition number of U in the diagonalization $K = U\Lambda U^{-1}$ for the fine and coarse meshes were found to be

	coarse	fine
$\text{cond}(U)$	2.35	2.57

Thus U is an extremely well conditioned matrix, and the eigenvectors of K are not becoming linearly dependent as the dimension of the finite element space increases.

In Figure 3.18, we were pleasantly surprised to observe that the eigenfunctions φ_j^* of the adjoint K^* look suspiciously similar to the functions ϕ_j from Fig. 3.17. Scaling the latter appropriately, we have perfect agreement aside from the small amplitude, high frequency noise that appears in the φ_j^* . Recall from Section 3.4.2 that φ_j^* is the j th column of $M^{-1}\bar{U}^{-T}$, and that φ_j^* can be interpreted as a linear functional which determines the j th coefficient in the eigenfunction expansion $w = \sum a_i \varphi_i$ via

$$a_j = (\varphi_j^*, w)_M. \quad (3.125)$$

Because the least accurately computed columns of U (those with large index) influence all the columns of \bar{U}^{-T} , even the low frequency dual vectors φ_i^* contain noticeable high frequency oscillations. Note, however, that because the φ_i^* are used as linear functionals, this high frequency noise does not significantly affect the coefficients a_j when w is smooth. The fact that the φ_i^* turn out to be multiples of the ϕ_i means that $\tilde{K} = K^*$ since we already knew that $sp(K) = sp(\tilde{K})$ and suspected that $sp(K) \subset \mathbb{R}$. On the one hand, this fact allows us to compute the φ_i^* more accurately, and on the other hand, it tells us that $B = B^*$. This numerical discovery has led us to prove it rigorously, which is almost enough to prove that the grain boundary diffusion problem is well posed. (The invertibility of U remains unproved, although the condition numbers we obtained for U above are quite convincing). See Section 3.4.9.

Finally, in Figure 3.19, we show contour plots of some of the elasticity variables for the steady state stress distribution in which the gradient of σ_{22} perfectly balances the electromigration force. The first two plots show the displacement variables u and v . Note that $g = v^+ - v^-$ is negative on the left end of the grain boundary and positive on the

right end because the atoms have been depleted on the left and deposited on the right. The horizontal component of displacement u is non-zero due to the Poisson contraction effect: the right side of the line is under compression and the left side is under tension, so the material expands transversally on the right and contracts on the left, leading to a negative value of u throughout. Along the grain boundary, σ_{22} is decreasing linearly, but off the grain boundary it behaves in a more complicated way subject to the Lamé equations with Dirichlet boundary conditions at the walls. The shear force τ is strongest near the ends because the Dirichlet boundary conditions on the walls must overcome the separation forces along the grain boundary, imparting vertical forces along walls with horizontal normals.

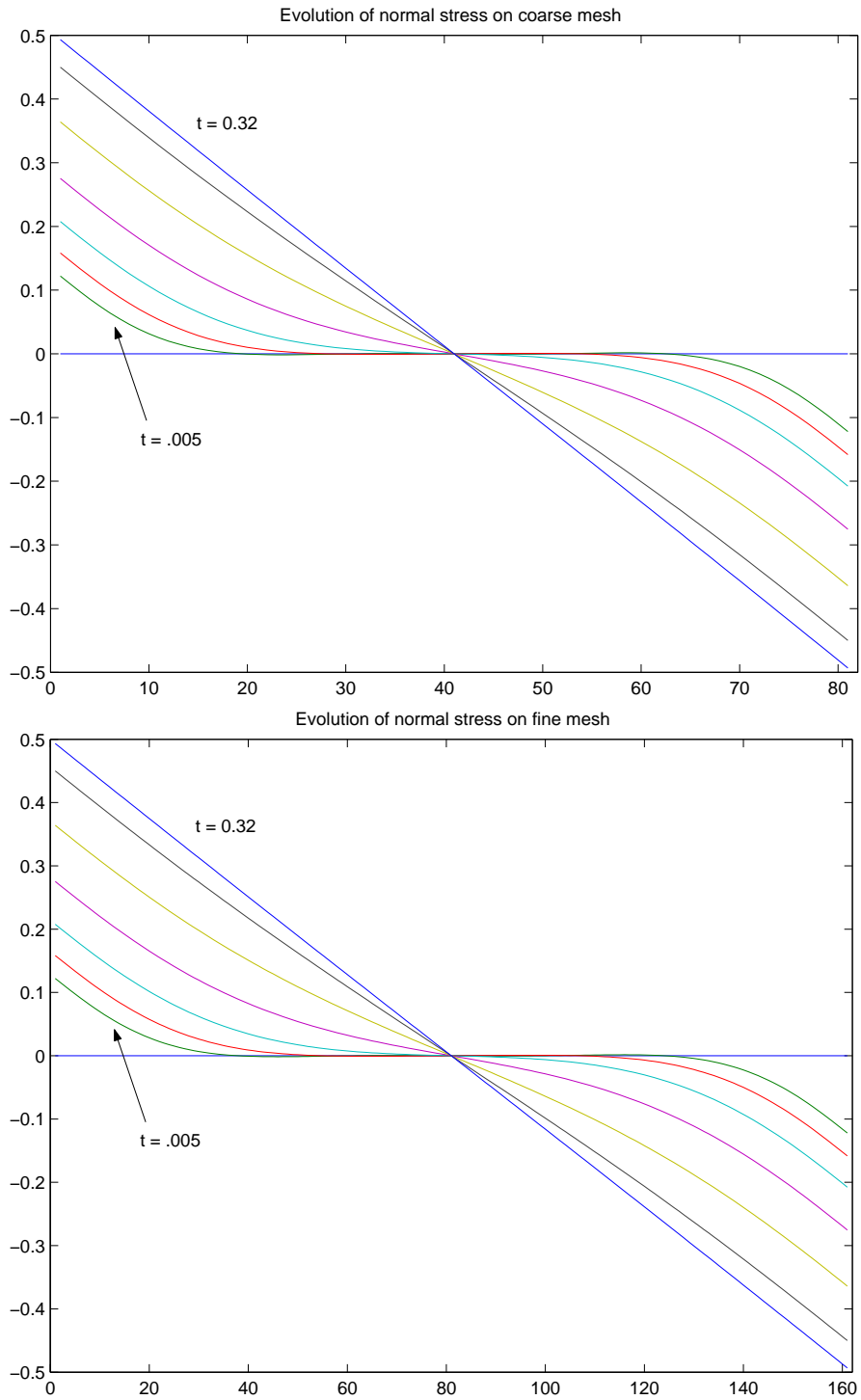


Figure 3.13: Evolution of the normal stress η along the grain boundary for the two meshes at $t = 0.005, 0.01, 0.02, 0.04, 0.08, 0.16, 0.32$.

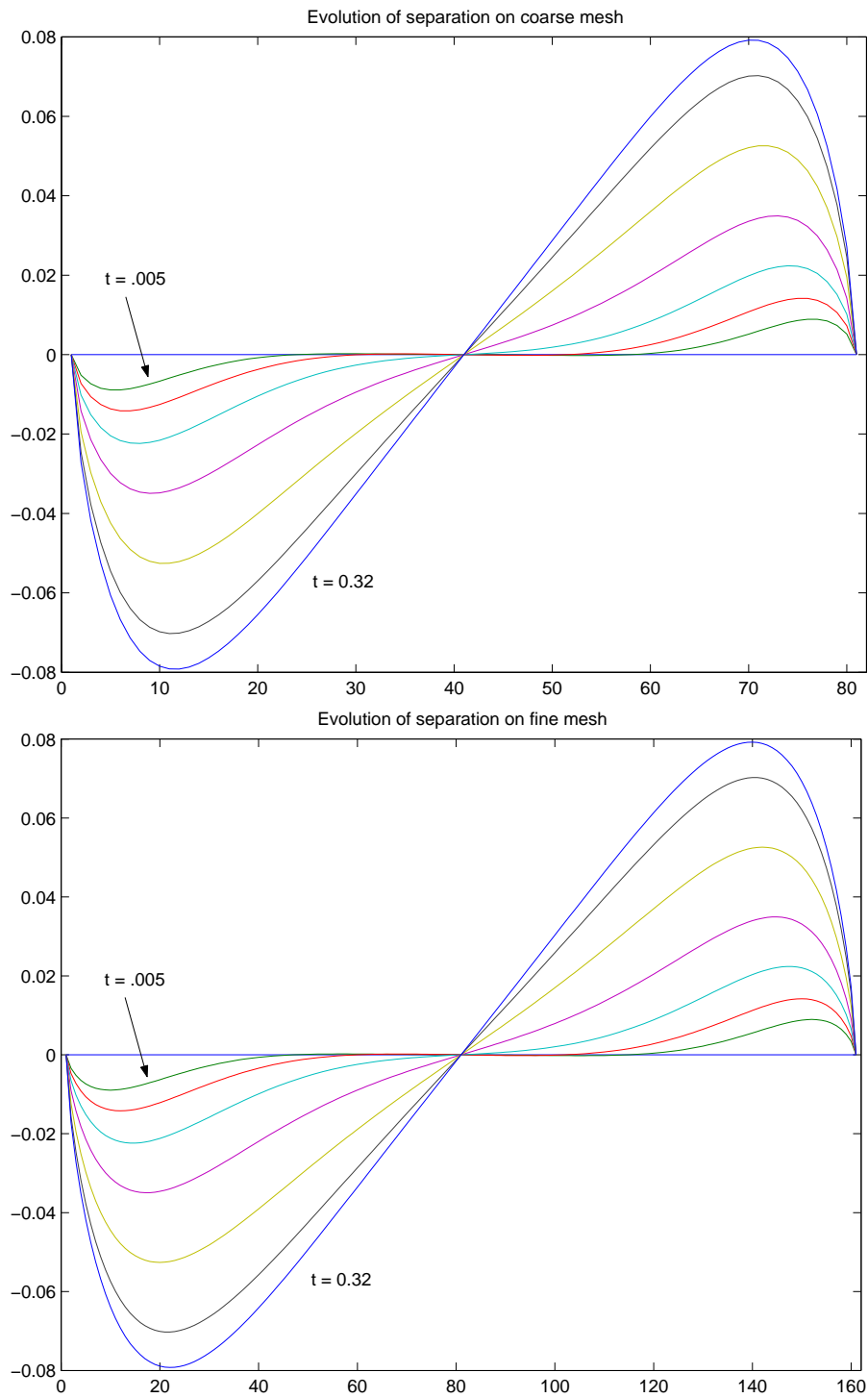


Figure 3.14: Evolution of the separation function g along the grain boundary for the two meshes at $t = 0.005, 0.01, 0.02, 0.04, 0.08, 0.16, 0.32$.

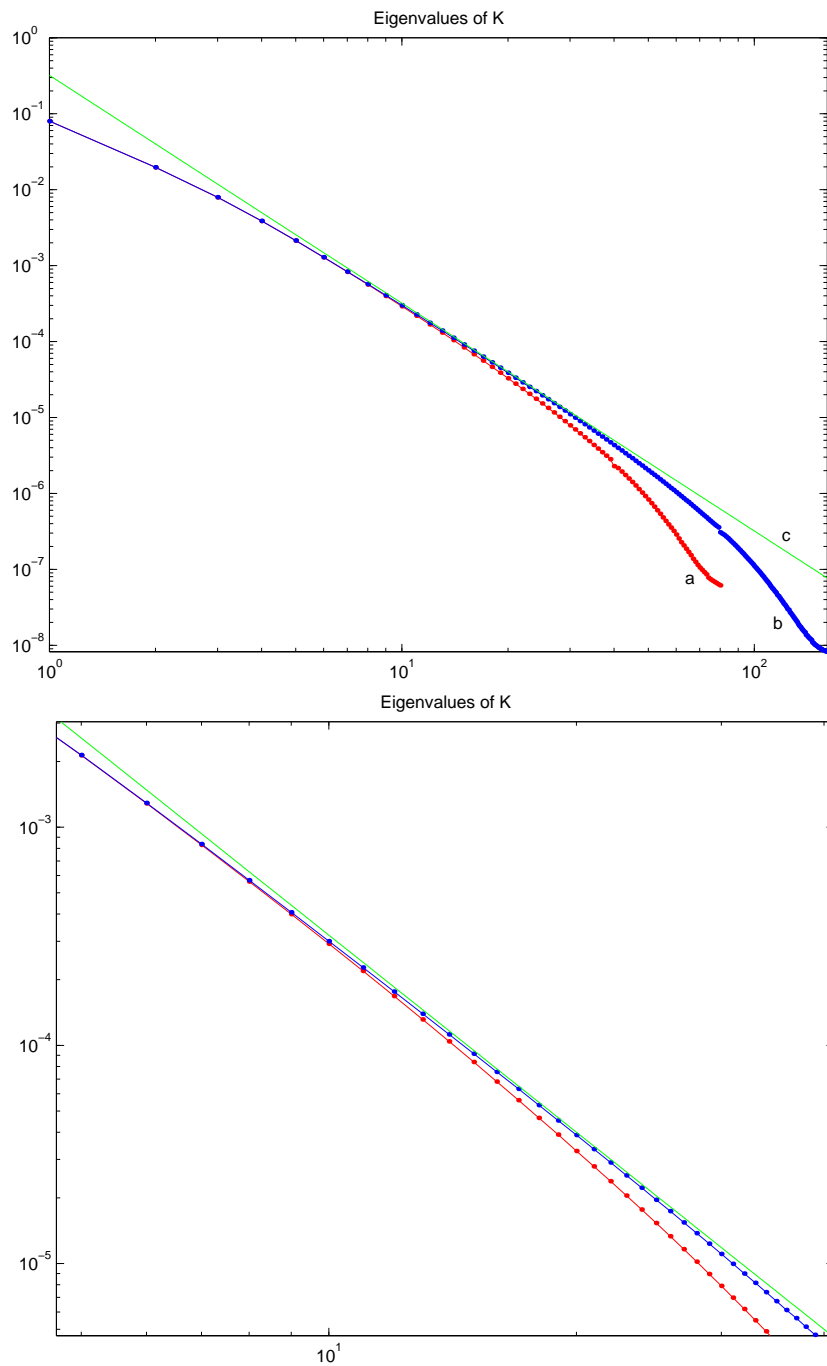


Figure 3.15: Log-Log plot of eigenvalues λ_j of K vs. index j . The red and blue curves (a) and (b) show the eigenvalues obtained from the coarse and fine meshes, respectively. The green line (c) is a plot of $0.32j^{-3}$, which appears to be the asymptotic limit of the spectrum of K for large j . In the bottom plot, we zoom in on a portion of the top plot.

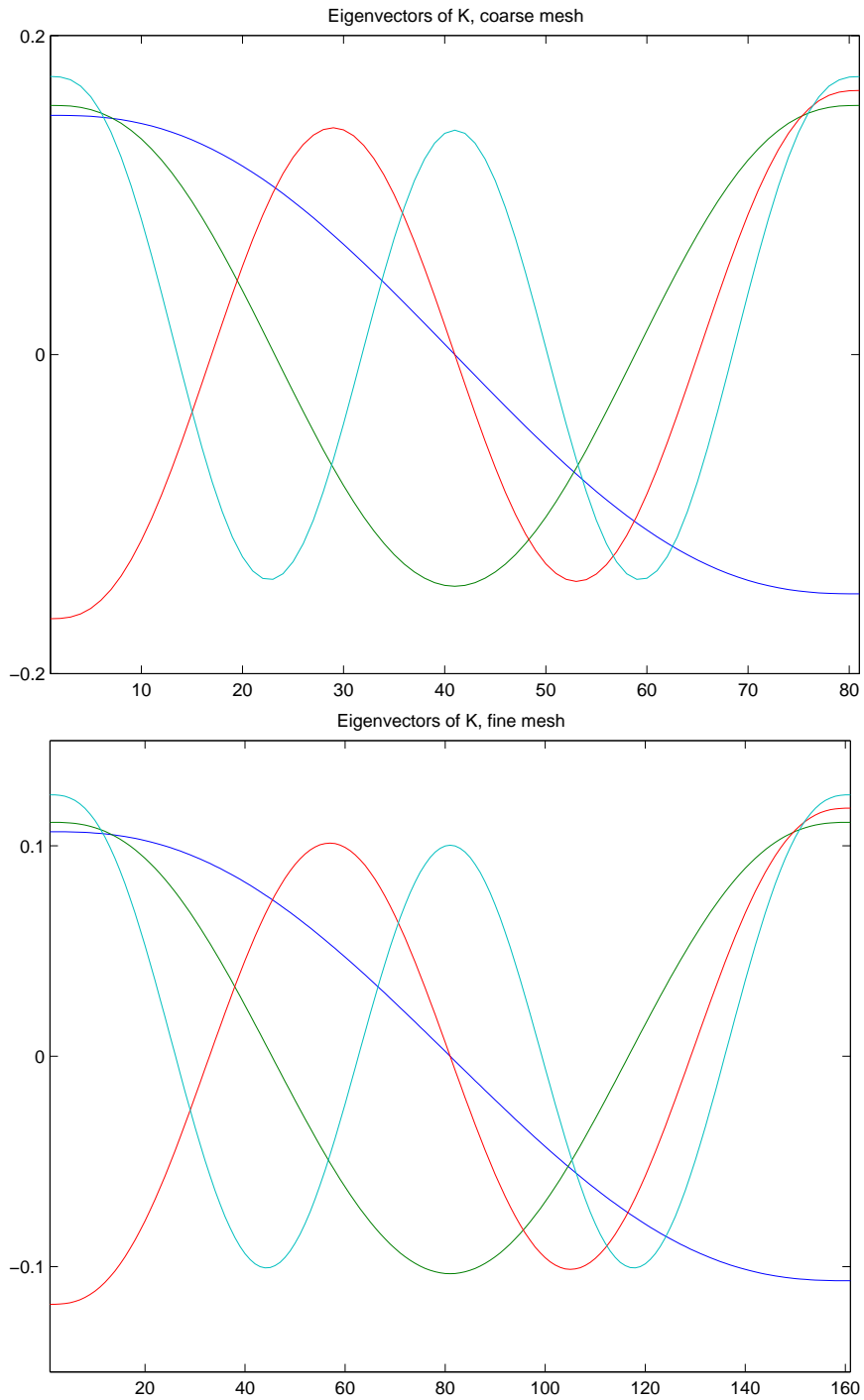


Figure 3.16: The first 4 eigenfunctions φ_k of K . Note that the eigenfunctions are smooth, oscillatory, and satisfy zero flux boundary conditions at the endpoints. The scales are arbitrary (normalized as vectors in R^n rather than in L^2).

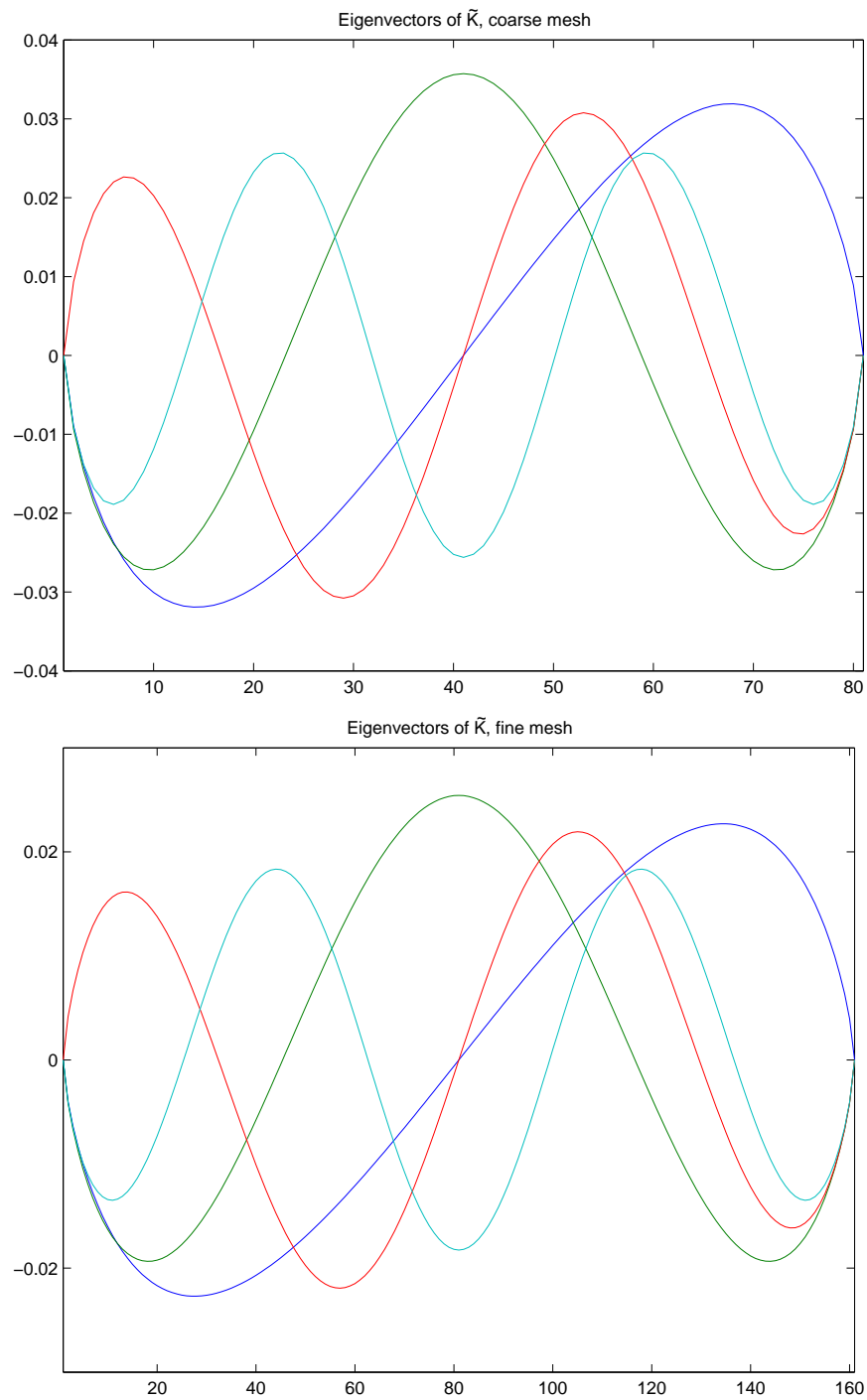


Figure 3.17: The first 4 eigenfunctions ϕ_k of \tilde{K} . Note that they are smooth, oscillatory, and satisfy the zero displacement boundary conditions at the endpoints. The scales are arbitrary (normalized as vectors in R^n rather than in L^2).

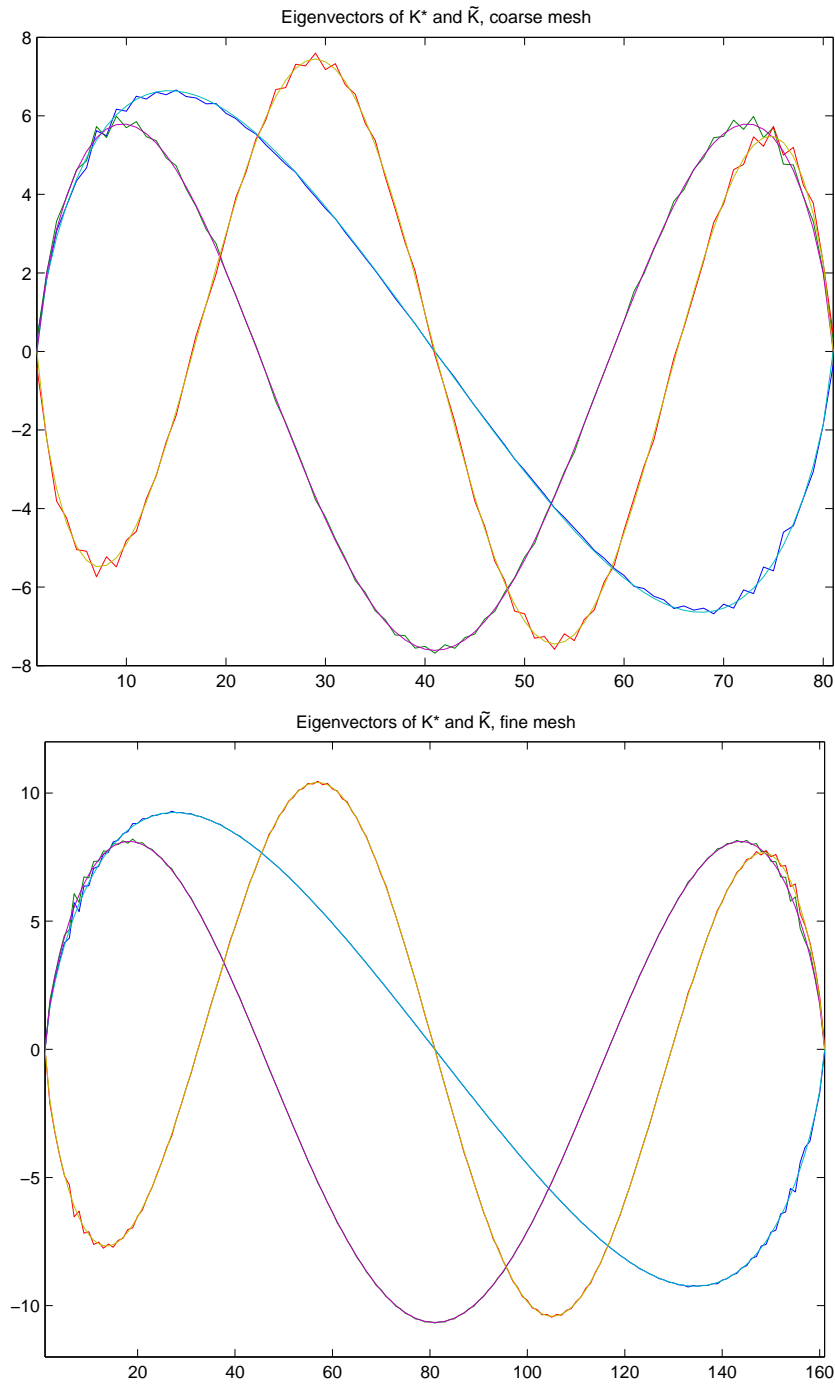


Figure 3.18: The first 3 eigenfunctions φ_k^* of K^* along with the corresponding (rescaled) eigenfunctions ϕ_k of \tilde{K} . A surprising discovery: $\tilde{K} = K^*$. The coefficients in the expansion $\eta = \sum a_k \varphi_k$ are determined by $a_k = \int \eta \varphi_k^*$, so these functions can be thought of as linear functionals.

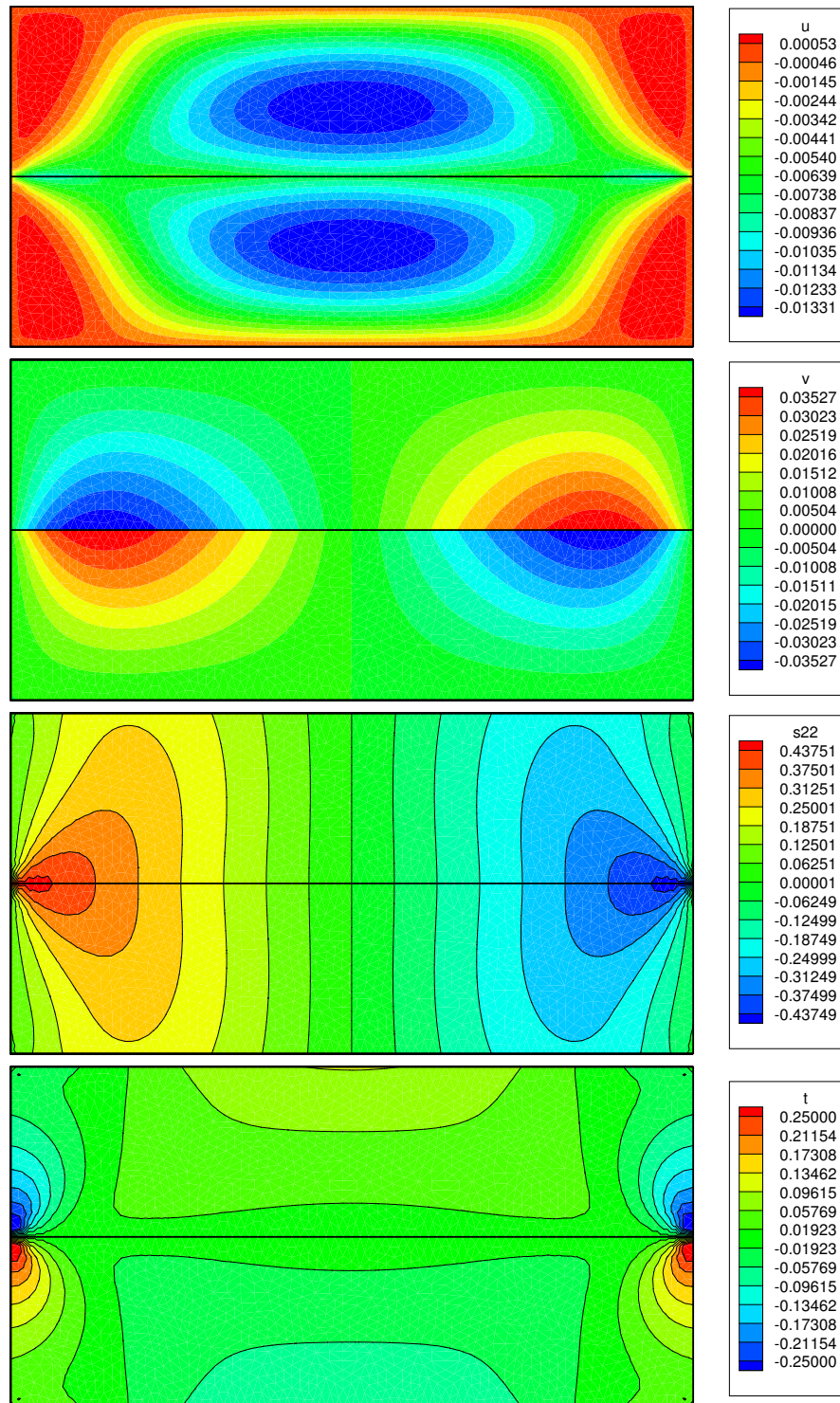


Figure 3.19: Steady state solution.

3.4.7 More Complicated Geometries

The approach used above to solve the grain boundary diffusion problem for a finite rectangular strip with a single symmetric grain boundary generalizes nicely to an arbitrary branched grain boundary structure. Let the grain boundary $\Gamma = \bigcup \Gamma_j$ be a union of closed line segments. Each Γ_j is given an arbitrary orientation, a local arclength parameter s , a tangent vector \mathbf{t} , and a normal vector \mathbf{n} ; see Fig. 3.20. The segments Γ_j can be grouped together into connected components as sets in R^2 . We denote a component by Γ_J , where J is the set of appropriate indices of the Γ_j which belong to the component. We denote the set of J 's by \mathcal{J} and the number of components by $N_{\mathcal{J}}$. Define the Hilbert space H by

$$H = L^2(\Gamma). \quad (3.126)$$

We define the operator $B : H \rightarrow H : \eta \mapsto g$ as follows. Let $w = (u, v, p, q, \gamma, \tau)^T$ be the solution of the Lamé system

$$Lw = 0 \quad (\text{c.f. Sec. 3.1}) \quad (3.127)$$

$$u = v = 0 \quad \text{along walls} \quad (3.128)$$

$$B_c w^\pm = (0, 0, \eta, \eta)^T \quad \text{along grain boundaries,} \quad (3.129)$$

where $w^\pm = (w^+, w^-)$ and B_c is the interface boundary condition matrix obtained by choosing θ so that $\mathbf{t} = (\cos \theta, \sin \theta)^T$, $\mathbf{n} = (-\sin \theta, \cos \theta)^T$, and defining

$$B_c = \begin{pmatrix} \cos \theta & \sin \theta & 0 & 0 & 0 & 0 & -\cos \theta & -\sin \theta & 0 & 0 & 0 & 0 \\ 0 & 0 & 0 & 0 & \sin 2\theta & \cos 2\theta & 0 & 0 & 0 & 0 & -\sin 2\theta & -\cos 2\theta \\ 0 & 0 & 1 & 0 & \cos 2\theta & -\sin 2\theta & 0 & 0 & 0 & 0 & 0 & 0 \\ 0 & 0 & 0 & 0 & 0 & 0 & 0 & 0 & 1 & 0 & \cos 2\theta & -\sin 2\theta \end{pmatrix}. \quad (3.130)$$

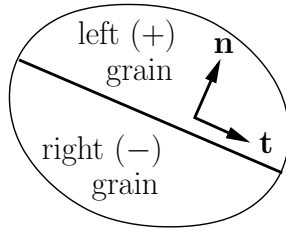


Figure 3.20: Arbitrary local orientation of grain boundary segment determines tangential and normal directions, left and right grain labels, etc.

In other words, in the notation of Eqn. (3.16) on page 39, u_{\parallel} , σ_s and σ_{\perp} are continuous across the grain boundary (which implies σ_{\parallel} is as well; see page 19), and $\sigma_{\perp} = \eta$ at the grain boundary. Then g is defined by

$$g = u_{\perp}^+ - u_{\perp}^- = \mathbf{n} \cdot [(u, v)_{left}^T - (u, v)_{right}^T]. \quad (3.131)$$

The operator B will be shown to be self-adjoint and negative in Section 3.4.9.

Define the subspace H_0 of H by

$$H_0 = \{f \in H : \int_{\Gamma_J} f = 0, \quad J \in \mathcal{J}\} \quad (3.132)$$

For each J in \mathcal{J} , define the function $e_J \in H$ by

$$e_J(x) = \begin{cases} 1 & x \in \Gamma_j \text{ for some } j \in J, \\ 0 & \text{otherwise.} \end{cases} \quad (3.133)$$

For each J , let $g_J = Be_J \in H$, and note that (e_J, \cdot) is the area functional of the J th component, i.e.

$$(e_J, f)_H = \int_{\Gamma_J} f ds. \quad (3.134)$$

Let $P \in \mathcal{B}(H)$ be the projection onto H_0 along the g_J , i.e.

$$P = id - \sum_{I, J \in \mathcal{J}} g_I W_{IJ} (e_J, \cdot). \quad (3.135)$$

Here W is the $N_{\mathcal{J}} \times N_{\mathcal{J}}$ matrix which has the property that

$$(e_I, g_K) W_{KJ} = \delta_{IJ}, \quad (\text{summation implied}). \quad (3.136)$$

W exists and is self-adjoint since B is self-adjoint and negative, and therefore the matrix $(e_I, g_K)_{IK}$ is invertible:

$$(W^{-1})_{IK} = (e_I, g_K) = (e_I, Be_K) = (Be_I, e_K) = (g_I, e_K). \quad (3.137)$$

If $(e_I, g_K)_{IK}$ were not invertible, then we could find numbers a_K such that for each I , $(e_I, Be_K)a_K = 0$; hence setting $x = e_K a_K$ we would get $(x, Bx) = 0$, a contradiction. The adjoint P^* of P is the projection along constants onto the space

$$H_0^* = \text{range}(P^*) = \{g_J : J \in \mathcal{J}\}^{\perp}, \quad (3.138)$$

i.e. P^* is given by

$$P^* = id - \sum_{I, J \in \mathcal{J}} e_I W_{IJ}(g_J, \cdot). \quad (3.139)$$

Because $B(\text{span}\{e_J\}) = \text{span}\{g_J\}$, we know that $B^*(\text{span}\{g_J\}^\perp) = \text{span}\{e_J\}^\perp$. But B is self-adjoint, $\text{span}\{e_J\}^\perp = H_0$, and $\text{span}\{g_J\}^\perp = H_0^*$, therefore

$$H_0 = B(H_0^*). \quad (3.140)$$

Note also that the invertibility of $(e_I, g_J)_{IJ}$ implies that $\text{span}\{e_J\} \cap H_0^* = \{0\}$ and $\text{span}\{g_J\} \cap H_0 = \{0\}$. Thus we have

$$P^*(H_0) = H_0^*, \quad P(H_0^*) = H_0. \quad (3.141)$$

We define the self-adjoint compact operator $G : H_0 \rightarrow H_0 : g \mapsto \eta$ by solving the Poisson equation

$$\frac{d^2}{ds^2} \eta(x_i(s)) = g(x_i(s)) \quad \text{along interior of each } \Gamma_i \quad (3.142)$$

$$\left. \frac{d}{ds} \right|_{s_0} \eta(x(s)) = 0 \quad x(s_0) \text{ a wall endpoint} \quad (3.143)$$

$$\sum_{i \in \{i_1, i_2, i_3\}} \left. \frac{d}{ds} \right|_0 \eta(x_i(s_0^\pm)) = 0 \quad x_i(s_0^i) \text{ a triple point, } \pm \text{ chosen outward.} \quad (3.144)$$

Note that it was necessary to restrict G to H_0 since there is no solution for $g \in H \setminus H_0$ and when $g \in H_0$ the solution is only defined up to addition of constants on each component Γ_J .

We now define the operators K and \tilde{K} to be

$$K = P^*GPB, \quad \tilde{K} = PBGP = BP^*GP = K^*. \quad (3.145)$$

The evolution of the normal stress $\eta(x, t)$ and the corresponding separation $g(x, t) = B\eta(x, t)$ is governed by

$$\frac{\partial}{\partial t} K\eta(x, t) = -\eta(x, t), \quad \frac{\partial}{\partial t} \tilde{K}g(x, t) = -g(x, t). \quad (3.146)$$

We begin by solving the eigenproblem

$$K\varphi_i = \lambda_i\varphi_i, \quad \tilde{K}\phi_i = \lambda_i\phi_i, \quad (\phi_i = c_i B\varphi_i), \quad (3.147)$$

where c_i is chosen so that

$$(\phi_i, \varphi_j)_H = \delta_{ij}. \quad (3.148)$$

There are precisely $N_{\mathcal{J}}$ eigenvalues λ_i equal to zero, and the rest are positive real numbers (c.f. Sec. 3.4.9). We order the λ_i so that all $\lambda_i = 0$ come first, and after that they form a decreasing sequence converging to zero. For any initial $\eta_0(x)$, the solution to (3.146) for *homogeneous* boundary conditions (i.e. no electric current) is given by

$$\eta(x, t) = \sum_{i=1}^{N_{\mathcal{J}}} a_i \varphi_i + \sum_{i=N_{\mathcal{J}}+1}^{\infty} a_i e^{-\lambda_i t} \varphi_i, \quad (3.149)$$

where

$$a_i = (\phi_i, \eta_0(x))_H. \quad (3.150)$$

Equivalently, we define $U : l^2 \rightarrow H$ to have the φ_i for columns, write $K = U(0 \oplus \Lambda)U^{-1}$, and have

$$\eta(x, t) = E_t \eta_0(x), \quad E_t = U[id \oplus \exp(-\Lambda^{-1}t)]U^{-1}. \quad (3.151)$$

When an electric current is present, we find the steady solution η_{steady} by solving Laplace's equation for the electrostatic potential to determine ψ on Γ , and then find constants c_J so that mass conservation holds on each component

$$\eta_{\text{steady}} = -\psi|_{\Gamma} + \sum_{J \in \mathcal{J}} c_J e_J \quad \Rightarrow \quad \forall J \in \mathcal{J}, (e_J, g_{\text{steady}}) = (e_J, g_0), \quad (3.152)$$

where $g_{\text{steady}} = B\eta_{\text{steady}}$. Normally we take g_0 to be identically zero, which physically means no grain growth has occurred prior to turning on the electric current. In that case the c_J are chosen to project $-\psi|_{\Gamma}$ onto H_0^* :

$$\eta_{\text{steady}} = P^*(-\psi|_{\Gamma}). \quad (3.153)$$

The evolution to the steady state is then determined using (3.151) via

$$\eta(x, t) = \eta_{\text{steady}}(x) + E_t[\eta_0(x) - \eta_{\text{steady}}(x)]. \quad (3.154)$$

In the computations, we construct K in several stages. To compute the separation to stress map B , we use the singularity capturing least squares finite element method developed in Chapter 5. We choose a mesh parameter h and choose equally spaced points no larger than h along each wall, and along the grain boundary. We triangulate each grain separately using a freely available triangulation program [71]. This leads to an unstructured mesh with duplicate nodes along grain boundaries and triple (quadruple, etc.) nodes at grain boundary junctions; see Figure 3.21.

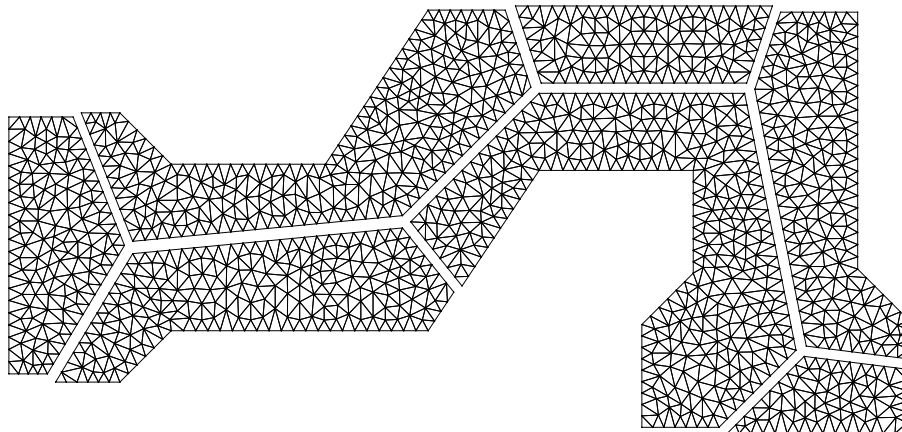


Figure 3.21: Each grain is triangulated separately, leading to an unstructured mesh with duplicate nodes along grain boundaries and triple nodes at triple junctions. Offsets have been added to the nodes of each grain here to show the finite element connectivity of the spacially coincident grain boundary nodes to the interior nodes. This particular mesh corresponds to a mesh parameter $h = 0.06$ for an interconnect line which fits in a rectangle of length 4.25 and height 2.

The branching structure of the grain boundary network leads to a challenging book-keeping problem, especially in light of the fact that additional basis functions are being used to capture asymptotic behavior near grain boundary junctions and endpoints. We set up a second finite element structure on the grain boundary network which is essentially one dimensional (except at junction points) and does not duplicate any nodes; e.g. there is a single node at a triple junction. We have several interwoven data structures that allow us to determine the index of the nodes in the ambient elasticity finite element space which coincide with a grain boundary node, determine which one is on the right or left, determine which self-similar basis functions contain the node in their support, etc. We also have data structures to go back the other way, i.e. nodes of the big finite element space carry information about whether they are on a grain boundary, what the boundary conditions look like there, which singular basis elements affect them, etc. Since no ordering of the grain boundary nodes is particularly natural, we order the endpoints first, and then arbitrarily sweep through the segments in a random order and assign node and edge indices. This makes visualization somewhat challenging since points which are spacially close are not necessarily labeled with nearby indices; see Fig. 3.22. We have found it useful to create an operator for each segment which maps the jumbled variables to a picture of the result on

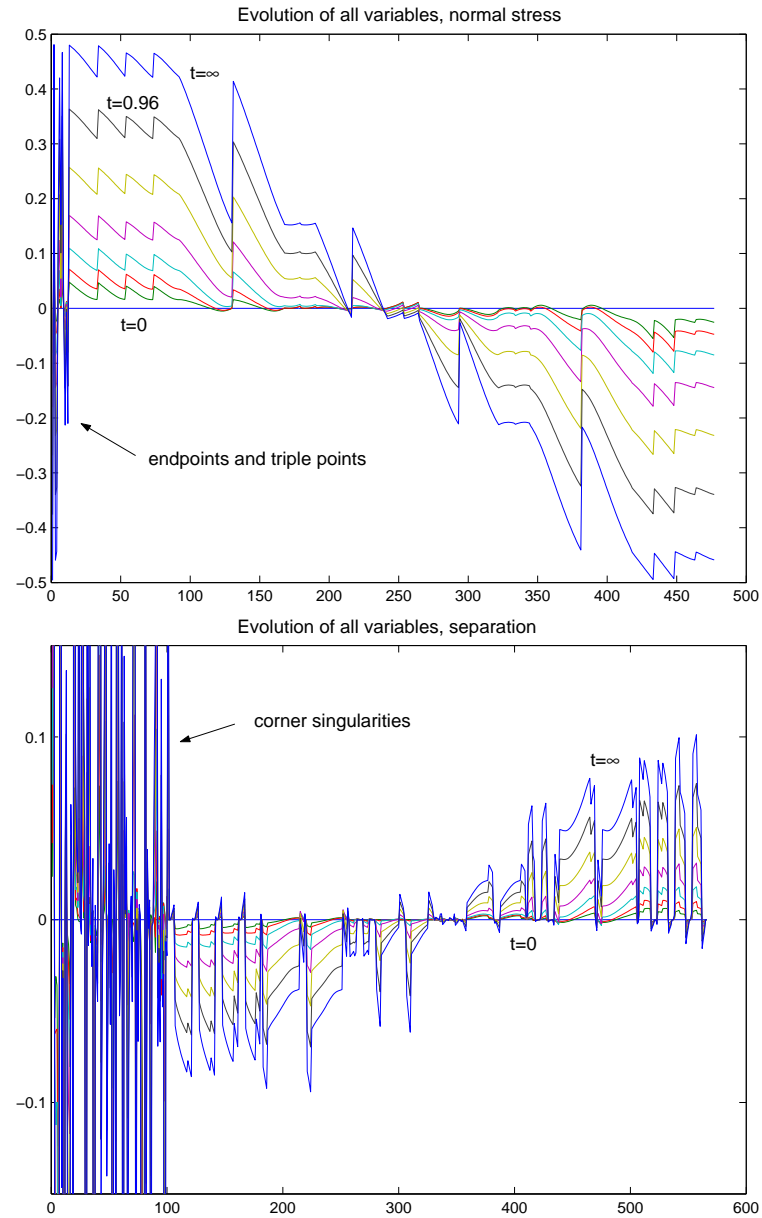


Figure 3.22: The normal stress variables are ordered by taking the grain boundary endpoints and triple points first, and then sweeping through the interior of each grain boundary segment. The separation variables include the special basis functions used to capture asymptotic behavior near corners and triple junctions. These basis functions all have zero normal stress on grain boundaries. The apparently large amplitude of the coefficients on these special basis functions is an artifact of how they are normalized in the code. This evolution will be further discussed in Section 3.4.8.

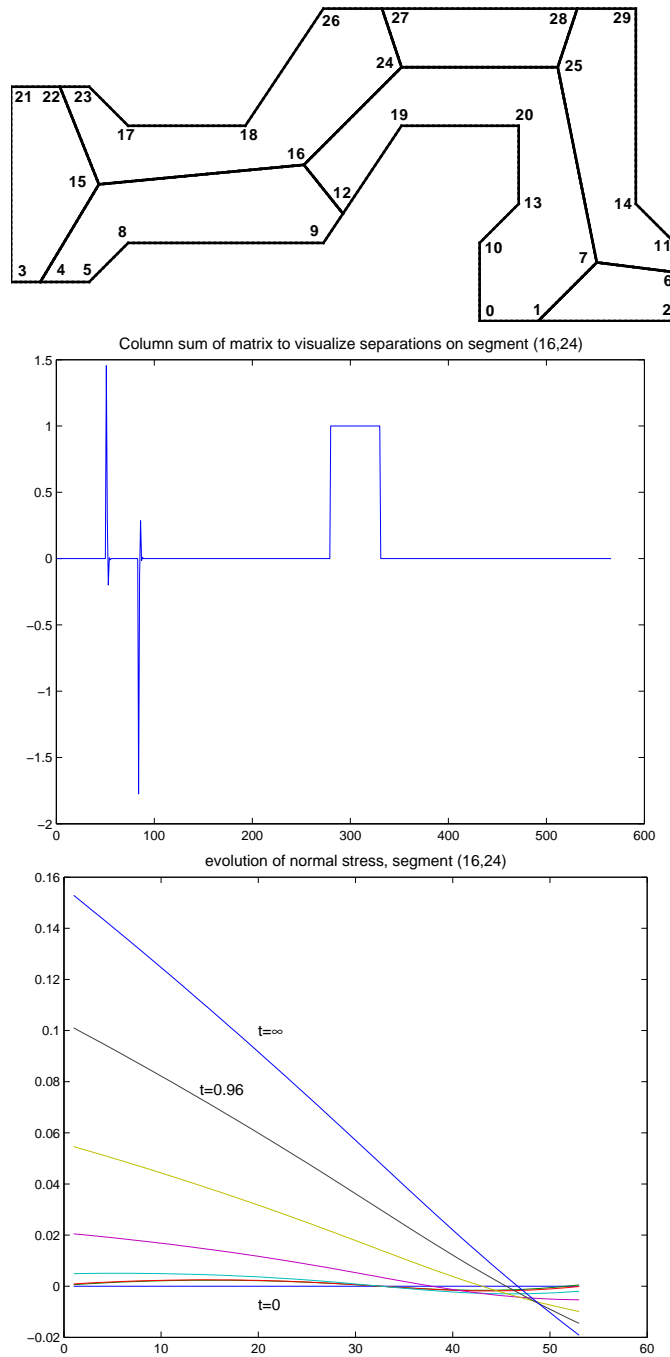


Figure 3.23: To visualize an evolution such as the one shown in Fig. 3.22, we define a matrix which maps the jumbled variables to a picture of the result on that segment, taking into account the singular basis functions. Shown here is the support of the operator for the segment from corner 16 to corner 24, and its use in visualizing the evolution on this segment.

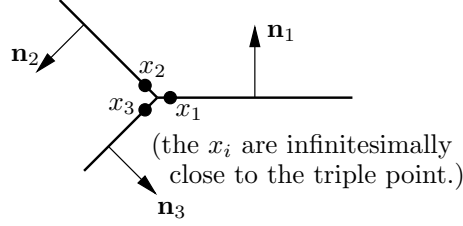


Figure 3.24: Compatibility condition on the separation function g at a triple point.

that segment; see Fig. 3.23.

The normal stress $\eta(x)$ is continuous on the grain boundary structure, and piecewise quadratic on any particular line element joining two nodes. At a triple point, $\eta(x)$ has a single value which is the limit approached along each incoming line element. This condition was derived in Chapter 2 (c.f. Eqn. (2.39)) as a requirement of chemical potential continuity:

$$\eta(x_1) = \eta(x_2) = \eta(x_3). \quad (3.155)$$

The separation $g(x)$ is more complicated. On any grain boundary segment it is continuous, but it has a different limit from the three incoming directions at a triple junction subject to the compatibility condition discussed in Chapter 2 (c.f. Eqn. (2.16)):

$$g(x_1)\mathbf{n}_1 + g(x_2)\mathbf{n}_2 + g(x_3)\mathbf{n}_3 = 0. \quad (3.156)$$

On each line element (sub-segment of a grain boundary segment), g is a sum of a quadratic function and possibly several power solution functions, just as in the simple horizontal geometry; see Fig. 3.12 on page 68. At triple points, a single singular basis function influences the nearby nodes of each incident segment. To enforce (3.156), we set the value of the quadratic portion of g on each incident line-element to zero at the triple point and use a power solution basis element with exponent $\alpha = 0$ to provide the separation degree of freedom there; the appropriate self-similar solution to model this separation always exists.

To compute G , we run through each line-element and compute its contribution to the stiffness matrix A and mass matrices M and \tilde{M} , just as we did for the simple horizontal geometry:

$$-A\eta = \tilde{M}g, \quad A_{ij} = (\partial_s \varepsilon_i, \partial_s \varepsilon_j)_{L^2}, \quad \tilde{M}_{ij} = (\varepsilon_i, e_j)_{L^2}, \quad M_{ij} = (\varepsilon_i, \varepsilon_j)_{L^2}. \quad (3.157)$$

Natural boundary conditions are used at all endpoints and triple points, which automatically enforces the conditions (3.143) and (3.144). The matrices A and M are symmetric $m \times m$ matrices; M is positive definite, and A has a kernel with dimension equal to the number of connected components of the grain boundary structure, with nullspace

$$\mathcal{N}_A = \text{span}\{e_J : J \in \mathcal{J}\}, \quad (\text{c.f. Eqn. (3.133)}). \quad (3.158)$$

On the orthogonal complement \mathcal{N}_A^\perp , A is positive definite. The $m \times n$ matrix \tilde{M} is not square due to the constraints on g at walls and the extra self-similar basis functions which affect g but not η . Our numerical approximation of G is the $m \times n$ matrix

$$G = \text{pinv}(A)M. \quad (3.159)$$

We compute the projections P and P^* from Eqns. (3.135) and (3.139) as follows. First define the $m \times N_{\mathcal{J}}$ matrix e to have columns e_J , i.e. the columns of e are a basis for \mathcal{N}_A . Then the g_J are the columns of Be , and P and P^* are given by

$$P = I - Be(e^T M B e)^{-1} e^T M, \quad P^* = I - e(e^T M B e)^{-1} e^T M B. \quad (3.160)$$

K and K^* are then formed using (3.145), the potential ψ is solved using Galerkin finite elements on the same mesh used to compute B , and $\eta(x, t)$ is found from (3.151), (3.153), and (3.154) in the same way that it was done for the simple horizontal geometry.

3.4.8 More Results

In this section we apply the method described above to two geometries. The first geometry was shown in Fig. 3.21 with a mesh parameter of $h = .06$, which led to a triangulation with 2366 triangles. The results here were obtained using a mesh with $h = .035$, 6686 triangles, 3797 vertices, 10476 edges, and 477 vertex and edge nodes along the grain boundary. The resulting linear system has 79920 unknowns, and must be solved 477 times to compute B . A total of 101 self-similar basis functions were used near corners and triple points (Fig. 3.25), several of them stabilized to avoid degeneracy; see Chapter 4. The second geometry (Fig. 3.31) consists of a straight interconnect line with a network of grain boundaries with two connected components. The mesh used has 6788 triangles, 3856 vertices, 10632 edges and 550 grain boundary nodes, leading to a linear system with 81336 variables that is solved 550 times to compute B . A total of 80 self-similar basis functions were used

near corners and triple points, stabilized when necessary. The condition number of U from Eqn. (3.151) was 9.74 for the first geometry and 21.7 for the second, so the eigenfunctions form a nice basis.

In Figures 3.26–3.28 we show the evolution to steady state of $g(x, t)$ and $\eta(x, t)$ along various segments of the grain boundary network. The evolution of the full set of interwoven variables was shown in Figure 3.22 on page 87. We point out two interesting features of this particular simulation. First, we note that ψ does not vary linearly from left to right due to the complicated geometry, so the steady state normal stress η_{steady} is not as simple on each segment as it was for the horizontal geometry. Second, along the segment from junction 24 to 27, the flux of material out of the segment through the junction changes sign midway through the evolution, which means that early in the evolution the grains are pulled together, but eventually extra material enters the segment and they are pushed apart. There are three things that contribute to this. First, the angle of the segment is such that $\psi(\mathbf{x})$ decreases as \mathbf{x} moves from \mathbf{x}_{24} to \mathbf{x}_{27} , therefore the electric field acts to keep $\eta(\mathbf{x}_{27}) > \eta(\mathbf{x}_{24})$. Second, the segment lies to the right of the “center of mass” of the network, so eventually $\eta(\mathbf{x}_{24})$ will be negative. And third, the segment is short, so it equilibrates more quickly than the structure as a whole. As a result, $\eta(\mathbf{x}_{27}, t)$ increases relative to $\eta(\mathbf{x}_{24}, t)$ on a shorter timescale than the scale on which $\eta(\mathbf{x}_{24}, t)$ settles into its eventual decreasing trajectory (pulling $\eta(\mathbf{x}_{27}, t)$ down with it).

In Figure 3.29, we illustrate the separation $g(x)$ of the steady state configuration by choosing a constant C (to make the displacements visible) and plotting $\mathbf{x} + C\mathbf{u}^+(\mathbf{x})$ and $\mathbf{x} + C\mathbf{u}^-(\mathbf{x})$ as \mathbf{x} traverses the grain boundary network. We also show a contour plot of the magnitude of the displacements in each grain, together with streamlines tangent to the displacement vector field. The general behavior is that material has been transported from the left end of the interconnect line to the right, causing the grains to move toward each other ($g < 0$) on the left side and to separate ($g > 0$) on the right. The magnitude is greatest near the left and right ends of the interconnect line, but still must go to zero at the walls.

Figure 3.30 contains contour plots of the steady state values of p , normalized energy density, and maximum shear stress. Recall that pressure is given by $-\mu p$ and energy density is given by $\sigma_{ij}\epsilon_{ij} = \mu \left[\frac{\kappa-1}{2} p^2 + \gamma^2 + \tau^2 \right]$. We see that the left and right ends of the line are generally in a state of tension and compression, respectively, due to the transport of mass from left to right. We also observe that the stresses are largest at the ends, especially

at re-entrant corners and grain boundary junctions where there are singularities.

In Figure 3.31 we show some of the steady state variables for the geometry with a grain boundary network with two connected components. On each component, material has been transported from left to right until the gradient of σ_{nn} balances the electromigration force. The break in the network in the middle of the line acts as a barrier to limit the effective length of the line. Large shear stresses develop on the top and bottom walls where they prevent the grain between the two grain boundary networks from being pushed to the right by grain growth on its left and grain annihilation on its right. The net result of the barrier, however, is to reduce the distance over which the stress gradient must balance the electromigration force, and hence the maximum stress is smaller than it would be for a single component grain boundary network on an interconnect line of this length. The idea is similar to the observation that the maximum height of the function $y = x - \frac{1}{2}$ on the unit interval is larger than the maximum height of

$$y = \begin{cases} x - \frac{1}{4} & 0 \leq x \leq \frac{1}{2}, \\ x - \frac{3}{4} & \frac{1}{2} < x \leq 1. \end{cases} \quad (3.161)$$

In real materials, mass transport occurs at passivation interfaces as well, so material can be transported from one such structure to the next. This possibility would lead to larger stresses at the ends of the interconnect line and smaller stresses in the middle. It is interesting, however, that if passivation interfaces can be made with small enough diffusion coefficients, they can effectively inhibit the development of stresses in an interconnect line with disconnected grain boundaries.

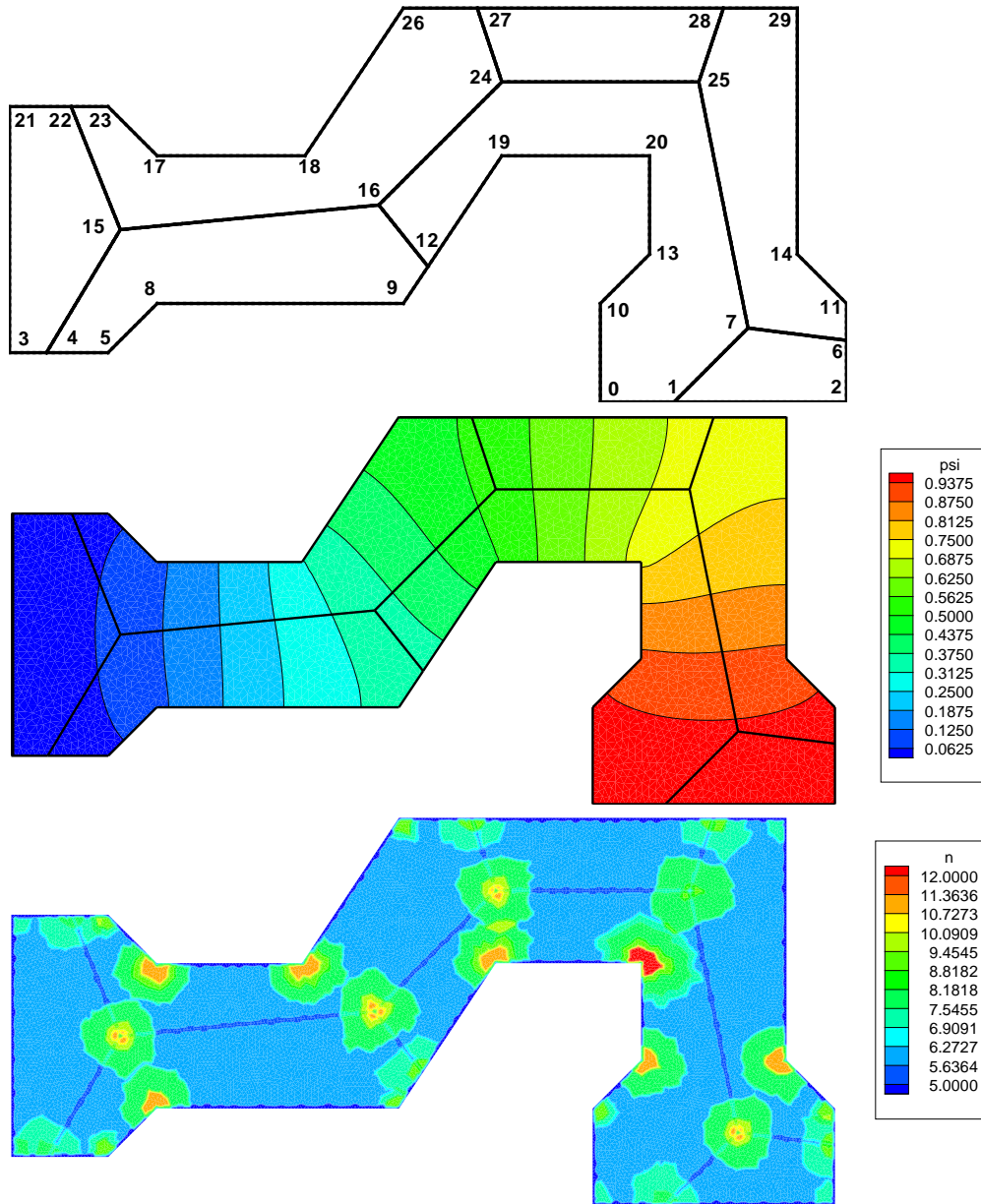


Figure 3.25: Top: Corners and grain boundary junctions are numbered arbitrarily. Middle: The electrostatic potential ψ satisfies Laplace's equation with Dirichlet boundary conditions at the ends and Neumann boundary conditions on the side walls. We use standard variational finite elements with quadratic elements on the mesh used in the elasticity problem to determine ψ along Γ . Bottom: A plot of the number of degrees of freedom that affect the variables at a given vertex or edge node. In this simulation, 101 extra basis functions near corners and junctions are used to capture asymptotic behavior.

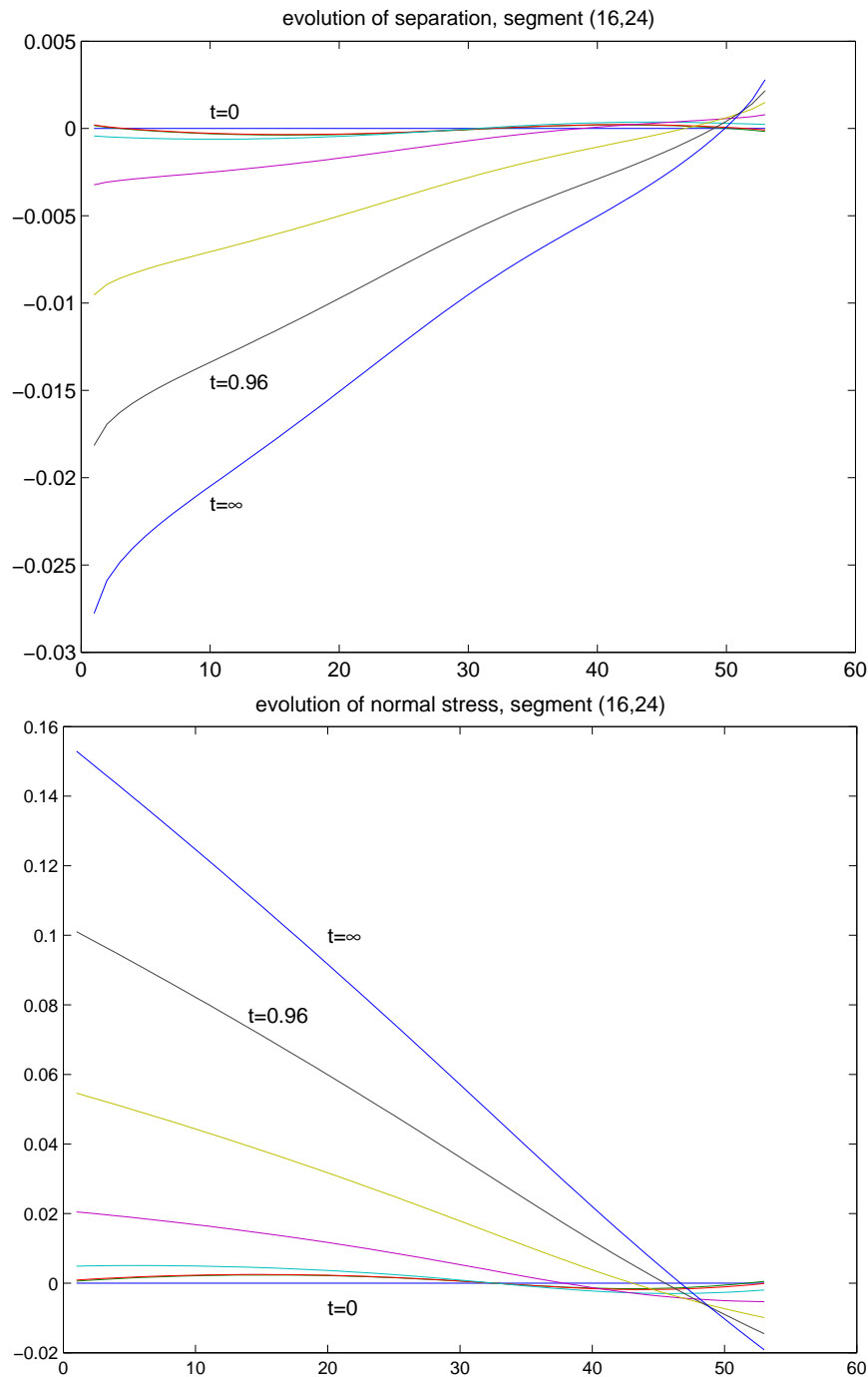


Figure 3.26: The evolution of g and η on the segment from junction 16 to junction 24 in Fig. 3.25. Times shown are $t = .03, .06, .12, .24, .48, .96, \infty$. The plot was obtained by applying the visualization operator for this segment (c.f. Fig. 3.23) to the evolution of the variables shown in Fig. 3.22 on Page 87.

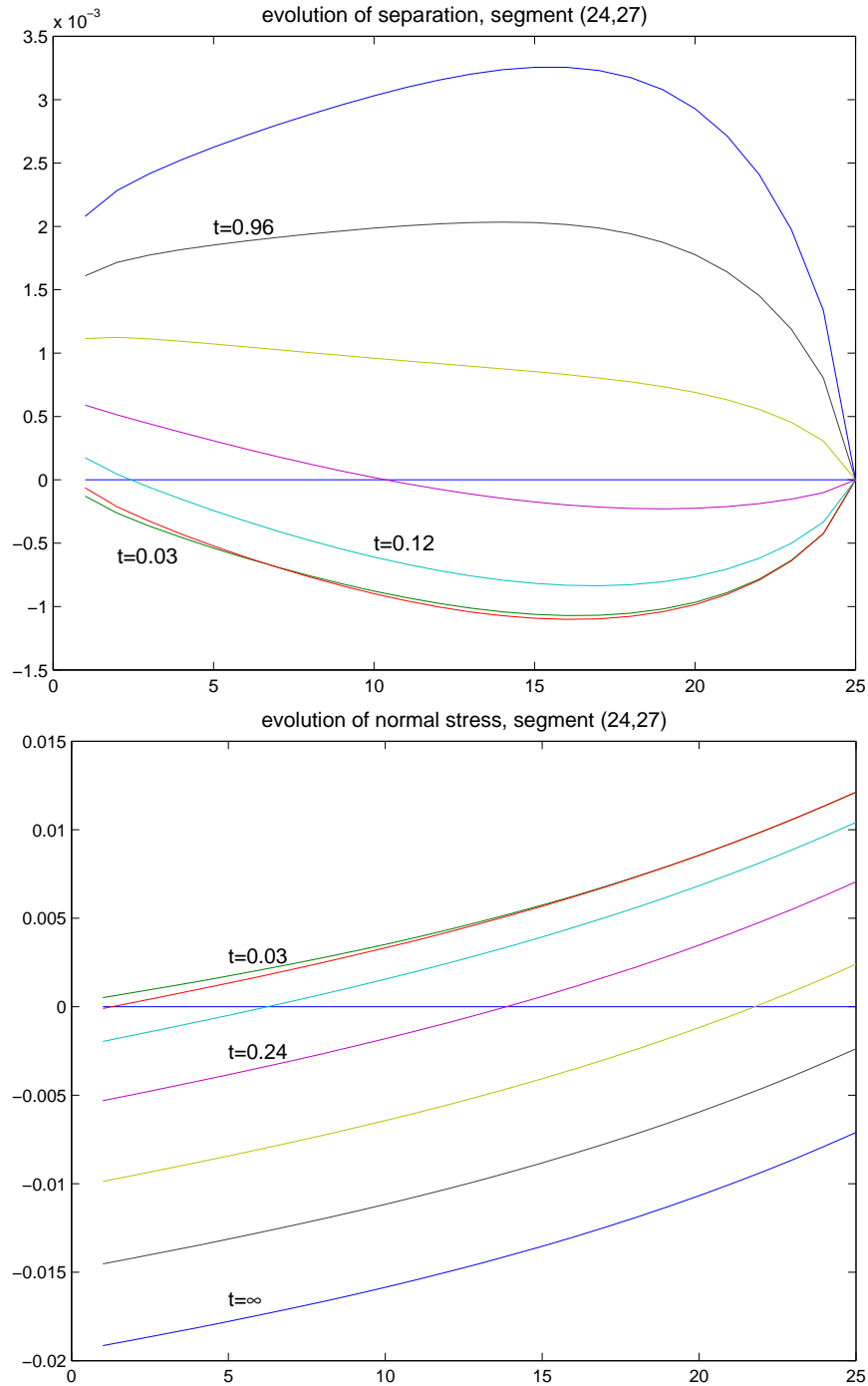


Figure 3.27: The evolution of g and η on the segment from junction 24 to junction 27 at $t = .03, .06, .12, .24, .48, .96, \infty$. Note that initially material leaves this segment, but the flux of mass at the triple point changes sign around $t = .045$ and ultimately the grains separate along this segment.

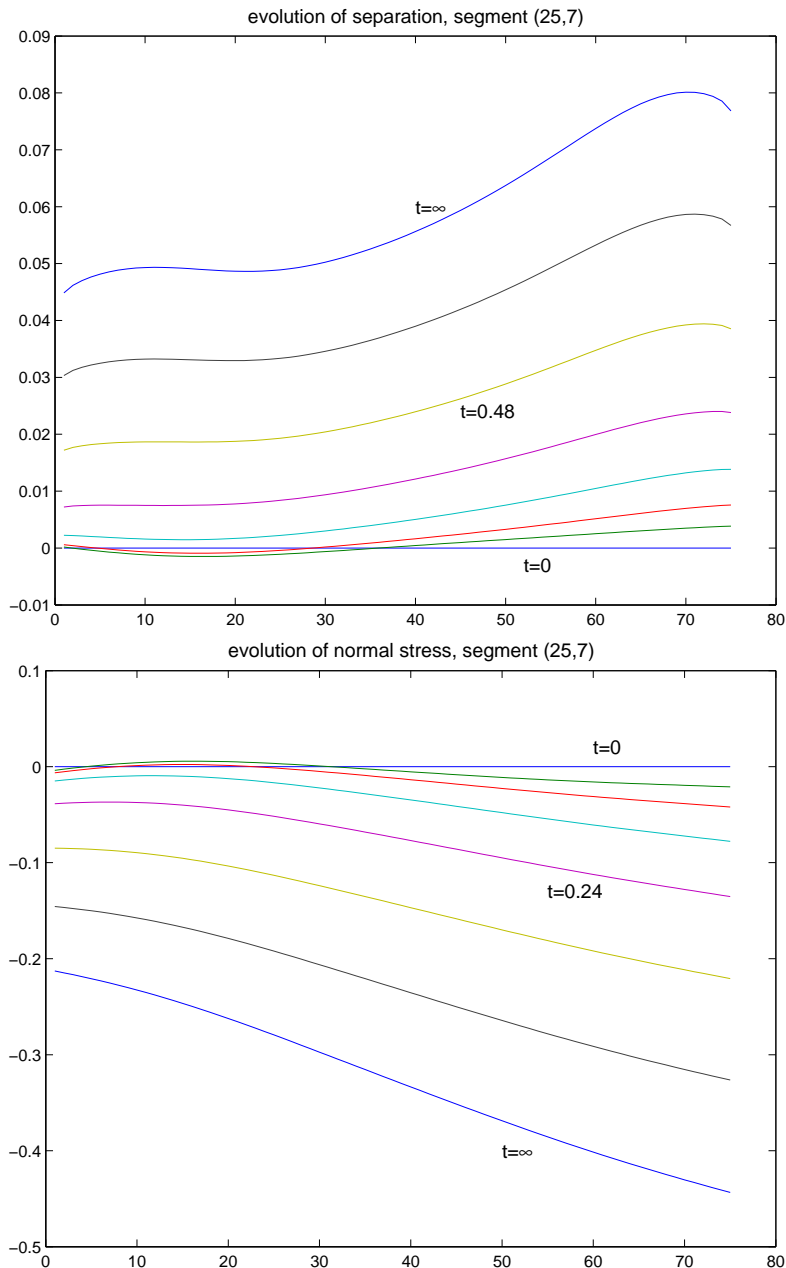


Figure 3.28: The evolution of g and η on the segment from junction 25 to junction 7 at $t = .03, .06, .12, .24, .48, .96, \infty$. Note that unlike the simple horizontal geometry, the steady state normal stress $\eta = P^*(-\psi|_{\Gamma})$ does not vary linearly along grain boundary segments. Also note that g develops an infinite slope at the endpoints due to singularities. Asymptotically, $g \sim \sum c_i r^{\lambda_i}$ with $\lambda_i^{(7)} \in \{0, .799, .886\}$ and $\lambda_i^{(25)} \in \{0, .725, .951\}$. The other stress components diverge at the ends (like $r^{\lambda-1}$ with $\lambda^{(7)} \in \{.799, .886\}$ and $\lambda^{(25)} \in \{.725, .951\}$), but η remains well behaved.

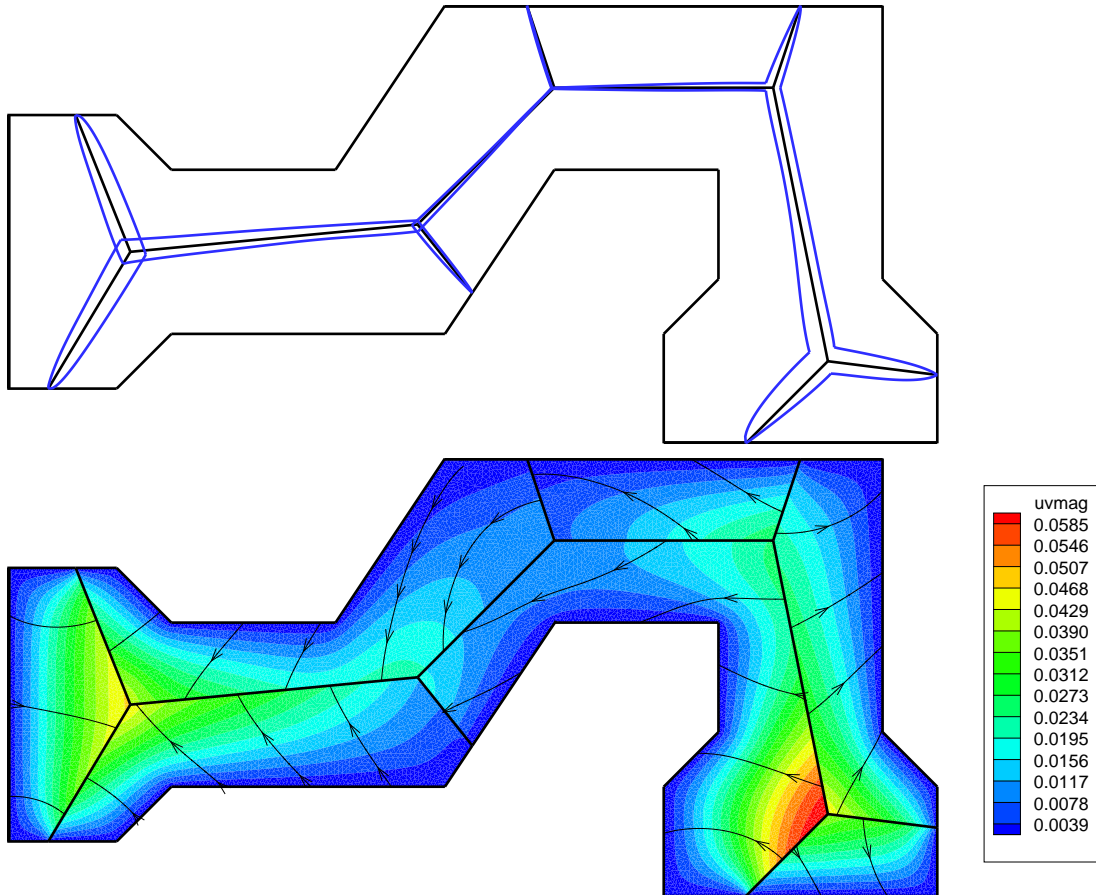


Figure 3.29: Top: Magnified view of the steady state separation $g(\mathbf{x})$, obtained by plotting $\mathbf{x} + C\mathbf{u}^+(\mathbf{x})$ and $\mathbf{x} + C\mathbf{u}^-(\mathbf{x})$ with \mathbf{x} along the grain boundary. Bottom: Contour plot of the magnitude of the displacements in each grain, together with streamlines tangent to the displacement vector field. Note that material is transported from the left end of the interconnect line to the right, causing the grains to move toward each other ($g < 0$) on the left side and to separate ($g > 0$) on the right.

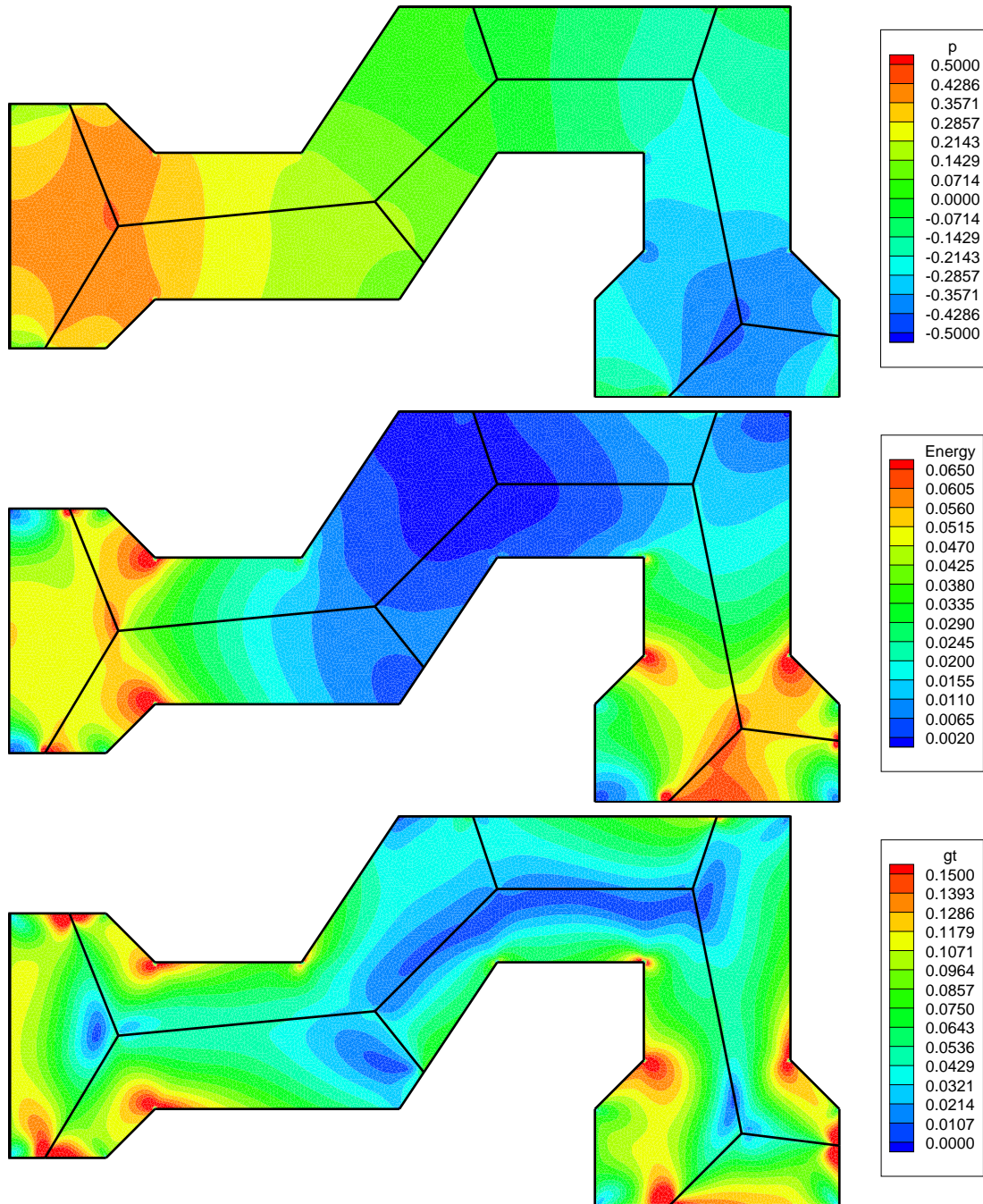


Figure 3.30: Contour plots of the steady state values of $p = \frac{1}{2}(\sigma_{11} + \sigma_{22})$, $\mu^{-1}\sigma_{ij}\epsilon_{ij} = \frac{\kappa-1}{2}p^2 + \gamma^2 + \tau^2$, and $(\gamma^2 + \tau^2)^{\frac{1}{2}}$. Note that the left and right ends of the line are generally in a state of tension and compression, respectively, due to the transport of mass from left to right. Also note that the stresses are largest where the grains have separated the most, and at re-entrant corners and grain boundary junctions where they have singularities.

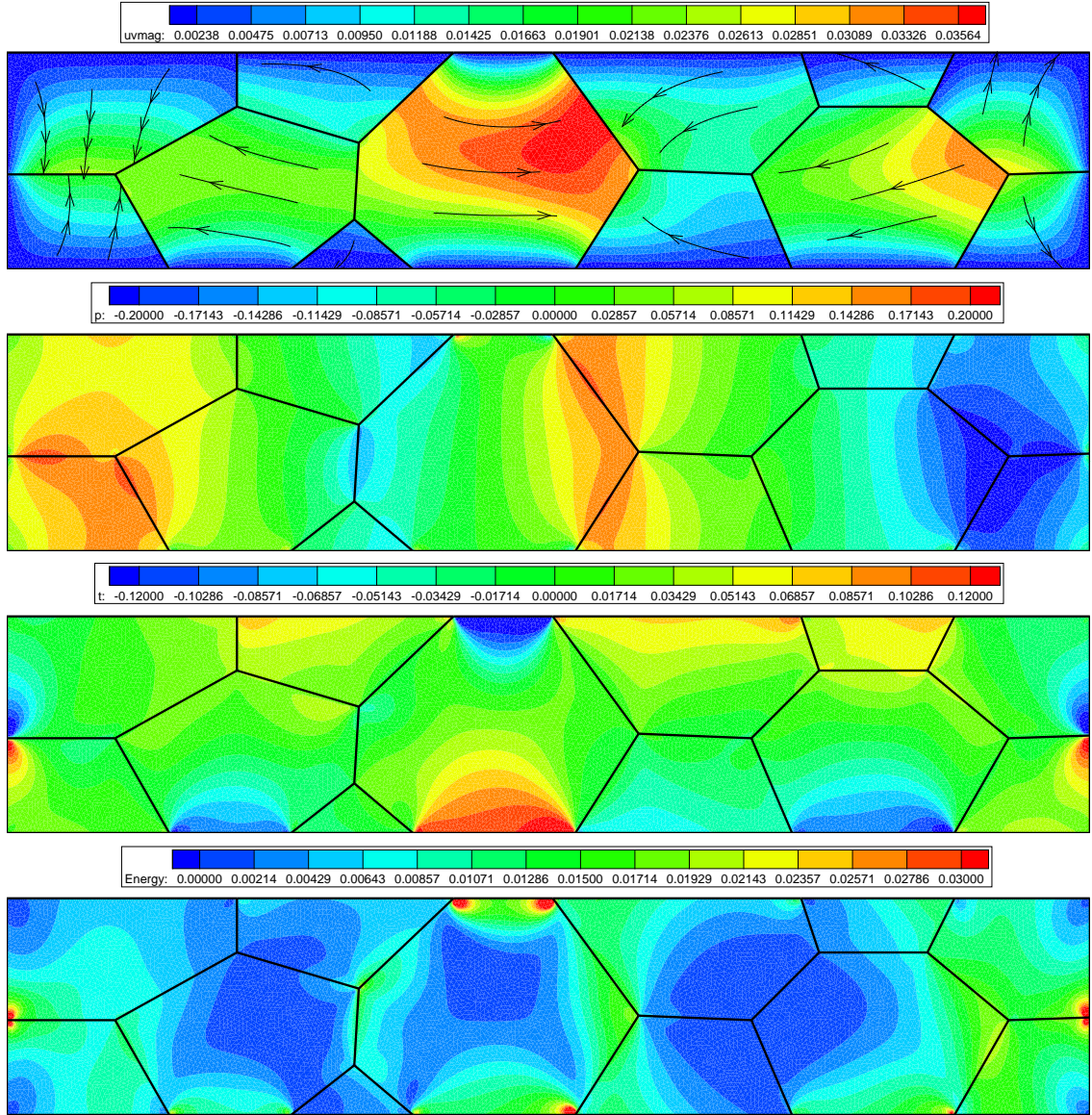


Figure 3.31: Contour plots of the steady state values of $(u^2 + v^2)^{\frac{1}{2}}$, p , τ , and $\frac{\kappa-1}{2}p^2 + \gamma^2 + \tau^2$ for a grain boundary network with two connected components. On each component, material has been transported from left to right until the gradient of σ_{nn} balances the electromigration force. The break in the network in the middle of the line acts as a barrier to limit the effective length of the line. Large stresses develop at the gb-wall junctions where the centermost grain is being pushed to the right by grain growth on its left and grain annihilation on its right, but is clamped in place at the top and bottom. The net result of the barrier, however, is to reduce the distance over which the stress gradient must balance the electromigration force, and hence the maximum stress is smaller than it would be for a single component grain boundary network on an interconnect line of this length.

3.4.9 Properties of B and K

The results illustrated in Fig. 3.18 provide evidence that B is self-adjoint. In this section, we prove that B is self-adjoint and negative, and that K has non-negative real eigenvalues with eigenfunctions which span a dense subspace of $L^2(\Gamma)$. As in Section 3.4.7, $\Gamma = \bigcup \Gamma_i$ is the grain boundary network. We are unable to prove that the eigenfunctions form a basis for $L^2(\Gamma)$, but provide a useful criterion to be tested numerically.

For convenience, in this section we treat the elasticity variables as truly two-dimensional, with stress, traction, and energy density having units $\frac{\text{force}}{\text{length}} = \frac{\text{energy}}{\text{area}}$. Let $\eta(\mathbf{x}, \theta)$ be a one-parameter family of normal stresses along Γ . Let $\mathbf{u}(x, y, \theta)$ and $\sigma(x, y, \theta)$ be the solution to the Lamé equations in the interior of each grain satisfying homogeneous Dirichlet boundary conditions at the walls and the four conditions $u_{\parallel}^+ = u_{\parallel}^-$, $\sigma_s^+ = \sigma_s^-$, $\sigma_{\perp}^+ = \sigma_{\perp}^- = \eta$ along grain boundaries. Then $g = B\eta$ is defined as before as $u_{\perp}^+ - u_{\perp}^-$ on Γ . Label the grains in some order, and let D_k be the k th grain. The elastic energy stored in the k th grain is given by

$$E_k(\theta) = \frac{1}{2} \int_{D_k} \sigma_{ij} \epsilon_{ij} dA, \quad (3.162)$$

and, with \mathbf{n} as in Fig. 3.32, Equation (2.24) on page 25 implies

$$\frac{\partial E_k}{\partial \theta} = \int_{\partial D_k} \mathbf{T}(\mathbf{x}(s), \theta) \cdot \frac{\partial}{\partial \theta} \mathbf{u}(\mathbf{x}(s), \theta) ds, \quad \mathbf{T} = \sigma(-\mathbf{n}) = \text{traction}. \quad (3.163)$$

Since $\mathbf{u}(\mathbf{x}, \theta) = 0$ for all θ when \mathbf{x} is on a wall, only grain boundary segments contribute to this integral. If we add the energies of all the grains to get the total elastic energy $E = \sum E_k$ stored in the interconnect line, each grain boundary segment will contribute two terms to an expression for $\partial_{\theta} E$, one when the left grain is traversed with increasing s , and one when the right grain is traversed with decreasing s . The orientation of Γ_j is arbitrary as a reversal

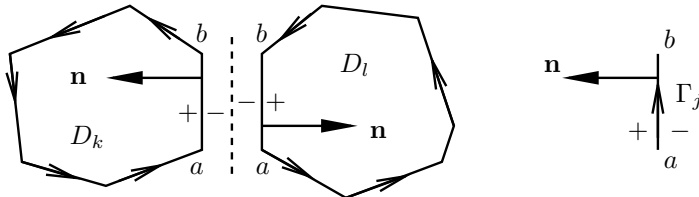


Figure 3.32: Each grain is traversed counterclockwise with unit inward normal \mathbf{n} . The contribution of a particular grain boundary segment to the total elastic energy $E = \sum E_k$ contains precisely one term from the left grain and one term from the right grain.

of the orientation also switches the left and right grain labels. The contribution from the left grain is given by

$$\int_{\Gamma_j} \sigma(-\mathbf{n}) \cdot \frac{\partial \mathbf{u}^+}{\partial \theta} ds \quad (3.164)$$

and the contribution from the right grain is given by

$$\int_{\Gamma_j} \sigma(\mathbf{n}) \cdot \frac{\partial \mathbf{u}^-}{\partial \theta} ds. \quad (3.165)$$

Since $\mathbf{u}^+ - \mathbf{u}^- = g\mathbf{n}$ and $\sigma(\mathbf{n}) \cdot \mathbf{n} = \eta$, we see that

$$\frac{\partial E}{\partial \theta} = - \sum_j \int_{\Gamma_j} \eta \frac{\partial g}{\partial \theta} ds = - \int_{\Gamma} \eta \frac{\partial}{\partial \theta} B \eta ds. \quad (3.166)$$

Setting $\eta = \theta \eta_0$ and integrating from 0 to 1, we find that

$$E[\eta_0] = -\frac{1}{2} \int_{\Gamma} \eta_0 B \eta_0 ds. \quad (3.167)$$

With $\eta = \eta_0 + \theta \eta_1$, we get

$$E[\eta_0 + \eta_1] - E[\eta_0] = - \int_{\Gamma} \eta_0 B \eta_1 - \frac{1}{2} \int_{\Gamma} \eta_1 B \eta_1 ds. \quad (3.168)$$

Combining (3.167), (3.168) and the corresponding result using $\eta = \eta_1 + \theta \eta_0$, we conclude that

$$\int_{\Gamma} \eta_0 B \eta_1 ds = \int_{\Gamma} \eta_1 B \eta_0 ds \quad (\eta_0, \eta_1 \in L^2(\Gamma)), \quad (3.169)$$

which shows that B is self-adjoint. By (3.167), B is also negative, i.e.

$$(\eta, B\eta)_{L^2(\Gamma)} < 0, \quad (\eta \in L^2(\Gamma) \setminus \{0\}). \quad (3.170)$$

I believe that $B : L^2(\Gamma) \rightarrow L^2(\Gamma)$ is a compact operator as well, but I don't have a proof.

The operator $G : H_0 \rightarrow H_0$ defined in Equations (3.142)–(3.144) on page 84 as the solution to the Poisson problem subject to various Neumann boundary conditions is also a compact, self-adjoint, negative operator. This can be proved easily using Green's function techniques from standard ODE theory. We define an auxiliary system of n ODE's on the unit interval ($0 < s < 1$) by defining $u_i(s)$ and $f_i(s)$ by

$$u_i(s) = \eta(\mathbf{x}_i^0 + s(\mathbf{x}_i^1 - \mathbf{x}_i^0)), \quad f_i(s) = l_i^2 g(\mathbf{x}_i^0 + s(\mathbf{x}_i^1 - \mathbf{x}_i^0)), \quad (3.171)$$

where n is the number of segments, $\mathbf{x}_i^{0,1}$ are the endpoints of segment i , and l_i is the length of the segment. In terms of the new variables, we have $u_i''(s) = f_i(s)$ with $2n$ boundary conditions of the form

$$M^0 u(0) + M^1 u'(0) + N^0 u(1) + N^1 u'(1) = 0. \quad (3.172)$$

For example, for a network with 3 grain boundary segments of lengths 1, 2, and 5 meeting at a triple point, we could parametrize each from outside in to get the boundary conditions

$$\begin{aligned} u_1'(0) &= 0 & u_2(1) - u_1(1) &= 0 \\ \frac{1}{2}u_2'(0) &= 0 & u_3(1) - u_1(1) &= 0 \\ \frac{1}{5}u_3'(0) &= 0 & u_1'(1) + \frac{1}{2}u_2'(1) + \frac{1}{5}u_3'(1) &= 0. \end{aligned} \quad (3.173)$$

Now we can apply standard theorems on boundary value problems for systems of ODE's (which account for the $N_{\mathcal{J}}$ dimensional kernel of $Lu = u_{xx}$ with these boundary conditions) to conclude that G well-defined, negative, and compact on the subspace H_0 ; see [20], [59].

We extend G to all of $H = L^2(\Gamma)$ by using the projections P and P^* from Eqns. (3.135) and (3.139) on page 83, and define K by

$$K = P^*GPB = AP, \quad A = P^*GP. \quad (3.174)$$

Since B is negative, self-adjoint, and compact, it can be diagonalized by an isometry $U : l^2 \rightarrow H$ such that

$$U^*BU = -D, \quad U^{-1} = U^*, \quad (3.175)$$

where D is an infinite diagonal matrix with a monotonic sequence of positive real numbers converging to zero along the diagonal. Since A is self-adjoint and compact, the operator $X : l^2 \rightarrow l^2$ given by

$$X = D^{\frac{1}{2}}U^*AUD^{\frac{1}{2}}. \quad (3.176)$$

is also self-adjoint and compact. Furthermore, X is non-positive and has an $N_{\mathcal{J}}$ dimensional kernel. Therefore there is a unitary $V : l^2 \rightarrow l^2$ and a diagonal matrix $\Lambda : l^2 \rightarrow l^2$ which satisfy the following properties:

- The first $N_{\mathcal{J}}$ entries of Λ are zero and the remaining entries form a decreasing sequence of positive real numbers converging to zero.
- V and Λ satisfy

$$V^*XV = -\Lambda, \quad V^{-1} = V^*. \quad (3.177)$$

For any diagonal matrix S , the columns of $W = AUD^{\frac{1}{2}}VD^{\frac{1}{2}}S$ are eigenvectors of $K = AB$ with eigenvalues equal to the diagonal of Λ :

$$\begin{aligned} KW &= A(UU^*)B(UU^*)AUD^{\frac{1}{2}}VD^{\frac{1}{2}}S = AU(-D^{\frac{1}{2}}D^{\frac{1}{2}})U^*AUD^{\frac{1}{2}}VD^{\frac{1}{2}}S = \\ &= -AUD^{\frac{1}{2}}XVD^{\frac{1}{2}}S = AUD^{\frac{1}{2}}V\Lambda D^{\frac{1}{2}}S = AUD^{\frac{1}{2}}VD^{\frac{1}{2}}S\Lambda = W\Lambda. \end{aligned} \quad (3.178)$$

In the last two steps, we used $XV = -V\Lambda$ and the fact that diagonal matrices commute. Note that because Λ has precisely $N_{\mathcal{J}}$ diagonal entries which are zero (the first ones), we may replace the first $N_{\mathcal{J}}$ columns of W with the e_J (which span the kernel of K), after which any finite collection of the columns of W are linearly independent.

Lemma 4. *The closure of $\text{range}(D^{\frac{1}{2}}VD^{\frac{1}{2}})$ is l^2 .*

Proof. Fix $x \in l^2$, $\epsilon > 0$. Choose n large enough that $\sum_n^\infty |x_i|^2 < \epsilon^2$. Define $F_k : l^2 \rightarrow l^2$ to be the diagonal matrix

$$(F_k)_{ii} = \begin{cases} (D_{ii})^{-\frac{1}{2}} & i < k \\ 0 & i \geq k \end{cases} \quad (3.179)$$

Then F_k is bounded and $D^{\frac{1}{2}}F = id_{k-1} \oplus 0$. Let $y = V^*F_n x$, (so that $\|D^{\frac{1}{2}}Vy - x\|^2 = \sum_n^\infty |x_i|^2 < \epsilon^2$) and choose m large enough that $\sum_m^\infty |y_i|^2 < \epsilon^2$. Let $z = F_m y$. Then $w = D^{\frac{1}{2}}z - y$ satisfies $\|w\|^2 = \sum_m^\infty |y_i|^2 < \epsilon^2$, hence

$$\|D^{\frac{1}{2}}VD^{\frac{1}{2}}z - x\| = \|D^{\frac{1}{2}}V(y + w) - x\| \leq \|D^{\frac{1}{2}}Vw\| + \|D^{\frac{1}{2}}Vy - x\| < (\|D^{\frac{1}{2}}\| + 1)\epsilon. \quad (3.180)$$

□

Lemma 5. *The closure of $\text{range}(G)$ is H_0 . The closure of $\text{range}(B)$ is H .*

Proof. $G : H_0 \rightarrow H_0$ and $B : H \rightarrow H$ are self-adjoint, compact, and strictly negative, so we may diagonalize them and use an argument similar to the proof of Lemma 4 to obtain the desired result. □

Lemma 6. *The closure of $\text{range}(A)$ is H_0^* .*

Proof. This follows from $A = P^*GP$, Lemma 5 and Equation (3.141):

$$P^*(H_0) = H_0^*, \quad P(H_0^*) = H_0. \quad (3.181)$$

□

Proposition 7. *The closure of the column span of W is H . In other words, the eigenfunctions of K are dense in H , and Jordan chains do not arise in the eigendecomposition.*

Proof. In the Banach space setting, it is easy to show that if $E_1 : X \rightarrow Y$ and $E_2 : Y \rightarrow Z$ are bounded operators and E_1 has dense range, then the closure of $\text{range}(E_2E_1)$ is the closure of $\text{range}(E_2)$. Using the above lemmas and the fact that U is invertible, this implies that $\text{range}(AUD^{\frac{1}{2}}VD^{\frac{1}{2}})$ is dense in H_0^* . Moreover, the invertibility of $(e_I, Be_J)_{IJ}$ as an $N_{\mathcal{J}} \times N_{\mathcal{J}}$ matrix (c.f. Eqn. (3.137)) gives that $\text{span}\{e_J\}$ complements H_0^* in H . \square

Applying B to both sides of $ABW = W\Lambda$, we see that $BA(BW) = (BW)\Lambda$, hence the columns of BW are eigenvectors of K^* . Moreover, since the column span of W is dense in H and the range of B is dense in H , the column span of BW is also dense in H . In general, if φ is an eigenvector of an operator E with eigenvalue λ , and ϕ is an eigenvector of E^* with eigenvalue μ , then

$$(\lambda - \bar{\mu})(\phi, \varphi) = (E^*\phi, \varphi) - (\phi, E\varphi) = 0. \quad (3.182)$$

Thus if $\lambda \neq \bar{\mu}$, ϕ and φ are orthogonal. Since K is compact, the dimension of any eigenspace is finite dimensional. Choose $\lambda \in \text{sp}(K) \setminus \{0\}$, and let $(j_0 < j \leq j_0 + n)$ be the range of indices for which $\lambda_j = \lambda$. Let $\Phi = (\phi_1, \dots, \phi_n)$ contain columns $j_0 + 1$ through $j_0 + n$ of W . We wish to find an $n \times n$ matrix C such that ΦC and $-B\Phi C$ are dual to one another in the sense that

$$(\phi_i C_{ij}, -B\phi_k C_{kl}) = \delta_{jl}. \quad (3.183)$$

Consider the matrix $R_{ij} = (\phi_i, -B\phi_j)$. Since B is self-adjoint and negative, R is self-adjoint and invertible. If R were not invertible, we could find numbers a_j such that for each i , $(\phi_i, -B\phi_j)a_j = 0$; hence setting $x = \phi_j a_j$ we would get $(x, -Bx) = 0$, a contradiction. Since R is self-adjoint and positive, there is a unitary $n \times n$ matrix Q and a diagonal matrix Σ with positive entries on the diagonal such that $R = U\Sigma U^*$. We then set $C = Q\Sigma^{-\frac{1}{2}}$ and verify that

$$(\phi_i C_{ij}, -B\phi_k C_{kl}) = \bar{C}_{ij} R_{ik} C_{kl} = (C^* R C)_{jl} = \delta_{jl}. \quad (3.184)$$

Thus we may replace columns $(j_0 < j \leq j_0 + n)$ of W with ΦC so that the columns of W and the columns of $-BW$ are dual in the sense that if φ_j is the j th column of W and ϕ_i is the i th column of $-BW$, then

$$(\phi_i, \varphi_j) = \delta_{ij}. \quad (3.185)$$

Note that for any diagonal $S : l^2 \rightarrow l^2$ with non-zero diagonal entries, replacing W by $\Phi = WS$ and $-BW$ with $\tilde{\Phi} = -BWS^{-1}$ gives another pair of matrices with columns that

are dual to one another. We wish to choose S so that the both Φ and $\tilde{\Phi}$ are bounded operators from $l^2 \rightarrow H$, in which case $\{\varphi_j\}$ and $\{\phi_i\}$ are each bases for H [34], $\tilde{\Phi} = (\Phi^{-1})^*$, and we have diagonalized K as

$$K = \Phi^{-1} \Lambda \Phi. \quad (3.186)$$

I don't know how to prove that an appropriate S exists that can do this (Λ^{-1} is a good candidate, replacing the $N_{\mathcal{J}}$ zeros on the diagonal with ones first), but it is still useful to know that K has a real spectrum consisting of zero together with a positive sequence converging to zero, that K has a dense spanning set of eigenfunctions, and that K has an $N_{\mathcal{J}}$ dimensional kernel spanned by the functions e_J , where e_J is constant on the J th component of the grain boundary network. The condition number of Φ can be checked in numerical experiments to indicate whether the eigenvectors of K are becoming linearly dependent as the dimension increases, and we have found that these matrices are very well conditioned; see Sections 3.4.6 and 3.4.8.

Chapter 4

Corner Singularities

In this chapter we present the numerical techniques we have developed for computing a basis to capture the asymptotic behavior of solutions to ADN-elliptic systems near corners and interface junctions. We have used the method to produce hundreds of self-similar (not always singular) solutions to augment our least squares finite element spaces for the grain growth problem; see Fig 3.25 on page 93. In Sections 4.1 and 4.2, we set up our notation and give several examples. In Sections 4.3, 4.4 and 4.6, we cover some of the basic theory which is prerequisite to understanding the later results. In Section 4.5, we give a new algorithm for removing rank deficiencies from an analytic matrix $\tilde{F}(\lambda, \theta)$ which plays an essential role in the numerical procedures. In Section 4.7, we explain how to compute critical exponents, with several new features of our implementation appearing in Section 4.7.1. In Section 4.8, we prove a new theorem which allows us to construct an algorithm for computing Keldysh chains and understanding the structure of the power solutions simply by knowing the boundary condition matrix $A(\lambda)$ and its first few derivatives. An interesting example is presented to illustrate the technique. In Section 4.9, we present a stabilization algorithm in which we remove near linear dependency from a basis of power solutions that have exponents clustered together in the complex plane. This method is essential for employing such self-similar functions in finite element computations, and has the nice feature that at a nearly critical angle of the geometry, it will give nearly the same basis as the Keldysh chain procedure of Section 4.8 at exactly the critical angle.

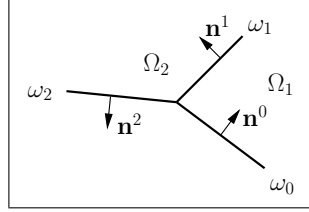


Figure 4.1: The angles ω_k divide \mathbb{R}^2 into several regions Ω_k .

4.1 Interface Problems

The problem of understanding the asymptotic behavior of the solution to an ADN-elliptic system near a corner is a local problem. There is a standard technique using cutoff functions which converts the problem on a finite domain with piecewise smooth boundary to a problem on an infinite wedge [36], [45], [54]. The asymptotic behavior of the solution to the principal part (c.f. Sec. 3.1) of the elliptic system (itself a homogeneous ADN system) for the infinite wedge determines the asymptotic behavior for the original problem. In this section, we restrict attention to interface problems for homogeneous ADN-elliptic systems on a union of such wedges. Suppose we are given

$$\omega_0 < \omega_1 < \cdots < \omega_K \leq \omega_0 + 2\pi, \quad (4.1)$$

and consider the K regions Ω_k in \mathbb{R}^2 given in polar coordinates by

$$\Omega_k = \{x \in \mathbb{R}^2 : 0 < r(x), \omega_{k-1} < \theta(x) < \omega_k\} \quad (k = 1, \dots, K). \quad (4.2)$$

Along each ray, we have unit tangent and normal vectors

$$\mathbf{t} = (\cos \omega_k, \sin \omega_k), \quad \mathbf{n} = (-\sin \omega_k, \cos \omega_k). \quad (4.3)$$

We denote the restriction of our variables $\{w_i\}_{i=1}^N$ to region Ω_k by w_i^k , and assume that the restriction M^k of our ADN-elliptic operator $M(x, y, \partial_x, \partial_y)$ to region Ω_k is independent of x and y , i.e. we allow for the possibility that the material parameters such as μ and κ in the case of elasticity change between regions, but require that they be constant within each Ω_k . We assume that each M^k is homogeneous of multi-degree. Summarizing Sec. 3.1, this means we have equation and variable indices s_i, t_j and an integer m such that

- $\sum_i (t_i + s_i) = 2m$ is even,

- either $M_{ij}^k(a, b) \equiv 0$ or the degree of $M_{ij}^k(a, b)$ as a polynomial in a and b is $s_i + t_j$,
- $\det M^k(a, b) \neq 0$ for all $(a, b) \in \mathbb{R}^2 \setminus 0$,
- the equation $[\det M^k(\xi + z\xi') = 0]$ as a polynomial in z has precisely m roots in the positive half-plane and m roots in the negative half-plane for any linearly independent $\xi, \xi' \in \mathbb{R}^2$.

We wish to solve $M^k w^k = f^k$ on each region Ω_k , subject to the boundary conditions

$$Bw = g, \quad (4.4)$$

which is an expression of the $2mK$ equations

$$B_i^0(\partial_x, \partial_y)w^1(r, \omega_0) = g_i^0(r) \quad (i = 1, \dots, m) \quad (4.5)$$

$$B_i^k(\partial_x, \partial_y)w^{k+1}(r, \omega_k) + \tilde{B}_i^k(\partial_x, \partial_y)w^k(r, \omega_k) = g_i^k(r) \quad (i = 1, \dots, 2m) \quad (4.6)$$

$$\tilde{B}_i^K(\partial_x, \partial_y)w^K(r, \omega_K) = g_i^K(r) \quad (i = 1, \dots, m). \quad (4.7)$$

Here B^k and \tilde{B}^k control the variables on the positive and negative side of ray ($\theta = \omega_k$), respectively, and ∂_x, ∂_y act on r and θ before ω_k is substituted for θ . If $\omega^K = \omega_0 + 2\pi$, conditions (4.5) and (4.7) are replaced with

$$B_i^0(\partial_x, \partial_y)w^1(r, \omega_0) + \tilde{B}_i^K(\partial_x, \partial_y)w^K(r, \omega_K) = g_i^0(r) \quad (i = 1, \dots, 2m). \quad (4.8)$$

Each B_i^k and \tilde{B}_i^k is a row vector assumed homogeneous of multi-degree, (i.e. stresses aren't added to displacements). This is expressed mathematically as a statement of the existence of boundary condition indices q_i^k such that

$$\deg B_{ij}^k(a, b) = q_i^k + t_j \quad \text{if } B_{ij}^k \neq 0, \quad (4.9)$$

$$\deg \tilde{B}_{ij}^k(a, b) = q_i^k + t_j \quad \text{if } \tilde{B}_{ij}^k \neq 0. \quad (4.10)$$

If $\omega_0 = \omega_K$, then we require $(q_i^0) = (q_i^K)$. These boundary conditions must satisfy the Lopatinskij covering condition, as discussed in Sec. 3.1.

4.2 Examples

Example 8. (Diffusion equation with discontinuous coefficients). We wish to solve

$$-\nabla \cdot \alpha_k \nabla u^k = F^k \quad \text{on } \Omega_k \quad (4.11)$$

subject to Dirichlet boundary conditions along $(\theta = \omega_0)$ and $(\theta = \omega_K)$ and continuity and flux boundary conditions at interior interfaces $(\theta = \omega_k)$. The flux is given by $\mathbf{j}^k = -\alpha_k \nabla u^k$, so we impose $u^{k+1} = u^k$ and $(\mathbf{j}^{k+1} - \mathbf{j}^k) \cdot \mathbf{n}^k = 0$ along the interface. We can put this in the above framework by defining $w^k = (u^k, -\alpha_k u_x^k, -\alpha_k u_y^k)^T$, $m = 1$, $(s_i) = (2, 1, 1)$, $(t_j) = (0, -1, -1)$, $(q_i^0) = (0)$, $(q_i^k) = (0, 1)$, $(q_i^K) = (0)$, $f^k = (F^k, 0, 0)^T$,

$$M^k(\partial_x, \partial_y) = \begin{pmatrix} 0 & \partial_x & \partial_y \\ \partial_x & \alpha_k^{-1} & 0 \\ \partial_y & 0 & \alpha_k^{-1} \end{pmatrix} \quad B^0 = \tilde{B}^K = (1, 0, 0),$$

$$B^k = -\tilde{B}^k = \begin{pmatrix} 1 & 0 & 0 \\ 0 & -\sin \omega_k & \cos \omega_k \end{pmatrix}. \quad (4.12)$$

Here we assume the Dirichlet data $g^0(r)$ and $g^K(r)$ are given, and all other $g^k(r) = (0, 0)^T$. This is a variant of the problem studied by Berndt in his dissertation [4].

Example 9. (Elasticity near a corner). We wish to solve the Lamé equations subject to Dirichlet boundary conditions along one ray and traction boundary conditions along the other; see Figure 4.2. Since there is only one region, we drop unnecessary superscripts, set $w = (u, v, p, q, \gamma, \tau)^T$ as in Section 3.1, and use

$$M_\kappa(a, b) = \begin{pmatrix} a & -b & 0 & 0 & 1 & 0 \\ b & a & 0 & 0 & 0 & -1 \\ -b & a & 0 & -\frac{\kappa+1}{2} & 0 & 0 \\ a & b & -\frac{\kappa-1}{2} & 0 & 0 & 0 \\ 0 & 0 & a & -b & 0 & 0 \\ 0 & 0 & b & a & 0 & 0 \end{pmatrix}, \quad f_{\mu, \kappa} = -\frac{2\mu^{-1}}{\kappa+1} \begin{pmatrix} 0 \\ 0 \\ 0 \\ 0 \\ F_1(x, y) \\ F_2(x, y) \end{pmatrix}, \quad (4.13)$$

$$m = 2, \quad (s_i) = (2, 2, 1, 1, 1, 1), \quad (t_j) = (0, 0, -1, -1, -1, -1). \quad (4.14)$$

The tangential and normal components of displacement $g_i^0(r)$ and traction $g_i^1(r)$ are specified along $(\theta = \omega_0)$ and $(\theta = \omega_1)$, respectively, and we have

$$B^0 = \begin{pmatrix} \cos \omega_0 & \sin \omega_0 & 0 & 0 & 0 & 0 \\ -\sin \omega_0 & \cos \omega_0 & 0 & 0 & 0 & 0 \end{pmatrix}, \quad \tilde{B}^1 = \mu \begin{pmatrix} 0 & 0 & 0 & 0 & \sin 2\omega_1 & \cos 2\omega_1 \\ 0 & 0 & 1 & 0 & \cos 2\omega_1 & -\sin 2\omega_1 \end{pmatrix} \quad (4.15)$$

with ADN indices $(q_i^0) = (0, 0)$ and $(q_i^1) = (1, 1)$.

Example 10. (Elasticity at a wall-gb-wall interface). The elastic constants μ and κ are assumed the same in both regions, so there is no need for superscripts on M and f , which

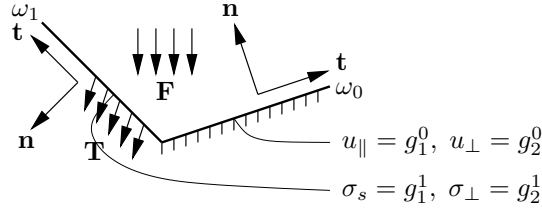


Figure 4.2: Geometry of Example 9: a corner with Dirichlet boundary conditions imposed along one ray and traction boundary conditions imposed along the other. Recall (page 39) that $u_{\parallel} = \mathbf{u} \cdot \mathbf{t}$, $u_{\perp} = \mathbf{u} \cdot \mathbf{n}$, $\sigma_s = \mathbf{t} \cdot \boldsymbol{\sigma} \mathbf{n}$, $\sigma_{\perp} = \mathbf{n} \cdot \boldsymbol{\sigma} \mathbf{n}$, and $\mathbf{T} = \boldsymbol{\sigma} \mathbf{n}$.

are again given by (4.13). Along $(\theta = \omega_0)$ and $(\theta = \omega_2)$, we have homogeneous dirichlet conditions

$$B^0 = \begin{pmatrix} \cos \omega_0 & \sin \omega_0 & 0 & 0 & 0 & 0 \\ -\sin \omega_0 & \cos \omega_0 & 0 & 0 & 0 & 0 \end{pmatrix}, \quad \tilde{B}^2 = \begin{pmatrix} \cos \omega_2 & \sin \omega_2 & 0 & 0 & 0 & 0 \\ -\sin \omega_2 & \cos \omega_2 & 0 & 0 & 0 & 0 \end{pmatrix} \quad (4.16)$$

with $g^0 = g^2 = (0, 0)^T$ and $(q_i^0) = (q_i^2) = (0, 0)$. Along $(\theta = \omega_1)$, we require that u_{\parallel} , σ_s and σ_{\perp} are continuous across the grain boundary (which implies σ_{\parallel} is as well; see page 19), and that $\sigma_{\perp} = \eta$ is specified along the grain boundary. Thus we define

$$B^1 = \begin{pmatrix} \cos \omega_1 & \sin \omega_1 & 0 & 0 & 0 & 0 \\ 0 & 0 & 0 & 0 & \mu \sin 2\omega_1 & \mu \cos 2\omega_1 \\ 0 & 0 & \mu & 0 & \mu \cos 2\omega_1 & -\mu \sin 2\omega_1 \\ 0 & 0 & 0 & 0 & 0 & 0 \end{pmatrix}, \quad g^1(r) = \begin{pmatrix} 0 \\ 0 \\ \eta(r) \\ \eta(r) \end{pmatrix}, \quad (4.17)$$

$$\tilde{B}^1 = \begin{pmatrix} -\cos \omega_1 & -\sin \omega_1 & 0 & 0 & 0 & 0 \\ 0 & 0 & 0 & 0 & -\mu \sin 2\omega_1 & -\mu \cos 2\omega_1 \\ 0 & 0 & 0 & 0 & 0 & 0 \\ 0 & 0 & \mu & 0 & \mu \cos 2\omega_1 & -\mu \sin 2\omega_1 \end{pmatrix}, \quad (q_i^1) = (0, 1, 1, 1).$$

Example 11. (Triple grain boundary junction). This time $\omega_3 = \omega_0 + 2\pi$ and Equations (4.5) and (4.7) are replaced with Equation (4.8). All pairs (B^0, \tilde{B}^3) , (B^1, \tilde{B}^1) , (B^2, \tilde{B}^2) have the form (4.17).

Example 12. (Several materials welded together). In each region, we have different elastic constants, so $M^k = M_{\kappa_k}$ and $f^k = f_{\mu_k, \kappa_k}$ from (4.13). We have $\omega_K = \omega_0 + 2\pi$, so we again use Equation (4.8). Along each weld, we require continuity of u_{\parallel} , u_{\perp} , σ_s and σ_{\perp} (which

together imply continuity of σ_{\parallel}). Each pair $(B^0, \tilde{B}^K), (B^1, \tilde{B}^1), \dots, (B^{K-1}, \tilde{B}^{K-1})$ has the form

$$\begin{aligned}
 B^k &= \begin{pmatrix} \cos \omega_k & \sin \omega_k & 0 & 0 & 0 & 0 \\ -\sin \omega_k & \cos \omega_k & 0 & 0 & 0 & 0 \\ 0 & 0 & 0 & 0 & \mu_{k+1} \sin 2\omega_k & \mu_{k+1} \cos 2\omega_k \\ 0 & 0 & \mu_{k+1} & 0 & \mu_{k+1} \cos 2\omega_k & -\mu_{k+1} \sin 2\omega_k \end{pmatrix} \\
 -\tilde{B}^k &= \begin{pmatrix} \cos \omega_k & \sin \omega_k & 0 & 0 & 0 & 0 \\ -\sin \omega_k & \cos \omega_k & 0 & 0 & 0 & 0 \\ 0 & 0 & 0 & 0 & \mu_k \sin 2\omega_k & \mu_k \cos 2\omega_k \\ 0 & 0 & \mu_k & 0 & \mu_k \cos 2\omega_k & -\mu_k \sin 2\omega_k \end{pmatrix}
 \end{aligned} \tag{4.18}$$

with $g^k = (0, 0, 0, 0)^T$ and $(q_i^k) = (0, 0, 1, 1)$. Here ω_0 is used in B^0 and ω_K is used in \tilde{B}^K to impose the welding conditions along $(\theta = \omega_0)$.

4.3 Mellin Transform

A useful theoretical tool for solving elliptic PDE on sectors in the plane is the Mellin transform [76]. Let $\lambda = c + is$. The Mellin transform of a function $f : \mathbb{R}_{\geq 0} \rightarrow \mathbb{C}$ such that $r^{-c-1}f(r) \in L^1(0, \infty)$ is given by

$$\tilde{f}(\lambda) = \int_0^\infty f(r)r^{-\lambda-1} dr. \tag{4.19}$$

With the substitution $r = e^y$, $dr = r dy$, we see that the Mellin transform is just the Fourier transform in disguise:

$$\tilde{f}(c + is) = \int_{-\infty}^\infty (f(e^y)e^{-cy}) e^{-isy} dy. \tag{4.20}$$

If $[f(e^y)e^{-cy} \in L^2(-\infty, \infty)]$, we may use the Fourier inversion formula to conclude

$$f(e^y)e^{-cy} = \frac{1}{2\pi} \int_{-\infty}^\infty \tilde{f}(c + is)e^{isy} ds. \tag{4.21}$$

This implies the Mellin inversion formula

$$f(e^y) = \frac{1}{2\pi} \int_{-\infty}^\infty \tilde{f}(c + is)e^{(c+is)y} ds, \tag{4.22}$$

which is more commonly expressed as a contour integral:

$$f(r) = \frac{1}{2\pi i} \int_{c-i\infty}^{c+i\infty} \tilde{f}(\lambda)r^\lambda d\lambda. \tag{4.23}$$

Note that if f is identically zero for large r and if there is a $c \in \mathbb{R}$ such that

$$r^{-c-1/2}f(r) \in L^2(0, \infty), \quad (4.24)$$

then changing variables we have

$$f(e^y)e^{-c} \in L^2(-\infty, \infty), \quad (4.25)$$

which together with (4.20) and the Paley–Wiener theorem [65] implies that $\tilde{f}(z)$ is analytic for $(\operatorname{Re} z < c)$ and its restriction to vertical lines form a bounded set in $L^2(-\infty, \infty)$. Integration by parts shows that if $f \rightarrow 0$ fast enough at 0 and ∞ , then

$$\widetilde{r\partial_r f}(\lambda) = \int_0^\infty (\partial_r f)r^{-\lambda} dr = fr^{-\lambda}\Big|_0^\infty + \int_0^\infty \lambda fr^{-\lambda-1} dr = \lambda\tilde{f}(\lambda). \quad (4.26)$$

If we have a function $f(r, \theta)$ defined in polar coordinates on a sector of the plane, we define its partial Mellin transform $\tilde{f}(\lambda, \theta)$ by taking the transform with respect to r treating θ as fixed. If we have a scalar differential operator $\mathcal{A}(\theta, \partial_\theta, r\partial_r)$, then by (4.26) the transform of $g(r, \theta) = \mathcal{A}(\theta, \partial_\theta, r\partial_r)f(r, \theta)$ is given by

$$\tilde{g}(\lambda, \theta) = \mathcal{A}(\theta, \partial_\theta, \lambda)\tilde{f}(\lambda, \theta). \quad (4.27)$$

Given an operator $M(\partial_x, \partial_y)$ which is homogeneous of multi-degree s_i and t_j , then substituting

$$\begin{aligned} \partial_x &= r^{-1}(\cos \theta r\partial_r - \sin \theta \partial_\theta) \\ \partial_y &= r^{-1}(\sin \theta r\partial_r + \cos \theta \partial_\theta) \end{aligned} \quad (4.28)$$

into

$$\operatorname{diag}(r^{s_i})M(\partial_x, \partial_y)\operatorname{diag}(r^{t_j}) \quad (4.29)$$

and using the general observation that

$$r\partial_r(r^\alpha f(r)) = r^\alpha (\alpha f(r) + r\partial_r f(r)), \quad (4.30)$$

we may move all occurrences of $r\partial_r$ to the right of lone powers of r in each term $C_{kl}\partial_x^k\partial_y^l r^{t_j}$ of $r^{s_i}M_{ij}(\partial_x, \partial_y)r^{t_j}$ to get a sum of terms of the form $r^{s_i}r^{-(k+l)}r^{t_j}\mathcal{A}_{kl}(\theta, \partial_\theta, r\partial_r)$. Because $M_{ij}(a, b)$ is a homogeneous polynomial in a and b of degree $s_i + t_j$, the powers of r cancel and we have

$$\operatorname{diag}(r^{s_i})M(\partial_x, \partial_y)\operatorname{diag}(r^{t_j}) = \mathcal{M}(\theta, \partial_\theta, r\partial_r). \quad (4.31)$$

For the interface problem, then, we may use the Mellin transform to convert the system of equations

$$M^k(\partial_x, \partial_y)w^k = f^k, \quad (4.32)$$

$$Bw = g \quad (4.33)$$

into a one parameter family of ODE's on a collection of intervals $\{(\omega_{k-1}, \omega_k)\}_{k=1}^K$ with boundary conditions which couple the variables of adjacent intervals:

$$\mathcal{M}^k(\theta, \partial_\theta, \lambda)\tilde{W}^k(\lambda, \theta) = \tilde{F}^k(\lambda, \theta), \quad (4.34)$$

$$\mathcal{B}\tilde{W} = \tilde{G}. \quad (4.35)$$

The meaning of (4.35) is that

$$\begin{aligned} \left[\mathcal{B}_i^0(\theta, \partial_\theta, \lambda)\tilde{W}^1(\lambda, \theta) \right]_{\theta=\omega_0} &= \tilde{G}_i^0(\lambda) & (i = 1, \dots, m), \\ \left[\mathcal{B}_i^k(\theta, \partial_\theta, \lambda)\tilde{W}^{k+1}(\lambda, \theta) + \tilde{\mathcal{B}}_i^k(\theta, \partial_\theta, \lambda)\tilde{W}^k(\lambda, \theta) \right]_{\theta=\omega_k} &= \tilde{G}_i^k(\lambda) & (i = 1, \dots, 2m), \\ \left[\tilde{\mathcal{B}}_i^K(\theta, \partial_\theta, \lambda)\tilde{W}^K(\lambda, \theta) \right]_{\theta=\omega_K} &= \tilde{G}_i^K(\lambda) & (i = 1, \dots, m), \end{aligned}$$

with obvious modifications based on (4.8) when $\omega_K = \omega_0 + 2\pi$. To do this we multiply the i th row of (4.32) by r^{s_i} and the i th row of the boundary conditions for the k th ray in (4.33) by $r^{q_i^k}$. We define $W_j^k(r, \theta) = r^{-t_j}w_j^k(r, \theta)$, $F_i^k(r, \theta) = r^{s_i}f_i^k(r, \theta)$, and $G_i^k(r) = r^{q_i^k}g_i^k(r)$. We then take the Mellin transform of the equations and boundary conditions using (4.31) to get (4.34) and (4.35). Once \tilde{W}^k is solved as a function of θ for each λ along a vertical line $\lambda = c + is$, the inverse Mellin transform (4.23) can be used to determine $W^k(r, \theta)$, from which we get the solution to the original problem $w_j^k(r, \theta) = r^{t_j}W_j^k(r, \theta)$.

4.4 Homogeneous Solutions

In this section we drop the superscript k indexing the different regions of the domain. Suppose that each $W_j(r, \theta) = r^{-t_j}w_j(r, \theta)$ behaves well enough at the origin that there is a constant c_1 such that for each fixed θ

$$r^{-c_1-1/2}W_j(r, \theta) \in L^2(0, \infty). \quad (4.36)$$

Recall that w is assumed identically zero for large r due to the cutoff function that was used to convert the problem to the sector geometry. Then as in (4.25), we conclude that

$\tilde{W}(\lambda, \theta)$ is analytic in λ for each fixed θ on $(\operatorname{Re} \lambda < c_1)$, and its restriction to vertical lines form a bounded set in $L^2(-\infty, \infty)$. When we use the inverse Mellin transform on \tilde{W} along a vertical line $(\operatorname{Re} \lambda = c)$ in the complex plane with $(c < c_1)$, we get W back. It frequently happens that \tilde{F} and \tilde{G} are analytic on a larger region $(\operatorname{Re} \lambda < c_2)$, where $(c_1 < c_2)$. In this case, the boundary value problem (4.34), (4.35) has a unique solution for each λ satisfying $(\operatorname{Re} \lambda < c_2)$ except at a finite number of isolated points $\lambda_\nu \in S$ with real part between c_1 and c_2 . Near each such $\lambda_\nu \in S$, \tilde{W} has the form

$$\tilde{W}(\lambda, \theta) = \sum_{p=1}^d \sum_{q=0}^{m_p-1} c^{(\nu,p,q)} (\lambda - \lambda_\nu)^{-q-1} \psi^{(\nu,p,q)}(\lambda, \theta) + V(\lambda, \theta), \quad (4.37)$$

$$\psi^{(\nu,p,q)}(\lambda, \theta) = \phi^{(\nu,p,0)}(\theta) + (\lambda - \lambda_\nu) \phi^{(\nu,p,1)}(\theta) + \dots + (\lambda - \lambda_\nu)^q \phi^{(\nu,p,q)}(\theta). \quad (4.38)$$

Here V is analytic at λ_ν and the $\phi^{(\nu,p,s)}(\theta)$ are the characteristic and associated functions [59] at λ_ν of the generalized eigenvalue problem $\mathcal{M}(\theta, \partial_\theta, \lambda)w = 0$, $\mathcal{B}w = 0$. Thus we have found a meromorphic continuation of \tilde{W} on $(\operatorname{Re} \lambda < c_2)$ which agrees with the Mellin transform of W on $(\operatorname{Re} \lambda < c_1)$. If we apply the inverse Mellin transform along a vertical line $\operatorname{Re} \lambda = c$ with $(c_1 < c < c_2)$, we will obtain a function $W_c(r, \theta)$ which is not necessarily equal to W . W_c can be shown [45, 54, 63, 36] to have more regularity at the origin than W , and $(W_c - W)$ is obtained from Equations (4.23) and (4.37) as a contour integral around a curve γ enclosing the λ_ν :

$$W_c(r, \theta) - W(r, \theta) = \sum_{p=1}^d \sum_{q=0}^{m_p-1} c^{(\nu,p,q)} \left[\frac{1}{2\pi i} \int_\gamma (\lambda - \lambda_\nu)^{-q-1} \psi^{(\nu,p,q)}(\lambda, \theta) r^\lambda d\lambda \right]. \quad (4.39)$$

Applying the residue theorem to the term in brackets and noting that

$$\operatorname{Res}_{\lambda_\nu} [(\lambda - \lambda_\nu)^{-s-1} r^\lambda] = \frac{1}{s!} (\ln r)^s r^{\lambda_\nu}, \quad (4.40)$$

we find that

$$\frac{1}{2\pi i} \int_\gamma \dots d\lambda = r^{\lambda_\nu} \left[\frac{1}{q!} (\ln r)^q \phi^{(\nu,p,0)}(\theta) + \dots + \frac{1}{0!} (\ln r)^0 \phi^{(\nu,p,q)}(\theta) \right]. \quad (4.41)$$

In summary, this means that when f and g approach zero fast enough at the origin, the solution w to (4.32) and (4.33) can be decomposed into a regular part $(\operatorname{diag}(r^{t_j})W_c$ above), and a singular part which is a sum of solutions to the homogeneous problem

$$M(\partial_x, \partial_y)w = 0, \quad Bw = 0 \quad (4.42)$$

of the form

$$w_j(r, \theta) = r^{\lambda+t_j} \left[\frac{1}{q!} (\ln r)^q \phi_j^0(\theta) + \cdots + \frac{1}{0!} (\ln r)^0 \phi_j^q(\theta) \right]. \quad (4.43)$$

In this expression, $\phi^0(\theta)$ satisfies

$$\mathcal{M}(\theta, \partial_\theta, \lambda)\phi = 0, \quad \mathcal{B}\phi = 0 \quad (4.44)$$

and ϕ^0, \dots, ϕ^q form a Keldysh chain of characteristic and associated functions (defined in Section 4.8) for (4.44). If the maximum length of this chain at λ_ν is m , then there will be m different singular functions obtained from (4.43) by taking $(q = 0, \dots, m-1)$.

The problem of finding the λ_ν for which solutions of the form (4.43) exist is equivalent to finding nontrivial solutions to (4.44), which is in turn equivalent to finding nontrivial solutions to

$$Mw = 0, \quad Bw = 0 \quad (4.45)$$

of the form

$$w_j(r, \theta) = r^{\lambda+t_j} \phi_j(\theta). \quad (4.46)$$

See Figure 4.3. Once the λ_ν are found, we can look for any associated functions $\phi^{(\nu,p,s)}$ that exist in addition to the eigenfunction $\phi^{(\nu,p,0)}$. (The index p accounts for the possibility that several linearly independent eigenfunctions exist with the same eigenvalue).

4.5 A Basis for $\mathcal{W}(\lambda)$

In this section we present a new constructive technique for finding an analytic basis for the space $\mathcal{W}(\lambda)$ (defined below) which is linearly independent for all λ . The method is illustrated for the case of elasticity, but applies equally well to fixing the degeneracies in the basis functions obtained using the construction in [21] for a general ADN-elliptic system which is homogeneous of multi-degree.

The first thing we need in order to find nontrivial solutions of the homogeneous boundary value problem is a basis for the space $\mathcal{W}(\lambda)$ without boundary conditions:

$$\mathcal{W}(\lambda) = \{w \in C^\infty(\Omega)^N : w_j = r^{\lambda+t_j} \phi_j(\theta), Mw = 0\}. \quad (4.47)$$

Here we let Ω refer to one of the Ω_k and let M denote M^k . One can prove [21] that the dimension of $\mathcal{W}(\lambda)$ is $2m$. Making use of (4.31), we see that any solution $w \in \mathcal{W}(\lambda)$ has

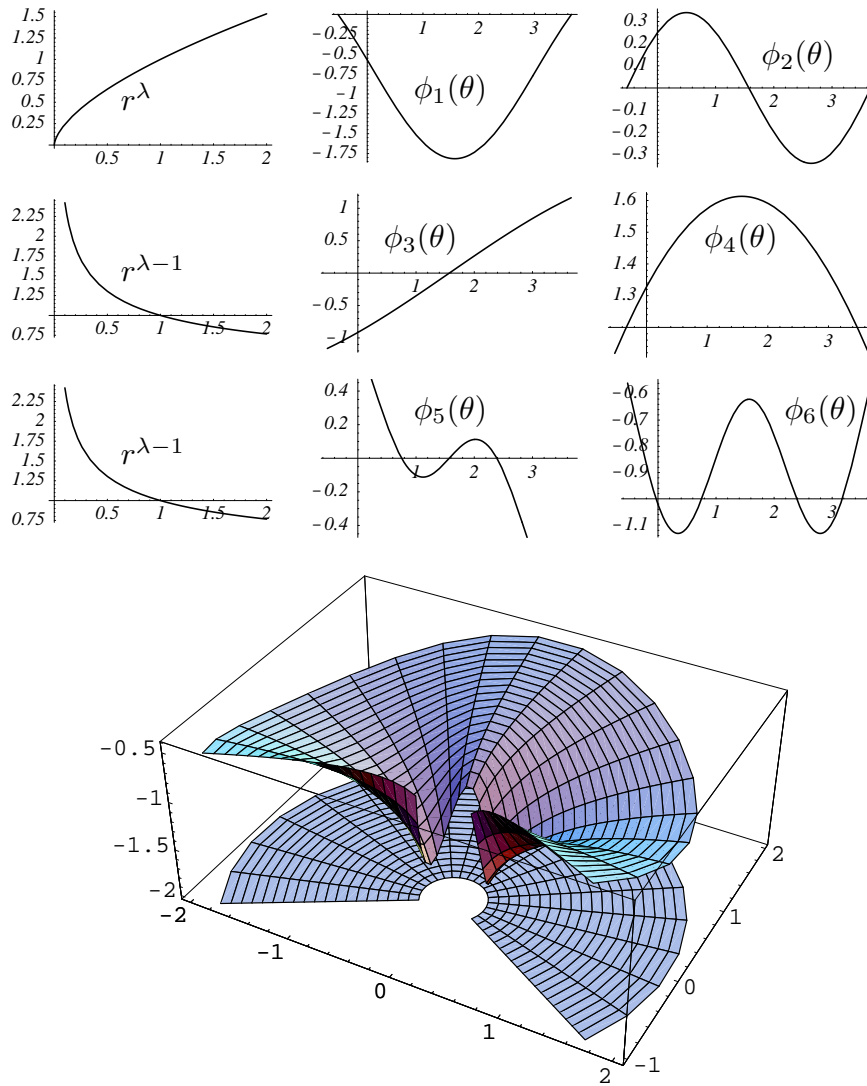


Figure 4.3: *Top:* Radial and angular dependence of the six components u, v, p, q, γ, τ of a nontrivial solution of the form $w_j(r, \theta) = r^{\lambda+t_j}\phi_j(\theta)$ ($\lambda = 0.6157$) to the incompressible Lamé equations with Dirichlet boundary conditions on each ray of the region ($-\pi/6 < \theta < 7\pi/6$). *Bottom:* A 3D plot of the variable τ .

the form $w_j = r^{\lambda+t_j}\phi_j(\theta)$ with $\phi \in \widetilde{\mathcal{W}}(\lambda)$:

$$\widetilde{\mathcal{W}}(\lambda) = \{\phi \in C^\infty(\omega_{k-1}, \omega_k)^N : \mathcal{M}(\theta, \partial_\theta, \lambda)\phi(\theta) = 0\}. \quad (4.48)$$

We wish to find an $N \times 2m$ matrix $\tilde{F}(\lambda, \theta)$ such that the columns of \tilde{F} span $\widetilde{\mathcal{W}}(\lambda)$ and the columns of $F(\lambda, r, \theta) = \text{diag}(r^{\lambda+t_j})\tilde{F}(\lambda, \theta)$ span $\mathcal{W}(\lambda)$.

Example 13. (Diffusion problem). Making use of the identities

$$\begin{aligned} \partial_x &= \cos \theta \partial_r - \sin \theta r^{-1} \partial_\theta, \\ \partial_y &= \sin \theta \partial_r + \cos \theta r^{-1} \partial_\theta, \end{aligned} \quad (4.49)$$

it is readily verified that $M(\partial_x, \partial_y)F(\lambda, r, \theta) = 0$, where

$$F(\lambda, r, \theta) = \begin{pmatrix} r^\lambda & & \\ & r^{\lambda-1} & \\ & & r^{\lambda-1} \end{pmatrix} \begin{pmatrix} \cos \lambda \theta & \theta \text{sinc } \lambda \theta \\ -\alpha \lambda \cos(\lambda-1)\theta & -\alpha \sin(\lambda-1)\theta \\ \alpha \lambda \sin(\lambda-1)\theta & -\alpha \cos(\lambda-1)\theta \end{pmatrix}, \quad (4.50)$$

$$M(\partial_x, \partial_y) = \begin{pmatrix} 0 & \partial_x & \partial_y \\ \partial_x & \alpha^{-1} & 0 \\ \partial_y & 0 & \alpha^{-1} \end{pmatrix}, \quad \text{sinc } z = \frac{\sin z}{z}. \quad (4.51)$$

Note that we have scaled the last column of $\tilde{F}(\lambda, \theta)$ so that the columns remains linearly independent when $\lambda \rightarrow 0$.

Example 14. (Elasticity). We need to find four linearly independent power solutions since $\dim \mathcal{W}(\lambda) = 2m = 4$. Recall from Section 3.1 that for analytic ϕ and ψ , if $w = (u, v, p, q, \gamma, \tau)^T$ is determined by

$$p + iq = 2\phi', \quad (4.52)$$

$$\gamma + i\tau = \bar{z}\phi'' + \psi', \quad (4.53)$$

$$u + iv = \frac{1}{2} [\kappa\phi - z\bar{\phi}' - \bar{\psi}], \quad (4.54)$$

then $M(\partial_x, \partial_y)w = 0$, with M as in (4.13). Since we want solutions of the form $r^{\lambda+t_j}\phi_j(\lambda, \theta)$, with $(t_j) = (0, 0, -1, -1, -1, -1)$, we try powers z^λ for ϕ and ψ :

$$\text{column 1: } \phi = 0, \quad \psi = 2z^\lambda, \quad (4.55)$$

$$\text{column 2: } \phi = 0, \quad \psi = 2iz^\lambda, \quad (4.56)$$

$$\text{column 3: } \phi = 2z^\lambda, \quad \psi = 0, \quad (4.57)$$

$$\text{column 4: } \phi = 2iz^\lambda, \quad \psi = 0. \quad (4.58)$$

This leads to the matrix $\tilde{F}(\lambda, \theta)$ given by

$$\begin{pmatrix} -\cos \lambda\theta & \sin \lambda\theta & \kappa \cos \lambda\theta - \lambda \cos(\lambda - 2)\theta & -\kappa \sin \lambda\theta + \lambda \sin(\lambda - 2)\theta \\ \sin \lambda\theta & \cos \lambda\theta & \kappa \sin \lambda\theta + \lambda \sin(\lambda - 2)\theta & \kappa \cos \lambda\theta + \lambda \cos(\lambda - 2)\theta \\ 0 & 0 & 4\lambda \cos(\lambda - 1)\theta & -4\lambda \sin(\lambda - 1)\theta \\ 0 & 0 & 4\lambda \sin(\lambda - 1)\theta & 4\lambda \cos(\lambda - 1)\theta \\ 2\lambda \cos(\lambda - 1)\theta & -2\lambda \sin(\lambda - 1)\theta & 2\lambda(\lambda - 1) \cos(\lambda - 3)\theta & -2\lambda(\lambda - 1) \sin(\lambda - 3)\theta \\ 2\lambda \sin(\lambda - 1)\theta & 2\lambda \cos(\lambda - 1)\theta & 2\lambda(\lambda - 1) \sin(\lambda - 3)\theta & 2\lambda(\lambda - 1) \cos(\lambda - 3)\theta \end{pmatrix}. \quad (4.59)$$

Unfortunately, the columns of \tilde{F} become linearly dependent at $\lambda = 0$. To remedy this defect, we use the following (new) procedure:

Algorithm 15. (Change of basis to obtain linear independence at $\lambda = 0$)

- Compute $\tilde{F}_0(\theta) = \tilde{F}(0, \theta)$.
- Let $k = \dim \ker \tilde{F}_0$, where \tilde{F}_0 is treated as a linear mapping from $\mathbb{C}^{2m} \rightarrow C^\infty(\mathbb{R})$.
- Find a basis $\{w_i\}_1^{2m}$ for \mathbb{C}^{2m} such that $\text{span}\{w_1, \dots, w_k\} = \ker \tilde{F}_0$.
- Replace $\tilde{F}(\lambda, \theta)$ by

$$\tilde{F}(\lambda, \theta) \left(\frac{w_1}{\lambda}, \dots, \frac{w_k}{\lambda}, w_{k+1}, \dots, w_{2m} \right). \quad (4.60)$$

- Repeat if the columns of $\tilde{F}(0, \theta)$ are not linearly independent.

This procedure is guaranteed to terminate because for any fixed $\theta_0 \neq 0$, the analytic family of $N \times 2m$ matrices $\tilde{F}(\lambda, \theta_0)$ has full rank except at $\lambda = 0$, so choosing any $\lambda_0 \neq 0$ and multiplying by any $2m \times N$ constant matrix C such that $C\tilde{F}(\lambda_0, \theta_0)$ is invertible, we find that $\det C\tilde{F}(\lambda, \theta_0)$ is an analytic function which is not identically zero. At $\lambda = 0$, it has a root of order p , say, and each time through the loop the order p decreases by the dimension of the nullspace of $\tilde{F}(0, \theta)$. If $\det C\tilde{F}(0, \theta_0) \neq 0$, then the columns of \tilde{F} must be linearly independent. Thus the procedure is guaranteed to terminate in no more than p steps.

In the current case, we have

$$\tilde{F}_0(\theta) = \begin{pmatrix} -1 & 0 & \kappa & 0 \\ 0 & 1 & 0 & \kappa \\ 0 & 0 & 0 & 0 \\ 0 & 0 & 0 & 0 \\ 0 & 0 & 0 & 0 \\ 0 & 0 & 0 & 0 \end{pmatrix}, \quad (4.61)$$

so we use $w_1 = (\kappa, 0, 1, 0)^T$, $w_2 = (0, -\kappa, 0, 1)^T$, $w_3 = (1, 0, 0, 0)^T$, and $w_4 = (0, 1, 0, 0)^T$. Replacing \tilde{F} by $\tilde{F} \cdot (w_3, w_4, \frac{w_1}{\lambda}, \frac{w_2}{\lambda})$ is equivalent to using the Muskhelishvili functions

$$\text{column 1: } \phi = 0, \quad \psi = 2z^\lambda, \quad (4.62)$$

$$\text{column 2: } \phi = 0, \quad \psi = 2iz^\lambda, \quad (4.63)$$

$$\text{column 3: } \phi = 2\lambda^{-1}z^\lambda, \quad \psi = 2\kappa\lambda^{-1}z^\lambda, \quad (4.64)$$

$$\text{column 4: } \phi = 2i\lambda^{-1}z^\lambda, \quad \psi = -2i\kappa\lambda^{-1}z^\lambda, \quad (4.65)$$

and we obtain the following matrix $\tilde{F}(\lambda, \theta)$ with linearly independent columns for all λ :

$$\begin{pmatrix} -\cos \lambda\theta & \sin \lambda\theta & -\cos(\lambda-2)\theta & -2\kappa\theta \operatorname{sinc} \lambda\theta + \sin(\lambda-2)\theta \\ \sin \lambda\theta & \cos \lambda\theta & 2\kappa\theta \operatorname{sinc} \lambda\theta + \sin(\lambda-2)\theta & \cos(\lambda-2)\theta \\ 0 & 0 & 4\cos(\lambda-1)\theta & -4\sin(\lambda-1)\theta \\ 0 & 0 & 4\sin(\lambda-1)\theta & 4\cos(\lambda-1)\theta \\ 2\lambda\cos(\lambda-1)\theta & -2\lambda\sin(\lambda-1)\theta & 2(\lambda-1)\cos(\lambda-3)\theta + 2\kappa\cos(\lambda-1)\theta & -2(\lambda-1)\sin(\lambda-3)\theta + 2\kappa\sin(\lambda-1)\theta \\ 2\lambda\sin(\lambda-1)\theta & 2\lambda\cos(\lambda-1)\theta & 2(\lambda-1)\sin(\lambda-3)\theta + 2\kappa\sin(\lambda-1)\theta & 2(\lambda-1)\cos(\lambda-3)\theta - 2\kappa\cos(\lambda-1)\theta \end{pmatrix}. \quad (4.66)$$

In the literature, some variant of the version of \tilde{F} presented in Eqn. (4.59) is always used, with the case $\lambda = 0$ treated as a special case; see [36, 35, 67, 23]. To our knowledge, no one has ever done anything to fix the problem at $\lambda = 0$ in order to obtain a single analytic matrix such as (4.66) whose columns span $\tilde{\mathcal{W}}(\lambda)$ for all λ .

4.6 The Boundary Condition Matrix $A(\lambda)$

When the material parameters change from one region to the next, we denote by $\mathcal{W}^k(\lambda)$ the space of all solutions to $M^k w = 0$ of the form

$$w_j(r, \theta) = r^{\lambda+t_j} \phi_j(\theta). \quad (4.67)$$

$\mathcal{W}^k(\lambda)$ is spanned by the columns of $F^k(\lambda, r, \theta) = \operatorname{diag}(r^{\lambda+t_j})\tilde{F}^k(\lambda, \theta)$ obtained in the examples of the previous section by replacing α by α_k in (4.50) and κ by κ_k in (4.66). The

power solutions of the interface problem $M^k w^k = 0$ correspond precisely to the functions

$$w^k(r, \theta) = F^k(\lambda, r, \theta) \cdot c^k \quad (4.68)$$

with $c^k \in \mathbb{C}^{2m}$. Thus a nontrivial solution to $M^k w^k = 0$, $Bw = 0$ exists if and only if there exist vectors c^k not all zero such that

$$\left[\mathcal{B}_i^0(\theta, \partial_\theta, \lambda) \tilde{F}^1(\lambda, \theta) c^1 \right]_{\theta=\omega_0} = 0 \quad (i = 1, \dots, m) \quad (4.69)$$

$$\left[\mathcal{B}_i^k(\theta, \partial_\theta, \lambda) \tilde{F}^{k+1}(\lambda, \theta) c^{k+1} + \tilde{\mathcal{B}}_i^k(\theta, \partial_\theta, \lambda) \tilde{F}^k(\lambda, \theta) c^k \right]_{\theta=\omega_k} = 0 \quad (i = 1, \dots, 2m) \quad (4.70)$$

$$\left[\tilde{\mathcal{B}}_i^K(\theta, \partial_\theta, \lambda) \tilde{F}^K(\lambda, \theta) c^K \right]_{\theta=\omega_K} = 0 \quad (i = 1, \dots, m). \quad (4.71)$$

We may organize this system of equations into a $2mK \times 2mK$ matrix equation $A(\lambda)C = 0$ by defining the vector $C = (c^1, \dots, c^K)^T$ of length $2mK$ and, for example with $K = 3$, defining the matrix

$$A(\lambda) = \begin{pmatrix} \mathcal{B}^0 \tilde{F}^1 & 0 & 0 \\ \tilde{\mathcal{B}}^1 \tilde{F}^1 & \mathcal{B}^1 \tilde{F}^2 & 0 \\ 0 & \tilde{\mathcal{B}}^2 \tilde{F}^2 & \mathcal{B}^2 \tilde{F}^3 \\ 0 & 0 & \tilde{\mathcal{B}}^3 \tilde{F}^3 \end{pmatrix} \begin{array}{l} \leftarrow m \text{ equations, } \theta = \omega_0, \\ \leftarrow 2m \text{ equations, } \theta = \omega_1, \\ \leftarrow 2m \text{ equations, } \theta = \omega_2, \\ \leftarrow m \text{ equations, } \theta = \omega_3. \end{array} \quad (4.72)$$

When $\omega_K = \omega_0 + 2\pi$ and $K = 3$, $A(\lambda)$ takes the form

$$A(\lambda) = \begin{pmatrix} \mathcal{B}^0 \tilde{F}^1|_{\theta=\omega_0} & 0 & \tilde{\mathcal{B}}^3 \tilde{F}^3|_{\theta=\omega_3} \\ \tilde{\mathcal{B}}^1 \tilde{F}^1|_{\theta=\omega_1} & \mathcal{B}^1 \tilde{F}^2|_{\theta=\omega_1} & 0 \\ 0 & \tilde{\mathcal{B}}^2 \tilde{F}^2|_{\theta=\omega_2} & \mathcal{B}^2 \tilde{F}^3|_{\theta=\omega_2} \end{pmatrix} \begin{array}{l} \leftarrow 2m \text{ equations,} \\ \leftarrow 2m \text{ equations,} \\ \leftarrow 2m \text{ equations.} \end{array} \quad (4.73)$$

Note that if $q_i^k + t_j = 0$ whenever $B_{ij}^k \neq 0$, (i.e. $B(a, b)$ is a constant matrix independent of a and b), then $\mathcal{B}_{ij}^k = B_{ij}^k$. Because we have reduced to the case of first order ADN systems, all boundary conditions of interest to us have this property.

A nontrivial solution to $A(\lambda)C = 0$ exists when $\lambda = \lambda_0$ if and only if the characteristic determinant

$$\Delta(\lambda) = \det A(\lambda) \quad (4.74)$$

has a zero at λ_0 . Since all entries of $A(\lambda)$ are holomorphic in λ , $\Delta(\lambda)$ is an entire function which is not identically zero since the boundary conditions satisfy the covering condition discussed in Sec. 3.1.

Example 16. (Diffusion equation with discontinuous coefficients, $K = 2$) Using (4.12) and (4.50) in (4.72) we get

$$A(\lambda) = \begin{pmatrix} \cos \lambda \omega_0 & \omega_0 \operatorname{sinc} \lambda \omega_0 & 0 & 0 \\ -\cos \lambda \omega_1 & -\omega_1 \operatorname{sinc} \lambda \omega_1 & \cos \lambda \omega_1 & \omega_1 \operatorname{sinc} \lambda \omega_1 \\ -\alpha_1 \omega_1 \operatorname{sinc} \lambda \omega_1 & \alpha_1 \cos \lambda \omega_1 & \alpha_2 \omega_1 \operatorname{sinc} \lambda \omega_1 & -\alpha_2 \cos \lambda \omega_1 \\ 0 & 0 & \cos \lambda \omega_2 & \omega_2 \operatorname{sinc} \lambda \omega_2 \end{pmatrix}, \quad (4.75)$$

$$\begin{aligned} \Delta(\lambda) = & -\frac{1}{2}(\alpha_1 + \alpha_2)(\omega_2 - \omega_0) \operatorname{sinc} \lambda(\omega_2 - \omega_0) + \\ & + \frac{1}{2}(\alpha_2 - \alpha_1)(\omega_2 - 2\omega_1 + \omega_0) \operatorname{sinc} \lambda(\omega_2 - 2\omega_1 + \omega_0). \end{aligned} \quad (4.76)$$

Example 17. (Elasticity on a wedge with various boundary conditions). For wall–wall, wall–traction, and traction–traction boundary conditions the matrix $A(\lambda)$ can be computed symbolically using (4.66), (4.72) and the appropriately modified version of (4.15). Since we assemble the $A(\lambda)$ in parts using these equations in practice, it is not particularly useful to record them here. The determinant of the resulting 4×4 matrices can be simplified to obtain:

$$\text{wall–wall: } \Delta(\lambda) = 4(\sin^2 \omega - \kappa^2 \omega^2 \operatorname{sinc}^2 \lambda \omega), \quad (4.77)$$

$$\text{wall–traction: } \Delta(\lambda) = -4\mu^2((1 + \kappa)^2 - 4\lambda^2 \sin^2 \omega - 4\kappa \sin^2 \lambda \omega), \quad (4.78)$$

$$\text{traction–traction: } \Delta(\lambda) = 64\mu^4 \lambda^2 (\sin^2 \lambda \omega - \lambda^2 \sin^2 \omega), \quad (4.79)$$

where $\omega = \omega_1 - \omega_0$. Note that $\lambda = 0$ is a zero of $\Delta(\lambda)$ in the traction–traction case. The corresponding power solutions correspond to rigid translations.

4.7 Computing the Roots of $\Delta(\lambda)$

In this section we describe a numerical method for computing the roots of $\Delta(\lambda)$ and finding the corresponding eigenfunctions ϕ . The method is based heavily on the method described in [23], with improvements made in its ability to handle multiple roots, find Keldysh chains, and to stabilize the resulting basis of singular functions. We also describe how to organize the algorithm to be well suited for use by a scripting language which calls the routine multiple times with different geometries and boundary condition types.

For the 4×4 matrices above, the complexity of computing the determinants and simplifying the resulting expressions symbolically is low enough that it can be done in a

second or two on a desktop computer. For the 8×8 case of a wall–gb–wall junction, it takes 10–15 minutes to compute the determinant symbolically, but the resulting expression is so complicated that it is completely worthless for finding roots. For the 12×12 case of a triple grain boundary junction, it is obviously futile to try to find the roots in this way.

A common numerical approach for determining the exponents is to solve the eigenvalue problem

$$\mathcal{M}^k(\theta, \partial_\theta, r\partial_r)\phi^k(\theta) = 0, \quad \mathcal{B}\phi = 0 \quad (4.80)$$

numerically using finite elements, for example. For the diffusion problem (left in the form of a second order scalar equation), we have $M^k(\partial_x, \partial_y) = -\alpha_k(\partial_x^2 + \partial_y^2)$, so $\mathcal{M}^k(\theta, \partial_\theta, r\partial_r) = -\alpha_k [(r\partial_r)^2 + \partial_\theta^2]$ and the eigenvalue problem which arises is a Sturm-Liouville problem:

$$[\lambda^2 + \partial_\theta^2] \phi^k(\theta) = 0, \quad \mathcal{B}\phi = 0. \quad (4.81)$$

For the Lamé system, the resulting eigenproblem is much more complicated; see [50, 60, 4] for more details.

As a starting point, we prefer to take the approach of Costabel and Dauge [23] for finding the zeros of $\Delta(\lambda)$, which is to use root finding algorithms for analytic functions using contour integrals. The basic idea is to make use of the identity

$$\sum_{z_k \in S} g(z_k) = \frac{1}{2\pi i} \int_{\partial S} g(z) \frac{f'(z)}{f(z)} dz \quad (4.82)$$

with $f(z) = \Delta(z)$ and appropriately chosen $g(z)$ to determine the roots z_k of f contained in S . If $g(z) = 1$, we obtain the number of roots enclosed. If one root is enclosed and we take $g(z) = z$, we obtain the root. If the contour contains N roots, we take $g(z) = z^n$ with n ranging from 1 to N to obtain the sums $s_n = \sum_{i=1}^N z_i^n$. For example, if $N = 3$, we will obtain the right hand side of the system of equations

$$\begin{aligned} z_1 + z_2 + z_3 &= s_1 \\ z_1^2 + z_2^2 + z_3^2 &= s_2 \\ z_1^3 + z_2^3 + z_3^3 &= s_3. \end{aligned} \quad (4.83)$$

It is a standard result from algebra [78] that the elementary symmetric functions

$$\sigma_j = \sum_{i_1 < \dots < i_j} z_{i_1} \cdots z_{i_j}, \quad (j = 1, \dots, N) \quad (4.84)$$

of the zeros $\{z_1, \dots, z_N\}$ are polynomials in the power sums. There is a recurrence relation between the s_j and the σ_j [26]:

$$\begin{aligned} \sigma_0 &= 1 \\ (-1)^n n \sigma_n + \sum_{k=0}^{n-1} (-1)^k \sigma_k s_{n-k} &= 0, \quad (n = 1, \dots, N). \end{aligned} \quad (4.85)$$

We define $a_j = (-1)^j \sigma_j$ so that

$$\prod_{j=1}^N (z - z_j) = \sum_{j=0}^N a_j z^{N-j}. \quad (4.86)$$

The recurrence (4.85) can then easily be used to determine the coefficients a_i of the monic polynomial whose roots are the z_i . The solution to (4.83), for example, are the roots of the polynomial with coefficients

$$a_0 = 1, \quad a_1 = -s_1, \quad a_2 = \frac{s_1^2 - s_2}{2}, \quad a_3 = -\frac{s_1^3 - 3s_1s_2 + 2s_3}{6}. \quad (4.87)$$

In [23], Costabel and Dauge use (4.82) with $f(z) = \Delta(z)$, making use of the identity

$$\frac{f'(z)}{f(z)} = \text{tr}(A^{-1}(z)A'(z)) \quad (4.88)$$

in the integrand. They isolate roots using $g(z) = 1$, and then find the roots using $g(z) = z$. They do not deal with the case of multiple (or nearly multiple) roots.

We have instead used Davies' method [26] for locating the zeros of an analytic function, which is obtained from (4.82) using integration by parts:

$$\frac{1}{2\pi i} \int_{\gamma} z^n \frac{f'}{f} dz = -\frac{n}{2\pi i} \int_{\gamma} z^{n-1} \log[f(z)] dz. \quad (\text{incorrect}) \quad (4.89)$$

This formula is incorrect because $\log[f(z)]$ is not single valued on γ . The imaginary part of $\log[f(z)]$ increases by $2\pi N$ as we traverse the contour since there are N zeros of $f(z)$ inside γ . The way to get around this problem is to choose any z^* inside γ , let $Z_k = z_k - z^*$, set $h(z) = (z - z^*)^{-N} f(z)$ (which does have a single valued logarithm on γ), and define s_n for $n \geq 1$ as

$$\begin{aligned} s_n &= \sum_{k=1}^N Z_k^n = \frac{1}{2\pi i} \int_{\gamma} (z - z^*)^n \frac{f'(z)}{f(z)} dz = \frac{1}{2\pi i} \int_{\gamma} (z - z^*)^n \frac{h'(z)}{h(z)} dz = \\ &= -\frac{n}{2\pi i} \int_{\gamma} (z - z^*)^{n-1} \log[h(z)] dz = -\frac{n}{2\pi i} \int_{\gamma} (z - z^*)^{n-1} \log[(z - z^*)^{-N} f(z)] dz. \end{aligned} \quad (4.90)$$

The recurrence (4.85) is then used to get the coefficients a_j , and we solve for the roots of $\prod_{j=1}^N (Z - Z_j) = \sum_{j=0}^N a_j Z^{N-j}$ by finding the eigenvalues Z_j of the matrix

$$\begin{pmatrix} -a_1 & -a_2 & \cdots & -a_{n-1} & -a_n \\ 1 & 0 & \cdots & 0 & 0 \\ 0 & 1 & \cdots & 0 & 0 \\ \cdots & \cdots & \cdots & \cdots & \cdots \\ 0 & 0 & \cdots & 1 & 0 \end{pmatrix} \quad (4.91)$$

using LAPACK. The original roots z_j are obtained using $z_j = Z_j + z^*$. Care must be taken to stay on the same branch of the logarithm as the contour is traversed.

4.7.1 Implementation

In our C++ implementation, we have developed an object-oriented approach for finding the roots. We define a class called *singular* which contains the matrices \tilde{F} and A along with methods for computing their entries for given values of λ , κ , μ and θ , as well as for computing $\det A$. The routine for computing A is a virtual method which is instantiated in subclasses (e.g. *wall_wall*, *wall_traction*, *traction_traction*, *wall_gb_wall*, *gb_gb_gb*, *weld4*, etc.) which contain information specific to the geometry and boundary conditions, such as the angles ω_k and the matrices B_{ij}^k . We have a class called *grid* which contains a pointer to a *singular* and a routine for calling this pointer's *compute_det* function to fill a uniform grid of points with values of $\Delta(\lambda)$; *grid* also contains methods for finding all boxes (4 adjacent points) which contain a crossing of the zero level sets of the real and imaginary parts of $\Delta(\lambda)$, and for clustering them into groups of adjacent boxes. See Figure 4.4.

Each such *cluster* is implemented as a class with methods for constructing a contour which surrounds it at a distance of half a grid cell, for computing 10 point gaussian quadrature weights on each segment of this contour to do the integrations involved in (4.90), and for finding the roots enclosed. For each root, a data file is written and an external call of Mathematica is made to repeat the calculation with higher precision using a circular contour centered at the computed root. In this external call, the trapezoidal quadrature rule is used, which leads to exponential convergence due to the analyticity of $\Delta(\lambda)$ and the fact that it is periodic on a circle. It is permissible for the circle to contain several tightly clustered roots. We have found that the roots computed initially using the line segments around the cluster are accurate to 12-14 digits for isolated roots, but can be significantly

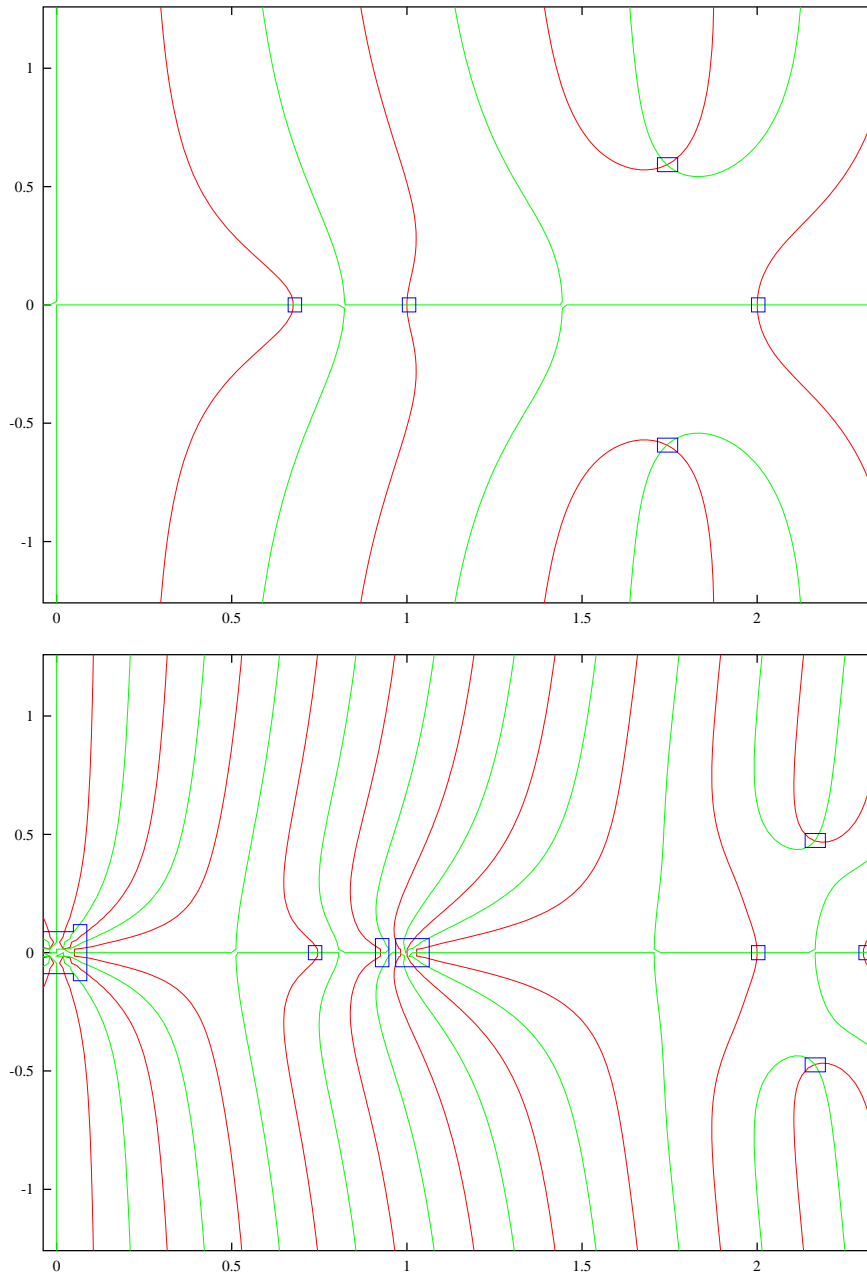


Figure 4.4: Contour plots of the zero level sets of the real and imaginary parts of $\Delta(\lambda)$ along with the contours generated by the clustering algorithm for finding roots. Top: wall-gb-wall geometry with $\omega_0 = 90^\circ$, $\omega_1 = 173^\circ$, $\omega_2 = 270^\circ$. Bottom: triple grain boundary junction with $\omega_0 = -174^\circ$, $\omega_1 = -51^\circ$, $\omega_2 = 45^\circ$, $\omega_3 = 186^\circ$. Note that some clusters contain multiple (or nearly multiple) roots which must be resolved accurately.

less accurate for multiple roots. A six-fold root has only about 3 digits of precision due to the extreme sensitivity of such a root on the coefficients of the polynomial. Calling Mathematica allows us to obtain full 16 digit accuracy for all roots and their corresponding power solutions. The implementation of Costabel and Dauge [23] does not deal with degenerate cases of multiple roots.

In addition to finding each of the roots λ_i of $\Delta(\lambda)$ in the desired region of the complex plane, the program determines the vectors C which span the nullspace of $A(\lambda_i)$. Each such C determines the corresponding vectors c^k in equation (4.68), yielding the desired power solution w of (4.45). If several roots are clustered together, the implementation stabilizes the power solution basis as described in Section 4.9. This new idea has proved to be very powerful in our grain growth computations. The information about the new basis functions is recorded in a file which can be read by the singularity capturing finite element method described in Chapter 5. For each geometry, the code also creates a contour plot image of the zero level set of the real and imaginary parts of $\Delta(\lambda)$ and saves it in a file for later reference (c.f. Fig. 4.4), which is useful in checking that no roots were missed. We have used the method to compute hundreds of singularity exponents and power solutions to obtain the results of Chapter 3. It has therefore been essential to have an automated process for finding the power solutions which can handle multiple types of geometries (wall-wall, wall-gb-wall, gb-gb-gb, wall-traction, etc.), and which can be called from a scripting language like Perl for each instance of a corner or grain boundary junction in the geometry.

4.8 Computing Pure and Associated Power Solutions

In this section we present an algorithm for finding Keldysh chains of associated functions $\phi^{(\nu,p,q)}(\theta)$ at the eigenvalue λ_ν of the generalized eigenproblem

$$\mathcal{M}(\lambda)\phi = 0, \quad \mathcal{B}\phi = 0. \quad (4.92)$$

Such an algorithm was not previously known, so the results of this section are new. The eigenvalue of interest throughout will be λ_ν , so we drop the index ν from the notation. We also suppress the index k designating the sector, understanding that $\phi^{(p,q)}(\theta)$ can have discontinuities at $\theta = \omega_k$ which are controlled by the boundary operator \mathcal{B} . We assume that \mathcal{B} does not depend on λ , which is the case for all physically meaningful boundary conditions due to the fact that we have reduced to a first order system; for example, in our formulation

of elasticity, traction boundary conditions may be expressed directly in terms of p , γ and τ without taking derivatives of u and v at the boundaries.

A good reference for the theory of characteristic and associated functions for boundary value problems in ordinary differential equations is the book by Naimark [59]. Because we have removed the degeneracy of our basis for $\widetilde{\mathcal{W}}(\lambda)$ using Algorithm 15, the columns of \widetilde{F} are analytic and everywhere linearly independent. As a result, we may apply the theory presented in [59] to conclude

Proposition 18. *The eigenvalues of (4.92) are the zeros of the function $\Delta(\lambda)$. If λ_0 is a zero of $\Delta(\lambda)$ of multiplicity m , then the multiplicity d of the eigenvalue λ_0 (the dimension of the eigenspace) cannot be greater than m . There exist d integers m_i such that*

$$m_1 + \cdots + m_d = m \quad (4.93)$$

and m functions

$$\phi^{(p,q)}(\theta), \quad (p = 1, \dots, d), (q = 0, \dots, m_p - 1) \quad (4.94)$$

such that

$$\mathcal{B}\phi^{(p,q)} = 0 \quad (4.95)$$

and

$$\mathcal{M}\phi^{(p,0)} = 0, \quad (4.96)$$

$$\mathcal{M}\phi^{(p,1)} + \frac{1}{1!}\partial_\lambda\mathcal{M}\phi^{(p,0)} = 0, \quad (4.97)$$

...

$$\mathcal{M}\phi^{(p,m_p-1)} + \frac{1}{1!}\partial_\lambda\mathcal{M}\phi^{(p,m_p-2)} + \cdots + \frac{1}{(m_p-1)!}\partial_\lambda^{m_p-1}\mathcal{M}\phi^{(p,0)} = 0, \quad (4.98)$$

where each derivative of \mathcal{M} is evaluated at λ_0 . The eigenspace is spanned by

$$\phi^{(1,0)}(\theta), \dots, \phi^{(d,0)}(\theta), \quad (4.99)$$

and each sequence

$$\phi^{(p,0)}(\theta), \dots, \phi^{(p,m_p-1)}(\theta) \quad (4.100)$$

is known as a Keldysh chain associated with the eigenfunction $\phi^{(p,0)}$.

Remark 19. Equations (4.95)–(4.98) are equivalent to requiring that the function $\psi^{(p,q)}(\lambda, \theta)$ given by

$$\psi^{(p,q)}(\lambda, \theta) = \phi^{(p,0)}(\theta) + (\lambda - \lambda_0)\phi^{(p,1)}(\theta) + \cdots + (\lambda - \lambda_0)^q \phi^{(p,q)}(\theta) \quad (4.101)$$

with ($q = m_p - 1$) satisfies

$$\mathcal{M}(\lambda)\psi^{(p,q)}(\lambda, \theta) = O(\lambda - \lambda_0)^{q+1}, \quad \mathcal{B}\psi^{(p,q)}(\lambda) \equiv 0. \quad (4.102)$$

The main idea to finding the associated functions is the following. With (4.102) as a guide indicating the key property of a Keldysh chain, we try to construct a function y which satisfies the equation exactly and the boundary conditions inexactly, and then read off the terms in the expansion:

$$\mathcal{M}(\lambda)y(\lambda, \theta) = 0, \quad \mathcal{B}y(\lambda) = O(\lambda - \lambda_0)^{m_p}, \quad (4.103)$$

$$y(\lambda, \theta) = \phi^0(\theta) + (\lambda - \lambda_0)\phi^1(\theta) + (\lambda - \lambda_0)^2\phi^2(\theta) + \cdots. \quad (4.104)$$

The general solution to $\mathcal{M}(\lambda)y(\lambda, \theta) = 0$ is

$$y(\lambda, \theta) = \tilde{F}(\lambda, \theta) \cdot a(\lambda). \quad (4.105)$$

We set ($q = m_p - 1$) and look for $a(\lambda)$ of the form

$$a(\lambda) = a_0 + (\lambda - \lambda_0)a_1 + \cdots + (\lambda - \lambda_0)^q a_q. \quad (4.106)$$

We wish to find the constant vectors a_i such that

$$\begin{aligned} \mathcal{B}y(\lambda) &= A(\lambda) \cdot a(\lambda) = \\ &= \left[A(\lambda_0) + (\lambda - \lambda_0)A'(\lambda_0) + \frac{1}{2}(\lambda - \lambda_0)^2 A''(\lambda_0) + \cdots \right] \times \\ &\quad \times [a_0 + (\lambda - \lambda_0)a_1 + (\lambda - \lambda_0)^2 a_2 + \cdots] = O(\lambda - \lambda_0)^{q+1}. \end{aligned} \quad (4.107)$$

Setting the coefficient of $(\lambda - \lambda_0)^s$ to zero for each term ($s = 0, \dots, q$), this is equivalent to requiring that

$$A(\lambda_0) \cdot a_0 = 0, \quad (4.108)$$

$$A(\lambda_0) \cdot a_1 + A'(\lambda_0) \cdot a_0 = 0, \quad (4.109)$$

...

$$A(\lambda_0) \cdot a_q + \cdots + \frac{1}{q!} A^q(\lambda_0) \cdot a_0 = 0. \quad (4.110)$$

We now determine the characteristic and associate functions using (4.104) and (4.105)

$$\phi^0(\theta) = \tilde{F}(\lambda_0, \theta) \cdot a_0 \quad (4.111)$$

$$\phi^1(\theta) = \tilde{F}(\lambda_0, \theta) \cdot a_1 + (\partial_\lambda \tilde{F})(\lambda_0, \theta) \cdot a_0 \quad (4.112)$$

...

$$\phi^q(\theta) = \tilde{F}(\lambda_0, \theta) \cdot a_q + \cdots + \frac{1}{q!} (\partial_\lambda^q \tilde{F})(\lambda_0, \theta) \cdot a_0. \quad (4.113)$$

Theorem 20. *If there exist vectors (a_0, \dots, a_q) satisfying (4.108)–(4.110), then the functions $\phi^1(\theta), \dots, \phi^q(\theta)$ given by (4.111)–(4.113) form a Keldysh chain for (4.92). Conversely, if a Keldysh chain $\phi^1(\theta), \dots, \phi^q(\theta)$ for (4.92) exists, then there are vectors (a_0, \dots, a_q) satisfying (4.111)–(4.113) such that (4.108)–(4.110) holds.*

Proof. Suppose we are given (a_0, \dots, a_q) satisfying (4.108)–(4.110). Define $a(\lambda)$, $y(\lambda, \theta)$ and $\phi^s(\theta)$ as above, and let

$$\psi(\lambda) = \phi^0(\theta) + \cdots + (\lambda - \lambda_0)^q \phi^q(\theta). \quad (4.114)$$

Then by construction, we have

$$\mathcal{B}\psi(\lambda, \theta) \equiv 0, \quad \mathcal{M}(\lambda)y(\lambda, \theta) \equiv 0, \quad y(\lambda, \theta) - \psi(\lambda, \theta) = O(\lambda - \lambda_0)^{q+1}. \quad (4.115)$$

Therefore

$$\mathcal{M}(\lambda)\psi(\lambda, \theta) = \mathcal{M}(\lambda)[\psi(\lambda, \theta) - y(\lambda, \theta)] = O(\lambda - \lambda_0)^{q+1}. \quad (4.116)$$

By Remark 19, this implies that ϕ^0, \dots, ϕ^q is a Keldysh chain.

Conversely, suppose we are given a Keldysh chain ϕ^0, \dots, ϕ^q . Define ψ as in (4.114) and choose an arbitrary θ_k in the interior of each segments (ω_{k-1}, ω_k) . Let $y(\lambda, \theta)$ be defined on each segment as the solution to the *initial* value problem

$$\mathcal{M}(\lambda)y(\lambda, \theta) = 0, \quad y(\lambda, \theta_k) = \psi(\lambda, \theta_k). \quad (4.117)$$

Recall that $\mathcal{M}y = 0$ is a first order system; if it were higher order, derivatives with respect to θ would also be used in the initial conditions. Standard ODE theory ensures that $y(\lambda, \theta)$ depends analytically on λ since \mathcal{M} and ψ are analytic in λ [20]. Taylor expanding

$$[\mathcal{M} + (\lambda - \lambda_0)\partial_\lambda \mathcal{M} + \cdots][y + (\lambda - \lambda_0)\partial_\lambda y + \cdots] = 0 \quad (4.118)$$

and setting the coefficient of each $(\lambda - \lambda_0)^s$ to zero, we conclude that on segment k , the functions

$$\frac{1}{s!} \frac{\partial^s y}{\partial \lambda^s}(\lambda_0, \theta), \quad \phi^s(\theta), \quad (s = 0, \dots, q) \quad (4.119)$$

satisfy the same ODE due to Equations (4.96)–(4.98). Differentiating (4.117) with respect to λ , we see that they also satisfy the same initial condition at θ_k . Therefore they are equal, which means $\psi(\lambda, \theta)$ is equal to the sum of the first $q + 1$ terms in the Taylor expansion of $y(\lambda, \theta)$. Since the columns of $\tilde{F}(\lambda, \theta)$ are a basis for the solution to $\mathcal{M}(\lambda)\phi(\theta) = 0$ and $y(\lambda, \theta)$ is analytic in λ and satisfies this equation for all λ , there is an analytic vector function $a(\lambda)$ such that

$$y(\lambda, \theta) = \tilde{F}(\lambda, \theta) \cdot a(\lambda). \quad (4.120)$$

Taylor expanding and recalling that the first $q + 1$ terms in the expansion for $y(\lambda, \theta)$ are the ϕ^s , we get the relations (4.111)–(4.113). Since the ϕ^s satisfy the boundary conditions, this implies that the a_i satisfy (4.108)–(4.110), as required. \square

In Figure 4.5, we present an algorithm based on this theorem for finding all Keldysh chains at λ_0 . The idea is to start with the kernel of A and build chains of subspaces of vectors a_i which satisfy (4.108)–(4.110). We extract the chains of length zero first, followed by those of length one, and so on.

Example 22. (T-shaped triple grain boundary junction). In Figure 4.6, we show a contour plot of the zero level sets of the real and imaginary parts of $\Delta(\lambda)$ for a T-shaped triple grain boundary junction. We use Equation (4.73) on page 121 to compute $A(\lambda)$, using the boundary condition matrices described in Example 11 on page 111 and $\tilde{F}(\lambda, \theta)$ given in Equation (4.66) on page 120. At $\lambda = 0$, we see by counting contours that $\Delta(\lambda)$ has a zero of order 6. If we compute the kernel of $A(0)$, however, we find that it has dimension 3. This means there must be associated functions present. Applying Algorithm 21, we set $p = 3$ and

$$V_0^0 = \begin{pmatrix} 1 & 0 & 0 & 0 & 0 & 0 & 0 & 0 & 0 & 0 & 0 & 0 & 0 \\ 1 & 0 & 0 & 0 & 1 & 0 & 0 & 0 & 1 & 0 & 0 & 0 & 0 \\ 0 & 1 & 0 & 0 & 0 & 1 & 0 & 0 & 0 & 1 & 0 & 0 & 0 \end{pmatrix}^T. \quad (4.121)$$

The columns of V corresponds physically to the following three self-similar solutions with exponent ($\lambda = 0$): region 1 moves rigidly left while the other two remain fixed (i.e. negative separation occurs along the vertical grain boundary); all regions move rigidly left; all regions

Algorithm 21. (Keldysh chains)

Keldysh_chains($n \times n$ matrix $A(\lambda)$, complex λ_0)

Returns a stack of all tuples of Keldysh chain vectors (a_0, \dots, a_q) for $A(\lambda)$ at λ_0 .

In what follows, A means $A(\lambda_0)$, A' means $A'(\lambda_0)$, etc.

$p = \dim \ker A$

$V_0^0 = n \times p$ matrix, columns form basis for $\ker A$.

$q = 0$

while $p > 0$

$q = q + 1$

$W_q = A'V_{q-1}^{q-1} + \dots + \frac{1}{q!}A^{(q)}V_{q-1}^0$. (W_q is $n \times p$)

$r = \dim [\text{colspan}(W_q) \cap \text{range}(A)]$

if $r > 0$

$C =$ any $p \times r$ matrix such that $W_q C = \text{colspan}(W_q) \cap \text{range}(A)$

$V_q^q =$ any $n \times r$ matrix such that $AV_q^q + W_q C = \{0\}$

for $i = 0, \dots, q - 1$

$V_q^i = V_{q-1}^i C$

if $r < p$

$E =$ any full rank $p \times (p - r)$ matrix such that the columns of E and C are linearly independent. Thus $\text{colspan}(W_q E) \cap \text{range}(A) = \{0\}$.

foreach column v of E

 chains.push_back($(V_{q-1}^0 v, \dots, V_{q-1}^{q-1} v)$).

$p = p - r$

 (note $p = r$ at this point)

return chains

Figure 4.5: Algorithm for finding all Keldysh chains at λ_0 .

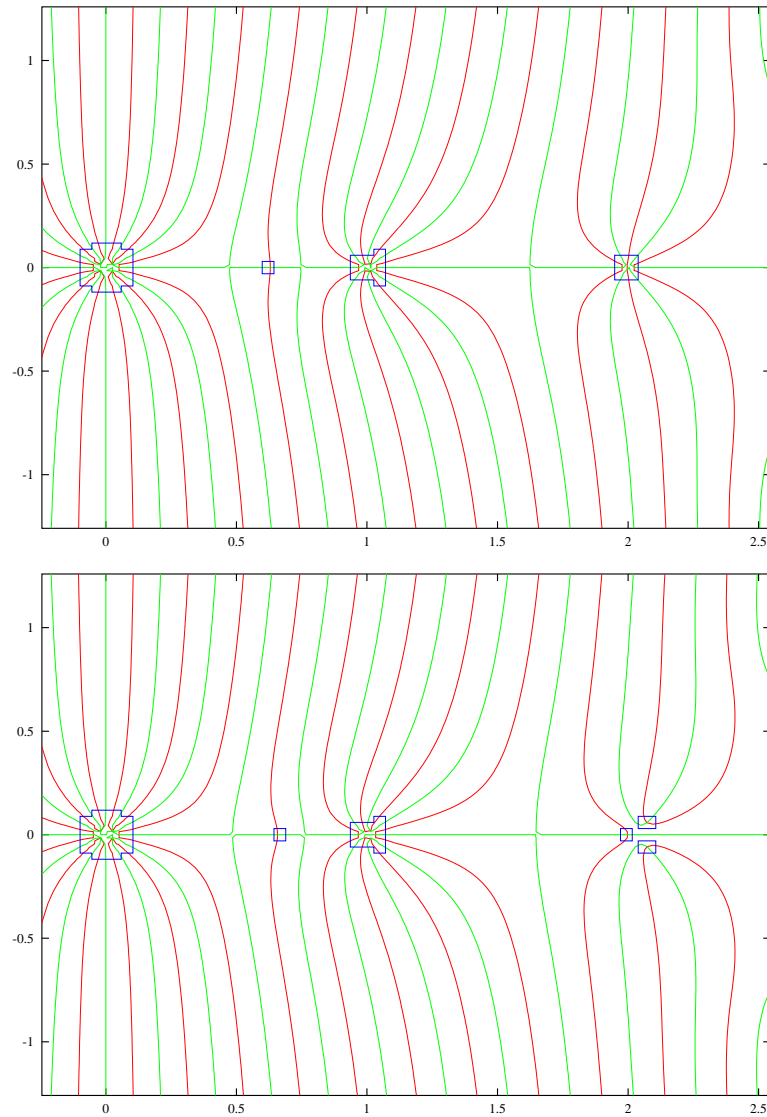


Figure 4.6: *Top*: Contour plot of the zero level sets of the real and imaginary parts of $\Delta(\lambda)$ for a T-shaped triple grain boundary junction with angles $\omega_0 = -90^\circ$, $\omega_1 = 90^\circ$, $\omega_2 = 180^\circ$, $\omega_3 = 270^\circ$ and elastic constant $\kappa = 1.6$. There is a zero of order 6 at $\lambda = 0$, a simple zero at $\lambda = 0.6298473$, a zero of order 4 at $\lambda = 1$, and a zero of order 3 at $\lambda = 2$. At $\lambda = 0$, the kernel of $A(\lambda)$ has dimension 3 and there are 3 linearly independent Keldysh chains of length two. At $\lambda = 1$ and $\lambda = 2$, the dimension of the kernel is respectively 4 and 3, so there are no associated functions at these values of λ . *Bottom*: When the geometry is perturbed, ($\omega_1 \rightarrow 80^\circ$ here), the root at $\lambda = 0$ remains unchanged (including Keldysh chain structure), the root at $\lambda = 1$ splits into a simple root at $\lambda \approx 1$ and a threefold root at $\lambda = 1$, and the root at $\lambda = 2$ splits into three simple roots, one equal to 2 and the others complex. This example illustrates many of the complicated possibilities that can occur.

move rigidly up. The reason they move left rather than right is due to the sign of the first column of $\tilde{F}(\lambda = 0, \theta)$ in Equation (4.66) on page 120. We compute $W_1 = A'V_0^0$ and find that $\text{colspan } W_1 = \text{range}(A)$, so $r = 3$. We take $C = I_{3 \times 3}$ and obtain

$$V_1^1 = \begin{pmatrix} 0 & 0 & \frac{-1}{\kappa+1} & 0 & 0 & -\frac{\pi(\kappa-1)}{2(\kappa+1)} & 0 & 0 & 0 & \frac{\pi(\kappa-1)}{2(\kappa+1)} & 0 & 0 \\ 0 & 0 & \frac{-1}{\kappa+1} & 0 & 0 & 0 & \frac{-1}{\kappa+1} & 0 & 0 & \frac{2\pi(\kappa-1)}{\kappa+1} & \frac{-1}{\kappa+1} & 0 \\ 0 & 0 & 0 & \frac{1}{\kappa+1} & 0 & 0 & 0 & \frac{1}{\kappa+1} & 0 & 0 & 0 & \frac{1}{\kappa+1} \end{pmatrix}^T, \quad (4.122)$$

$$V_1^0 = V_0^0 C = V_0^0. \quad (4.123)$$

Since $r = p$, there are no characteristic functions which aren't tied in with an associated function, so no chains are added to the stack on this iteration. The second time through the loop, we get $W_2 \cap \text{range}(A) = \{0\}$, so $r = 0$. This means there are no chains of length greater than two, so we move to the case ($r < p$), take $E = I_{3 \times 3}$, and add the three chains (a_0, a_1) , (b_0, b_1) , (c_0, c_1) to the stack, where

$$\begin{aligned} a_0 &= \left(1 \ 0 \ 0 \ 0 \ 0 \ 0 \ 0 \ 0 \ 0 \ 0 \ 0 \ 0 \right)^T \\ b_0 &= \left(1 \ 0 \ 0 \ 0 \ 1 \ 0 \ 0 \ 0 \ 1 \ 0 \ 0 \ 0 \right)^T \\ c_0 &= \left(0 \ 1 \ 0 \ 0 \ 0 \ 1 \ 0 \ 0 \ 0 \ 1 \ 0 \ 0 \right)^T \\ a_1 &= \left(0 \ 0 \ \frac{-1}{\kappa+1} \ 0 \ 0 \ -\frac{\pi(\kappa-1)}{2(\kappa+1)} \ 0 \ 0 \ 0 \ \frac{\pi(\kappa-1)}{2(\kappa+1)} \ 0 \ 0 \right)^T \\ b_1 &= \left(0 \ 0 \ \frac{-1}{\kappa+1} \ 0 \ 0 \ 0 \ \frac{-1}{\kappa+1} \ 0 \ 0 \ \frac{2\pi(\kappa-1)}{\kappa+1} \ \frac{-1}{\kappa+1} \ 0 \right)^T \\ c_1 &= \left(0 \ 0 \ 0 \ \frac{1}{\kappa+1} \ 0 \ 0 \ 0 \ \frac{1}{\kappa+1} \ 0 \ 0 \ 0 \ \frac{1}{\kappa+1} \right)^T. \end{aligned} \quad (4.124)$$

Since $p = 0$, there are no more chains left to be found, so the stack of Keldysh chains is returned to the calling program. Recalling that the w_j^k refers to the j th component of the solution w on the k th region, the corresponding six self-similar power solutions obtained from Equation (4.43) on page 116 are given by:

$$\{w^1 = (-1, 0, \dots)^T, \quad w^2 = (0, 0, \dots)^T, \quad w^3 = (0, 0, \dots)^T\} \quad (4.125)$$

$$\{w^1 = (-1, 0, \dots)^T, \quad w^2 = (-1, 0, \dots)^T, \quad w^3 = (-1, 0, \dots)^T\} \quad (4.126)$$

$$\{w^1 = (0, 1, \dots)^T, \quad w^2 = (0, 1, \dots)^T, \quad w^3 = (0, 1, \dots)^T\} \quad (4.127)$$

$$\left\{ \begin{aligned} w^1 &= \left(\frac{\cos 2\theta - (\kappa + 1) \ln r}{\kappa + 1}, \frac{\sin 2\theta - (\kappa - 1)\theta}{\kappa + 1}, \dots \right)^T \\ -w^2 &= w^3 = \left(0, \frac{\pi(\kappa - 1)}{2(\kappa + 1)}, \dots \right)^T \end{aligned} \right\} \quad (4.128)$$

$$\left\{ \begin{array}{l} w^1 = w^2 = \left(\frac{\cos 2\theta - (\kappa + 1) \ln r}{\kappa + 1}, \frac{\sin 2\theta - (\kappa - 1)\theta}{\kappa + 1}, \dots \right)^T \\ w^3 = \left(\frac{\cos 2\theta - (\kappa + 1) \ln r}{\kappa + 1}, \frac{(2\pi - \theta)(\kappa - 1) + \sin 2\theta}{\kappa + 1}, \dots \right)^T \end{array} \right\} \quad (4.129)$$

$$\left\{ w^1 = w^2 = w^3 = \left(-\frac{\sin 2\theta + (\kappa - 1)\theta}{\kappa + 1}, \frac{\cos 2\theta + (\kappa + 1) \ln r}{\kappa + 1}, \dots \right)^T \right\} \quad (4.130)$$

We have checked that each of these solutions satisfies the boundary conditions and the Lamé equations, as expected.

4.9 Stabilizing the Self-Similar Basis Functions

As we saw in the T-shaped grain boundary junction example of Figure 4.6, the roots of the characteristic equation $\Delta(\lambda) = 0$ can be very close to one another without being a multiple root. When this happens, the basis functions obtained in their natural power solution form can be nearly linearly dependent, which means that unnecessarily large coefficients can appear in the asymptotic expansions. The most unusual situation that we have encountered corresponds to the checkerboard welding problem where two materials with different μ and κ occupy the first and third quadrants and the second and fourth quadrants, respectively. In Figure 4.7, we show contour plots of the zero level sets of the real and imaginary parts of $\Delta(\lambda)$ when $\mu_1 = 1$, $\mu_2 = 10$, $\kappa_1 = 1$, $\kappa_2 = 2.4$. Thus an incompressible material is welded to a stiffer but compressible material. There are four distinct roots clustered together near $\lambda = 2.8 \pm .96i$, and if something special isn't done, the functions w^ν given by

$$w_j^\nu(r, \theta) = r^{\lambda_\nu + t_j} \phi_j^\nu(\theta) \quad (\nu = 1, \dots, 4) \quad (j = 1, \dots, 6) \quad (4.131)$$

which span the power solution basis near the top cluster, for example, will be practically linearly dependent, and useless in a finite element code.

Suppose that the points λ_ν , ($\nu = 1, \dots, \nu_{\max}$) are zeros of $\Delta(\lambda)$ that are clustered together. Suppose for simplicity that the dimension n_ν of $\ker A(\lambda_\nu)$ is equal to the order of the zero of $\Delta(\lambda)$ at λ_0 , i.e. there are no nontrivial Keldysh chains to deal with. (Generally, the Keldysh chains arise in the limit when the roots become exactly equal to each other, so this assumption is very reasonable in practice). For each λ_ν , we have n_ν vectors

$$a^{(\nu,p)} = \begin{pmatrix} a^{(\nu,p,1)} \\ \dots \\ a^{(\nu,p,K)} \end{pmatrix}, \quad \begin{array}{l} a^{(\nu,p,k)} \in \mathbb{C}^{2m} \quad (m \text{ from ADN theory}) \\ p = 1, \dots, n_\nu \quad (K = \text{number of regions}) \end{array} \quad (4.132)$$

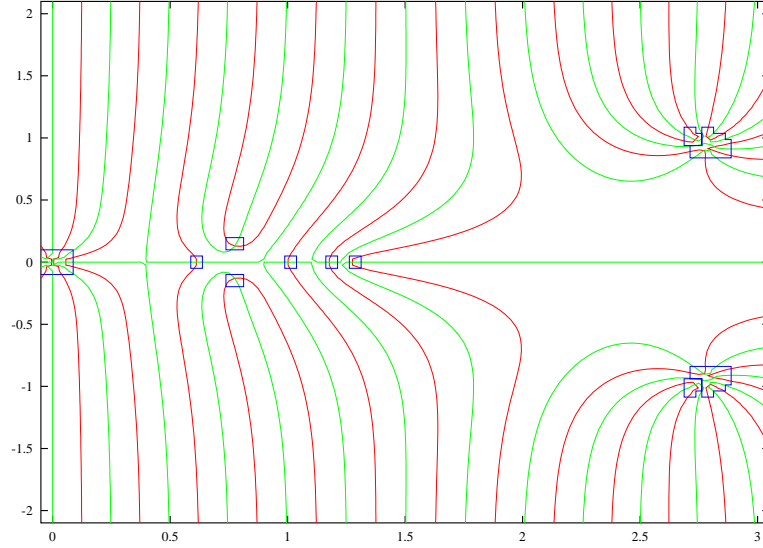


Figure 4.7: Contour plot of the zero level sets of the real and imaginary parts of $\Delta(\lambda)$ for a checkerboard pattern of two materials with Lamé coefficients $\mu_1 = 1$, $\mu_2 = 10$, $\kappa_1 = 1$, $\kappa_2 = 2.4$. Note the four nearly identical roots near $\lambda = 2.8 \pm .96i$.

such that the n_ν nontrivial power solutions to the boundary value problem $M(\partial_x, \partial_y)w = 0$, $Bw = 0$ are given by

$$w^{(\nu,p,k)}(r, \theta) = F^k(\lambda_\nu, r, \theta) \cdot a^{(\nu,p,k)}. \quad (4.133)$$

Here the index k specifies the restriction of $w^{(\nu,p)}$ to region Ω_k . Because the λ_ν are clustered together and the basis matrices $F^k(\lambda, r, \theta)$ depend analytically on λ , the $F^k(\lambda_\nu, r, \theta)$ will not change very much as the index ν changes. Indeed this is what we mean when we say the points are clustered together. Since the $F^k(\lambda, r, \theta)$ do not become rank deficient for any value of λ (due to Algorithm 15), near linear dependency of the $w^{(\nu,p)}$ must be a consequence of near linear dependency of the $a^{(\nu,p)}$.

Working in \mathbb{C}^{2mK} , we do a QR factorization of the $(n = n_1 + \dots + n_{\nu_{\max}})$ vectors $a^{(\nu,p)}$, finding orthogonal vectors $q^{(\nu,p)}$ and an $n \times n$ upper triangular matrix R such that, after assigning an arbitrary order to the (ν, p) , we have

$$a^{(\nu_j,p_j)} = \sum_{i=1}^n q^{(\nu_i,p_i)} R_{ij}. \quad (4.134)$$

Since the columns of $q^{(\nu_j,p_j)} = \sum_i a^{(\nu_i,p_i)} (R^{-1})_{ij}$ are orthonormal in \mathbb{C}^{2mK} , we use R^{-1} to

stabilize the power solution basis to obtain a new basis

$$v^{(\nu_j, p_j, k)}(r, \theta) = \sum_{i=1}^n F^k(\lambda_{\nu_i}, r, \theta) \cdot a^{(\nu_i, p_i, k)}(R^{-1})_{ij}. \quad (4.135)$$

We then use the $v^{(\nu, p)}(r, \theta)$ in the applications.

Obviously this won't work if $n > 2mK$, but we have never encountered a situation for which this was a concern. For example, the welding problem of Figure 4.7 has $2mK = 16$ with $n = 4$ at each cluster.

As a typical example from the simulations of Chapter 3, consider the case of a triple grain boundary junction with $\kappa = 1.6$, $\omega_0 = -90^\circ$, $\omega_1 = 80^\circ$, $\omega_2 = 180^\circ$, $\omega_3 = 270^\circ$ (see the bottom plot of Figure 4.6). There are two roots very close together with

$$\lambda_1 = 1.0, \quad \lambda_2 = 0.993965370442. \quad (4.136)$$

We compute an orthonormal basis $a^{(1,1)}$, $a^{(1,2)}$, $a^{(1,3)}$ for the nullspace of $A(\lambda_1)$, and a unit vector $a^{(2,1)}$ which spans the nullspace of $A(\lambda_2)$. The QR factorization yields an R equal to

$$\begin{pmatrix} 1 & 0 & 0 & 0.942397312276 \\ 0 & 1 & 0 & -0.1115950807344 \\ 0 & 0 & 1 & 0.312809607674 \\ 0 & 0 & 0 & -0.0397994110277 \end{pmatrix}, \quad (4.137)$$

and the small diagonal entry shows that the basis was indeed poorly conditioned. Inverting R and applying it as in (4.135), we obtain

$$\begin{aligned} v^{(1,p)}(r, \theta) &= w^{(1,p)}(r, \theta), \quad (p = 1, 2, 3) \\ v^{(2,1,k)}(r, \theta) &= F^k(\lambda_1, r, \theta) \cdot x_1^k + F^k(\lambda_2, r, \theta) \cdot x_2^k \end{aligned} \quad (4.138)$$

$$\begin{pmatrix} x_1^1 \\ x_1^2 \\ x_1^3 \end{pmatrix} = \begin{pmatrix} 0.0000000000 \\ -14.01115636607 \\ 0.0000000000 \\ -8.75697272879 \\ 0.0000000000 \\ 11.55282653062 \\ 0.0000000000 \\ 7.22051658164 \\ 0.0000000000 \\ 11.11218024269 \\ 0.0000000000 \\ 6.94511265168 \end{pmatrix} \quad \begin{pmatrix} x_2^1 \\ x_2^2 \\ x_2^3 \end{pmatrix} = \begin{pmatrix} -0.1325049098813 \\ 14.26550909261 \\ 0.0465944534498 \\ 8.35000836633 \\ -0.382710667398 \\ -11.31651187973 \\ 0.1809796983307 \\ -7.59862002305 \\ -0.374395709498 \\ -10.87465303354 \\ 0.1757946545638 \\ -7.32515618632 \end{pmatrix}. \quad (4.139)$$

Note that x_1^k and x_2^k are behaving as something of a finite difference operator on the two matrices $F^k(\lambda_1)$, $F^k(\lambda_2)$. As we take the angle ω_1 to 90° , it is reasonable to expect that this procedure will capture any logarithm terms that might arise in a Keldysh chain at the critical angle when λ_1 and λ_2 coalesce. This is because $F^k(\lambda, r, \theta)$ has the form

$$\text{diag}(r^{\lambda+t_j})\tilde{F}^k(\lambda, \theta), \quad (4.140)$$

so appropriate differencing can lead to derivatives of $r^{\lambda+t_j}$ with respect to λ , giving logarithm terms. In this particular case, the limiting angle has $A(\lambda = 1)$ with a four dimensional kernel, so no Keldysh chains arise and hence no logarithm terms will appear. But in general, this is how our stabilization procedure at a nearly critical angle will give nearly the same basis as the Keldysh chain procedure at exactly the critical angle.

Chapter 5

XFOSLS

In this chapter we describe our implementation of the First Order System Least Squares Finite Element method (known as FOSLS [15]) for the Lamé equations, which has been extended to include self-similar basis functions near corners and interface junctions to capture asymptotic behavior. We will refer to the method as XFOSLS, borrowing terminology from the developers of XFEM [25]. We defer rigorous convergence and error analysis studies to later work, and focus here on the design of efficient algorithms and data structures to handle the considerable complexity of interface boundary conditions and overlapping singular basis functions.

Each extra basis function is a linear combination of self-similar power solutions. In the most typical case it consists of a single function with components of the form $w_j(r, \theta) = r^{\lambda+t_j}\phi_j(\theta)$, but Keldysh chains with logarithm terms and stabilized linear combinations of nearly linearly dependent power solutions with clustered exponents are also used when needed; see Chapter 4. We generically refer to the extra basis functions as “singular functions” even though they often represent non-singular stress fields such as rigid body motions, or correspond to exponents with real part greater than one.

Each singular function has a near region where it is a solution to the PDE, a fringe region where it transitions to zero, and a far region where it is zero. Singular functions corresponding to exponents with smaller real parts are given larger supports to give the singularity room to die out and become well approximated by the standard quadratic basis functions. The beauty of the least squares finite element framework over the Galerkin framework for adjoining singular functions is that because they satisfy the PDE in the near and far regions, only the fringe region is relevant for computing the inner products.

Therefore inner products only need to be computed in regions where the functions are well-behaved, and numerical integration schemes like Gaussian quadrature work well. By contrast, to adjoin singular functions in variational finite elements, special methods must be used to get the integrations right, and it would be difficult to compute inner products between overlapping singular functions.

We refer back to Section 1.6 for background information about the Least Squares Finite Element Method and our motivation for developing XFOSLS. Some of the major strengths of the method are as follows:

- The stress and displacement variables may both be modeled in nice continuous spaces without having to satisfy an inf-sup condition. This is a huge advantage in the grain growth problem of Chapter 3 since the stress and displacement variables are coupled together in an evolution equation.
- The condition number of the linear system is $O(h^{-2})$ even for problems like the bi-harmonic equation where the Galerkin method is $O(h^{-4})$.
- XFOSLS can be used in many practical cases that FOSLS cannot due to the fact that singularities can destroy H^2 regularity even when the data is smooth. XFOSLS only requires that the *regular* part of the solution satisfy an H^2 regularity condition.
- There is an a-posteriori measure of the error J which indicates where the finite element space is having difficulty resolving the solution.
- Very complicated interface boundary conditions can be implemented.
- It is easier to augment the space with singular functions than in the Galerkin setting.
- Singularities are captured explicitly, and the accuracy of the solution does not degrade near corners and triple junctions.
- Stable combinations of self-similar functions are used to avoid ill-conditioned linear systems as a result of adjoining extra basis functions.
- The operator K from chapter 3 could not have been computed effectively without many of these properties.

In Section 5.1, we describe an object-oriented approach to representing corner singularities, which allows us to handle the case of a stabilized cluster almost as easily as a pure power solution, and allows the same code to be used for different elliptic systems with only the form of the basis matrix $F(\lambda, r, \theta)$ changing from one case to the next. In Section 5.2 we show how to find the fringe region efficiently, and describe the way in which the singular functions transition to zero across the fringe region. In Sections 5.3 and 5.4 we show how to implement complicated boundary conditions using affine subspaces. In Section 5.5, we describe the minimization problem that we wish to solve numerically. In Section 5.6, we show how to effectively handle overlapping basis functions when setting up the corresponding linear system of equations. In Section 5.7, we compare the solution obtained using XFOSLS to the Galerkin solution near a corner, and also solve the elastic equations in the incompressible limit on a complicated geometry with re-entrant corners to show the effectiveness of the method outside of the electromigration problem.

5.1 Data Structures for Extending the Finite Element Space

Suppose we are given a geometry consisting of several polygonal domains Ω_k which are bounded by a collection of segments Γ_i of wall or interface type. We number each corner in the geometry arbitrarily, using the term corner from now on to include the case of a junction between several regions Ω_k . We choose a mesh parameter h and divide each Γ_i into equally sized subsegments of length less than or equal to h . Each region Ω_k is triangulated separately using freely available software [71], with offsets added to the node numbers so that the first node of the $(k + 1)$ st region follows the last node of the k th region. The edge and element connectivity information is offset accordingly. This means that each region has its own copy of the nodes along an interface, which facilitates the possibility of jump discontinuities in some of the variables. See Figure 5.1. A node is added at the midpoint of each edge of the mesh, and we distinguish between vertex and edge nodes. Edge nodes are also duplicated across interfaces.

Each corner is analyzed by the methods of Chapter 4, and for each stabilized singular function that we wish to incorporate into the finite element basis, we add an entry to a vector *singularities* of objects of type *singularity*. Each *singularity* contains a vector *lambda[term]* and a triply-indexed complex vector *weights[term][region][column]*. Here *term* is indexing power solutions in a stabilized cluster and runs from 0 to *num_terms* - 1, *region*

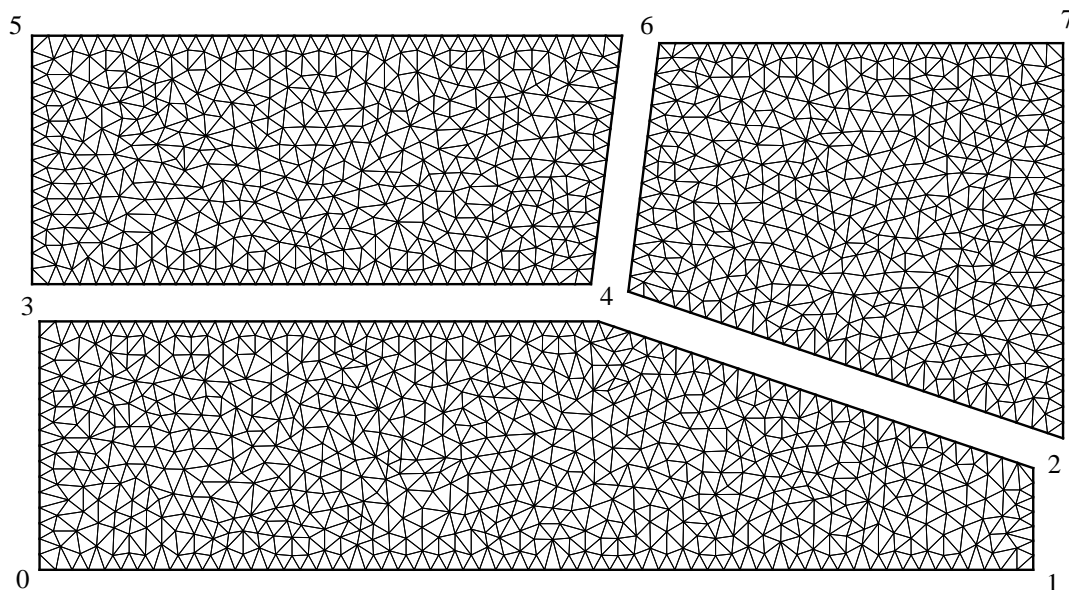


Figure 5.1: Each grain is triangulated separately, leading to an unstructured mesh with duplicate nodes along grain boundaries. This particular mesh corresponds to a mesh parameter $h = 0.033$ for an interconnect line of unit height and length two.

is indexing the Ω_k which touch the corner, and *column* contains the coefficients to use on the columns of $F^{region}(\lambda_{term}, r, \theta)$ and runs from 0 to $3 = 2m - 1$, (m from ADN theory). When λ is a complex eigenvalue of the boundary value problem (4.44), it is easy to show that $\bar{\lambda}$ is also an eigenvalue, and that the span of the basis functions obtained from λ and $\bar{\lambda}$ is the same as the span of the real and imaginary parts of the basis functions for λ alone. Therefore when a *singularity* with complex entries is added to *singularities*, it is added twice – once with the field *imaginary* equal to 0, and once with the field equal to 1. The class *singularity* has a member function *compute* which takes a location and an index ($0 \leq j < N$) (specifying, in the case of elasticity, u , v , p , q , γ , or τ), and returns the value of the j th component of the stabilized cluster of power solutions at the point. This function must determine which region the point is in so that it can apply the correct collection of weights to the correct $F^{region}(\lambda_{term}, r, \theta)$ for each *term* in the cluster. For this purpose, *singularity* also contains a vector *angles* which contains the ω_k of the incident grain boundary segments.

The class *singularity* described above is implemented as a base class from which classes such as *elast_sing* or *poisson_sing* are derived. These subclasses implement only an

auxiliary function *compute2* called by *compute*, where they substitute the appropriate form of F for the PDE they correspond to.

5.2 The Fringe Region

Each *singularity* is assigned a parameter *fringe_radius* which describes the size of its support in units of h . Starting at the corner node of each region Ω_k touching the corner, we use the following algorithm to obtain all nodes and triangles within the desired support radius:

Algorithm 23. (Finding the fringe region)

```

Tag the corner node and put it on the stack.
while the stack is non-empty
    pop node from the stack, mark it as "near"
    tag all untagged nodes and triangles adjacent to this node
    add newly tagged nodes that lie within the desired radius to the stack
    mark newly tagged triangles with "near" or "fringe"
untag everything that was tagged, record the information

```

A triangle is marked "fringe" if it has a node within the radius and a node outside of it; see Figure 5.2. Only vertex nodes are used in this algorithm. Edge nodes are "near" if both endpoints are "near". For each "near" node and each "near" and "fringe" triangle, we add ordered pairs $(sing_idx, node_num)$, $(sing_idx, tri_num)$ to the associative containers (i.e. dynamic sets) *sing_and_node*, *sing_and_tri_near*, *sing_and_tri_fringe* which can later be unwrapped in lex-order to record the *singularity* indices which influence a given node or triangle.

Our heuristic for choosing *fringe_radius* is that basis functions with $(0 < \text{Re } \lambda < 1)$ should be given a large radius (e.g. 7), and basis functions with $(\text{Re } \lambda > 1)$ should be given a small radius (e.g. 2). Here λ is the value of *lambda[term]* with the smallest real part. The idea is that strong singularities should be given room to die out and become well approximated by the standard quadratic basis functions while non-singular self-similar solutions are prevented from becoming too linearly dependent on the quadratic basis functions. Self-similar solutions such as rigid body translations ($\lambda = 0$) or rigid rotations ($\lambda = 1$) are not adjoined since these motions can already be captured exactly by the quadratic elements. For grain boundary triple junctions, we pin the standard basis functions to be equal to each

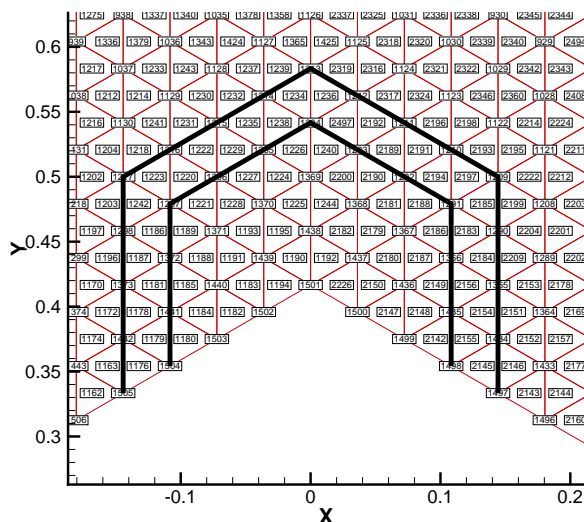


Figure 5.2: The fringe region of a regular hexagonal mesh corresponding to $fringe_radius=3$. Nodes within a radius of $3h$ inclusive are “near” nodes. Triangles with some near nodes and some far nodes are “fringe” triangles. If several singularities exist at the corner, each may have a different $fringe_radius$.

other at the triple junction, and adjoin the self-similar basis function with $\lambda = 0$ which corresponds to stress free separation. This separation is only defined up to the addition of a rigid translation to all the grains, so we choose the unique separation which pins the grain of lowest index. The standard quadratic basis functions at the triple point node then govern where the pinned grain moves to, and the others retain their positions relative to this one. This will be discussed in more detail in Section 5.4

As mentioned above, each node and triangle keeps track of the indices of the vector *singularities* that correspond to basis functions which affect that node or triangle. On a given triangle, the components w_j of the solution can be decomposed into three parts. The first part w_j^q is quadratic, the second w_j^s is a sum of function values of *singularities* for which the triangle is “near”, and the third w_j^t is a sum of nearly quadratic transition functions which transition to zero the *singularities* for which that triangle is in the “fringe”. Let T be a “fringe” triangle to *singularity* s , and for the sake of explanation, suppose that s is the only *singularity* for which T is a “fringe” triangle. We write $s_j(x)$ to denote the value returned by $s.compute(x,j)$. If T has only one vertex p “near” s , then $w_j^t(x)$ is the quadratic

function which agrees with $s_j(x)$ at p and is zero at the other 5 nodes of the triangle. If T has two vertices “near” s , $w_j^t(x)$ is a sum of two pieces. The first piece $q_j(x)$ is the quadratic function which agrees with $s_j(x)$ at the three “near” nodes and is zero at the other three. The second piece $e_j(x)$ is equal to $s_j(x) - q_j(x)$ along the “near” edge of the triangle, is zero at the “far” vertex of the triangle, and varies linearly along rays joining points on the “near” edge to the “far” vertex. We assume (by our heuristic choice of *fringe_radius*) that the “near” edge is far enough from the corner at which s is centered that $s_j(x)$ varies smoothly enough along the “near” edge that $e_j(x)$ is small, so we throw away this term when computing the stiffness and mass matrices. In effect, we are using quadratic functions for the fringe transition.

5.3 An Affine Subspace

As mentioned earlier, each grain is triangulated separately, with double and triple nodes along grain boundaries and at triple junctions. We let each of these nodes carry *vars_per_node* degrees of freedom (e.g. u, v, p, q, γ, τ), and let each element of the vector *singularities* carry a single degree of freedom. Edge nodes do not have to carry the same number of degrees of freedom as vertex nodes. If we wish to use quadratic displacements and linear stress variables on each element, we let *vars_per_node* be 6 for vertex nodes and 2 for edge nodes. This is easily done with an object oriented approach. This defines a linear space V which we refer to as the space of “physical variables”. The variables have discontinuities across interfaces when the double and triple nodes have different values for their variables.

To enforce boundary conditions or other constraints on the variables, we construct a space $X = R^n$ of “free variables” and a space $G = R^d$ of “data”, and define a linear mapping

$$\phi : X \times G \rightarrow V \tag{5.1}$$

which gives the corresponding physical state. For fixed $g \in G$,

$$\phi_g(x) := \phi(x, g) \tag{5.2}$$

is an affine mapping onto an affine subspace of V .

To implement this idea in our code, we set up a vector *eqn* of integers and a vector *alpha* of double precision real numbers, and assign to each node an array of integers

$idx[0..vars_per_node]$ such that the value of the solution w_j at the node is given by

$$val[j] = \sum_{k=idx[j]}^{idx[j+1]-1} alpha[k]*soln[eqn[k]] + \sum_{k=jmp_idx[j]}^{jmp_idx[j+1]-1} jmp_alpha[k]*data[jmp_eqn[k]]. \quad (5.3)$$

Here $soln$ is a vector in X , $data$ is a vector in G , and we are essentially using packed row format to store the linear mapping $\phi(x, g)$.

To get the *singularity* basis functions to fit with this data strategy, we take the convention that the first num_sing entries of $soln$ refer to the singular basis functions. When we are setting up the values of eqn and $alpha$ for a given node, we run through the next batch of ordered pairs $(sing_idx, node_num)$ of the associative container $sing_and_node$ which have the current node's index in the second slot. This gives a list $sing_this_node$ of *singularity* indices which have the node as a “near” node, and also gives the indices of $soln$ which correspond to the *singularity* basis functions. We now go through each of the $vars_per_node$ variables and fill the j th variable's range of eqn and $alpha$ as follows. First, we set $idx[j]$ to the length of eqn (= length of $alpha$). For each $sing_this_node$, we add the index of the *singularity* (call it s) to eqn (increasing the size of eqn by one), and add the value of $s.compute(node_location, j)$ to $alpha$ (increasing the size of $alpha$ by one). If the node is an interior node with no boundary conditions specified, we increase the size of the vector $soln$ by one and add its index to eqn and 1.0 to $alpha$. If the node is affected by boundary conditions, we parse the boundary condition string (see below) for this node to determine how many free and jump (i.e. data) variables the j th component depends on, what their indices in $soln$ and jmp_soln are, and what the corresponding weights $alpha$ and jmp_alpha are. The appropriate number of entries are added to eqn , jmp_eqn , $alpha$ and jmp_alpha , at which point the node's value of $idx[j+1]$ is set to the length of eqn .

In this way, the nodes can obtain their values which correspond to any $soln$ and $data$ using (5.3) without calling the *compute* method of any *singularity* objects. If we wish to zoom in on a region of the solution and look at points in the interior of the triangles as in Fig. 5.6 on page 157, then we have to decompose the solution on the triangle into its regular part (a quadratic function), singular part (a sum of results from *compute* from *singularity* objects for which the triangle is “near”), and transition part (a quadratic function obtained from *singularity* objects for which the triangle is a “fringe” triangle). This requires additional book-keeping which we omit here.

5.4 Boundary Conditions

As we explained in Chapter 4, the self-similar basis functions satisfy homogeneous boundary conditions on each boundary (or interface) segment which is incident to the corner (or junction). Thus as long as the fringe regions transition these functions to zero before they meet any other boundary segments, the self-similar basis functions are invisible to the boundary conditions. Because the solution near a corner or junction decomposes into the sum of a regular part and a singular part, and because the singular part satisfies homogeneous boundary conditions, we may treat the regular (quadratic) variables in our finite element space as if no singularities were present when deriving relationships between the variables at corners and junctions for the purpose of imposing boundary conditions.

As mentioned in the previous section, each boundary node is assigned a boundary condition string which carries information about the free and jump variables which affect it. In our implementation, each string is generated when the mesh is generated (using Perl) and is stored in a boundary condition file which the C++ code reads as part of the problem specification. The boundary condition file is set up to be moderately human readable, consisting of fields such as shown in Figure 5.3. The first line in this example indicates that the node is an edge node (as opposed to a vertex node) connecting vertex nodes numbered 2726 and 2727; it also tells us that the node lies on the grain boundary and that this segment runs from corner 24 to corner 27 in Figure 3.25 on page 93. The header of the previous entry in the file looks like

```
vertex 2726 G 24 27
```

which illustrates the vertex node case. The next 12 lines give the dependence of each of the six physical variables u, v, p, q, γ, τ on the free and jump variables. The first line, for example, tells us that u depends on the two free variables numbered 1649 and 1651 with weights $(-.316)$ and $(-.949)$, which get appended to *eqn* and *alpha* after the *singularity* information is included.

Example 24. (Wall) Let the grain lie to the left of a boundary segment oriented along $\mathbf{t} = (\cos \theta, \sin \theta)$. In addition to $u = v = 0$ at the node, we impose compatibility conditions on p, q, γ, τ obtained from

$$\begin{pmatrix} u_x & u_y \\ v_x & v_y \end{pmatrix} \cdot \begin{pmatrix} \cos \theta \\ \sin \theta \end{pmatrix} = 0 \quad (5.4)$$

edge	2726	2727	G	24	27
2	1649	-0.31622776601683805		1651	-0.94868329805051377
2	1649	0.94868329805051377		1651	-0.31622776601683805
1	1655	0.5			
1	1653	1.0			
2	1655	0.39999999999999997		1654	-0.60000000000000002
2	1655	-0.30000000000000001		1654	-0.79999999999999993
0					
0					
1	243	0.5			
0					
1	243	-0.39999999999999997			
1	243	0.30000000000000001			

Figure 5.3: Typical entry in the boundary condition file.

and

$$\begin{aligned}
 u_x &= \frac{\kappa - 1}{4}p - \frac{1}{2}\gamma, & v_x &= -\frac{\kappa + 1}{4}q + \frac{1}{2}\tau, \\
 u_y &= \frac{\kappa - 1}{4}p + \frac{1}{2}\gamma, & v_y &= \frac{\kappa + 1}{4}q + \frac{1}{2}\tau,
 \end{aligned} \tag{5.5}$$

which give

$$\begin{pmatrix} \gamma \\ \tau \end{pmatrix} = \begin{pmatrix} \cos 2\theta & -\sin 2\theta \\ -\sin 2\theta & -\cos 2\theta \end{pmatrix} \cdot \begin{pmatrix} \frac{\kappa-1}{2}p \\ \frac{\kappa+1}{2}q \end{pmatrix}. \tag{5.6}$$

Thus we set up two free variables corresponding to p and q and no jump variables. The purpose of the compatibility conditions is to improve the condition number of the system when self-similar functions with $\text{Re } \lambda > 1$ are added.

Example 25. (Grain Boundary) We have one jump variable corresponding to σ_{\perp} and seven free variables corresponding to u_{\parallel} , u_{\perp}^{-} , u_{\perp}^{+} , q^{-} , q^{+} , σ_s , and σ_{\parallel} . The physical variables are

obtained from the free and jump variables via

$$u^\pm = \cos \theta u_{\parallel} - \sin \theta u_{\perp}^\pm, \quad (5.7)$$

$$v^\pm = \sin \theta u_{\parallel} + \cos \theta u_{\perp}^\pm, \quad (5.8)$$

$$p = \frac{1}{2}\sigma_{\parallel} + \frac{1}{2}\sigma_{\perp}, \quad (5.9)$$

$$q^\pm = q^\pm, \quad (5.10)$$

$$\gamma = -\frac{1}{2}\cos 2\theta \sigma_{\parallel} + \sin 2\theta \sigma_s + \frac{1}{2}\cos 2\theta \sigma_{\perp}, \quad (5.11)$$

$$\tau = \frac{1}{2}\sin 2\theta \sigma_{\parallel} + \cos 2\theta \sigma_s - \frac{1}{2}\sin 2\theta \sigma_{\perp}. \quad (5.12)$$

see Figure 5.3 above for an example of a boundary condition file entry for this case. The entry shown corresponds to a node on the positive side. The coincident node on the negative side is the same except that 1651 and 1653 are replaced by 1650 and 1652, respectively.

Example 26. (Wall–Wall) At a corner where two walls meet, all variables are zero, so there are no equations or jumps. This would be too restrictive if we weren't using singular functions to capture the asymptotics near the corner.

Example 27. (Wall–GB–Wall) Let the geometry of the wall–GB–wall junction be given as in Fig. 5.4. As in Example 24, along the wall we have

$$\begin{pmatrix} \gamma \\ \tau \end{pmatrix} = \begin{pmatrix} \cos 2\theta_1 & -\sin 2\theta_1 \\ -\sin 2\theta_1 & -\cos 2\theta_1 \end{pmatrix} \cdot \begin{pmatrix} \frac{\kappa-1}{2}p \\ \frac{\kappa+1}{2}q^\pm \end{pmatrix}. \quad (5.13)$$

Since γ , τ and p are continuous across the grain boundary, and since we are working with the regular part of the solution, γ , τ and p are treated as continuous variables at the junction. From (5.13), this implies that $q^+ = q^-$ at the junction. Along the grain boundary, we have

$$p + \gamma \cos 2\theta_2 - \tau \sin 2\theta_2 = \sigma_{\perp}. \quad (5.14)$$

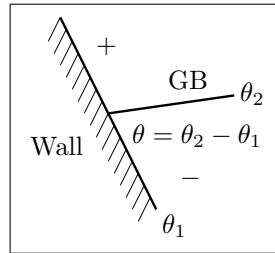


Figure 5.4: Geometry of a junction where a grain boundary meets a wall.

Combining these, we get that

$$p = -\frac{\frac{\kappa+1}{2} \sin 2\theta}{1 + \frac{\kappa-1}{2} \cos 2\theta} q + \frac{1}{1 + \frac{\kappa-1}{2} \cos 2\theta} \sigma_{\perp} = -aq + b\sigma_{\perp}. \quad (5.15)$$

Thus we have one equation and one jump: q is free, σ_{\perp} is data, and the physical variables are determined by

$$u = v = 0, \quad (5.16)$$

$$p = aq + b\sigma_{\perp}, \quad (5.17)$$

$$q = q, \quad (5.18)$$

$$\gamma = \left(a \frac{\kappa-1}{2} \cos 2\theta - \frac{\kappa+1}{2} \sin 2\theta \right) q + b \frac{\kappa-1}{2} \cos 2\theta \sigma_{\perp}, \quad (5.19)$$

$$\tau = \left(-a \frac{\kappa-1}{2} \sin 2\theta - \frac{\kappa+1}{2} \cos 2\theta \right) q - b \frac{\kappa-1}{2} \sin 2\theta \sigma_{\perp}. \quad (5.20)$$

Example 28. (Triple grain boundary junction) As discussed in Section 5.2, we glue the three nodes at the triple point together as far as the regular basis functions are concerned, and model the separation separately using a self-similar function with ($\lambda = 0$). Since we are given σ_{\perp} along the three incident grain boundary segments, and because they are all equal to each other at the triple point (by chemical potential continuity), the stress tensor must be of the form $\eta\delta_{ij}$ at the triple point. To see this, let η be the limiting value of σ_{\perp} along each grain boundary, and note that along grain boundary i , we have

$$p + \gamma \cos 2\theta_i - \tau \sin 2\theta_i = \eta. \quad (5.21)$$

Thus p , γ and τ satisfy

$$\begin{pmatrix} 1 & \cos 2\theta_1 & -\sin 2\theta_1 \\ 1 & \cos 2\theta_2 & -\sin 2\theta_2 \\ 1 & \cos 2\theta_3 & -\sin 2\theta_3 \end{pmatrix} \begin{pmatrix} p \\ \gamma \\ \tau \end{pmatrix} = \begin{pmatrix} \eta \\ \eta \\ \eta \end{pmatrix}. \quad (5.22)$$

The determinant of the matrix on the left is $4\sin(\theta_3 - \theta_2)\sin(\theta_2 - \theta_1)\sin(\theta_1 - \theta_3)$ and ($p = \eta, \gamma = \tau = 0$) is a solution, so unless two of the grain boundaries are colinear, the stress tensor equals $\eta\delta_{ij}$. In the exceptional case of a colinear grain boundary structure like the T-shaped junction studied in Section 4.9 on page 135, the stress variables will have another degree of freedom. We capture this one with a self-similar solution with $\lambda = 1$ to avoid special cases in the boundary condition setup procedure. As we saw in Section 4.9,

the behavior in the nearly colinear case is quite interesting. As the angle approaches 180° , a root of $\Delta(\lambda)$ comes in and “kisses” the root at $\lambda = 1$ (of multiplicity 3) creating a nullspace of dimension 4 instead of 3. It then turns around and decreases again as the angle passes through 180° . Since we capture this behavior in a stable way (see Sec. 4.9), there is nothing “discontinuous” happening in our finite element space at the critical angle.

We therefore have five free variables (u, v, q_0, q_1, q_2) and one jump (p) at a triple grain boundary junction, and the 18 physical variables are determined via

$$u_0 = u_1 = u_2 = u, \quad (5.23)$$

$$v_0 = v_1 = v_2 = v, \quad (5.24)$$

$$q_1, q_2, q_3 \text{ are free,} \quad (5.25)$$

$$p_0 = p_1 = p_2 = p, \quad (5.26)$$

$$\gamma_0 = \gamma_1 = \gamma_2 = 0, \quad (5.27)$$

$$\tau_0 = \tau_1 = \tau_2 = 0. \quad (5.28)$$

5.5 A Minimization Problem

In the First Order System Least Squares method for the problem $Lw = f$, we seek the minimizer of the residual

$$J = \frac{1}{2} \sum_1^N \|L_i w - f_i\|_2^2 = \frac{1}{2} a(w, w) - \sum_1^N (L_i w, f_i)_2 + \frac{1}{2} \sum_1^N (f_i, f_i)_2 \quad (5.29)$$

over all functions in our affine subspace, where $a(w^1, w^2) = \sum_1^N (L_i w^1, L_i w^2)_2$ [15]. Redundant differential relationships between the variables which follow from the other equations are also included in L . As we saw in Section 3.1.1, the Lamé system is equivalent to the equations

$$u_x - v_y = -\gamma, \quad (5.30)$$

$$u_y + v_x = \tau,$$

$$v_x - u_y = \frac{\kappa + 1}{2} q, \quad (5.31)$$

$$v_y + u_x = \frac{\kappa - 1}{2} p,$$

and one of the two sets of equations

$$\begin{aligned}\gamma_x - \tau_y &= p_x + \mu^{-1}F_1, \\ \gamma_y + \tau_x &= -p_y - \mu^{-1}F_2,\end{aligned}\tag{5.32}$$

or

$$\begin{aligned}p_x - q_y &= -\frac{2\mu^{-1}}{\kappa + 1}F_1, \\ p_y + q_x &= -\frac{2\mu^{-1}}{\kappa + 1}F_2.\end{aligned}\tag{5.33}$$

Either set (5.32) or (5.33) can be derived from the other and equations (5.30), (5.31). However, using both of them in the sum (5.29) can dramatically improve the condition number of the stiffness matrix as a result of placing tight control on the derivatives of the stress variables rather than relying on (5.30) and (5.31) to control the stresses. The resulting L and f look like

$$Lw = \begin{pmatrix} \partial_x & -\partial_y & 0 & 0 & 1 & 0 \\ \partial_y & \partial_x & 0 & 0 & 0 & -1 \\ -\partial_y & \partial_x & 0 & -\frac{\kappa+1}{2} & 0 & 0 \\ \partial_x & \partial_y & -\frac{\kappa-1}{2} & 0 & 0 & 0 \\ 0 & 0 & \partial_x & -\partial_y & 0 & 0 \\ 0 & 0 & \partial_y & \partial_x & 0 & 0 \\ 0 & 0 & \partial_x & 0 & -\partial_x & \partial_y \\ 0 & 0 & \partial_y & 0 & \partial_y & \partial_x \end{pmatrix} \begin{pmatrix} u \\ v \\ p \\ q \\ \gamma \\ \tau \end{pmatrix} = \begin{pmatrix} 0 \\ 0 \\ 0 \\ 0 \\ -\frac{2\mu^{-1}}{\kappa+1}F_1 \\ -\frac{2\mu^{-1}}{\kappa+1}F_2 \\ -\mu^{-1}F_1 \\ -\mu^{-1}F_2 \end{pmatrix} = f.\tag{5.34}$$

Note that because we have imposed more equations than are appropriate for an ADN system with 6 variables, the right hand side must satisfy constraints in order for a solution to exist. We are interested in the case that $\mathbf{F} = 0$, so this will not cause difficulties. This particular choice of L has not been used before, and has the advantage of being uniformly well behaved in the parameter κ even in the incompressible limit $\kappa \rightarrow 1$. See also [16].

5.6 Constructing the Stiffness and Jump Matrices

The following theorem is a straightforward generalization of a standard result in the finite element literature [10]:

Theorem 29. *Let V be a linear space, $a : V \times V \rightarrow \mathbb{R}$ a symmetric, bilinear, non-negative definite form, V_0 a subspace on which $a|_{V_0 \times V_0}$ is positive definite, and $V_g = g + V_0$ for some*

fixed $g \in V$. Then for any linear functional l ,

$$J(v) = \frac{1}{2}a(v, v) - \langle l, v \rangle \quad (5.35)$$

is minimized over V_g at u if and only if

$$a(u, v) = \langle l, v \rangle \quad (\text{all } v \in V_0). \quad (5.36)$$

There is at most one such solution.

Applying this theorem in the case that $l = 0$, we obtain for any $u \in V_g$ that

$$\left[a(v, u) = 0 \quad \forall v \in V_0 \right] \Leftrightarrow \left[u \text{ minimizes } J(v) = \frac{1}{2}a(v, v) \text{ over } V_g \right]. \quad (5.37)$$

In our case, referring to ϕ_g from Eqn. (5.2) and J from Eqn. (5.29), we wish to minimize $J(w)$ over $w \in \text{range}(\phi_g)$. We transfer this problem over to our free variables by seeking the function $x \in \mathbb{R}^n$ which minimizes

$$J(x) = \frac{1}{2}a(\phi_g(x), \phi_g(x)). \quad (5.38)$$

Equation (5.37) implies that x satisfies

$$a(\phi_0(y), \phi_g(x)) = 0, \quad (\text{all } y \in \mathbb{R}^n), \quad (5.39)$$

which is equivalent to

$$a(\phi_0(y), \phi_0(x)) = -a(\phi_0(y), \phi_g(0)), \quad (\text{all } y \in \mathbb{R}^n). \quad (5.40)$$

Defining

$$A_{ij} = a(\phi_0(e_i), \phi_0(e_j)), \quad B_{ij} = a(\phi_0(e_i), \phi_{e_j}(0)), \quad (5.41)$$

this is true for all $y \in \mathbb{R}^n$ if and only if

$$Ax = -Bg. \quad (5.42)$$

A is known as the stiffness matrix, and we call B the jump matrix.

In the usual way, we compute A and B element by element. This can be done since $a(\cdot, \cdot)$ is an integral over the domain, and decomposes into a sum over triangles

$$a(w^1, w^2) = \sum_{T \in \mathcal{T}} a_T(w^1|_T, w^2|_T), \quad a_T(w^1, w^2) = \sum_{i=1}^N \int_T (L_i w^1)(L_i w^2) dA. \quad (5.43)$$

On a given triangle, $\phi_g(x)$ is a sum of quadratic terms and self-similar functions which satisfy the PDE exactly. As a result, the self-similar functions are invisible to $a(\cdot, \cdot)$ except on the fringe, where they are transitioned to zero quadratically. Let K be the number of quadratic degrees of freedom on the triangle. If all 6 variables are modeled quadratically, $K = 36$. If the stress variables are modeled linearly while displacements are modeled quadratically, $K = 24$. We construct the $K \times K$ matrix E on triangle T given by

$$E_{ij} = a(\epsilon_i, \epsilon_j), \quad (5.44)$$

where ϵ_i is identically zero for all variables but one, and for that variable is quadratic (or possibly linear if $K = 24$), is equal to 1 at one node, and is equal to zero at the others. This is done using standard gaussian quadrature methods to compute the integrals of (5.43) exactly, making use of Level 3 BLAS routines to make the computation fast.

The contribution to the stiffness matrix due to triangle T is obtained from E through

$$S^T E S, \quad (5.45)$$

where S is a $K \times n$ sparse matrix such that Sx gives the values at the nodes of triangle T corresponding to the free variables x , subject to the condition that if x_i corresponds to a *singularity* object, (i.e. $i < \text{num_sing}$), then the contribution is only taken into account if the triangle is a “fringe” triangle for that *singularity*. Since each node carries all the necessary information for a row of S , we run through each node’s *eqn* and *alpha* variables and do a sparse row to sparse column conversion employing the same trick we used before to record “near” and “fringe” attributes. The trick is to set up an associative container (a map in this case) which takes ordered pairs (*row*, *column*) to *alpha* values, and then to unwrap them in lex order so that the rows come out one column at a time. The condition of whether or not the *singularity* object contains the triangle as a fringe triangle can be checked very rapidly since the triangle has the singularities for which it is a fringe recorded in increasing order. Once S is stored in sparse column layout, (only non-empty columns are recorded, of course), it is a simple matter to compute the matrix product $S^T E S$ efficiently. The result is added to the sparse matrix A after the entire sparse matrix $S^T E S$ has been computed. A similar procedure is used to compute the contribution of triangle T to B .

Once the matrix A is set up, we factor it using a variant of the min-degree heuristic known as *sym_amd* to re-order the columns, and use our sparse Cholesky solver as described in Section 3.4.5.

5.7 Results

The primary numerical results were shown in Chapter 3. In Figure 3.25 on page 93, we showed a plot of the number of degrees of freedom that affect the variables at each node. In that computation, 101 extra basis functions near corners and junctions were used to capture asymptotic behavior, with many overlapping fringe regions. See also Figures 3.19, 3.29, 3.30, and 3.31 on pages 81, 97, 98, and 99, in which steady state displacement and stress distributions for the grain boundary diffusion problem were shown for various geometries.

In Figures 5.5, 5.6, and 5.7, we compare the steady state solution to the grain growth problem near a corner using XFOSLS (top) and standard Galerkin C^0 quadratic finite elements (bottom). It was necessary to refine the grid near the corner significantly in the Galerkin method, and even after doing so the solution near the corner lacks sufficient smoothness to be used effectively in the computation of K in Chapter 3. When viewed on a large scale, the solutions appear to agree perfectly, but when we zoom in on one of the corners, we find that the stress components obtained using the Galerkin method have very large discontinuities near the corner, and exhibit a large discrepancy between the specified traction (Lagrange multiplier) and the stress obtained from the displacements via the Lamé relations. In contrast, using a much coarser mesh, XFOSLS easily resolves the singularity smoothly.

In Figure 5.8, in order to show that XFOSLS works well uniformly in κ , we show the solution to the incompressible Lamé equations (i.e. the Stokes equations) on a hexagonal donut-shaped geometry with re-entrant corners. The inner hexagon remains fixed while the outer hexagon has boundary conditions corresponding to rotation clockwise by a radian. The fields “rotg” and “roth” are obtained from γ and τ via $\text{roth} = \gamma \sin 2\theta + \tau \cos 2\theta$ and $\text{rotg} = \gamma \cos 2\theta - \tau \sin 2\theta$, where θ is the polar coordinate with origin at the center of the geometry. Note that adjoining singular solutions spreads the error J evenly throughout the domain.

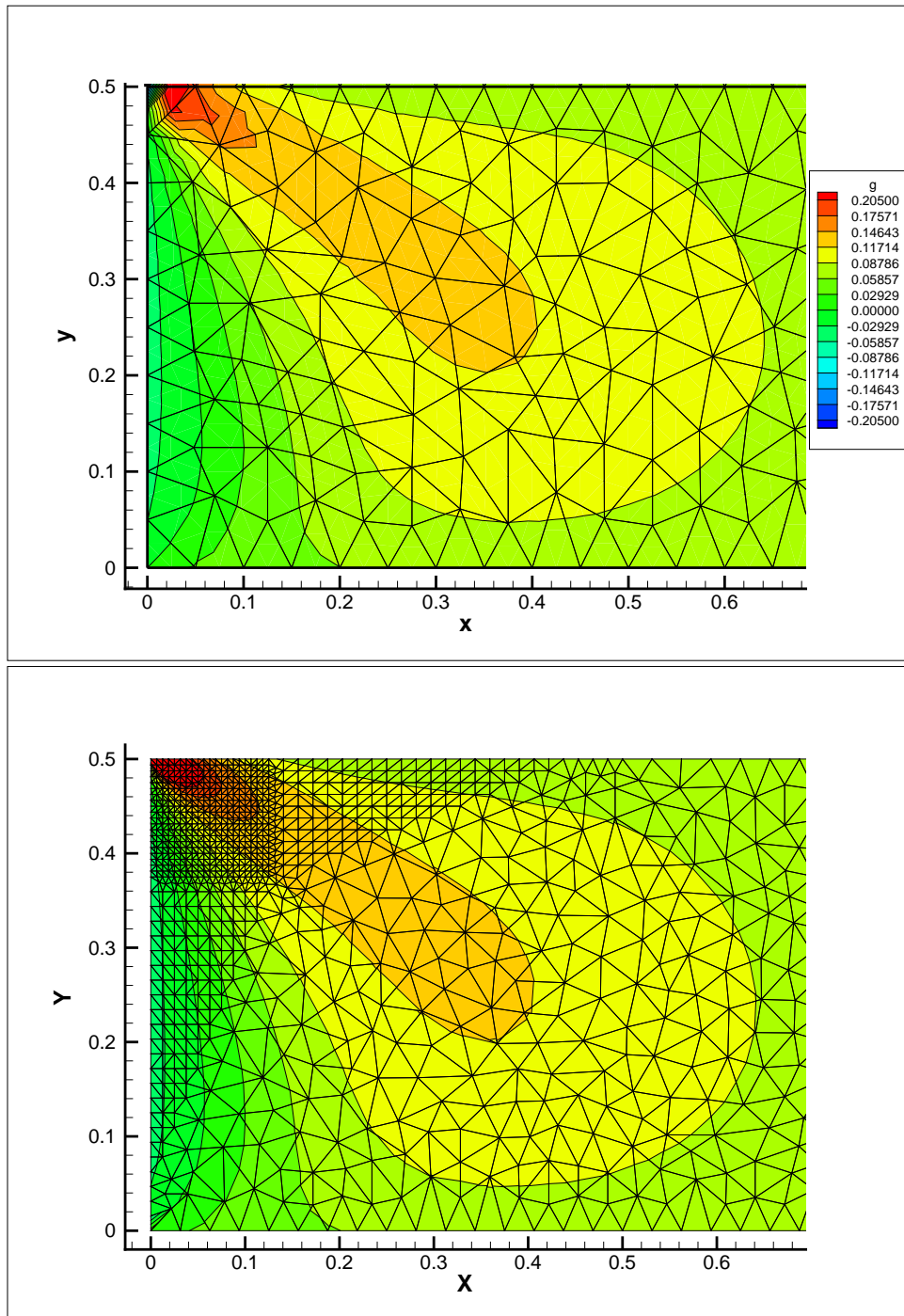


Figure 5.5: Comparison of γ for the steady state solution to the grain growth problem near a corner using XFOSLS (top) and standard Galerkin finite elements (bottom). The roughness of the contours in the top plot is an artifact of visualization, where linear interpolation is being used to compute contour lines on the four sub-triangles joining the six nodes of each triangular element; see also Figure 5.6.

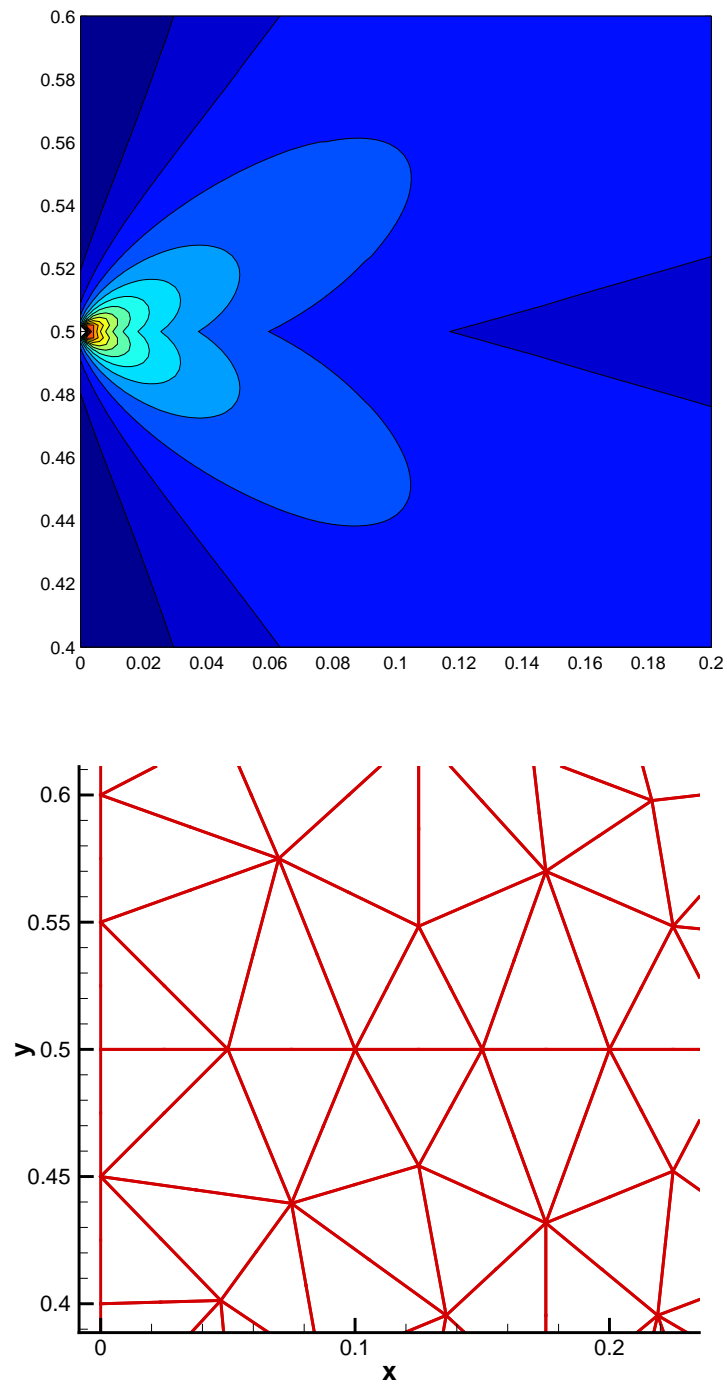


Figure 5.6: A contour plot showing the behavior of the solution γ from Figure 5.5 near a grain boundary junction with a wall. Points were uniformly sampled within the triangles of the mesh shown.

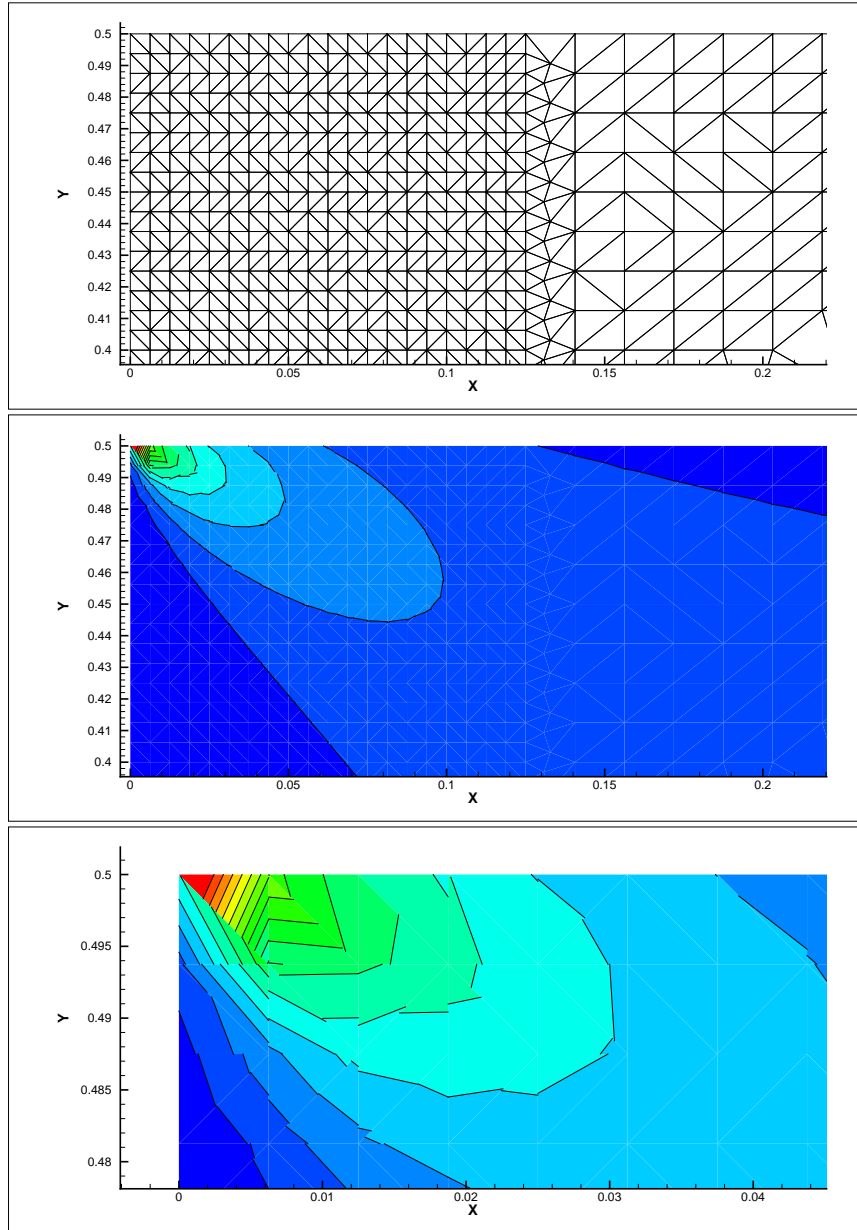


Figure 5.7: The solution obtained via the Galerkin method with a much finer grid still exhibits undesirable behavior near the corner, where the stress obtained via Lagrange multipliers differs significantly from the stress obtained by differentiating the displacements.

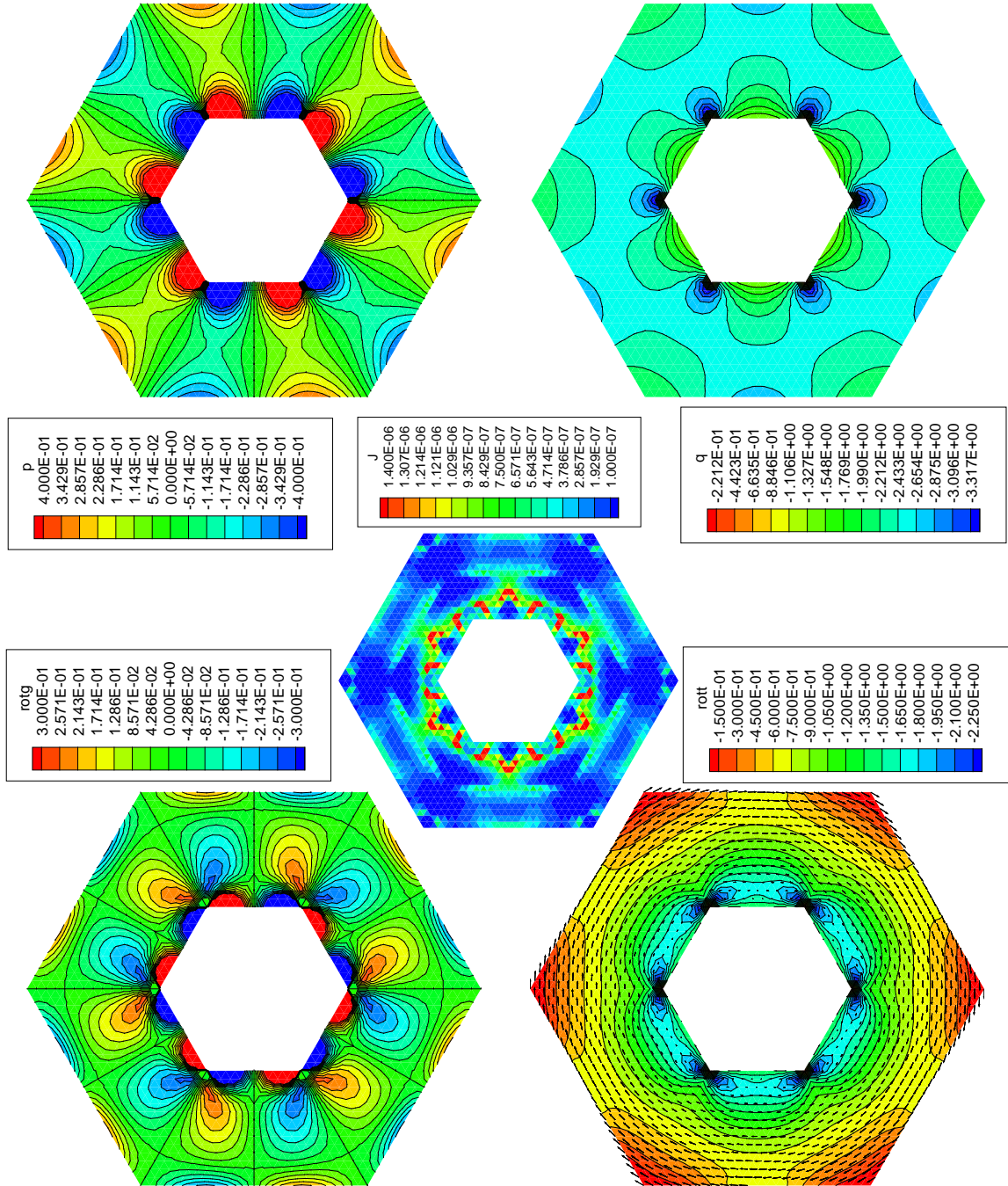


Figure 5.8: The solution of the Lamé equations with $\kappa = 1$ on a hexagonal geometry. Here the inner hexagon remains fixed while the outer hexagon has boundary conditions corresponding to rotation clockwise by a radian.

Chapter 6

Conclusion

The grain boundary diffusion problem turned out to be a very interesting mathematical problem because of the interplay between stiffness, non-locality, non-selfadjointness, singular behavior, and correspondence with physical phenomena. It was impossible to blindly apply a numerical method without first understanding a great deal about the asymptotic behavior of the stress variables near corners and junctions, and carefully thinking through the way the desired boundary conditions should influence the evolution of the grain boundary separation. (We learned this the hard way). On the other hand, it was not until we successfully implemented the numerical method that we learned that the operator B was self-adjoint and thought of a proof that K had a real, non-negative spectrum with a set of eigenfunctions spanning a dense subspace of $L^2(\Gamma)$. Much of our theoretical knowledge was obtained through struggling with the rather unforgiving numerical challenges of the problem.

Placing the grain boundary diffusion problem back into the larger model with void and vacancy evolution, it would be interesting to study the behavior of the solution in the vicinity of a junction where a void meets a grain boundary. Here again, questions of appropriate boundary conditions arise, thermodynamic arguments are murky, and singularities in the stress tensor and electric field together with the stiffness inherent in grain boundary diffusion and curvature driven surface diffusion make the problem difficult to attack theoretically and numerically.

Bibliography

- [1] S. Agmon, A. Douglis, and L. Nirenberg. Estimates near the boundary for solutions of elliptic partial differential equations satisfying general boundary conditions ii. *Comm. Pure Appl. Math.*, 8:35–92, 1964.
- [2] A. Averbuch, M. Israeli, I. Ravve, and I. Yavneh. Computation for electro-migration in interconnects of micro-electronics devices. *Journal of Computational Physics*, 167:316–371, 2001.
- [3] A. K. Aziz, R. B. Kellogg, and A. B. Stephens. Least squares methods for elliptic systems. *Mathematics of Computation*, 44(169):53–70, 1985.
- [4] Markus Berndt. *Adaptive Refinement and the Treatment of Discontinuous Coefficients for Multilevel First-Order System Least Squares (FOSLS)*. PhD thesis, University of Colorado at Boulder, 1999.
- [5] Markus Berndt, Thomas A. Manteuffel, and Stephen F. McCormick. Local error estimates and adaptive refinement for first-order system least squares (FOSLS). *Electronic Transactions on Numerical Analysis*, 6:35–43, 1997.
- [6] Andrew J. Bernoff, Andrea L. Bertozzi, and Thomas P. Witelski. Axisymmetric surface diffusion: Dynamics and stability of self-similar pinchoff. *Journal of Statistical Physics*, 93(3/4):725–776, 1998.
- [7] I. A. Blech. Electromigration in thin aluminum films on titanium nitride. *Journal of Applied Physics*, 47(4):1203–1208, 1976.
- [8] I. A. Blech and Conyers Herring. Stress generation by electromigration. *Applied Physics Letters*, 29(3):131–133, 1976.

- [9] A. F. Bower and D. Craft. Analysis of failure mechanisms in the interconnect lines of microelectronic circuits. *Fatigue and Fracture of Engineering Materials and Structures*, 21:611–630, 1998.
- [10] Dietrich Braess. *Finite Elements – Theory, fast solvers, and applications in solid mechanics*. Cambridge University Press, Cambridge, 1997.
- [11] J. H. Bramble and A. H. Schatz. Rayleigh-Ritz-Galerkin-methods for Dirichlet’s problem using subspaces without boundary conditions. *Comm. Pure Appl. Math.*, 23:653–675, 1970.
- [12] J. H. Bramble and A. H. Schatz. Least squares for $2m$ th order elliptic boundary-value problems. *Math. Comp.*, 25:1–32, 1971.
- [13] J. W. Cahn and J. E. Taylor. Surface motion by surface diffusion. *Acta metall. mater.*, 42(4):1045–1063, 1994.
- [14] Z. Cai, T. A. Manteuffel, S. F. McCormick, and J. Ruge. First-order system LL^* (FOSLS*): Scalar elliptic partial differential equations. *SIAM Journal on Numerical Analysis*, 39(4):1418–1445, 2001.
- [15] Zhiqiang Cai, Thomas A. Manteuffel, and Stephen F. McCormick. First-order system least squares for second-order partial differential equations: Part ii. *SIAM Journal on Numerical Analysis*, 34(2):425–454, 1997.
- [16] Zhiqiang Cai, Thomas A. Manteuffel, and Stephen F. McCormick. First-order system least squares for the Stokes equations, with application to linear elasticity. *SIAM Journal on Numerical Analysis*, 34(5):1727–1741, 1997.
- [17] Zhiqiang Cai, Thomas A. Manteuffel, Stephen F. McCormick, and Seymour V. Parter. First-order system least squares (FOSLS) for planar linear elasticity: pure traction problem. *SIAM Journal on Numerical Analysis*, 35(1):320–335, 1998.
- [18] C. L. Chang. A least squares finite element method for the Helmholtz equation. *Comput. Methods Appl. Mech. Engrg.*, 83:1–7, 1990.
- [19] Philippe G. Ciarlet. *Mathematical Elasticity*, volume 1. North-Holland, Amsterdam, 1993.

- [20] Earl A. Coddington and Norman Levinson. *Theory of Ordinary Differential Equations*. Krieger Publishing Company, Malabar, Florida, 1984.
- [21] Martin Costabel and Monique Dauge. Construction of corner singularities for agmon-douglis-nirenberg elliptic systems. *Math. Nachr.*, 162:209–237, 1993.
- [22] Martin Costabel and Monique Dauge. Stable asymptotics for elliptic systems on plane domains with corners. *Comm. Partial Differential Equations*, 19(9):1677–1726, 1994.
- [23] Martin Costabel, Monique Dauge, and Yvon Lafranche. Fast semi-analytic computation of elastic edge singularities. *Computer Methods in Applied Mechanics and Engineering*, 190:2111–2134, 2001.
- [24] Monique Dauge. *Elliptic Boundary Value Problems in Corner Domains – Smoothness and Asymptotics of Solutions*, volume 1341 of *Lecture Notes in Mathematics*. Springer-Verlag, Berlin, 1988.
- [25] C. Daux, N. Moes, J. Dolbow, N. Sukumar, and T. Belytschko. Arbitrary branched and intersecting cracks with the extended finite element method. *International Journal for Numerical Methods in Engineering*, 48:1741–1760, 2000.
- [26] B. Davies. Locating the zeros of an analytic function. *Journal of Computational Physics*, 66(1):36–49, 1986.
- [27] James W. Demmel. *Applied Numerical Linear Algebra*. SIAM, Philadelphia, 1997.
- [28] J. E. Dendy, Jr. Black box multigrid. *J. Comput. Phys.*, 48(3):366–386, 1982.
- [29] Gaetano Fichera. Existence theorems in elasticity. *Handbuch der Physik*, VIa/2:347–389, 1972.
- [30] Gerald B. Folland. *Introduction to Partial Differential Equations*. Princeton University Press, Princeton, 1995.
- [31] L. P. Franca, T. J.R. Hughes, A. F. D. Loula, and I. Miranda. A new family of stable elements for nearly incompressible elasticity based on a mixed petrov-galerkin finite element formulation. *Numerische Mathematik*, 53:123–141, 1988.
- [32] Leopoldo P. Franca and Thomas J.R. Hughes. Two classes of mixed finite element methods. *Computer Methods in Applied Mechanics and Engineering*, 69:89–129, 1988.

- [33] Daniel Fridline. *Finite Element Modeling of Electromigration and Stress Voiding in Microelectronic Interconnects*. PhD thesis, Brown University, 2001.
- [34] I. C. Gohberg and M. G. Krein. *Introduction to the Theory of Linear Nonselfadjoint Operators*, volume 18 of *Translations of Mathematical Monographs*. American Mathematical Society, Providence, RI, 1969.
- [35] P. Grisvard. Singularités en élasticité. *Archive for Rational Mechanics and Analysis*, 107(2):157–180, 1989.
- [36] P. Grisvard. *Singularities in Boundary Value Problems*, volume 22 of *Research Notes in Applied Mathematics*. Masson, Paris, 1992.
- [37] Conyers Herring. *Surface Tension as a Motivation for Sintering, chapter 8 of The Physics of Powder Metallurgy*. McGraw-Hill Book Company, New York, 1951.
- [38] Paul S. Ho and Thomas Kwok. Electromigration in metals. *Rep. Prog. Phys.*, 52:301–348, 1989.
- [39] D. Hull and D. Rimmer. the growth of grain-boundary voids under stress. *Philosophical Magazine*, 4:673–687, 1959.
- [40] H. Huntington and A. Grone. Current-induced marker motion in gold wires. *Journal of Physics and Chemistry of Solids*, 20(1):76–87, 1961.
- [41] Jim Douglas Jr. and Jean E. Roberts. Global estimates for mixed methods for second order elliptic equations. *Math. Comp.*, 44:39–52, 1985.
- [42] R. Kirchheim. Stress and electromigration in Al-lines of integrated circuits. *Acta metall. mater.*, 40(2):309–323, 1992.
- [43] Charles Kittel. *Thermal Physics*. W. H. Freeman and Company, New York, 2nd edition, 1980.
- [44] Charles Kittel. *Introduction to Solid State Physics*. John Wiley and Sons, New York, 7th edition, 1996.
- [45] V. A. Kondrat'ev. Boundary problems for elliptic equations in domains with conical or angular points. *Trans. Moscow Math. Soc.*, 16:227–313, 1967.

- [46] V. A. Kondrat'ev and O. A. Oleinik. Boundary-value problems for partial differential equations in non-smooth domains. *Uspekhi Mat. Nauk.*, 38(2):1–86, 1983.
- [47] M. A. Korhonen, P. Borgesen, K. N. Tu, and Che-Yu Li. Stress evolution due to electromigration in confined metal lines. *J. Appl. Phys.*, 73(8):3790–3799, 1993.
- [48] L. D. Landau and E. M. Lifshitz. *Theory of Elasticity*. Butterworth–Heinemann, Oxford, 3rd edition, 1986.
- [49] Stefan I. Larimore. An approximate minimum degree column ordering algorithm (COLAMD/SYMAMD). Master's thesis, University of Florida, 1998.
- [50] D. Leguillon and E. Sanchez-Palencia. *Computation of Singular Solutions in Elliptic Problems and Elasticity*. John Wiley and Sons, New York, 1987.
- [51] R. J. Leveque and Z. Li. the immersed interface method for elliptic equations with discontinuous coefficients and singular sources. *SIAM J. Numer. Anal.*, 31(4):1019–1044, 1994.
- [52] Zhilin Li, Hongkai Zhao, and Huajian Gao. A numerical study of electro-migration voiding by evolving level set functions on a fixed cartesian grid. *journal of computational physics*, 152:281–304, 1999.
- [53] Jian-ke Lu. *Complex Variable Methods in Plane Elasticity*. World Scientific, Singapore, 1995.
- [54] V. G. Maz'ya and B. A. Plamenevskij. Estimates in L^p and in Hölder classes and the Miranda-Agmon maximum principle for solutions of elliptic boundary value problems in domains with singular points on the boundary. *Amer. Math. Soc. Transl.(2)*, 123:1–56, 1984.
- [55] Charles B. Morrey, Jr. *Multiple Integrals in the Calculus of Variations*. Springer-Verlag, New York, 1966.
- [56] W. W. Mullins. Mass transport at interfaces in single component systems. *Metallurgical and Materials Transactions A*, 26A(8):1917–1929, 1995.
- [57] N. I. Muskhelishvili. *Some Basic Problems of the Mathematical Theory of Elasticity*. P. Noordhoff, Groningen, 2nd english edition, 1963.

- [58] N. I. Muskhelishvili. *Singular Integral Equations*. Dover Publications, Inc., New York, 2nd edition, 1992.
- [59] M. A. Naimark. *Linear Differential Operators, Part I*. Frederick Ungar Publishing Co., New York, 1967.
- [60] P. J. Papadakis and I. Babuška. A numerical procedure for the determination of certain quantities related to the stress intensity factors in two-dimensional elasticity. *Appl. Mech. Engrg.*, 122:69–92, 1995.
- [61] Gert K. Pedersen. *Analysis Now*. Springer-Verlag, New York, 1989.
- [62] A. I. Pehlivanov, G. F. Carey, and R. D. Lazarov. Least squares mixed finite elements for second order elliptic problems. *SIAM Journal on Numerical Analysis*, 31(5):1368–1377, 1994.
- [63] B. A. Plamenevskij. Elliptic boundary value problems in domains with piecewise smooth boundary. In M. S. Agranovich, Yu. V. Egorov, and M. A. Shubin, editors, *Partial Differential Equations IX*, volume 79 of *Encyclopaedia of Mathematical Sciences*. Springer, Berlin, 1997.
- [64] P.J. Rous, T. L. Einstein, and Ellen D. Williams. Theory of surface electromigration on metals: application to self-electromigration on cu(111). *Surface Science*, 315:L995–L1002, 1994.
- [65] Walter Rudin. *Real and Complex Analysis*. McGraw Hill, New York, 1987.
- [66] Walter Rudin. *Functional Analysis*. McGraw Hill, New York, 1991.
- [67] Anna-Margarete Sändig, Uwe Richter, and Rainer Sändig. The regularity of boundary value problems for the Lamé equations in a polygonal domain. *Rostock. Math. Kolloq.*, 36:21–50, 1989.
- [68] M. E. Sarychev, Y. V. Zhitnikov, L. Borucki, C. L. Liu, and T. M. Makhviladze. General model for mechanical stress evolution during electromigration. *Journal of Applied Physics*, 86(6):3068–3075, 1999.
- [69] M. Schimschak and J. Krug. Electromigration-induced breakup of two-dimensional voids. *Physical Review Letters*, 80(8):1674–1677, 1998.

- [70] J. A. Sethian. *Level Set Methods and Fast Marching Methods – Evolving Interfaces in Computational Geometry, Fluid Mechanics, Computer Vision, and Materials Science*. Cambridge University Press, Cambridge, 1999.
- [71] Jonathan R. Shewchuk. *Triangle: A Two-Dimensional Quality Mesh Generator and Delaunay Triangulator*. School of Computer Science, Carnegie Mellon University, Pittsburgh, 1996. Available at: <http://www.cs.cmu.edu/~quake/triangle.html>.
- [72] Rolf Stenberg. On the construction of optimal mixed finite element methods for the linear elasticity problem. *Numerische Mathematik*, 48:447–462, 1986.
- [73] Ben G. Streetman and Sanjay Banerjee. *Solid State Electronic Devices*. Prentice Hall, New Jersey, 2000.
- [74] John C. Strikwerda. *Finite Difference Schemes and Partial Differential Equations*. Chapman and Hall, New York, 1989.
- [75] N. Sukumar, N. Moës, B. Moran, and T. Belytschko. Extended finite element method for three-dimensional crack modelling. *International Journal for Numerical Methods in Engineering*, 48:1549–1570, 2000.
- [76] E. C. Titchmarsh. *Introduction to the Theory of Fourier Integrals*. Oxford University Press, Oxford, 2nd edition, 1948.
- [77] King-Ning Tu, James W. Mayer, and Leonard C. Feldman. *Electronic Thin Film Science for Electrical Engineers and Materials Scientists*. Macmillan Publishing Company, New York, 1992.
- [78] B. L. van der Waerden. *Modern Algebra*. Unger, New York, 1949.
- [79] L. R. Volevich. On general systems of differential equations. *Soviet Math.*, 1:458–461, 1960.
- [80] L. R. Volevich. On the theory of boundary value problems for general elliptic systems. *Soviet Math.*, 4:97–100, 1963.
- [81] Peter Van Zant. *Microchip Fabrication – A Practical Guide to Semiconductor Processing*. McGraw–Hill, New York, 2000.

- [82] Mark W. Zemansky and Richard H. Dittman. *Heat and Thermodynamics*. McGraw-Hill, New York, 7th edition, 1997.